Mixture Preparation of Gaseous Fuels for Internal Combustion Engines Using Optical Diagnostics

A thesis submitted in fulfilment of the requirements for the degree of Doctor of Philosophy

Thomas James Rogers

B.ENG

School of Aerospace Mechanical and Manufacturing Engineering

College of Science Engineering and Health

RMIT University

October 2014

Declaration

I hereby declare that:

i. Except where due acknowledgement has been made, the work is that of the candidate alone (see the Higher Degrees by Research – editing policy);

ii. The work has not been submitted previously, in whole or in part, to qualify for any other academic award;

iii. The content of the thesis is the result of work which has been carried out since the official commencement date of the approved research program;

iv. Any editorial work, paid or unpaid, carried out by a third party is acknowledged;

v. Ethics procedures and guidelines have been followed

Thomas James Rogers

October, 2014

Acknowledgements

Dr Campbell Aitken of Express Editing Writing and Research provided professional editing services in accordance with the Institute of Professional Editors' Guidelines for editing research theses (approved by the Deans and Directors of Graduate Studies).

With any great endeavour, no individual alone has the ability to succeed. In this acknowledgement I express my sincerest thanks to all those whom helped, guided and even turned a blind eye throughout this pursuit.

First and foremost, Dr Lucien Koopmans is gratefully acknowledged for seeing potential in an otherwise ordinary student. Your generous teaching on all things engineering (and life) is incomparable. I am indebted to the opportunity you provided and for making me a better engineer.

Dr Petros Lappas, my principal advisor in the latter half of my tenure, your passion for science was a constant source of inspiration. Your meticulous eye for detail pushed me to achieve more than my expectation – for which I am thankful.

I wish to also extend my gratitude to Prof Aleksandar Subic and Prof Kevin Massey for their guidance, assistance and support. I owe a great many thanks to Prof Simon Watkins, my unofficial advisor, for mentoring me unreservedly. I am also in appreciation of several faculty whom offered constant motivation for me to become a well-rounded researcher and academic. I would like to particularly thank: Dr Mohammed Fard, Dr Martin Leary, Dr Caleb White and Mr Geoff Pearson. Throughout the numerous conversations over the last five years, typically over a screaming coffee machine, small pearls of wisdom would always be offered freely and without obligation. My collection of such wisdom is substantial beyond your realisations. Dr Prashanth Karra is thanked for his contribution to the PIV experiments and the entrainment calculations.

The technical staff of the SAMME are also recognised as contributors to this work for materialising the resources for the Green Engine Laboratory and my own experimental needs. I would particularly like to thank Mr Brett Vincent, Mr Patrick Wilkins, and Mr Don Savvides. Likewise Mr Thierry Perret-Ellena's support with the design elements of this project are appreciated.

Mr Phred Petersen, our likeminded sense of humour and our various discussions on end-grain and hops kept my mind on the bigger picture. More importantly, your ability to capture the seemingly invisible and your willingness to freely share your knowledge of photography is greatly appreciated. The time we shared in the laboratory behind mirrors and cameras resolving flow structures (among other things) are some of my fondest learning experiences.

To my parents who sacrificed throughout my child and early adulthood so that I could pursue and achieve my desires I am truly thankful. I have never taken my privileges in receiving an education for granted, but perhaps unacknowledged ‘till now.

Lastly, to Chloe my beautiful partner who endured five years of my absence; thank you for being my all and everything. I couldn’t have completed this degree without your love, encouragement and wisdom. Any success I have will undoubtedly be owed to you; in small and great ways.

“Power lines are a reminder of man's ability to generate electricity”

Darryl Kerrigan

Contents

THIS PAGE IS INTENTIONALLY BLANK

List of Figures

List of Tables

Nomenclature

Abbreviation	Description
A	Area
$aEOI$	After end of injection
$aSOI$	After start of injection
$aTDC$	After top dead centre
$BMEP$	Brake mean effective pressure
$bTDC$	Before top dead centre
c	Speed of Sound, constant
C	Velocity decay coefficient
C_D	Drag or Discharge coefficient
C_u	Velocity decay coefficient
C_X	Barrel Length or Mach Disc location constant
CAD	Crank angle degrees
CI	Confidence interval
CNG	Compressed natural gas
COV_{IMEP}	Coefficient of variation IMEP
DI	Direct injection
D_{MD}	Mach disc diameter or height
EOI	End of injection
FPS	Frames per second
f	Focal Length or cylinder fill level
GDI	Gasoline direct injection
ICE	Internal combustion engine
$IMEP$	Indicated mean effective pressure
HSV	High speed video
i	Axial pixel coordinate
j	Radial pixel coordinate
J	Momentum flux
K_1	Entrainment constant

K_2'	Entrainment coefficient
Kn_p	Knudsen number
l	Mean free path length
L	Length scale
LPM	Litres per minute
m	Mass
$\dot{m}$	Mass flow rate
M	Mach number, Molar mass
N	Nozzle or sample size
NCL	Nozzle centre line
$NEDC$	New European Drive Cycle
NPR	Nozzle pressure ratio
NTS	Not to scale
px	Pixel(s)
PFI	Port fuelled injection
PIV	Particle image velocimetry
Pr	Probability
PR	Pressure ratio
r	Radial coordinate
s	Self-similarity index
Re	Reynolds number
ROI	Region of interest
SOI	Start of injection
SI	Spark ignition
St	Stokes number
t	Time
TDC	Top dead centre
$TDCF$	Top dead centre firing
TKE	Turbulent kinetic energy
u	Velocity, radial component
U	Spatial mean of $\bar{u}$
v	Velocity, axial component
V	Velocity, Spatial mean of $\bar{v}$
x	Axial coordinate

X_c	Non-dimensional core length
X_{MD}	Barrel length or axial location of Mach disc
y	Radial coordinate
z	Axial coordinate

Greek and Special Characters

α	Mach disc reflection angle
λ	Wavelength or air fuel ratio
ρ	Density
τ	Characteristic time
σ	Standard deviation
θ	Angle
$\|V\|$	Resultant velocity
$\acute{}$, $'$	Instantaneous velocity fluctuation (acute/apostrophe)
$\bar{}$	Mean (overbar)

Subscripts

Δ	Time-scale for interrogation-window limited eddies
0	Origin
a or amb	Ambient
CL	Centerline
e	Exit or entrained ($\dot{m}_e$)
eq	Equivalent
exit	Nozzle exit
F, f	Fluid
j	Jet
MD	Mach disc
n	Nozzle
o	Supply
P	Particle

ps	Pseudo
rms	Root mean square
SL	Shear-layer
t	Throat or time-scale for large eddies
TP	Triple point

Abstract

The flow and mixing behaviour of high pressure directly injected fuel is important in the study of spark-ignition engines owing to its strong influence on the combustion process. This in turn governs emissions and power generation, which are important considerations in contemporary vehicle design.

Whilst liquid fuel delivery has and continues to be a topic of detailed research, there is a deficit in the understanding of gaseous fuel delivery. Three topics remain largely neglected for high pressure CNG fuel injection in spark-ignition engines: i. the targeting and dispersion behaviour of the gaseous fuel jet, ii. the transient jet behaviour near the nozzle exit region ("*nearfield*") and iii. the effects of the jets on the in-cylinder flow and turbulence.

Using optical diagnostics that include schlieren high-speed imaging and particle image velocimetry (PIV), this work addresses the knowledge deficit. The investigation primarily covers jets issued from a direct injector for gaseous fuels that was constructed in-house. A constant volume chamber was employed to replicate engine-like conditions quiescently, allowing isolation of the injection delivery phenomena.

For topic i, jet targeting behaviour was characterised by axial and radial penetration, spread angle and projected area. The targeting profile of a freestream jet is in good agreement with previously established density normalised incompressible jet relationhips. Additionally, empirical correlation is provided between the jet dispersion and pressure ratio ($8.3 < \mathrm{PR} < 400$) for conditions when the jet impinges on the cylinder boundaries.

For topic ii, the injector needle lift profile was found to be a dominant factor in controlling nearfield compressible and incompressible flow structures. The presence of the needle was shown to reduce the Mach disc location downstream of the nozzle by $\sim 45\%$, at steady-state conditions. Moreover, in transient conditions the Mach disc location and diameter are shown to correlate strongly with the needle lift profile. This result highlights the importance of including the dynamic internal geometry of the injector when modelling fuel jet behaviour; a typical omission in the numerical modelling field.

The evolution of the compressible fuel jet features are measured for the first time at fine temporal resolution ($12 - 22$ μs intervals). The jet-to-air shear-layer thickness and outer jet-boundary width are shown to develop in direct proportion to the Mach disc diameter. The high-resolution characterisation of such features is important for stratified engine operation where a slightly mistimed jet may result in misfire due to the large velocities across the spark-plug electrode.

In relation to topic iii, PIV was used to capture the flow velocity in two key regions: the air in the nearfield and the ignition zone where a spark plug would be conventionally placed. Velocity maps of the entire jet and surrounding in-cylinder region were taken for two instances after start of injection: 215 and 415 μs. They were also acquired when the fuel occupied 30% and 50% of the combustion chamber volume.

The rate of air entrainment into the jet is shown to be proportional to the fuel delivery rate. The entrainment rate was also found to steadily increase with increasing delivery time aSOI (within the measurement time domain). Spatially, the nearfield entrainment coefficient, K'_2, is shown to remain constant at a mean value of $K'_2 = 0.123$. Moreover, the displacement of air caused from the impinging induced jet vortices is shown to feed air into the nearfield entrainment region. Consequently, for the highest PR experiments ($PR320$ and 400) the nearfield entrainment coefficient, K'_2, is shown to increase $\sim 65\%$, relative to the lower PR experiments.

Ignition region turbulent kinetic energy levels induced by the impinging jet are conducive to good flame propagation where mean values (0.5-$19\ m^2/s^2$) are similar to those created by typical air induction bulk-flow. Mean flow velocities are also within an acceptable spark plug ignition range (1.8-$21.0\ m/s$). Both flow properties are shown to be heavily influenced by the proximity of the jet boundary. As a result of the ignition and nearfield region measurements, a clear understanding of the transient nearfield processes has been developed to help one design appropriate fuel delivery and combustion strategies.

1. Introduction

1.1 Motivation and Scope

The key motivation behind this work is the reduction of passenger vehicle emissions. It is well understood and widely accepted that passenger vehicle transportation contributes considerably to the reduction of air quality, particularly in urban areas, where air pollution increases public health risks and environmental detriment (i.e. (Shindell et al., 2011)). Gaseous-fuelled passenger vehicles offer two main advantages over their liquid-fuelled counterparts: a reduction in harmful pollutants; chiefly carbon-dioxide and particulate matter, and a lower reliance on traditional liquid fossil fuels, leading to increased national energy supply resiliency. To this end, the use of compressed natural gas is an attractive option for fuelling passenger vehicles.

The combustion characteristics of compressed natural gas spark-ignited internal combustion engines are well known, with extensive literature on the subject. The continual improvement in specific power and lower emissions output has driven the development of direct-injection gaseous engines as both dual (McTaggart-Cowan et al., 2006) and single fuel solutions (Caley and Cathcart, 2006). Preceding combustion, an appropriate air-fuel mixture must be formed and for direct injection engines the most influential part of this process is the fuel delivery into the cylinder.

Direct injection of gaseous fuels governs the combustion process in two distinct manners. Firstly, the fuel distribution and concentration is controlled by the delivery and mixing process. Secondly, the injection event disrupts and controls the in-cylinder flow and turbulence (Salazar and Kaiser, 2011). These two effects are cyclical – where one effects the other, and are compounded by other influences, for example: gas-exchange. If actual air-fuel concentration levels are ignored, the targeting and dispersion behaviour of the fuel jet is still of substantial importance.

The study of direct injection gaseous fuel delivery and mixture preparation is not new. Several studies have shown the freestream targeting behaviour of gas jets experimentally (Baert et al., 2010, Johansen et al., 2013, Yu et al., 2013b) and numerically (Abraham, 1996, Ouellette and Hill, 2000, Post et al., 2000, Abani and Reitz, 2007, Owston et al., 2008, Bonelli et al., 2013). Additionally, impinging jets on cylinder boundaries at engine-relevant conditions have also been investigated numerically (Gerke, 2007, Baratta et al., 2008, Baratta et al., 2011) and experimentally (Salazar and Kaiser, 2009, Bruneaux et al., 2011, Yu et al., 2012, Bovo and Rojo, 2013).

The existing literature, whilst extensive, has the following key deficits:

1. Most experimental studies consider Hydrogen or inert/non-fuel gases. Methane or CNG (a blend fuel with methane as the majority) are rarely employed.
2. Pressure ratios are typically investigated at a range of 3 to 50, typically under 20 and very few works exceeding pressure ratios above 50.
3. Most studies detail the steady-state conditions in great detail but fail to address the starting transient region. Very little detail is provided for times <1.0 ms after start of injection. In fact, to the author's knowledge only one article details the transient evolution of the compressible flow structures of a highly underexpanded (NPR>2) fuel jet: (Lacerda, 1987).
4. Very few experimental (or numerical) examples are provided on gaseous fuel delivery at late-injection conditions – where the combustion may be regarded as stratified and where physical boundaries influence the fuel delivery and in-cylinder flow dynamics.

These gaps in the present literature can be categorised into three main research objectives, through the characterisation of the:

i. targeting and dispersion behaviour of the gaseous fuel jet
ii. transient jet behaviour near the nozzle exit region ("*nearfield*")
iii. effects of the jets on the in-cylinder flow and turbulence

In the present work, these three research objectives are investigated to yield a more complete understanding of high-pressure direct-injection, CNG mixture preparation.

1.2 Research Questions

With the scope of research, defined through the three research objectives, a series of more discrete questions are raised. This thesis is guided by the following research questions:

1. *Can highly resolved imaging provide quantitative insight into transient turbulent jet structures and characteristics?*
2. *What influence does the density ratio have on the jet flow-characteristics and on the mixture process?*
3. *How do the shock phenomena affect the internal structure of the fuel jet and the surrounding regions immediately after jet delivery?*
4. *How does a high pressure-ratio influence the jet flow-characteristics and the mixture process?*
5. *Can the nearfield entrainment rate be quantified using current particle image velocimetry methods for early stages of transient jet development?*
6. *How do non-dynamic physical boundaries influence mixture formation (i.e. impingement)?*

1.2 Thesis Organisation

The goal of this thesis is to provide a comprehensive characterisation of gaseous fuel jets. Free and impinging jets are studied using optical diagnostics to gain a fuller understanding of fuel delivery mixture preparation relevant to contemporary spark-ignition internal combustion engines.

Chapter 2 introduces the essential concepts, descriptions, and most importantly, highlights the state of the art. This chapter takes the form of a literature review outlining what has been done and remains to be studied – this constitutes the present research opportunities. The chapter is divided in two main sections; the first deals with engine related concepts whilst the second details the aspects of free and impinging jets.

Chapter 3 covers the investigation principals and methods. Detailed discussions are provided on the two main optical diagnostic methods used in the study: schlieren high speed imaging and particle image velocimetry (PIV). Additionally, the fuel employed and the injectors from which it is issued are specified. The approach on how the data are treated, post-processed and analysed statistically is also provided.

Chapter 4 covers tests in which schlieren high-speed imaging is used to identify jets issued at low pressure ratios. The jets considered reach a maximum pressure ratio of twelve and thus are "*low*" in comparison to the main objective of the thesis where pressure ratios exceed forty. Regardless, in Chapter 4 a detailed characterisation of freestream and impinging jets is provided where multiple fuels are employed to study variation in fuel density. The measurements and analysis used in this chapter represent the type of characterisation necessary when evaluating fuel jet targeting for mixture preparation.

Chapter 5 presents the flow characteristics of high pressure CNG fuel jets. This Chapter studies, much in the same manner as Chapter 4, two flow areas: the incompressible macro structures and the compressible internal features of the highly underexpanded jets. Jets are issued impulsively from a 1.00 mm diameter nozzle and are representative of direct injection conditions. The interplay between key flow characteristics are discussed where links between the incompressible and compressible flow structures are shown. The compressible features are shown to be highly dependent on the pressure ratio and the presence of the injector needle geometry. Chapter 5 predominately presents schlieren imaging to resolve the critical flow features with a contribution from PIV techniques when resolving the Mach disc location.

Chapter 6 deals with the research questions surrounding high pressure ratio mixture formation and exclusively covers jets issued into a quiescent in-cylinder-like environment. It provides detail on how the fuel jet behaves in in-cylinder gas densities found during engine operation. The flow characteristics of high-pressure CNG jets are made apparent with discussion on the: ambient air entrainment, ambient air flow structures, jet recirculation as well as the flow-structures and turbulence levels formed within the ignition zone. Other interesting features such as the condensate produced upon the high in-jet exit velocity when *realistic* fuel compositions are introduced and discussed for the first time. This chapter exclusively deals with impinging CNG jets.

Concluding the thesis is Chapter 7 where the main research contributions are summarised against the research objectives. This overall conclusion chapter sits in contrast to the conclusions at the end of Chapters 4, 5 and 6 which explicitly address individual research.

THIS PAGE IS INTENTIONALLY BLANK

2. Background and Literature Review

This chapter is divided into two main sections. The first is application-based with, and contains discussion of engine operation and fuel delivery. The second provides detailed information on the more fundamental aspects of turbulent jets with discussion centred on flow behaviour and the structures of jets.

2.1 Engine Fuelling Requirements

The brake-specific output of modern spark-ignition (SI) engines is continually in-line with consumer and legislative requirements. A consequence of this trend is increased demand on the engine fuel system. From a delivery perspective, two main objectives are central to the implementation of gaseous-fuelled engines. These objectives are to:

1. Form a correct mixture, homogeneous or stratified, within the small operating window between intake valve closure and the start of ignition.

2. Design a reliable injector that will not only supply adequate fuel but be affordable for passenger vehicle engines.

The first objective is the focus of this thesis, while the second is outside the scope of the research but is a key enabler if gaseous fuel is to take place in the mainstream. The injection time window for a typical engine is shown below in Figure 1. The window available, ~6-40 ms, is inversely proportional to the engine speed. Engine speed is only one of several determinants of fuelling requirements but a crucial one due to the short available time in which injection is possible for a direct injection (DI) spark-ignition engine.

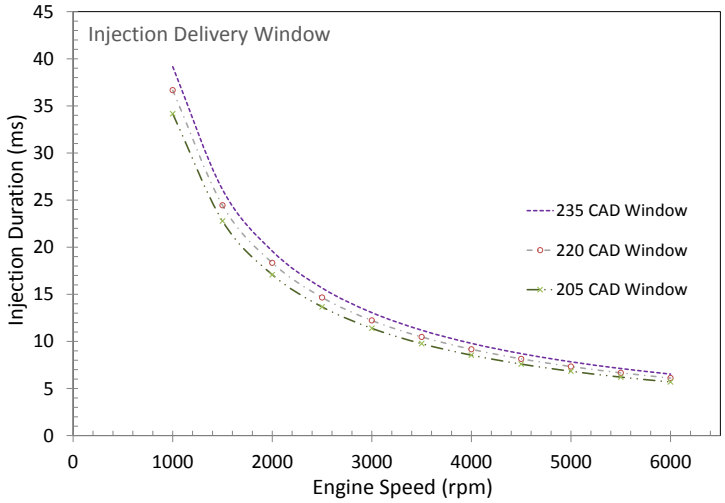

Figure 1, Injection duration window for a typical DI engine.

It is apparent that to accomplish the requirements of injection at high speed a fast-acting, high-flow rate injector is needed. These injection times are further diminished if there is to be a period of air-fuel mixing in the cylinder prior to ignition, when the injector has ceased delivery. Kaiser and White (2008) suggested the mixing time for gaseous DI hydrogen engines is in the order of 4-20 ms.

Figure 2 presents the requirements of a typical fuel injection system for a modern turbocharged DI gasoline engine (representative of a cross-section of current OEM standards). The necessary energy levels required for each injection event are depicted for an entire engine map. The energy delivered is shown against brake mean effective pressure (BMEP) and speed (rpm). This depiction allows one to appreciate the requirements for real-world end-users as all operational losses (friction, volumetric efficiency, thermal et cetera) are accounted for.

The pale red region shown in Figure 2 represents the portion of the engine calibration map in which stoichiometric ($\lambda = 1$) operation is necessary to meet legislatively mandated emissions levels. Stoichiometric operation in this region allows the best possible reduction of pollutants in the aftertreatment system. Stoichiometric conditions are typically cyclic, not absolute, to achieve reduction of conflicting pollutants or regeneration of particulate filters. Conversely, outside of the legislative window, which is operationally governed by the relevant drive cycle (typically the NEDC), emission reduction is deprioritised in favour of torque/power and component protection at the upper limits.

It can be seen in Figure 2 that energy requirements increase significantly with increasing load (BMEP), speed (rpm) and mixture concentration (AFR); a range between 256 and 3139 Joules per injection event is required across the entire map. Unsurprisingly, this ~1200% increase in energy reduces the metering accuracy of fuel injectors, evidently at their operational limits. Fortunately, a

window exists in which accurate metering is of most importance; where exhaust emissions are measured, a decreased but still significant operational range of 840%.

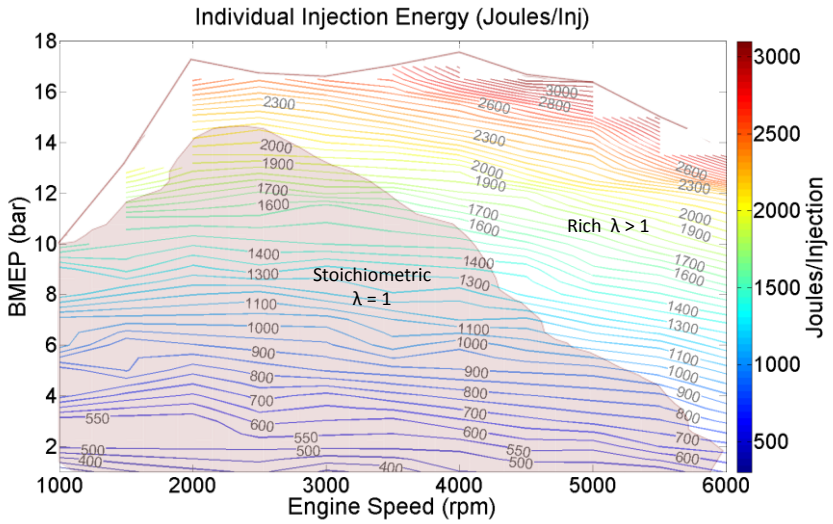

Figure 2, Representative energy requirements per injection across a full engine map. Source data: confidential.

The work described in this thesis focused exclusively on a window that reflects the day-to-day driving experienced by most SI-engiend vehicles regardless of their powertrain configuration. The window selected combines a speed range of 2000 to 4000 rpm and part-load operation of 2.0 to 4.0 Bar BMEP. This area is also a key range for emissions testing and has opportunities for a wide open throttle (WOT) stratified operation mode (Hemdal et al., 2011). The energy and fuelling requirements are summarised in Table 2.

2.2 Delivery of Alternative Fuels – Energy, Mass and Volume

In this section a brief snapshot of the delivery features of gaseous and liquid fuels is presented to better scope the overarching delivery requirements and to provide insight into the mechanisms which affect the amount of fuel delivered. A holistic investigation of time, mass and energy can be applied to yield the fullest picture and attempt to decouple some variables.

Gaseous fuels, relative to gasoline, have limitations due to their mass-density. For example the gravimetric density of methane, hydrogen and model-gasoline (iso-octane) are 0.080, 0.650 and 692 kg/m^3, respectively. The liquid fuel thus has a density some three orders of magnitude higher than its gaseous counterparts. Furthermore, for a truer comparison at engine conditions, correlation to a stoichiometric mixture yields volumetric energy content of 3041 and 3189 kJ/m^3 for methane and hydrogen respectively, whilst iso-octane has a substantially higher energy density of 3704 kJ/m^3 (Verhelst and Wallner, 2009). This energy/mass/volume conundrum requires larger fuel injector orifices (effective opening areas), higher delivery pressures and increased injection durations for gaseous fuels. These three requirements are fraught with technological issues where; sealing/delivery problems arise due to combustion deposits or the lack of fuel lubricity, a larger energy input is required for higher pressure compressibility on-board pressure amplification is needed, and there is inadequate time to deliver enough mass particularly under high-load high-speed conditions.

Figure 3 contains a comparison between DI compressed natural gas (CNG) and gasoline. For an identical injector to achieve a mass delivery of 7.6 mg, CNG requires a 2.0 ms injection duration at an 80 bar supply pressure, whilst the same mass for gasoline is achieved at half the fuel pressure in under one-third of the time (0.6 ms[1]). The energy supplied for combustion is different (approx. 50 vs. 44 MJ/kg), but the problem is obvious –trade-offs must be made.

This problem is compounded further if we introduce hydrogen, another highly attractive alternative fuel. Figure 3 shows that use of hydrogen leads to an order-of-magnitude reduction in mass delivered (0.76 mg per 2.0 ms). The consequences of the physical properties of fuel on delivery mass are highlighted in Figure 3, where CNG and hydrogen are presented alongside three intermediate fractions: 25%H_2/CH_4, 50%H_2/ CH_4 and 75%H_2/ CH_4. Interestingly adding 25% hydrogen to methane causes a mere 3% drop in mass. This 3% mass loss is easily compensated for when accounting for the energy delivery gain; hydrogen easily surpasses both gasoline and CNG with 120 MJ/kg. Beyond the 25%H_2/CH_4 fraction, substantial variance exists between the gases with respect to mass delivered.

[1] Taken from OEM confidentially supplied data sheet and not as tested by author.

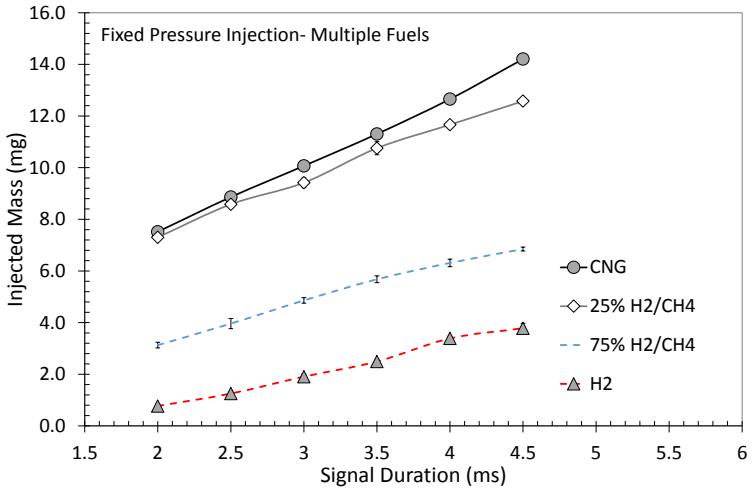

Figure 3, Consequences of fuel properties on mass delivery. Data obtained from a high-pressure direct injector operated at PR80.

For this consideration alone and all the other research put forward on H_2CNG blends there is a strong push for commercialisation of this blend, even potentially skipping CNG altogether. The industry is converging on a commercially available blend of CNG 20-30% hydrogen (National Petroleum Council, 2012) for reasonable emissions reduction benefit without affecting base-engine reliability. This concentration level also reflects good environmental value at a net energy perspective (Villante and Genovese, 2012). Moreover, it has been shown that even small additions of hydrogen (10%) to highly-concentrated CO_2 natural gas (land-fill gas) has substantial advantages (Porpatham et al., 2007).

As the fuel delivery mass is a function of the fuel's physical and chemical make-up the appropriate delivery of gaseous fuel is also a concern for port fuel injection (PFI) engines. PFI gaseous SI engines represent the vast majority of engines today and are unlikely to be phased out in the next several years, particularly in developing countries such as Thailand and India. A simple comparison between PFI and DI injection mass is presented in Figure 4 below. It is shown that for small DI injection masses an increase factor of 4.88 (on average) in mass exists between CNG and hydrogen. This factor is 2.42 (on average) for the PFI injector. The challenges of delivering enough hydrogen, even compared to a relatively poor performer like CNG are apparent.

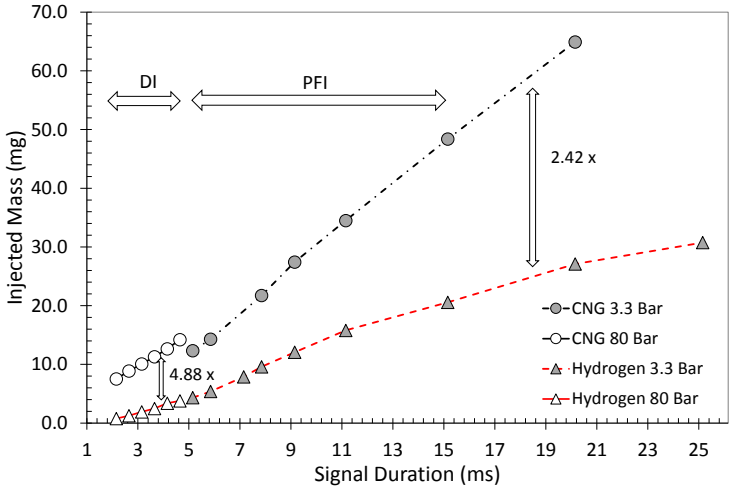

Figure 4, CNG and Hydrogen mass delivery for a low-pressure port-fuel injector and a high-pressure direct injector.

The challenge of fuel-air mixing to achieve a desirable concentration (typically homogeneous across the cylinder volume) is compounded by the fact that fluidic mixing is a function of the ratio of viscous forces between the two fluids (Lee et al., 2004). Akin to friction, the shearing of the fuel-air media at their interface short-term mixing, with other attributes like buoyancy and free-dispersion rates affecting time windows typically outside of DI ICE conditions. The mixture of a gaseous jet in a quiescent environment can be defined through forced convection and turbulent diffusion transport considerations.

An advantage of liquid fuels is that the (partial) phase-change from liquid to vapour is a positive attribute because convective currents due to rapid cooling are introduced, aiding the mixture preparation. This advantage is obviously not present with single-phase gas injection. Some key physical and chemical properties that affect the fuel delivery process for liquid and/or gas fuels are noted in Table 1.

Table 1, Fuel properties affecting fuel delivery requirements.

Density (kg/m^3)	Kinematic Viscosity (m^2/s)	Heat of Vaporisation (kJ/kg)
Molecular Weight (g/mol)	Dynamic Viscosity (Pa.s)	Speed of Sound (m/s)
Specific Volume (m^3/kg)	Momentum Flux (J)	Vapour Pressure (bar)

A set of injection mass and volume figures for CNG, hydrogen and iso-octane is outlined in Table 2 for a fixed energy value based on the mean representation for the operational window considered (2000-4000 rpm, 2.0-4.0 bar BMEP). These seemingly basic values form the fundamental delivery requirements for an individual fuel injector.

Table 2, Energy, mass and volume requirements for present work. Values obtained and calculated for a window between 2000-4000 rpm and 2.0-4.0 bar BMEP.

	CNG	*Hydrogen*	*iso-Octane*	
Mean (Joules)	602	602	602	Energy
Minimum (mg)	10.260	4.275	12.512	Mass
Maximum (mg)	15.380	6.408	18.756	
Mean (mg)	12.054	5.022	14.700	
Mean (mL)	183.197 x 10^{-3}	67.989 x 10^{-3}	21.243 x 10^{-3}	Volume (100 bar, 298 K)

Table 2 highlights the overarching P-V relationship for a gas density according to ideal gas laws. Note that the volume fraction of hydrogen, a low molecular mass fuel, is substantially smaller than that of CNG. The hydrogen delivery volume is offset by its substantially greater volumetric energy density (kJ/m^3). To give this point further perspective, Figure 5 presents the ideal gas law at two temperatures across the typical pressure delivery range expected in a gas fuelled engine. Again, it can be seen that there are substantial advantages in delivering a high pressure fuel, but this leads to the questions: *are there negative consequences and can an optimal delivery pressure be defined*?

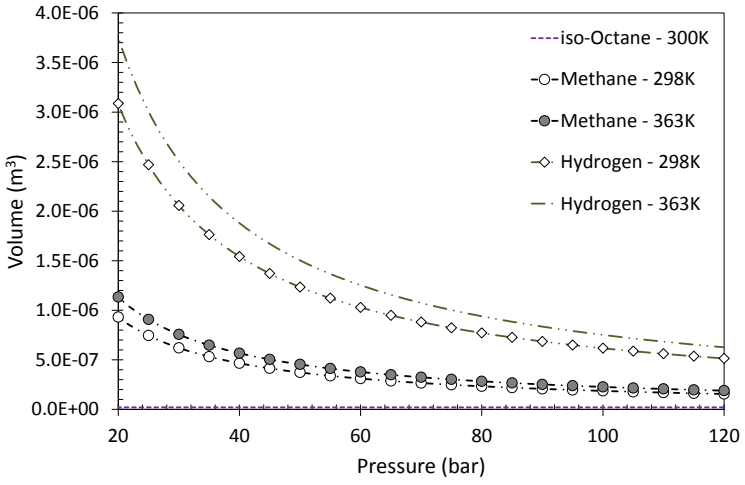

Figure 5, Pressure and temperature volume effects for a constant energy (602 Joules) and mass (fuel specific).

Figure 5 shows that, for a constant engine-realistic fuel mass delivered, the volume delivered substantially decreases beyond 40 bar pressure. As the pressure is increased the volume of the gaseous fuels will asymptote toward the incompressible *iso*-octane. The volume requirement is derived from the underlying energy requirement of 602 Joules using the ideal gas law and density relationships below:

Equation 1, Ideal Gas Law. Source: (Jones and Hawkins, 1960)

$$V = \frac{nMRT}{P}$$

Equation 2, Ideal Gas density. Source: (Jones and Hawkins, 1960)

$$\rho = \frac{MP}{RT}$$

where, n, M, R, T for the specific gas are the number of moles, molar mass, gas constant and temperature respectively.

It should now be clear that the relationships between fuel delivery and engine operation are determined by numerous variables and that full isolation of such parameters is not straightforward, but made simpler if all engine and fuel delivery requirements are collapsed to energy. In this work, energy is the basis for all investigations. Figure 6 below gives a summarised dependency flow-chart centred on this principle.

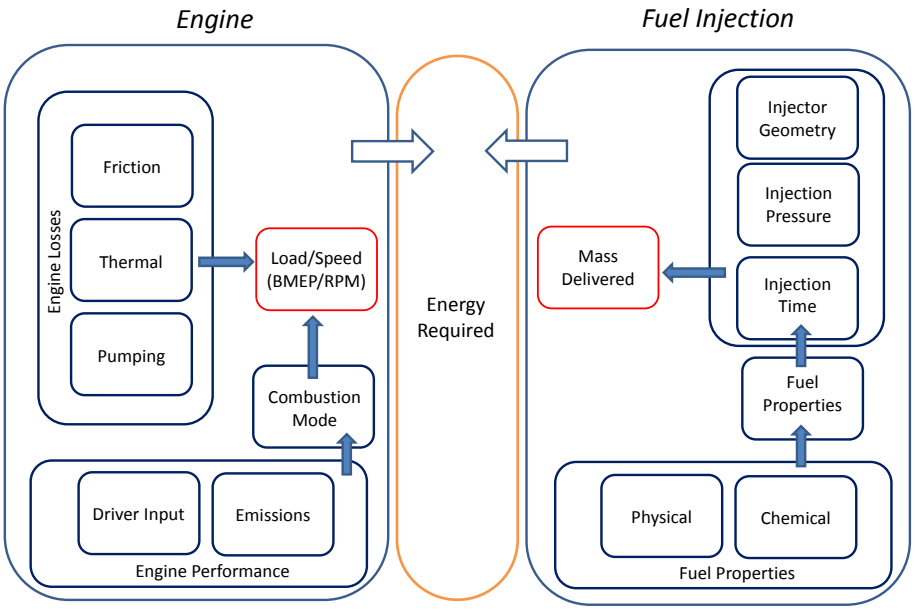

Figure 6, Summary flowchart of fuel delivery and engine operation.

The conditions in which fuel is injected in a DI scenario are outlined below, with the in-cylinder conditions outlined graphically in Figure 7 through Figure 9. This data represents the quiescent conditions imparted on the fuel delivery.

Bulk in-cylinder air motion is crucial for adequate mixture formation in homogeneous (early injection) operational modes, whilst for late injection (i.e. stratified) modes air motion is emphasised toward air-fuel concentration targeting. It has been shown, however, that due to the significant difference in flow velocities between injection and environmental flow, the bulk flow has a reduced

impact on fuel delivery during the injection process. Moreover, experiments have shown that the early injection of a gaseous fuel, when the ambient flow is substantially high, will in fact disrupt the ambient flow field (Kaiser and White, 2008) and increase the thermal losses in doing so (Verhelst and Wallner, 2009). In more recent work, Salazar and Kaiser (2011) experimentally demonstrated that the injection process can reverse the tumble motion set up by the intake and cylinder head geometry. The effect in-cylinder flow has on combustion is outlined in section 2.3.

Figure 7 demonstrates the typical pressure and temperature conditions observed in an SI engine at full load. This modelled profile is for a conventional gasoline DI engine[2] (different to the one outlined in Figure 1 and Figure 2) operated under mechanically ideal conditions, in which the peak combustion pressure is located at approximately 15 CAD aTDC. Full modelling conditions are outlined in Appendix I. It can be observed that the mean full-load in-cylinder pressures and temperatures are below ~10 bar and ~600 K prior to ignition.

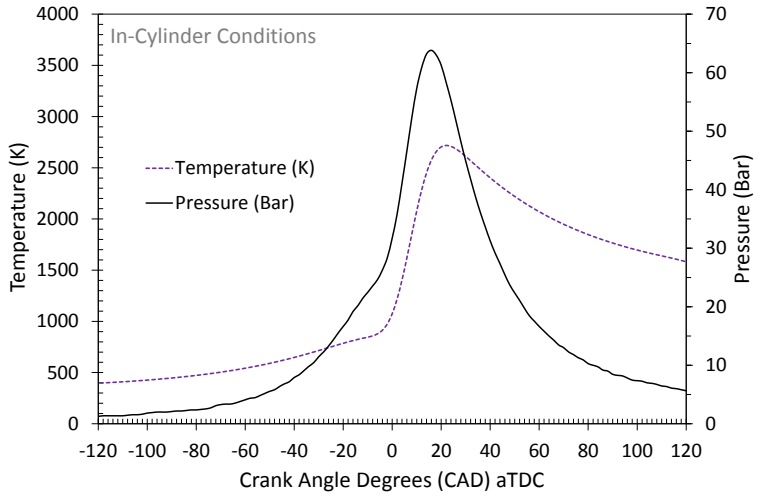

Figure 7, Mean full load in-cylinder temperature and pressure conditions across 1000-6000 rpm.

Figure 8 shows a more focused view of the part load in-cylinder pressure and temperature – the focus of the work described in this thesis where emissions are tightly regulated. The most obvious variation from full-load operation is the substantially lower in-cylinder pressure owing to the throttling of intake air. Of note is the higher than ambient temperature during the intake phase (up to 120 CAD bTDC as indicated) largely due to the residual gas temperature from the previous combustion cycle. This temperature profile is an estimate at operational conditions (90°C) and thus is not representative of either cold- or hot-start conditions. The temperature curve in Figure 8 is a probable 10-15% overestimation, but it is indicative nevertheless.

[2] The same as a parallel investigation by the author: MARTI-ALDARAVI, P., ROGERS, T. J., DE BENITO, E., HEMDAL, S. & DAHLANDER, P. 2012. A comparison of non-reactive fuel sprays under realistic but quiescent engine conditions for SGDI. *International Conference on Liquid Atomization and Spray Systems.* Heidelberg, Germany.

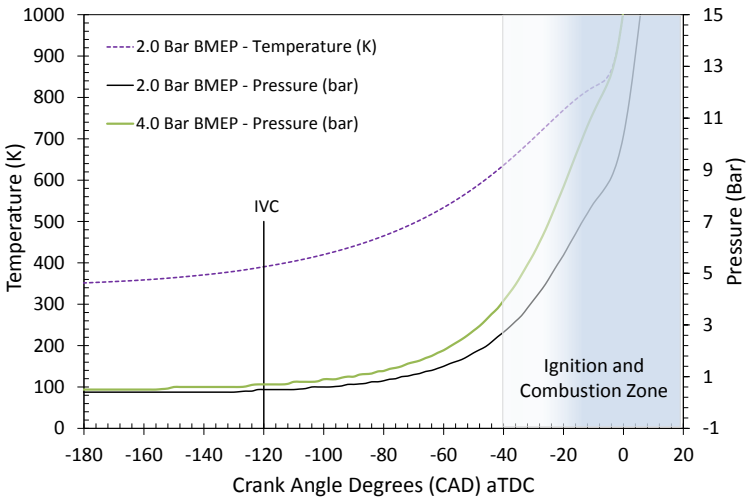

Figure 8, Part load, 2000-4000 rpm averaged in-cylinder conditions.

Gas density is relatively low when the gas temperature offsets the pressure increase due to compression. The density is also substantially lower at part-load conditions in which the throttle limits the intake manifold pressure. Some gains are of course made due to compressional effects within the cylinder head ports from appropriate valve timing. The simulated gas density curve is provided in Figure 9.

The final metric of in-cylinder conditions is the relative distance between the piston crown and fuel injector tip. This geometrical configuration is critical for spray targeting purposes where a physical boundary is imposed. The minimum distance exhibited in Figure 9 is 13.0 mm, occurring at TDC.

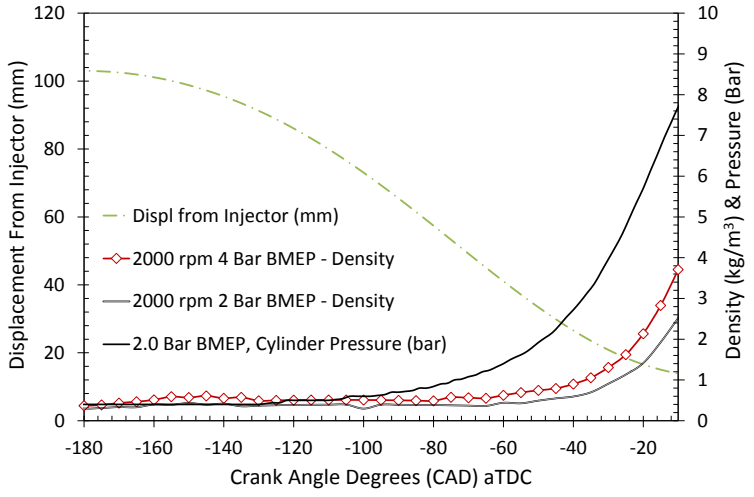

Figure 9, Part load, 2000-4000 rpm averaged in-cylinder conditions with piston to injector tip displacement and cylinder air density.

This section on delivery of alternative fuels has described some of the relevant challenges when delivering fuel at low and high pressures under PFI and DI conditions respectively. Moreover, the

basic fuel delivery and engine in-cylinder conditions used throughout this work have been outlined. The energy, mass and volume requirements of gaseous fuels have been derived from a window of engine operation: 2000-4000 rpm and 2.0-4.0 bar BMEP. The quiescent conditions for in-cylinder environment have been provided through a simple 1D engine simulation. The next section will present and discuss the relevant dynamic in-cylinder flow conditions.

2.3 In-Cylinder Flow Conditions for Direct Injection Engines

The in-cylinder flow is a crucial aspect governing mixture formation and combustion performance and hence the overall engine outputs. Hill and Zhang (1994) provide thorough review of the subject. Whilst this work deals directly with quiescent conditions, it is essential to understand how the effect of in-cylinder flow affects the fuel delivery process and vice versa. The in-cylinder flow can be categorised into two flow fields: bulk and local. The bulk flow field is attributed to the geometric configuration of the engine and is typically defined by the plane of motion. Tumble is aligned to the radial-axial plane, with swirl aligned to the radial-azimuthal plane. Tumble motions are reduced as the piston decreases the cylinder volume on the compression stroke. Swirl, however, can be largely maintained. These bulk flow motions are dependent on engine speed and mode of operation, for example, valve deactivation or flow control devices (intake mounted flaps). The composition of the media is also a determinant of the flow magnitude at which fluidic properties can vary (temperature, density and residual fraction).

Local flow field effects are the small-scale flow perturbations induced when setting up and reducing the large scale motions. These finer flow scales have a substantial effect on the initial flame kernel development and propagating flame front (Hill and Dansehyar, 1987). Typically, measures of turbulence intensity, kinetic energy and shear strain are employed to resolve the finer scales of fluid behaviour. The scales of regular turbulence inquiry can be considered as defined by the Reynolds number.

An overview of the high-level physical dependencies on combustion is presented in Figure 10. This process map expands, in detail, on the higher level requirements depicted in Figure 6 The injection process is central in this flowchart and has direct effects on the combustion propagation and ambient flowfield. It can also be clearly seen that there are many factors which ultimately affect in-cylinder flow and combustion.

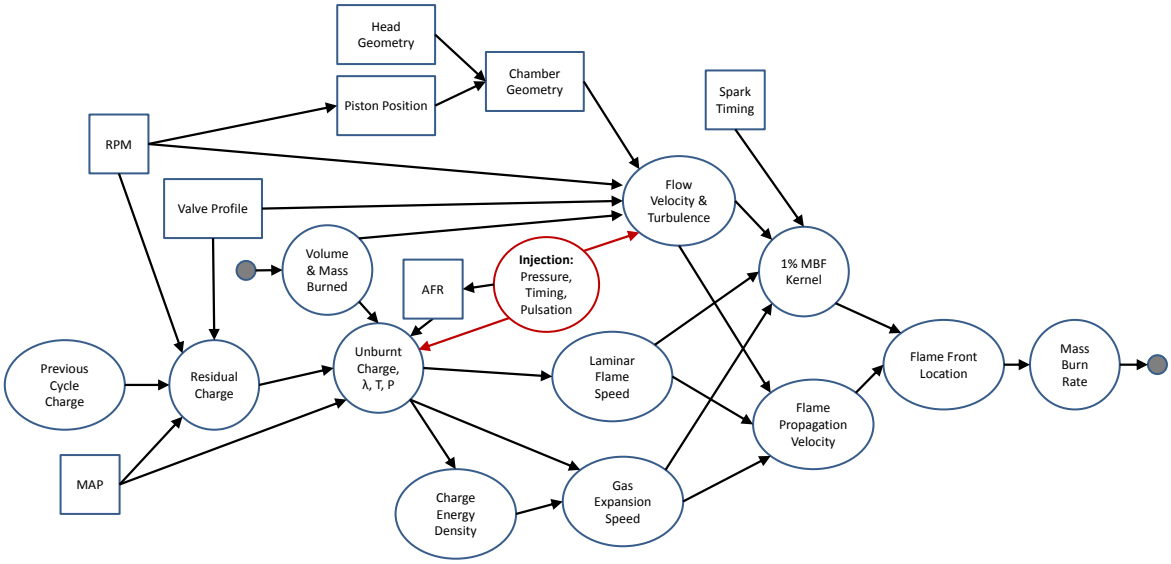

Figure 10, Combustion physics flowchart for a DI SI engine. Adapted from: (Bates, 1991).

With the typical gas injection velocity magnitude, $|V|$, substantially higher than the bulk flow the injection process can alter the pre-existing in-cylinder flow. The most relevant work in this regard is that of Salazar & Kaiser. (2011) in which high-pressure direct hydrogen injection was shown to disrupt the bulk flow enough to reverse the tumble direction. Additionally, in high-tumble conditions the injection-generated vortex survived as a large scale motion close to TDC where combustion could potentially be enhanced (Salazar and Kaiser, 2011).

An example of the velocity magnitude profile across the entire four-stroke cycle is shown in Figure 11; the greatest speeds are seen within the gas-exchange periods. This is unsurprising due to the high mass exchange. More useful in terms of mixture preparation is the region (as denoted below) between $270°$ and $30° \, CA \, bTDC$, the fuel delivery window. A substantial change in $|V|$ ($30 - 5$ m/s) is observed across this period, and within this magnitude profile a coherent tumble structure is formed and then decomposed as the piston nears TDC (Baum et al., 2014). The literature suggests that the bulk velocity magnitude is approximately 2-10 m/s at the point of late injection (Fajardo and Sick, 2007, Kaiser and White, 2008, Baum et al., 2013).

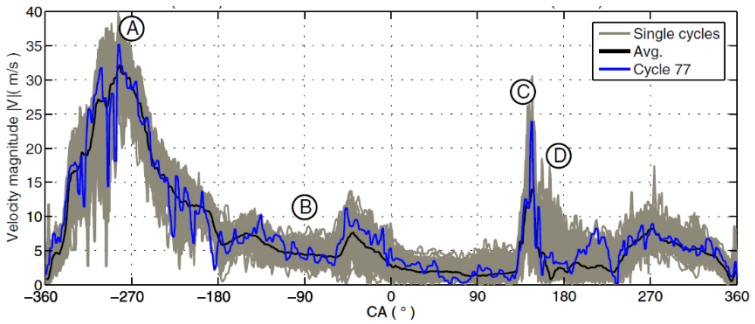

Figure 11, In-cylinder flow magnitude for a SI engine operated at 800 rpm with an average intake pressure of 0.95 bar. Source: (Baum et al., 2014).

Assessing the in-cylinder kinetic energy is a meaningful determinant of the level of turbulent fluctuations. Whilst length scales are still not apparent the energy profile for a spatial or temporal domain will provide additional information for addressing mixing and combustion concerns. Likewise for the velocity magnitude profile, a strong initial turbulence level is due to the flow past the intake valve(s). The turbulence level is reduced as the bulk-field takes coherence, but upon compression these large-scale structures are decomposed into smaller eddies. The increase in turbulence is aligned to the increase in rotational energy as the tumble flow is *'squished'* in the decreasing cylinder volume (Mahmood et al., 1996). This late increase in kinetic energy is favourable in SI engines where the bulk motion should by now have mixed and positioned the air/fuel mixture to a desired concentration and location, respectively. The focus therefore is now on early kernel development and flame propagation. An example of temporal changes to the in-cylinder turbulent energy level is shown below in Figure 12.

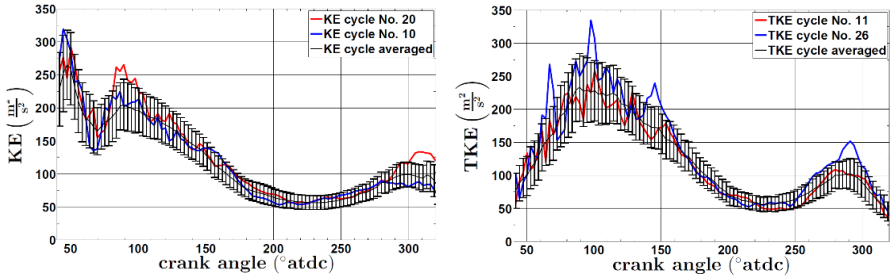

Figure 12, In-cylinder kinetic and turbulent kinetic energy. Source: (Karhoff et al., 2013).

Recent work has revealed the influence of flow velocity on the misfire propensity and on the electrical discharge profile across the spark-gap, as depicted in Figure 13 (Shichida et al., 2014). The authors showed that at 10 m/s the likelihood of misfire increased due to in-plane flow to the electrode arm. The authors concluded that this is due to heat transfer losses more than twice those that occur in the unobstructed case, where the early flame kernel is quenched by the electrode arm.

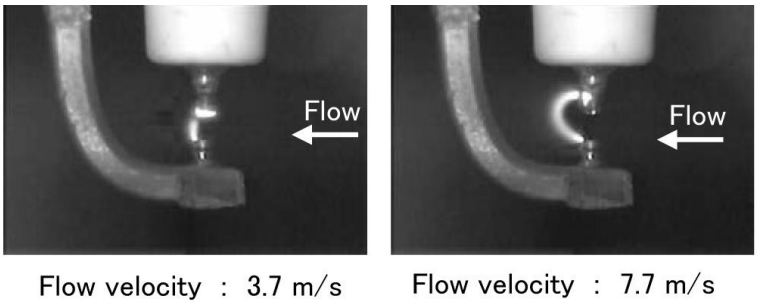

Figure 13, Spark-Plug electrical discharge profile in cross-flow. Source: (Shichida et al., 2014).

With the spark plug and injector being in close proximity (i.e., c.a. 10mm) in modern passenger vehicle engines, understanding and predicting the in-cylinder flow field is of highly important.

2.4 Turbulent Gaseous Jets

Appropriate mixture preparation of gaseous jets is of particular importance for operation strategy (i.e. BMEP and COVimep at a given speed and load point) and also for emission generation a continually reducing target. Isolating and understanding gaseous-fuel jets under classical and engine-like conditions will increase the knowledge of mixture preparation for internal combustion engines.

The nature of a jet (or plume) can be described as a puff or as a transient vortex type. The first scenario leads to the bulk of fluid mass being contained within a detached head, and has been seen in experiments involving incorrectly operating injector solenoids. Transient vortex jets are typical of the desired fuel injection event, in which a plume feeds the jet head with a relatively constant mass and momentum. This transient jet will be exclusively covered in this work.

Typical gaseous injectors employ a round symmetrical exit nozzle, thus the jet itself may be considered to be axisymmetric. However, more often than not the actual free jet exhibits some (largely minor) irregularities. These irregularities arise from non-uniform environments in which fluidic (density, pressure, flow and temperature) and geometrical (i.e. wall interaction) conditions influence jet structure development.

For delivery into an engine, the jet will almost inevitably interact with a solid surface, hence impingement will occur; the jet structure will change and thermo-fluidic processes will follow depending on the boundary conditions of the specific environments. In the research described in this thesis, two jet types will be examined – free and impinging.

A classical free jet can be deconstructed into two main regions of interest: 1) quasi-steady and 2) a transient[3] vortex head. The overall structure resembles that of a plume jet as shown in Figure 14.

[3] The jet vortex head is unsteady and thus termed a transient component due to the significant geometric changes which can occur whilst the jet develops and once fully developed (steady-state mass flow and constant axial penetration). The jet head is also defined by its large-scale counter-rotating vortices.

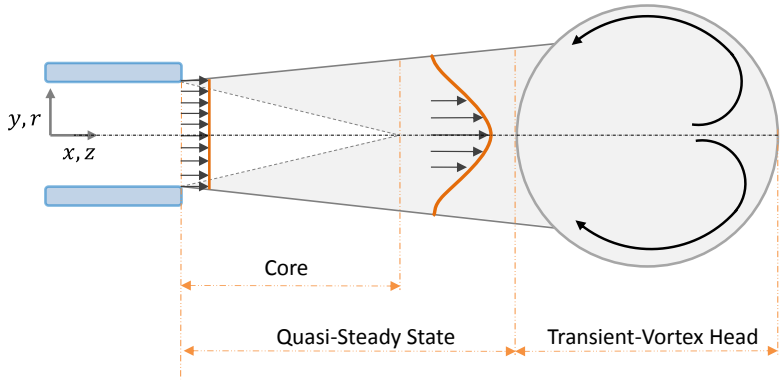

Figure 14, Turbulent transient jet structure. Adapted from: (Ouellette 1996).

2.5 Isentropic Flow Considerations

This section briefly introduces the fundamental relationships which govern ideal flow in jets. To simplify the flow process they are often considered to be steady and isentropic; that is, no transformations exist due to friction or heat or otherwise. This is of course a thermodynamic simplification, as dissipative processes exist in jets due to irreversible processes such as heat transfer and diffusion (mixing). Regardless, the use of such simplification is useful for the prediction of behaviour utilising the following selected relationships.

Considering the mass and momentum laws for isentropic compressible flow, one can derive Equation 3, where the relationship of the fluid speed of sound, a, or Mach number, M, is given relative to velocity, v, and density, ρ.

Equation 3, Speed of sound for isentropic conditions. Source: (Jones and Hawkins, 1960).

$$\rho \, v \, dv = a^2 d\rho$$

Hence the sonic velocity of a gas can be represented by the change in pressure relative to the change in density either side of a shock wave, and can be represented as:

Equation 4, Isentropic sonic velocity of a gas. Source: (Jones and Hawkins, 1960).

$$c = \sqrt{\left(\frac{dP}{d\rho}\right)}$$

By combining mass and momentum conservation with the speed of sound, the Mach number relationship can be found. This is based on a change in area, A, as experienced within for example, a nozzle.

Equation 5, Isentropic Flow for simple compressible flow. Source: (Seitzman, 2001).

$$\frac{dA}{A} = \frac{dp}{\rho v^2}(1 - M^2) = -\frac{dv}{v}(1 - M^2)$$

where, $p\ or\ P$, represents the fluid pressure. Inspection of Equation 5 yields the summary of area, pressure, velocity and temperature represented in Table 3 for classic nozzle flow.

Table 3, Mach number considerations for isentropic flow. Source: (Jones and Hawkins, 1960, Seitzman, 2001).

	Conditions	
$M < 1$	$dA/dP > 0, dA/dv < 0$	$A\uparrow = p\uparrow = v\downarrow = T\uparrow$
$M = 1$	$dA/dP = 0, dA/dv = 0$	
$M > 1$	$dA/dP < 0, dA/dv > 0$	$A\uparrow = p\downarrow = v\uparrow = T\downarrow$

From Equation 6 and Figure 15, it can be seen that the mass flow profile is governed by the geometric and ideal conditions of the model gas. The effects of gas properties (constant pressure and temperature), R (J/Kg.K) and γ (kJ/mol.K / kJ/mol.K) are also observable. The jets considered in the present work are issued from a quiescent upstream reservoir, and thus only sonic velocity, *M* =1, at the nozzle exit exists assuming the critical pressure ratio across the nozzle is met. Any increase in nozzle-exit mass flow is due to an increase in upstream supply pressure, P_o, as shown in the right-hand plot of Figure 15.

Equation 6, Ideal compressible gas mass flow. Adapted from: (Seitzman, 2001).

$$\frac{\dot{m}}{A} = \frac{P_o}{\sqrt{RT_o}} \frac{\sqrt{\gamma}M}{\left(1 + \frac{\gamma - 1}{2}M^2\right)^{\frac{\gamma+1}{2(\gamma-1)}}} \quad \& \quad \dot{m} = \frac{AP_e}{\sqrt{T_e}}\sqrt{\frac{\gamma}{R}}\, M \left(1 + \frac{\gamma - 1}{2}M^2\right)^{-\frac{\gamma+1}{2(\gamma-1)}}$$

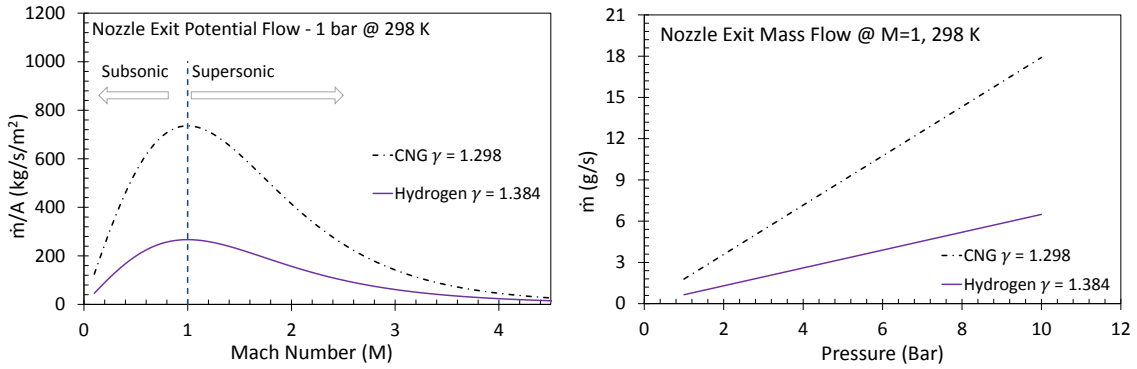

Figure 15, Isentropic exit mass flow for an increasing Mach number (left) and increasing pressure at M=1 (right). Results presented at 298K and a throat diameter of 3.65 mm.

For the case of underexpanded compressible jets, Birch et al. (1984) proposed a simplified isentropic model which incorporates a pseudo-nozzle diameter to conform to classical theories. This model has been adopted by others (e.g. (Ouellette, 1996, Petersen, 2006)) and is in Figure 16. The model is based on the assumption that no mixing takes place in the first shock-formation region and corresponding adjustment period and thus mass conservation occurs (Birch et al., 1984).

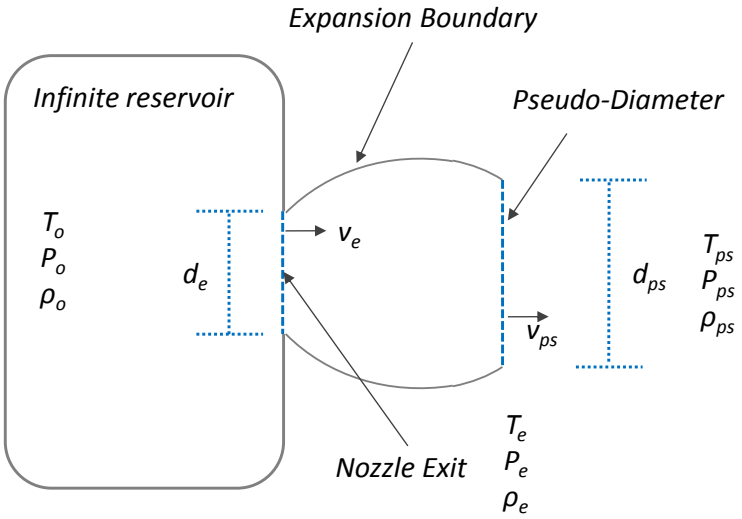

Figure 16, Pseudo-diameter underexpansion model. Adapted from: (Birch et al., 1984).

Classical theory suggests the following conditions at the reservoir and nozzle exit at the minimum throat area where $M = 1$ (Equation 7-9).

Equation 7, Isentropic critical nozzle exit pressure. Source: (Shapiro, 1953).

$$P_e = P_o \left(\frac{2}{\gamma + 1}\right)^{\frac{\gamma}{\gamma - 1}}$$

Equation 8, Isentropic critical nozzle exit temperature. Source: (Shapiro, 1953).

$$T_e = T_o \left(\frac{2}{\gamma + 1}\right)$$

Equation 9, Isentropic critical nozzle exit density. Source: (Shapiro, 1953).

$$\rho_e = P_o \left(\frac{2}{\gamma + 1}\right)^{\frac{1}{\gamma - 1}} \frac{W}{RT_o}$$

where, W and R are the molecular mass of the fluid delivered and the universal gas constant respectively. Further downstream, at the axial jet location of the pseudo-diameter, Birch et al., (1984) gave the following representation (Equation 10).

Equation 10, Pseudo-diameter representation. Source: (Birch et al., 1984).

$$\left(\frac{d_{ps}}{d_e}\right)^2 = C_d\left(\frac{P_o}{P_{ps}}\right)\left(\frac{T_{ps}}{T_o}\right)^{\frac{1}{2}}\left(\frac{2}{\gamma+1}\right)^{\frac{\gamma+1}{2(\gamma-1)}} = C_d\frac{v_e}{v_{ps}}\frac{\rho_e}{\rho_{ps}}$$

where C_d is defined as the discharge coefficient and v_e and v_{ps} are the velocities at the nozzle and upstream pseudo-diameter locations respectively. The nozzle velocity can be classically represented through Equation 11 below.

Equation 11, Isentropic nozzle velocity. Source: (Birch et al., 1984).

$$v_e = \sqrt{\left[\left(\frac{2\gamma}{\gamma+1}\right)\frac{RT_o}{W}\right]} \quad v_e = \sqrt{\left[\left(\frac{2\gamma}{\gamma-1}\right)\left(\frac{RT_o}{M}\right)\left(1-\left(\frac{P_e}{P_o}\right)^{\frac{\gamma-1}{\gamma}}\right)\right]}$$

where *R* is the universal gas constant and *M* is the molecular weight. A discharge coefficient, C_d, can be employed in determination of the discrepancy between theoretical and actual flow conditions (Equation 12).

Equation 12, Mass flow rate at isentropic choked conditions.

$$\dot{m} = C_d A\sqrt{\gamma\rho P\left(\frac{2}{\gamma+1}\right)^{\frac{\gamma+1}{\gamma-1}}}$$

where C_d is the ratio of actual over theoretical mass flow and thus for isentropic ideal calculations is denoted as unity whereas in reality substantially lower discharge coefficient are expected (by approx. 10 to 30% (Baert et al., 2010, Benito, 2010)).

Similarly to Equation 6, Equation 13 prescribes the equivalent jet diameter, D_j, for a fully expanded jet. The value of D_j will always be greater than that of D for underexpanded jets, for which the relationship between D_j and D is derived from the mass flux conservation laws (Tam and Tanna, 1982).

Equation 13, Fully expanded effective jet diameter. Source: (Panda and Seasholtz, 1999, Tam and Tanna, 1982)

$$\frac{D_j}{D} = \left[\frac{1+\frac{\gamma-1}{2}M_j^2}{1+\frac{\gamma-1}{2}M_d^2}\right]^{\frac{\gamma+1}{4(\gamma-1)}}\left(\frac{M}{M_j}\right)^{1/2} \qquad OR \qquad D_j = \frac{D}{\sqrt{M_j}}\left[\frac{1+\frac{\gamma-1}{2}M_j^2}{1+\frac{\gamma-1}{2}M_d^2}\right]^{\frac{\gamma+1}{4(\gamma-1)}}$$

The nozzle exit conditions are now defined from classical nozzle flow equations and are utilised in this work through initially quiescent upstream conditions, a sonic throat and a relationship that normalises exit conditions to the compressible underexpanded features. With the general isentropic jet assumptions outlined, the actual description of the gas jet can now be introduced.

2.6 Turbulent Underexpanded Axisymmetric Jets

Some high-level definitions are presented to characterise the gaseous-fuel jets under consideration; this section then presents discussion of the flow characteristics experienced within the jet.

A free jet is has no geometrical constraint on its development from the nozzle exit. Free aerodynamic jets exist in many forms, from thermal plumes rising through the atmosphere, exhaust gases from an aerospace engine and coating processing in industrial manufacturing. They act in a transient nature; where the jet develops up to a point of equilibrium with its environment reaching steady-state conditions at constant massflow delivery. The axisymmetric structure (about the axial/longitudinal coordinates) is derived from, the symmetrically round delivery nozzle.

An impinging jet is constrained by physical boundary interactions. The relative distance of an impinging surface from the delivery nozzle dictates the change in free jet structure. It has been shown, that the jet exhibits uninhibited free-flow behaviour until immediately before surface contact (Rogers et al., 2015).

Turbulent jets exist when a Reynolds number above 3×10^3 is reached. The highly turbulent CNG jets presented in this work exist between $56 \times 10^3 < Re_{exit} < 991 \times 10^3$, as calculated for nozzle exit conditions assuming steady-state flow.

The Mach number defines how the flow is treated in terms of conservation laws. As Mach numbers at the nozzle are always above 0.8 and typically remain above 0.3 downstream of the nozzle, the jets are considered in the compressible domain. Table 4 categorises these high-level flow considerations.

Underexpansion of a gaseous jet occurs when the critical pressure ratio of delivery-to-environment pressure is met or exceeded. This results in the fluid expanding in the ambient environment, leading to complex compressible flow behaviour. For the conditions relevant to this work the jet exiting a fuel injector orifice can be considered to be within the underexpanded range with the vast majority considered to be highly under expanded. The critical pressure for CNG jets, as used in this thesis, is considered to be approximately 1.83, as calculated from Equation 7.

Table 4, Mach number considerations for flow regimes

Mach Range	*Velocity*	*Nature*	*Outcome*
< 0.3	Subsonic	Incompressible	-
0.3 < 0.8	Subsonic	Compressible	-
0.8 < 1.2	Transonic	Compressible	Shock wave formation, mixed flow regime
1.2 < 3.0	Supersonic	Compressible	Shock wave formation
3.0 >	Hypersonic	Compressible	Shock wave formation and other phenomena present

It was shown earlier in Figure 14 that several distinct features exist for a free- axisymmetric turbulent jet. These features are discussed with respect to two main regions, the *nearfield* and the *farfield.* (This division is somewhat arbitrary if considering transient jets within the earlier stages of development.) A conception of the flow profile of a transient, moderately underexpanded jet is offered in Figure 17.

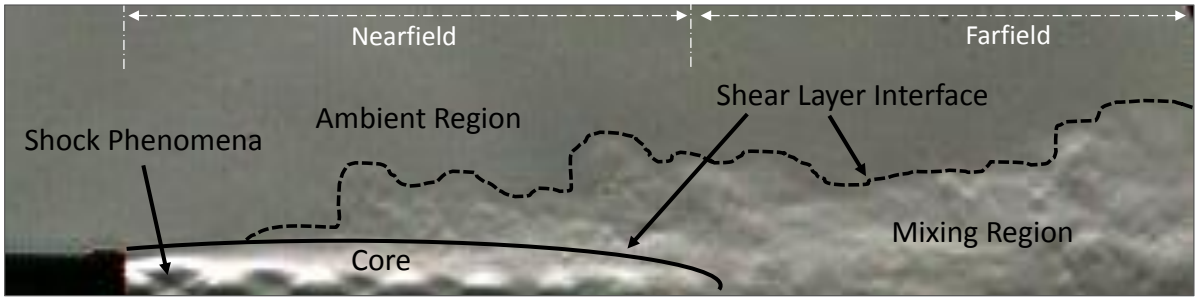

Figure 17, Transient moderately underexpanded jet, with large scale feature defined.

2.6.1 Nearfield Region

Nearfield conditions play an important role in overall jet characteristics and have been studied for a wide range of jets since the 1940s. In this text, the nearfield region will be classified as $0<x/d<10$ and predominately covering the nozzle exit and main compressible underexpansion region. One of the earliest researchers to note the importance of the exit region was Johannesen (1957) who wrote: *"…the strength of the internal shock waves had a very marked effect on the development of the mixing region and thereby on the spreading of the jet."*

When the critical pressure ratio is achieved, nozzle exit velocities are limited to the sonic gas velocity. Above the critical pressure ratio, the choking limit will thus be reached. Compressible flow behaviour will ensue and the jet will assume an underexpansion profile. For highly underexpanded jets, a single-barrel Mach disk is formed upon immediate exit (Ewan and Moodie, 1986). Weak underexpansion exists for pressure ratios between 1 and 1.1; thereafter they are said to be moderately then highly underexpanded. Donaldson and Snedeker, (1971) outline the three main processes for turbulent free- jets; *Subsonic*, *Moderately Underexpanded* and *Highly Underexpanded*, detailed in Figure 18:

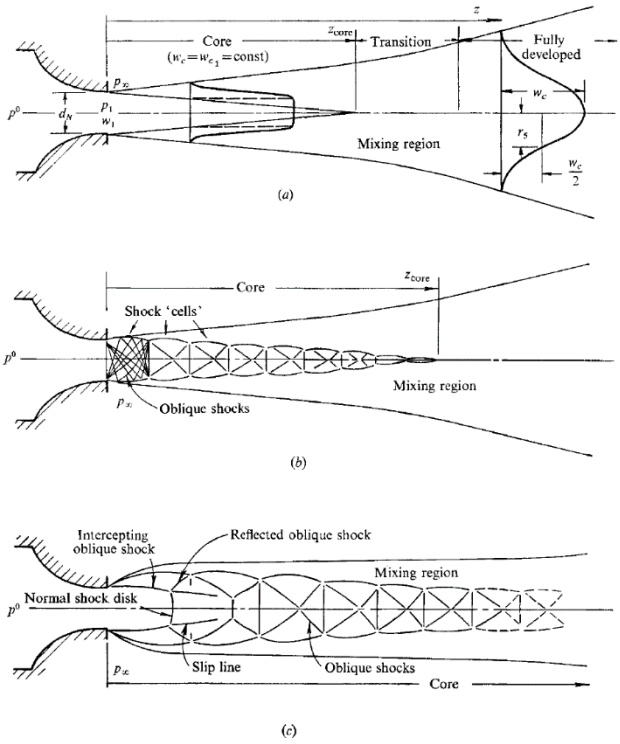

Figure 18, Flow process regime for a turbulent free jet at increasing nozzle pressure ratios. a) Subsonic. b) Moderately underexpanded: 1.1<PR≤2.0. c) Highly underexpanded 2.0≤PR< ∞. Source: (Donaldson and Snedeker, 1971)

The most interesting aspect of a turbulent jet is the spatial distribution and size of the mixing region. From the above depiction it can be asserted that the size of the mixing region diminishes for a larger core region if the axial jet development is independent of the nearfield core region. This is the case when the jet propagates to a substantial axial length, owing to the highly developed turbulent structure (Namer and Ötügen, 1988, Hill and Ouellette, 1999). For example, for a fixed axial penetration length the mixing region (volume) is proportional to the core region. Therefore, if a high pressure ratio is utilised a larger compressible flow region will enlarge the total core region and as a consequence the mixing region will be reduced. The compressible flow region found between the nozzle exit and the normal shock is a region where no mixing occurs due to the impenetrable shock boundaries and the highly supersonic velocities; this region will thus be an obstacle for fuel delivery and mixture preparation.

The classical underexpanded jet is typically categorised for steady-state jets. For fuel delivery the treatment of a steady or quasi-steady jet is inadequate, particularly when a fully steady-state (massflow delivered and jet development) jet may not be realised due to the very short pulsation times. To this end, one must also consider the transient evolution of the jet where the flow process may differ. For a transient jet the velocity will obviously accelerate and decelerate with the change in delivery pressure at the SOI and EOI respectively. This raises the question; *what is contribution of mixing within the nearfield at pre- and steady-state conditions*?

Donaldson and Snedeker's (1971) experiments with air jets led them to suggest that the level of underexpansion is categorised by the nozzle-exit pressure ratios ($NPR = P_e/P_a$) represented in Table 5. The authors also offered a depiction of the transitional flow effects (imaged with schlieren photography) for a turbulent air-jet with an increasing pressure ratio.

Table 5, Underexpansion regimes according to nozzle exit pressure.

Underexpansion Regime	*NPR*
Weak	$1.0 < \sim 1.1$
Moderate	$1.1 \lesssim 2.0$
High	$2.0 \lesssim \infty$

For most situations the NPR exists within the highly underexpanded region. It can be seen that for a gas exiting a nozzle at the speed of sound (i.e. 450 ms^{-1} for methane at 350 K (Ouellette, 1996)), several complex phenomena take place in this initial nearfield region. Firstly, as the gas immediately passes the physical nozzle threshold, the velocity of the gas rapidly accelerates in the form of expansion waves. This is due to the large differentials in pressure, velocity and density between the injected gas and surrounding media. These expansion waves accelerate to where the boundary of the flow resists this expansion and reflects the waves in the form of compression shock waves. Coalescence of these oblique shock waves forms a barrel-shaped region of supersonic flow, with a normal shock (often termed the Mach disc) at the leading edge. The intersection of this shock coalescence is known as the triple point location. The normal shock offers a pathway for the compression wave. At the triple point, the compression waves can follow two pathways. Firstly, expansion waves will be directed to the jet at a near-normal angle to the incoming oblique compression waves. These expansion waves exist as a reflection shock. The second flow pathway is provided where a low pressure region is created at the boundary between the reflected and normal shock; this discontinuity, known as a slip line, allows for the expanding gases to continue axially until downstream mixing intervenes. The simplified highly underexpanded phenomenon of a gas jet is depicted in Figure 19.

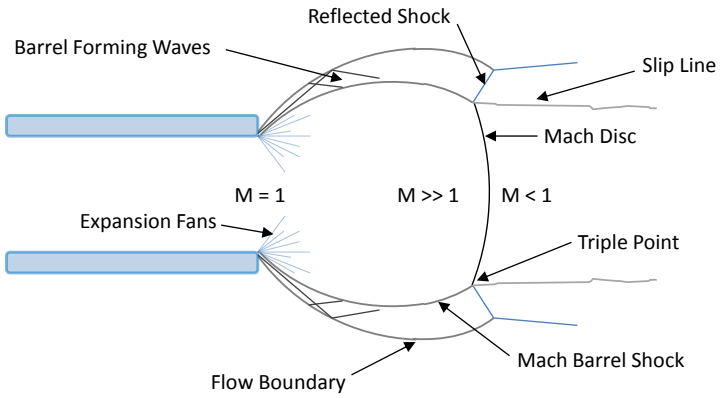

Figure 19, Highly underexpanded phenomena for a gas jet exiting a nozzle.
Reproduced from (Ewan and Moodie, 1986).

This initial barrel shock said to extend for "*a few*" nozzle diameters (Ewan and Moodie, 1986) and depending on the gas dynamics the process may be repeated several times over (Petersen, 2006). This repetition is limited by the viscous losses within the jet and turbulent mixing with the ambient environment (Seitzman, 2001). The dissipation of the pressure (and temperature) instabilities by the shear layer is marked at the end of the core region. This topic will be continued in the following sections.

As the gas is expanded into the ambient environment an expansion wave is initiated in the opposite direction (reverse to flow direction), continuing up the nozzle at the speed of sound for the fluid injected. On the upstream side of the injector valve the same acoustic wave is present within the fuel rail. The effect of this transient pressure wave on a high pressure liquid diesel plume structure is the subject of much discussion (and contention) (Benito, 2010). This transient wave is, however, of known concern for subsequent injection events in all high pressure fuelling systems, as the pressure instability can cause deficits in fuel mass delivery. The effects may cause fuel metering uncertainty and thus affect combustion and emissions generation.

Expansion waves originate at the sharp edges of the nozzle orifice due to the Prandtl-Meyer expansion fan process. These waves are independent of the expanding waves issued from the expanding fluid effects. The Prandtl-Meyer expansion fans are dependent on the nozzle orifice geometry, which is modelled to comprise several small radii changes. This process is regarded as an isentropic and generally represented as quasi-1D. As the sonic or supersonic flow rounds the nozzle exit corner, expanding and accelerating, they release a series of Mach-lines or expansion fan waves whose first and last angle are determined by the expressions given in Figure 20 below. In the lower half of Figure 23 several streak lines are observed within the Mach-barrel which appear to emanate from a virtual nozzle edge and terminate (*or at least appear to*) near the triple point. These streaks constitute the Prandtl-Meyer expansion lines.

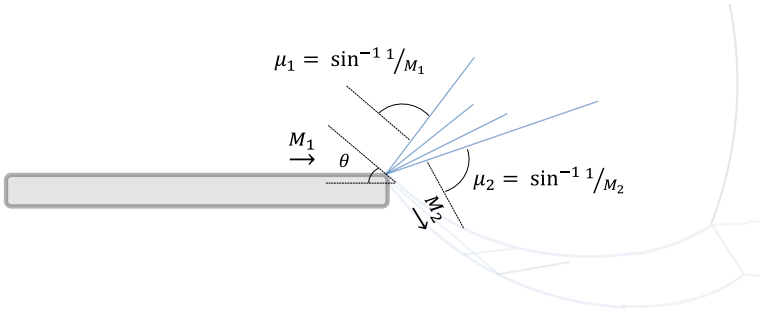

Figure 20, Prandtl-Meyer expansion fan angle calculation. Source: (Seitzman, 2001).

The nearfield region of a gas jet, particularly the influence of pressure ratios, has been shown to influence the mixing properties of fuel and ambient air (Owston et al., 2008). Several phenomena exist within the nearfield region and have been the subject of many studies for steady state, i.e. (Johannesen, 1957) and transient jets (Radulescu and Law, 2007).

2.6.1.1 Shock Wave Propagation

As briefly introduced above, several shock events occur within an underexpanding jet which intensify as the pressure ratio and thus Mach number is increased. Typically, isentropic ideal gas equations are employed to quantify the 1-D flow phenomena. Under isentropic considerations the Mach number is defined as (Equation 14):

Equation 14, Mach number. Source: (Shapiro, 1953).

$$M = {V}/{c} = {V}/{\sqrt{(\partial p/\partial \rho)}}$$

Where $V, c, p \; and \; \rho$ are the velocity, speed of sound, pressure and density respectively. An ideal Mach number is often represented as the isentropically fully expanded jet with the denotation of M_j (i.e. (Panda and Seasholtz, 1999)).

The underexpansion induced shock formation can be further elaborated from the general introduction given in section 2.6.1 with segmentation into the three generalised categories: weak, moderately and highly underexpanded. This categorisation was introduced in the work of Donaldson and Snedeker (1971), as previously mentioned.

For the moderately underexpanded steady jet, the gas expands on exit with the expansion fans crossing the centreline (C_L) according to the Prandtl-Meyer expansion, the waves meet their axisymmetric counterpart and reverse at equal incidence angles (as per Figure 20 equations). Once reversed the waves will continue to the boundary layer where the shear forces induced by the small-scale mixing between the jet and ambient fluid will contain the waves. The compression waves will now vector toward the centreline as oblique shock waves. The occurrence of these waves is

controlled by the pressure equilibrium process; the jet will expand and contract upon itself in this core region, producing a decreasing and increasing pressure profile along its centreline. When viewed as a simplistic 2-D slice the formation is akin to a diamond-like structure of varying size, hence the oft-referred term Mach Diamonds.

The underexpansion process is detailed in Figure 21 below. The corresponding expansion and compression waves are represented by the dashed blue and red lines respectively. The recurrence of these Mach diamonds has been thoroughly studied and is generally well understood. Pack (1948) provided further detail on the formation and traversing nature of shock waves within the underexpanded supersonic jet core, and suggested that the process will be repetitive as long as the flow velocity behind the shockwave remains supersonic.

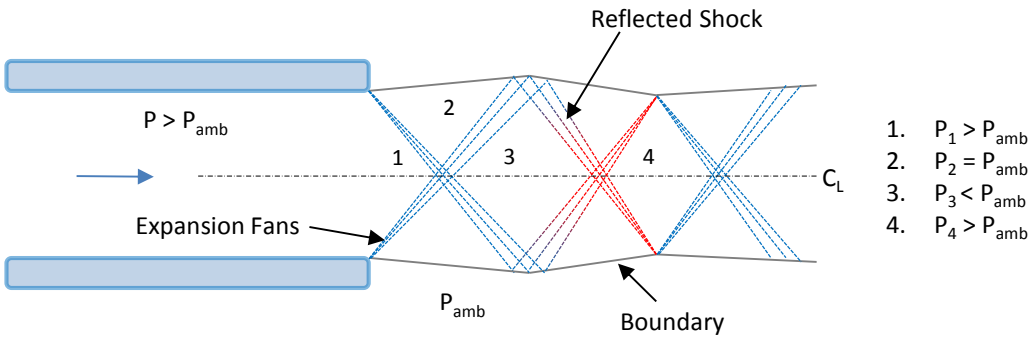

Figure 21, Moderate underexpansion process highlighting Mach diamond formation.

The repetition of these underexpansion events is dependent on the pressure ratio, which is self-evident given that it is a pressure equilibrium induced process. This process occurs up to a nozzle exit pressure ratio of ~2, after which the compressible flow behaviour changes and takes on a higher underexpansion regime.

For the highly underexpanded jet, the oblique shockwaves reflecting from the boundary surface will often coalesce to form a Mach disc (normal shock) at the centre of the jet. The incident reflected shock continues to the boundary layer and the process continues as captured in Figure 22 below. More curvature in the jet core-to-boundary layer segments is depicted here as it is more representative of the actual three-dimensional flow. The work of Pack (1948) provides great detail on the formation and traversing of shock waves within underexpanded, supersonic jets giving numerical solutions for the locations of physical events if rationalised to two-dimensions. The Mach barrel in the nozzle exit region is formed when the expansion process is significantly strong, as the gas exiting the nozzle at high pressure ratios accelerates well above Mach 1 and in doing so creates a substantially low-pressure region (lower than ambient).

Expanding on the depiction of the first shock event in Figure 19, Figure 22 illustrates the one-dimensional process expected for a highly underexpanded jet. It can be seen that the flow will

transition back to the processes associated with a moderately underexpanded jet, in that a repeated, secondary normal shock may form due to the accelerating supersonic gas. This process once again depends on the magnitude of the NPR, and hence the momentum decay within the jet. The likelihood of secondary normal shocks is typically low (for the vast majority of the work considered here) where it is said that the first normal shock dominates the downstream core region to a substantial distance (Donaldson and Snedeker, 1971). Oblique shocks will persist, as before, until the decay of the jet core region.

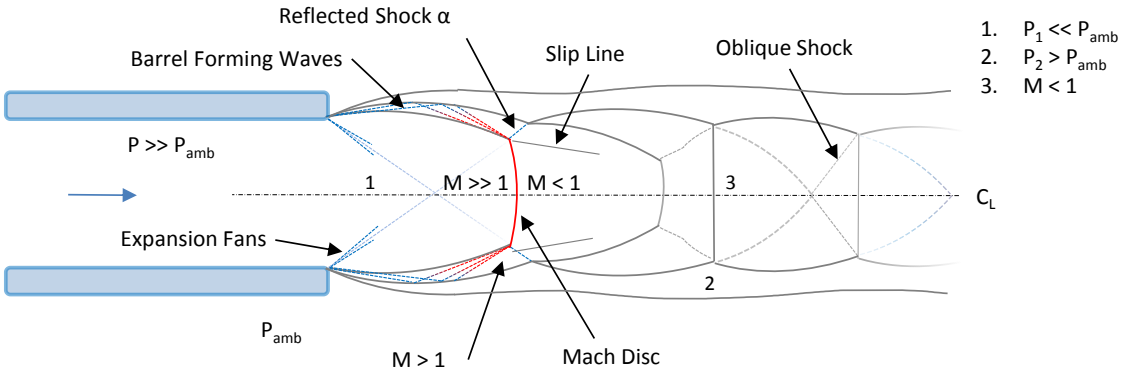

Figure 22, Highly underexpanded process with Mach disc Formation.

The highly underexpanded jet is easily distinguished from its moderate and weak counterparts, with clear examples already presented and briefly discussed. The distinguishing feature in highly underexpanded jets is the well-defined Mach barrel formation preceding the normal shock, simplified in Figure 19. Perhaps one of the most detailed images of a highly underexpanding jet imaged with Particle Image Velocimetry (PIV) was published by Chauveau et al. (2006), reproduced in Figure 23, where one can clearly see the intricate flow detail particularly at the boundary layer. Of note is the dense particle field surrounding the radial (top and bottom) regions of the barrel-shock, where these waves are reflected and the viscous mixing occurs thereafter between the boundary of the core region and the environment.

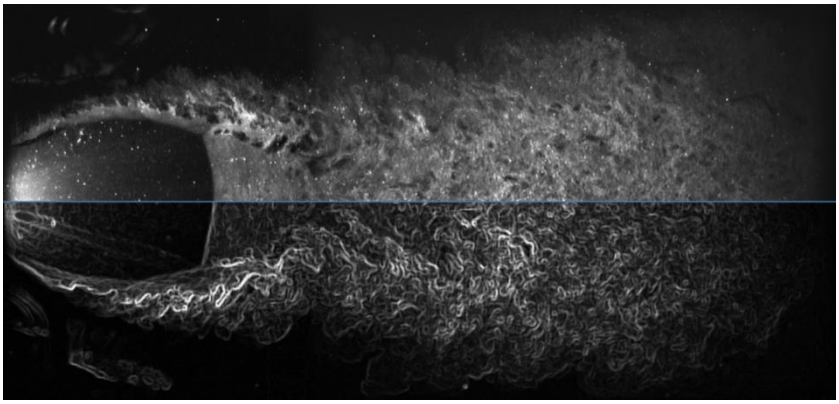

Figure 23, Nearfield PIV image. Original: (Chauveau et al., 2006). Top half: original image and Bottom Half: with edges highlighted.

Panda and Seasholtz, (1999) provided experimental detail of the density ratio within the jet, as shown in Figure 24. The marked locations on the schlieren images relate to the Rayleigh scattering interrogation positions where the gas velocity and density are measured. This figure also depicts the significant structural differences between moderately (M_j = 1.43) and highly (M_j = 1.80) underexpansion processes (at left and right respectively).

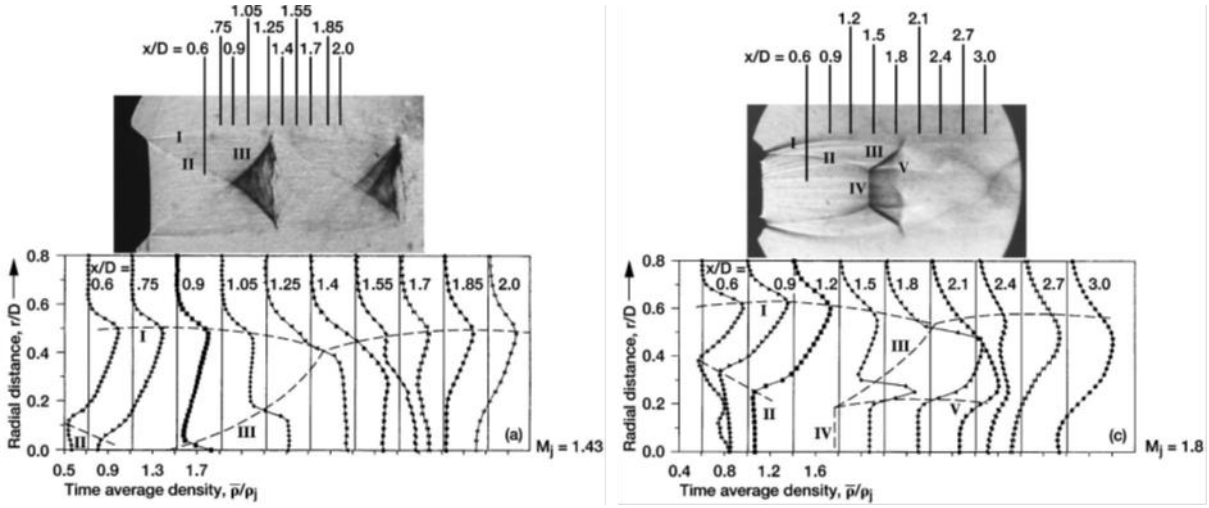

Figure 24, Density measurements in the nearfield for M = 1.43 (left) and M =1.80 (right), resp. Source: (Panda and Seasholtz, 1999)

2.6.1.2 Barrel Length

The distance between the nozzle exit and the normal shock (Mach disc) location is known as the barrel length. Within this text, the terminology 'Mach disc location' (x_{MD}/d) and 'barrel length' are used interchangeably. The downstream region preceding the Mach disc location is accelerating and wholly supersonic and is contained within oblique shock wave boundaries. This region is impenetrable to ambient air entrainment and thus is a region where no jet-to-air mixing occurs. For the early development times in transient jets, the evolution of these nearfield compressible structures also has a bearing on the flow development. It is therefore pertinent to study the influences on barrel length and the effect barrel length has on early flow development. This aligns with the research's first two objectives of the characterisation of the targeting and dispersion behaviour of the gaseous fuel jet and the transient jet behaviour near the nozzle exit region.

To the author's knowledge, Love et al. (1957) were the first to show the dependency of barrel length on pressure ratio at sonic exit velocities and steady-state conditions. The significance of their work is largely underestimated; they characterised a very broad jet pressure range ($1 < NPR < 105$). The most commonly cited work, however, is by Ashkenas and Sherman (1966), who were the first to empirically correlate the pressure ratio to the location of the first Mach disc. Their

correlation, derived from the experimental work of Bier and Schmidt (1961) for nitrogen, argon and air jets at $15 \leq PR \leq 17000$, is expressed in Equation 15:

Equation 15, Barrel length approximation. Source: (Ashkenas and Sherman, 1966).

$$\frac{X_{MD}}{D_n} = C_X \sqrt{\frac{P_o}{P_a}}$$

where, C_X, a constant, is given as 0.67. In more recent works the value of C_X is shown to depend on experimental conditions with values around 0.60-0.65 (for example: (Addy, 1981, Ewan and Moodie, 1986, Maté et al., 2001, Vuorinen et al., 2013)).

In the same year as Ashkenas and Sherman (1966), Crist et al. (1966) studied a multitude of sonic gas jets issued from converging round nozzles, tested up to extremely high pressure ratios (300,000:1). They also explored temperatures of up to 4,200° K. This investigation produced the following conclusions (Crist et al., 1966):

- The barrel length is independent of:
  - Ratio of specific heats
  - Condensation
  - Nozzle exit geometry (lip)
  - Absolute pressure level
- The Mach disc diameter size
  - increases with a decrease in the ratio of specific heats, γ
  - increases with gas condensation (γ dependent)
  - decreases with increased stagnation density (ρ_0)

Whilst Equation 15 provided a good fit for the high pressure ratio conditions tested it was also representative of lower, pressure ratios (Addy, 1981). Addy (1981) concurred with Crist et al. (1966) in finding that barrel length was largely independent of nozzle geometry (type and size). Equation 15 uses the convenient square root pressure-ratio relationship to express this phenomenon. More recently, it was shown that the internal nozzle geometry is a governing factor in the barrel length determination for $15 \leq PR \leq 90$ (Hatanaka and Saito, 2012).

Ewan and Moodie, (1986) produced an empirical fit for the barrel length at a similar pressure ratio and nozzle exit range to Addy (1966), but utilising, the nozzle exit pressure, P_e instead of the upstream stagnation pressure. Ewan and Moodie', (1986) linear approximation provided good agreement for their conditions up to an exit pressure ratio ~ 10, after which overestimation of the barrel length would occur. A typical snapshot of the average C_X values and their fits are provided in

Figure 25 for pressure ratios under consideration. It is evident from Figure 25 that barrel length increases with increasing pressure ratio.

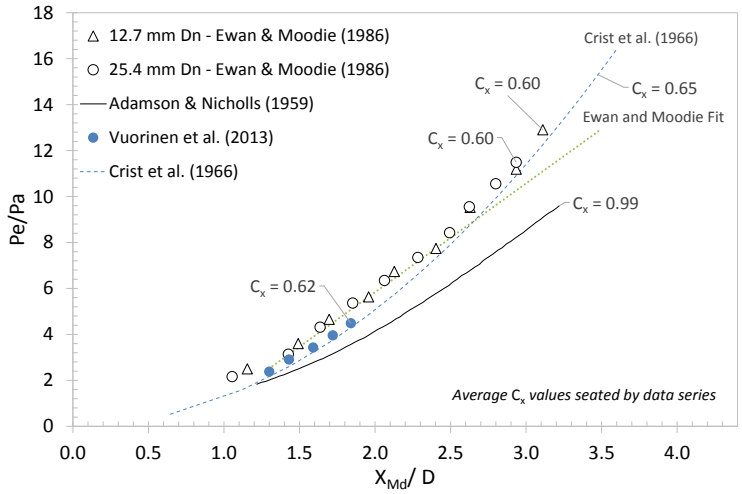

Figure 25, Barrel length distance (Mach disc location) from various sources. Source Data: as marked.

Literature on nearfield compressible structures for unsteady jets is scarce. Only a small number of works detail the transient nature of underexpanded compressible features (Scarcelli et al., 2012, White and Milton, 2008). Lacerda (1987) gives the greatest and most relevant detail where pressure ratios of PR3, 20, 50 and 100 were used for three gases: Helium, Nitrogen and Sulphur Hexafluoride. A burst disc was placed at a close distance upstream of a converging nozzle to initiate the gas delivery which. Lacerda (1987) not only details the features at good resolution (temporally, and to a lesser extent spatially) but covers pressure ratios experienced in DI fuel delivery within the early stages (<1ms aSOI) of jet delivery.

It can be seen from Figure 26 that the structures evolve rapidly after impulse and that a substantial lateral oscillation occurs in doing so. The density ratio also has substantial influence on the development. Moreover, when considering a fixed time, $t = 500\,\mu s$ (*akin to* aSOI), the pressure ratio has a substantial bearing on the size of the structure. It is apparent that this is the most dominant effect on Mach disc location and diameter.

It can be seen from Figure 26 that the shock structures evolve rapidly after impulse and that a substantial lateral oscillation occurs in doing so. The density ratio also has substantial influence on the development. Moreover, when considering a fixed time, $t = 500\,\mu s$ (*akin to* aSOI), the pressure ratio has a substantial bearing on the size of the structure. It is apparent that this is the most dominant effect on Mach disc location and diameter.

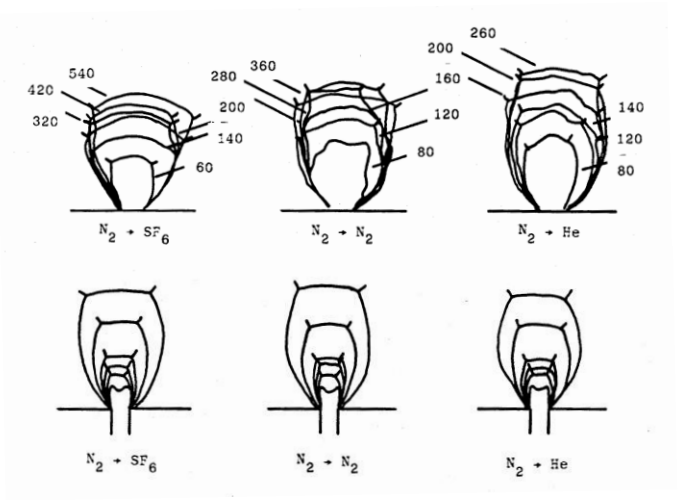

Figure 26, Impulsively start shock structures. Top row, constant PR100 where numbers denote µs after start. Second row depicts the influence of PR at t = 500 µs. Columns represent density variations. Source: (Lacerda, 1987).

The time-resolved shock structure trends reveal the pressure-based evolution of the Mach disc location (Figure 27). The sharp initial rise moves faster than the predicted pressure build up, and once quasi-steady pressures are reached, minor delivery pressure fluctuations induce oscillations (Lacerda, 1987). Again, the fluid density and absolute density ratio has a bearing on the evolution of the Mach disc location but once at steady state has only minor influence.

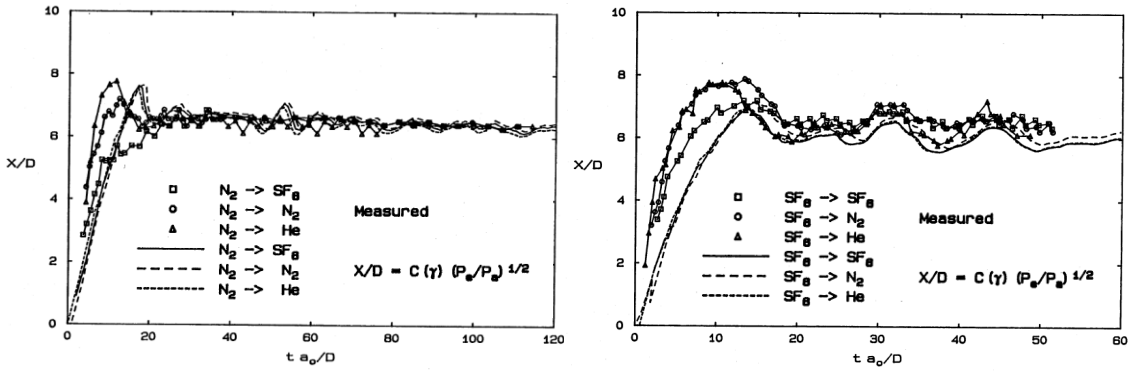

Figure 27, Mach disc location evolution for impulsively started PR100 jets; nitrogen (left) and Sulphur Hexafluoride (right). Source: (Lacerda, 1987).

More recently, Hatanaka et al. (2012) also measured the evolving barrel length (Figure 28). This was achieved using schlieren and PLIF methods and highlighted the effect of upstream pressure changes. Whilst Hatanaka et al. illustrated the transient (time history) nature of a jet, their work is not representative of conditions expected for fuel delivery. The change in barrel length is a result of the changing nozzle-exit pressure which was built up initially and subsequently reduced via changes to the upstream condition. The delivery time used by Hatanaka et al. appears to be very large, as the solenoid valve was positioned far upstream of a stagnation chamber and the time history suggests a quasi-steady-state >1.3 ms, and the stagnation chamber was allowed to deplete significantly.

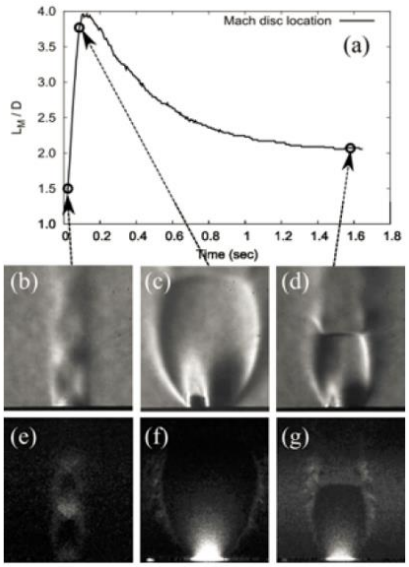

Figure 28, Pressure-reduced transient Mach disc location (a) for an air jet with schlieren (b-d) and LIF comparative images (e-g) Source: (Hatanaka et al., 2012).

Hatanaka and Saito (2012) computationally studied the influence of upstream stagnation chamber width, W, for straight, converging and diverging nozzle profiles. In all three scenarios, the smallest plenum chamber to nozzle diameter ratio ($W/D_j = 1$) typically produced the largest barrel lengths. The effects were greatest for the straight, round nozzle $(l/d = 10/5\ mm)$[4]; exit diameter changed in proportion to the plenum chamber. The results are shown in Figure 29, alongside the classical results of Crist et al. (1966).

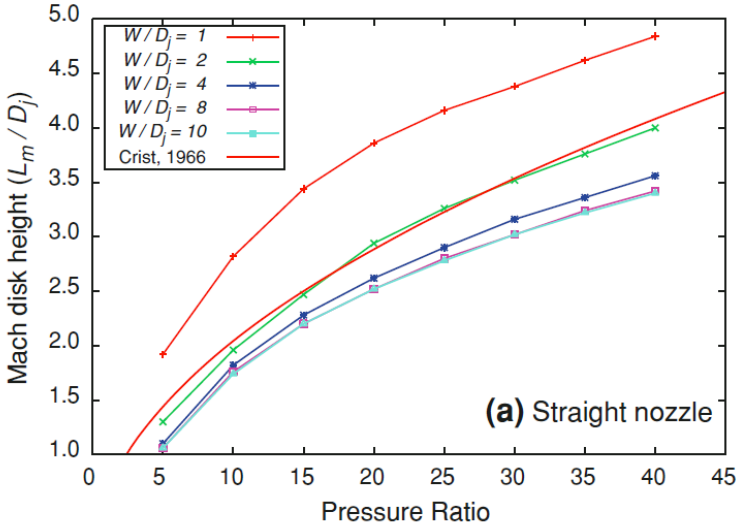

Figure 29, Effect of straight nozzle upstream geometry on Mach disc diameter. Source: (Hatanaka and Saito, 2012).
NB: nozzle exit edge has a slight, undisclosed chamfer.

[4] The l/d ratio is the same utilised in the high pressure ratio results chapters.

This result is interesting as it shows that the geometry immediately upstream of the nozzle exit influences the compressible structure formation. Given a geometrically complex environment such as that found inside a fuel injector, the question becomes: *What effect does a moving or stationary needle have on the flow structures?* This subject is investigated for high PR gas delivery in section 5.3 and in explicitly in 5.3.1.1.

The numerical results for the straight nozzle case at a $PR\ 20$ condition are shown in Figure 30, which compares two upstream geometries. Four key flow observations can be made about the influence of the upstream stagnation chamber geometry:

i. The flow preceding the nozzle exit is very different where the large plenum chamber width (and thus shorter nozzle length, l) yields large velocity changes in the nozzle throat section.
ii. The barrel length and Mach disc diameter are substantially different spatially.
iii. A higher flow velocity preceding the Mach disc is achieved in the smaller plenum chamber width (longer nozzle length, l).
iv. The ambient region at the shear-layer adjacent to the Mach disc appears to have a varied velocity profile. This could result in entrainment or mixing variation.

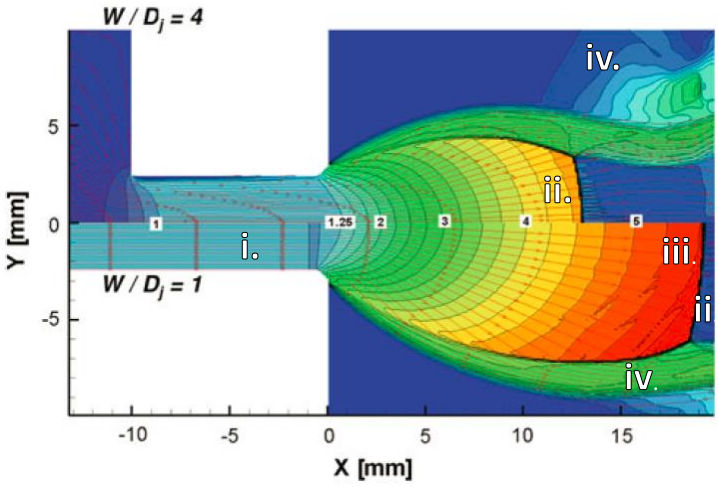

Figure 30, Mach number distribution of PR 20 jet, comparing two upstream geometries. ***NB:*** nozzle exit edge has a slight, undisclosed chamfer. Source: (Hatanaka and Saito, 2012).

Hatanaka and Saito (2012), also note the fact that the velocity profile within nozzle geometry will also have bearing on the mass flow rate, an important consideration for the constraints of injector fuel delivery. They also studied Mach disc diameter, which is the topic of the next section.

2.6.1.3 Mach Disc Diameter

Like barrel length, Mach disc diameter is a thoroughly studied structure of sonic underexpanded jets. In this work the term 'Mach disc diameter' refers to the radial size of the normal shock (it also is referred to as the 'height' in some texts). Determination of the normal shock size gives a clear indication to the strength of the underexpansion process – as with the barrel length. Whilst not as commonly studied as the barrel length, it is a popular metric in defining the steady-state jet nearfield structure. Moreover, the diameter (size) of the normal shock determines the overall area (volume) of the wholly compressible flow region, and thus understanding and predicting the Mach disc diameter improves the understanding of jet development and mixture preparation.

Crist et al. (1966) defined an empirical relationship between the steady-state Mach disc diameter and the jet pressure ratio, akin to the linear Ashkenas and Sherman (1966) term for barrel length (Equation 16):

Equation 16, Mach disc diameter expression. Source: (Crist et al., 1966).

$$\frac{D_{MD}}{D_n} \approx C_1 \sqrt{\frac{P_0}{P_a}}$$

where C_1 is an undefined constant. Variation in D_{MD} was also apparent for jets of varying density. This variation was attributed to condensation leading to a decrease in the stagnation pressure and increase in static pressure - leading to a shift in equilibrium at the barrel shear layer and thus altering the structure of the Mach disc (Crist et al., 1966). Addy (1981) represented the Mach disc diameter of steady-state air jets at a range of nozzle geometries, resulting in the empirical expression in Equation 17 below:

Equation 17, Mach disc diameter expression. Source: (Addy, 1981).

$$\frac{D_{Md}}{D_n} = C_1 \sqrt{\left(\frac{P_0}{P_a} - C_2\right)}$$

where C_1 and C_2 are constants assigned according to the nozzle geometry – a converging or sharp-edged orifice with $C_1 = 0.36\ and\ C_2 = 3.9$ and $C_1 = 0.31\ and\ C_2 = 5.0$ respectively. The effects of nozzle geometry were recently studied numerically (Otobe et al., 2008). Otobe et al. (2008) extended the work of Addy (1981) (whose results were in close correlation with oneanother) by highlighting the influence of barrel structure (i.e. curvature and vena contracta) on the Mach disc. The work reveals the correlation between expanding barrel angle and pressure ratio, and in turn the Mach disc diameter. The Mach disc diameter was shown to be influenced by the nozzle geometry but adequate pressure ratio normalisation was achieved if an equivalent nozzle diameter (Equation

23) was employed. That is, the shape of the internal (in their case, converging) geometry is the key influence, not the absolute diameter of the nozzle.

Similar to the detailed characterisation by Otobe (2008), Hatanaka and Saito (2012) related the Mach disc diameter to nozzle geometry. This was conducted at substantially higher pressure ratios than DI pressure ratios. A brief summary of the results in the literature is provided in Figure 31.

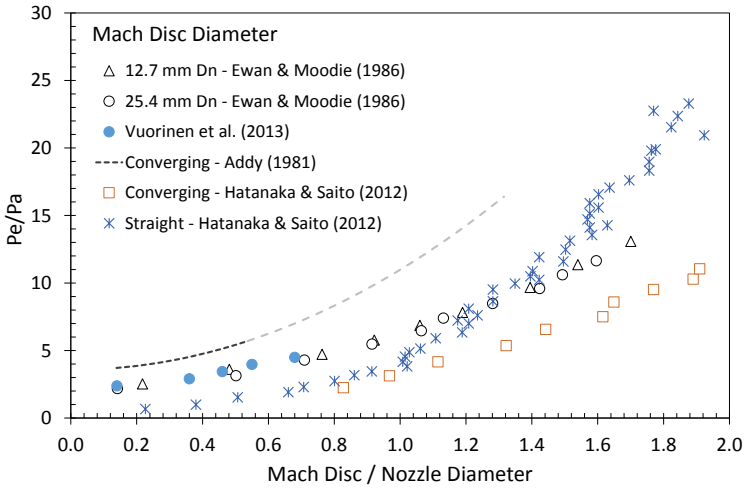

Figure 31, Mach disc diameter. Sources as labelled.

It can be seen that there is substantial spread in Mach disc diameter measurements, which can be attributed to the variation in nozzle and upstream geometry, density ratio or measurement technique. With no firm consensus it appears this attribute of transient (and steady-state) supersonic jets and the role it has on other jet regions are in need of condition-specific investigation.

2.6.2 Farfield Region

The quasi-steady region trails the vortex head and acts as a 'plume' to which mass and momentum is delivered. This region is particularly interesting as it accounts for a large proportion of the overall jet and the entrainment rate has been shown to remain constant throughout this region (Owston et al., 2008). More importantly, it is a region where the vast majority of mixing occurs and thus is crucial to fuel delivery applications. Additionally, the farfield region is the area to which the first objective of this thesis is principally tied: the characterisation of the targeting and dispersion behaviour of the gaseous fuel jet. The characterisation and measurement of the farfield region is of equal importance to the third objective, which relates the effects of the jet on the in-cylinder flow and turbulence. The farfield region is the most commonly studied region with respect to engine/combustion research, but like the nearfield region, the transient behaviour of fuel jets issued at high pressure ratios is still largely unknown.

2.6.2.1 Axial Development

The axial penetration of a fuel jet is the most widely studied parameter; it is a straightforward measurement and yields a substantial amount of information about the fuel delivery. Typically, the penetration is studied as an absolute measure, in mm or x/d or as a derivative of time (velocity). The location of the jet tip, x, can be produced from the velocity-decay constant and the equivalent nozzle diameter (Equation 23), producing Equation 18, with similar adaptations as shown by (Abraham, 1996), for example.

Equation 18, Jet tip axial penetration length. Source: (Ra et al., 2005).

$$x = \sqrt{2\ C\ u_{exit}\ d_e\ t}$$

Ouellette and Hill (2000) normalised the penetration length of the jet to examine the self-similarity as the jet develops for an increasing injection time. After applying momentum conservation laws, they proposed the following model for penetration location, x:

Equation 19, Jet tip axial penetration length for a compressible jet. Source: (Ouellette and Hill, 2000).

$$x = \Gamma\left(\frac{\dot{M}_n}{\rho_{amb}}\right)^{\frac{1}{4}} t^{\frac{1}{2}}$$

where, Γ is the proportionality constant as defined by the gradient of the remaining terms, $\dot{M}_n$ is the momentum injection rate and t is the time aSOI. Recently, Johansen et al. (2013), employed the equation proposed above in a study of compressible, high pressure ratio helium jets in which they found good agreement, albeit with slightly lower values of Γ and greater values of self-similarity, with the results previously reported by Ouellette and Hill (2000).

Self-similarity, s, is represented through an approach utilised by Ouellette (1996) and Johansen et al. (2013) and is a strong representation of how the flow develops. Geometrically, once the relationship between axial and radial extents is constantly proportional then self-similarity is said to be achieved. This constant is achieved through the relationship given in Equation 20 as follows.

Equation 20, Self-similarity index, *s*, for a jet measurements.

$$s = \frac{y}{x}$$

Where y and x are the radial and axial maximum penetrations respectively. This proportionality index is useful in transposing individual relationships of axial or radial development and as a good indicator for numerical comparisons.

Petersen (2006) also discussed the scaling laws typically employed, mainly in incompressible flows, concluding with the generalised penetration law as expressed in Equation 21 being the most universal (based on the proportionality constant utilised in Equation 19).

Equation 21, Penetration scaling law. Source: (Petersen, 2006).

$$\frac{x - x_0}{d_{eq}} = \alpha \left(\frac{t u_n}{d_{eq}}\right)^{\frac{1}{2}}$$

The proportionality constant, α, is reported as having a range between 2.14 and 3.00 (Petersen, 2006, Johansen et al., 2013). Alternatively, Equation 19 and Equation 21 can be rewritten in a more convenient form as follows (Equation 22):

Equation 22, Completed axial penetration scaling law, density and time. Source: (Ouellette and Hill, 2000).

$$\frac{x}{d_{eq}} = \Gamma \left(\frac{\pi}{4}\right)^{\frac{1}{4}} \left(\frac{t u_n}{d_{eq}}\right)^{\frac{1}{2}}$$

where, d_{eq} is the equivalent nozzle exit diameter (first introduced as the pseudo-nozzle diameter) and Γ is the proportionality constant. This scaling parameter can be derived from Equation 10 when incorporating a discharge coefficient, the ideal gas laws and equal velocities at the pseudo-diameter and nozzle exit. This scaling-relationship has been popular within the literature, for example; (Abraham, 1996, Ouellette, 1996, Owston, 2010, Panda and Seasholtz, 1999). This scaling method (Equation 23) uses conservation of mass principles when treating the expanding nearfield region, where it is assumed that injected mass flux is conserved up to the location of the Mach disc (Owston et al., 2008).

Equation 23, Equivalent nozzle exit diameter. Source: (Owston et al., 2008) Originally Thring and Newby (1953).

$$d_{eq} = d_e \left(\frac{\rho_{exit}}{\rho_{amb}}\right)^{1/2}$$

Baert et al. (2010) studied the effects of NPR and circular nozzle geometry, d_e and l/d by employing a momentum-density-time normalisation. The study was performed for jets issued under direct injection conditions. Figure 32 shows that in both cases the individual penetration (per $(J/\rho_{amb})^{1/4}$) collapses linearly, with a high level of certainty. This highlights the usefulness of the scaling term when comparing pressure ratio or nozzle geometry.

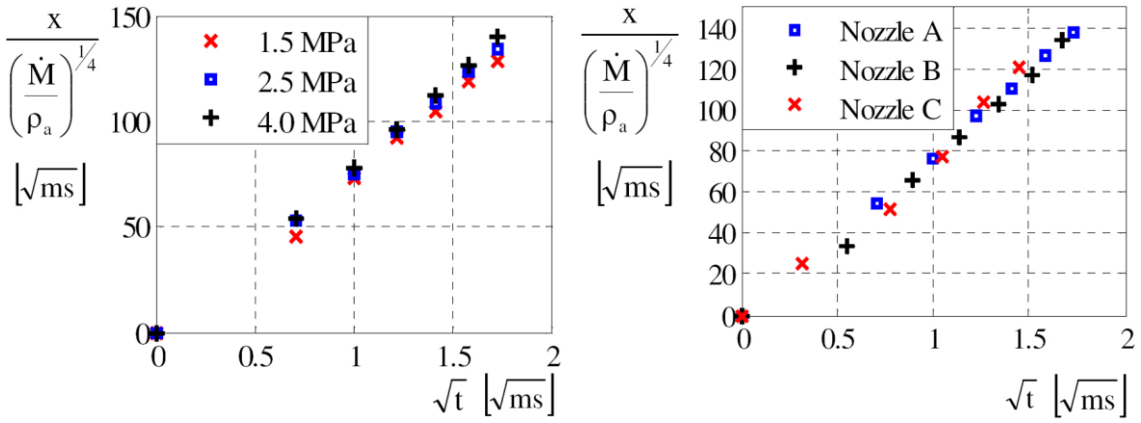

Figure 32, Non-dimensional jet tip penetration for increasing pressure (left) and nozzle geometry (right). Source:(Baert et al., 2010) .

Equation 24 can also be applied to express the jet concentration decay, which gives a reasonable indication of fuel concentration. Originally this was represented in terms of enthalpy (Kleinstein, 1964, Witze, 1974) and later used simply as mass fraction (Ewan and Moodie, 1986).

Equation 24, Kleinstein concentration decay for mass fraction. Source: (Ewan and Moodie, 1986).

$$Y_o = 1 - exp\left[-\frac{1}{K\frac{x}{r_{eq}}\left(\frac{\rho_{eq}}{\rho_{exit}}\right)^{1/2} - X_c}\right]$$

where the terms K and X_c were defined from Kleinstein (1964) as 0.104 and 0.700, respectively (Ewan and Moodie, 1986).

It is apparent that a large amount of data can be obtained on the axial development of transient jets. Various equations can be employed to resolve the nature of a free jet using, compressible, incompressible and varying density ratio considerations.

2.6.2.2 Radial Development and Spread Angle

The radial development of a steady-state jet is governed by the turbulent mixing and entrainment processes. This process is cyclic, as momentum from fuel delivery is exchanged with the entrained fluid, resulting in a spreading mixing region (Namer and Ötügen, 1988). The surrounding fluid may be entrained into the jet from either the turbulent diffusion (the small-eddy mixing at the outer jet shear layer) or the bulk convection from the large pressure and temperature difference between the jet core and ambient media. Ungate et al. (1975) showed that the incompressible jet spread angle becomes constant once fully turbulent Reynolds numbers are achieved. Spread angles in the order of 20-25° were obtained (Ungate et al., 1975). Supporting the constant-turbulence;

constant spread angle notion, Ricou and Spalding., (1961) show that for steady-state air jets the ambient air entrainment rate remains constant for $Re > 3 \times 10^4$, with Hill (1972) conferring consistent entrainment rates for a given axial location.

Likewise jets issued into quiescent media at equal density have been shown to develop proportionally in the axial and radial domains. Since the jets propagate in a self-similar fashion, a universal spread angle of approximately 24° exists (Cushman-Roisin, 2014). For compressible transient jets issued at high pressure ratios, self-similarity is not achieved until substantial axial development. Additionally, these jets are assumed to represent a conical shape. For highly underexpanded jets the nearfield region - as previously depicted - exhibits larger spread angles, with the barrel-like structures dictating the angle (Otobe et al., 2008).

The velocity of the jet will decrease with the additional mass entrained, and as such much of the literature on jet spreading rates has been developed from a radial velocity perspective. The mass of the jet increases while the velocity decreases at constant momentum conditions (Horn and Thring, 1956). Boguslawski and Popiel. (1979) offered the following velocity spreading relationship (Equation 25), which, as before relies on jet self-similarity.

Equation 25, Velocity spreading rate of a turbulent free jet. Source: (Boguslawski and Popiel, 1979).

$$Velocity\ Spreading\ Rate = \frac{r_{0.5}}{(x + a)}$$

Where $r_{0.5}$, represents the radius at which the velocity is half of its maximum and $a = -0.5d$.

The large range of geometric spread angle measurements for transient jets found in the literature suggests that there is a broad discrepancy in the evaluation of turbulent jet spread. This is further discussed in section 3.7.6.2. Consistent transient-jet angles have proved difficult to measure (Chitsaz et al., 2013) even at low pressure ratios, at which the influence of underexpansion is relatively minor.

2.6.2.3 Velocity Profiles and Self-Similarity

In this section the velocity profile evolution within the nearfield and farfield region is discussed and the importance of these measurements is highlighted. Profiling the jet velocity distributions provide essential behavioural information on the flow process (e.g. the spreading and hence mixing rate, as discussed in the previous section).

The studies by (Johannesen, 1957) and (Love et al., 1959) were some of the first experimental works to comprehensively detail the velocity fields of compressible jets issued at underexpansion pressure ratios. Around this period numerical theories were also being developed (e.g. (Warren,

1953). Since then, many works have detailed the velocity field profiles periodically up to the present era. Before the 1980s the works were conducted typically with hot-wire anemometry (Witze and Dwyer, 1976), an intrusive but highly reliable technique. In subsequent years the research increasingly relied on unobtrusive laser diagnostics to measure the finer-scale flow structures and the global evolution of coherent structures. The latter produced a significant step forward in knowledge of the environments in which these jets exist. One of the more detailed velocity analysis works came from Hussein et al. (1994), who employed both laser Doppler and hot wire anemometry.

The velocity-induced shearing at the edge of a turbulent jet entrains the surrounding fluid and thus, an exchange in kinetic energy exists between the jet and quiescent media. As gaseous fuels have low density, the velocity is an important determinant of the mixing with the surrounding air. The velocity magnitude at the centreline remains unaffected to the point when the shearing and thus energy lost due to momentum conversion takes over.

The shear effects will eventually envelop the core region, resulting in the theoretically represented triangular core shape. This is evident when considering an incompressible jet in Figure 33, where the magnitude of the centreline velocity remains constant throughout the nearfield region with the outer velocities, however, decaying to the radial boundary in an approximately Gaussian behaviour. The centreline velocity will decrease once the nearfield region subsides. This decay in velocity will initially taper off somewhat slowly and then accelerate according to the square root approximation presented (Schlichting and Gersten, 2000). This decay structure is also reflected in the work of Warren (1953). The velocity profile in the farfield regions will be addressed in subsequent sections.

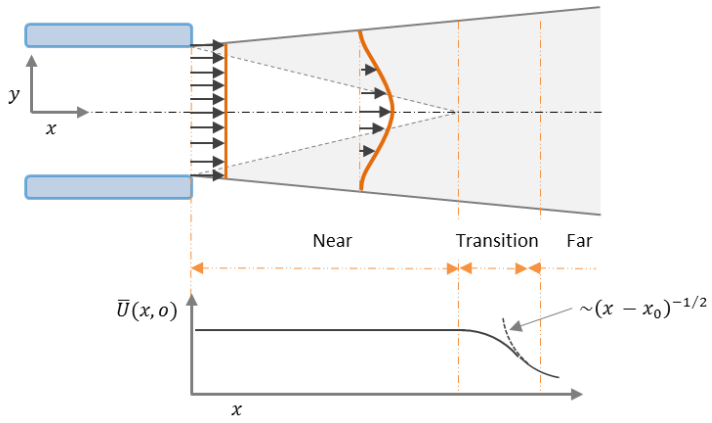

Figure 33, Incompressible turbulent jet transition field. Reproduced from: (Schlichting and Gersten, 2000).

Zuckerman and Lior (2006) proposed that the end of the core region occurs when "the centreline flow dynamic pressure (proportional to the speed squared) reaches 95% of its original value", which they suggest to be four to eight nozzle diameters for free jets. Figure 34 depicts the

velocity distribution in the core and transition regions. This depiction not only displays the velocity magnitudes but gives a good description of the increasing mass flow within the jet as the ambient air is entrained.

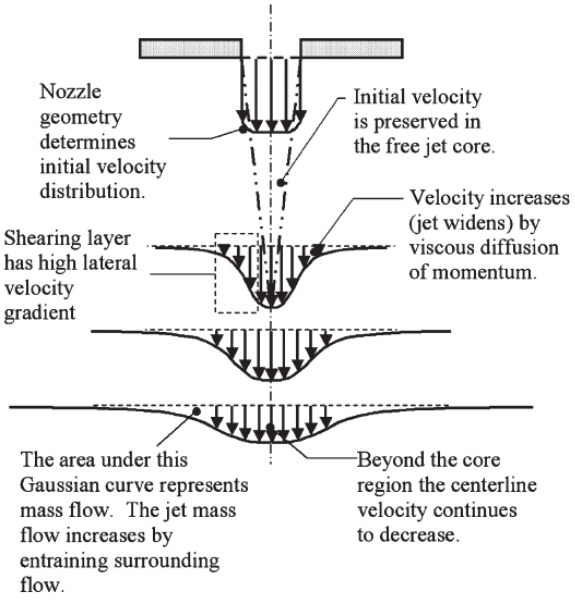

Figure 34, Velocity profile of an incompressible free jet. Source: (Zuckerman and Lior, 2006)

It is worth briefly explaining the development of the radial jet velocity profile to understand the process within the jet core. Initially, the exit velocity profile is uniform (Ricou and Spalding, 1961, Musculus, 2009) with a 'top hat' profile, and is at its highest magnitude due to insufficient time to interact with the ambient air. As more momentum is exerted on the jet front, the jet boundaries will begin the shearing process, forming small-scale vortices whilst the core remains stable (Hyun et al., 1995). The velocity profile will then widen in the radial direction with the velocity at the axial centreline remaining constant due to the constant mass being fed into the developing jet and the dispersion of the surrounding jet. When the internal energy of the jet drops below that of the surrounding jet the core region will be enveloped, resulting in a Gaussian-like velocity profile, tapering down towards the jet boundary and nearing zero (Hill, 1972) against the ambient air layer. The centreline velocity will continue to reduce beyond this point. As indicated by Zuckerman and Lior (2006), the end of the core region can easily be related back to a velocity squared function. Hence, the radial velocity profile is an important consideration when modelling a jet numerically.

The formulation of the jet centreline velocity decay was the subject of an article by Witze (1974) who's model (based on Kleinstein (1964)) correlated well to the large validation data set of compressible jets under both iso- and non-thermal conditions. The expression for centreline velocity decay proposed in this work is given in Equation 26.

Equation 26, Centreline velocity decay. Source: (Witze, 1974)

$$\bar{u}_c(\bar{x}) = 1 - exp\left[\frac{-1}{K\bar{x}\left(\frac{\rho_{amb}}{\rho_{exit}}\right)^{1/2} - X_c}\right]$$

Where, x and r are the axial and radial coordinates, respectively, $\bar{x} = x/r_j$ and X_c represents the potential core length constant. Based on the work of Kleinstein (1964), in which the two constants $X_c = 0.70$ and $K = 0.074$ were proposed, (for $\bar{x}\left(\frac{\rho_{amb}}{\rho_{exit}}\right)^{1/2} \geq 9.46$) Witze (1974) also provided an expression for the calculation of axial jet core length location as (Equation 27):

Equation 27, Potential core length. Source: (Witze, 1974).

$$\bar{x}_{core} = \frac{0.70}{K\left(\frac{\rho_{amb}}{\rho_{exit}}\right)^{1/2}}$$

The eddy viscosity coefficient was extensively studied by Eggers (1966) for supersonic jets, and comparison was made to the seminal studies of Warren (1957) and Kleinstein (1963). Moreover, Witze's (1974) examination of his large dataset enabled the conclusion that the eddy viscosity proportionality constant, K[5], could be represented individually for subsonic and supersonic jets as follows in Equation 28 and Equation 29. These expressions proved to fit well to a range of super- and subsonic conditions with Reynolds numbers ranging from; 2.46 x 10^4 to 2.22 x 10^7, a Mach number range of 0.067 to 2.60, and an NPR between 0.35 and 2.38 (Witze, 1974).

Equation 28, Subsonic proportionality constant for core length. Source: (Witze, 1974)..

$$K_{subsonic} = 0.08(1 - 0.16M_{exit})\left(\frac{\rho_{amb}}{\rho_{exit}}\right)^{-0.22}$$

Equation 29, Supersonic proportionality constant for core length. Source: (Witze, 1974).

$$K_{supersonic} = 0.063\left(M_{exit}^2 - 1\right)^{-0.15}$$

The Kleinstein-Witze expression introduced in Equation 26 was again utilised and substantiated in work carried out by Ewan and Moodie (1986), albeit in the form represented below. This expression was recently validated for engine-like DI conditions by Baert et al., (2010).

[5] K is also referred to in some text as the entrainment constant or the kinematic constant.

Equation 30, Kleinstein-Witze centreline axial decay velocity adopted by (Ewan and Moodie, 1986).

$$\frac{u_{CL}}{u_{exit}} = 1 - exp\left[-\frac{1}{K\left(\frac{\rho_{amb}}{\rho_{exit}}\right)^{1/2}\frac{x}{r} - X_c}\right]$$

The radial velocity profile is another well studied parameter in turbulent free jets. Quite often the radial velocity is related to the centreline velocity and, as previously noted, is a useful measure of the jet spreading rate. One of the better visual representations of experimental and numerical radial velocity distributions is presented in Figure 35, captured for the nearfield region $(x/d < 12)$ (Boguslawski and Popiel, 1979).

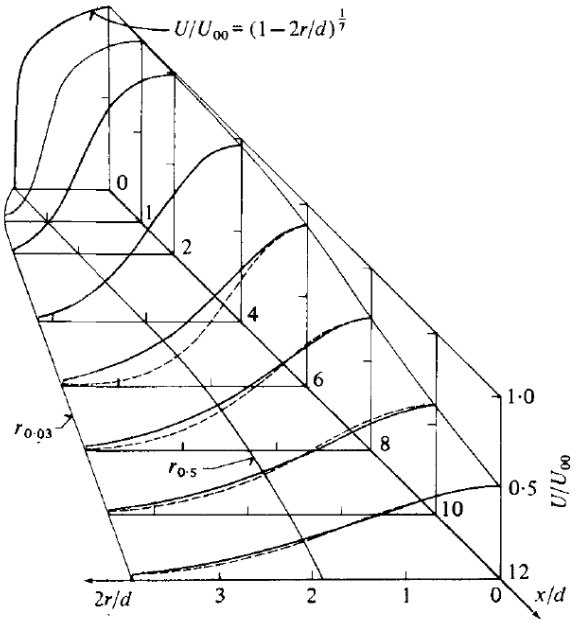

Figure 35, Radial velocity profile for experimental (solid line) and numerical (dashed line) for a turbulent air jet issued at constant temperature. Source: (Boguslawski and Popiel, 1979).

Boguslawski and Popiel (1978) note that under subsonic conditions the radial velocity profile becomes self-similar, that is, the centreline velocity decay is proportional to the spreading rate, for $x/d > 8$, and as seen in Figure 35 the numerical relationship fits the data quite well according to Equation 31:

Equation 31, Radial velocity profile. Source: (Boguslawski and Popiel, 1979).

$$\frac{U}{U_o} = exp\left[-108\left(\frac{r}{x+a}\right)^2\right]$$

where, $a = -0.5d$ is the virtual origin from the nozzle exit. A similar relationship is given by (Warren, 1953) and employed by (Ewan and Moodie, 1986).

The radial and axial velocity profiles are a key determinant of flow development. The shape of the radial profiles are important for fuel delivery flows; the mixing rate at the shear layer is dependent on such a profile, as is the entrainment rate. Moreover, the rapidly rising magnitude of the radial velocity profile may inhibit the ignition at late injection times (stratified operation) if the jet were to encroach on the electrode with the jet-velocity exceeding the ignition threshold.

2.6.2.4 Entrainment

Ricou and Spalding (1961) injected a gaseous jet into a porous chamber where an air supply through the chamber walls was controlled and measured for the determination of gaseous entrainment rate. The authors suggested that the flow rate entering via chamber walls was equal to the entrained air mass when there was no axial pressure gradients detected in the gas jet. Although length and time scales are not directly within the scope of this thesis, Ricou and Spalding's work provides a fundamental understanding of entrainment phenomena. This method of obtaining the entrainment rate was also employed by Hill (1972). More recently, laser diagnostics (LDV and PIV) have been employed to determine the ambient air entrainment of gas jets (Andriani et al., 1996, Capone et al., 2012), as have numerical methods (Post et al., 2000, Song and Abraham, 2003). The predominant equation used for the determination of the mass entrainment rate of the otherwise quiescent fluid surrounding the jet is given in the following expression:

Equation 32, Mass entrainment at normal angles to the jet axis. Source: (Ricou and Spalding, 1961).

$$\dot{m}_e = \int_0^\infty 2\pi\bar{\rho}\bar{u}\, y dy$$

where, the massflow entrained, $\dot{m}_e$, is a function of the mean ambient density, $\bar{\rho}$, velocity, $\bar{u}$, and a spatial location for the jet radius, r. In order to normalise entrainment, the jet massflow (determined by the mass injected ($\dot{m}_f$), or excess momentum flux (J) injected and the jet-to-air density ratio can be employed resulting in the entrainment coefficient. The entrainment coefficient, K_2', is employed in the following relationship (Figure 33).

Equation 33, Entrainment constant and coefficient. Source: (Ricou and Spalding, 1961).

$$K_1 = \frac{\dot{m}_e + \dot{m}_f}{x{J^{1/2}}{\rho_{amb}}^{1/2}} = K_2' \left(\frac{1}{4}\pi\right)^{1/2} \left(\frac{\rho_{jet}}{\rho_{amb}}\right)^{1/2}$$

where K_1, is the entrainment constant. For round nozzles the relationship between the two constants is defined through:

Equation 34, Entrainment coefficient to constant relationship. Source: (Hill, 1972).

$$K_2' = \frac{2K_1}{\sqrt{\pi}}$$

The kinetic momentum flux can be written in the form of Equation 35. If J is assumed to remain constant in the axial direction and the initial velocity profile, U, has a top hat profile then the constant $C_j = 1$ (Abraham, 1996). More recently, Ra. et al (2005) incorporates of jet momentum flux too in defining jet behaviour.

Equation 35, Kinetic momentum flux for a free jet. Source: (Abraham, 1996).

$$J = C_j \pi U_{jet\ CL}^2 \frac{d^2}{4}$$

The entrainment coefficient can be related back to the governing conditions through the relationship in Equation 36 if a uniform density and velocity across the nozzle is assumed.

Equation 36, Entrainment coefficient. Source: (Andriani et al., 1996, Ricou and Spalding, 1961).

$$K_2' = \frac{d\dot{m}_e}{dz}\left(\frac{d}{\dot{m}_{exit}}\right)\left(\frac{\rho_{exit}}{\rho_{amb}}\right)^{1/2}$$

The entrainment coefficient can also be presented in a convenient form as follows:

Equation 37, Entrainment coefficient. Source: (Cossali et al., 2001).

$$\frac{\dot{m}_e + \dot{m}_f}{\dot{m}_f} = K_2'\left(\frac{x}{d}\right)\left(\frac{\rho_{amb}}{\rho_{exit}}\right)^{1/2}$$

Cossali et al. (2001) argue that the value of K_2' is not constant in the transient region, citing the transient nature of the flow and lack of self-similar velocity profiles. When their transient jet approached steady-state conditions, a K_2' value similar to Ricou and Spalding, (1961) was produced. The air-jet experiments of Cossali et al. (2001) were, however, undertaken at low pressure ratios (PR1.44 and 2.2), so the nearfield influences would have remained largely unaffected by compressible flow features.

Whilst very few publications deal with the transient jet entrainment rate, many deal with steady flow conditions. A comparison of steady-to-unsteady conditions was, however, provided by Andriani et al. (1996), who made LDV measurements across a theoretically defined cone angle. This method is typically employed method where the actual jet boundary is largely unknown. It is not fully representative of discrete conditions at the jet boundary but does afford a good tool for comparing various jet conditions. Andriani et al., (1996) investigated gas jets issued at a density-ratio range

between 1.048 and 1.709 and an NPR of 1.4 to 2.5, with no induced temperature ratio. For the unsteady region of the jets, they proposed the relationship outlined in Equation 38.

Equation 38, Entrainment coefficient. Source: (Andriani et al., 1996).

$$K_2' = 0.0718\left(\frac{x}{d} + 7.77\right)^{0.460} \qquad \left(for \frac{x}{d} < 18\right)$$

For axial locations outside of $7 < x/d < 15$, the unsteady jet produced a greater entrainment rate than the steady-state jet and the non-linear nearfield dependence of axial velocity on x was exhibited. The influence of the travelling vortex head is discussed as an influential factor on the unsteady entrainment rate (Cossali et al., 2001).

The value of the steady-state nearfield entrainment coefficient varies widely in the literature with citations in the range between $0.183 < K_2' < 0.457$ (Boguslawski and Popiel, 1979, Schlichting and Gersten, 2000). This range is of course dependent on the accuracy of the experimental method, jet conditions and most importantly the point in the jet's temporal and spatial development at which measurements are taken. Hill (1972) the effect of jet Reynolds numbers on ambient entrainment, concluding that entrainment coefficient was independent of Re and strongly dependent on the axial distance. This conclusion represents jets in a fairly typical Re range of 6-20 x 10^4, as represented in Figure 36 below (Hill, 1972).

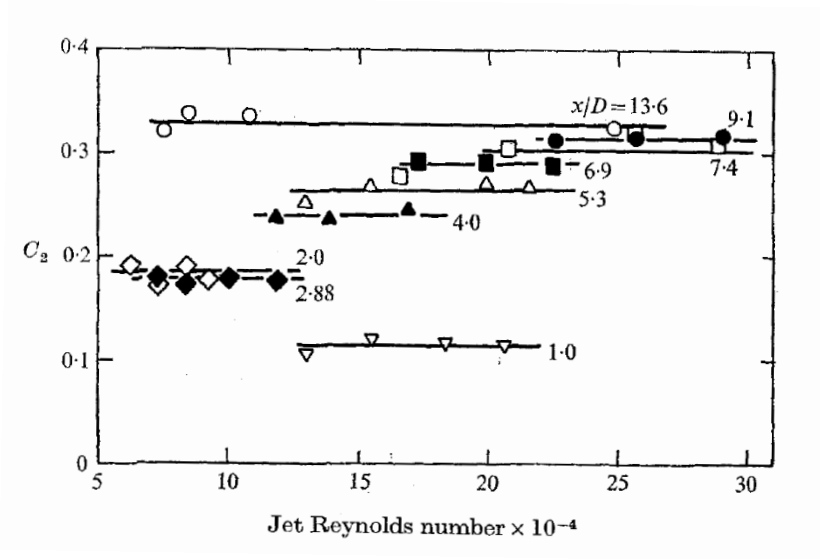

Figure 36, Effect of Re number on the entrainment coefficient in the initial region. Source: (Hill, 1972).

The effect of Re on the entrainment rate was first presented some 10 years earlier where constant entrainment rate and hence coefficient is seen for jets with an increasing Re number above 2.5 x 10^4 (Ricou and Spalding, 1961). Prior to this Reynolds number, the rate of entrainment increased exponentially.

For jets at constant Re number and in the initial region, Boguslawski and Popiel (1979) measured a linear entrainment rate bounded by the relationship of $0.183(x/d)$ for $x/d < 12$. This linear trend was also identified by Andriani et al. (1996) as defined previously through Equation 38. Ricou and Spalding (1961) demonstrated that a strong linear trend exists for x/d values in excess of ~25 for jets of varying density and buoyancy, and that the variation in specific entrainment can be collapsed with reasonable success to a singular profile (used in Equation 36) for jets above $Re = 2.5\ x\ 10^4$. This relationship has been employed in numerous subsequent studies (Abraham, 1996, Ouellette, 1996). This relationship is proposed to be dependent on the local excess momentum flux, J, where $K_1 = 0.282$.

Conversely, the entrainment in the jet exit region can also be nonlinear (Figure 37). Hill (1972) employed a porous-walled chamber to measure the entrainment rate, a technique very similar to that of Ricou and Spalding (1961), and a somewhat nonlinear relationship was found in the initial region. Beyond the initial region the entrainment rate remained relatively constant at a value of $K_2' = 0.32$ for $x/d \geq 13$.

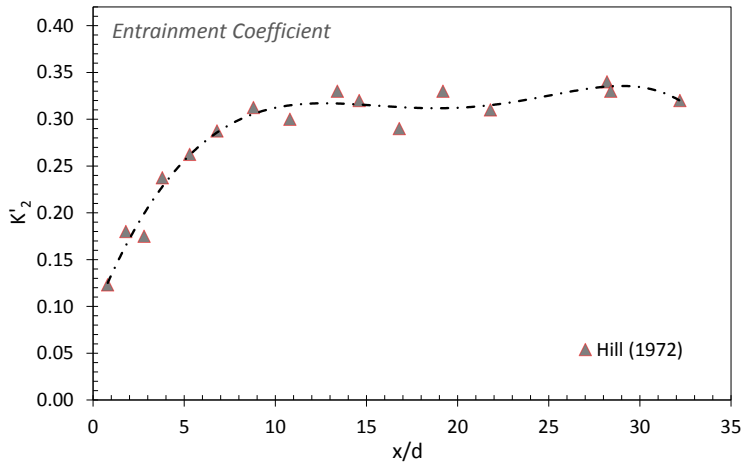

Figure 37, Entrainment coefficient in the near and far field for a steady turbulent round jet. Source data: (Hill, 1972).

It is apparent from Figure 37 that the entrainment in the nearfield region is substantially lower than the developed region. Abraham (1996) undertook a substantial review of the variation observed in the entrainment constant, concluding that the exact value of this constant is only known within a factor of about 2. This uncertainty reduces the accuracy of modelling such jets numerically (Abraham, 1996). Abraham (1996) asserted that an effect of nozzle geometry (l/d) on this constant is apparent, where for short convergent nozzles $(l/d = 1)$ entrainment rate is greater (0.26 to 0.32) than for longer nozzles $(l/d \gg 1)$. A later article by Post, Abraham and colleagues (2000), presented a comprehensive overview of the literature on the variability in the entrainment constant. Figure 38 exhibits a mix of experimental and numerical data, showing that for the majority of studies the mass entrained increases until the steady fully-developed jet is attained.

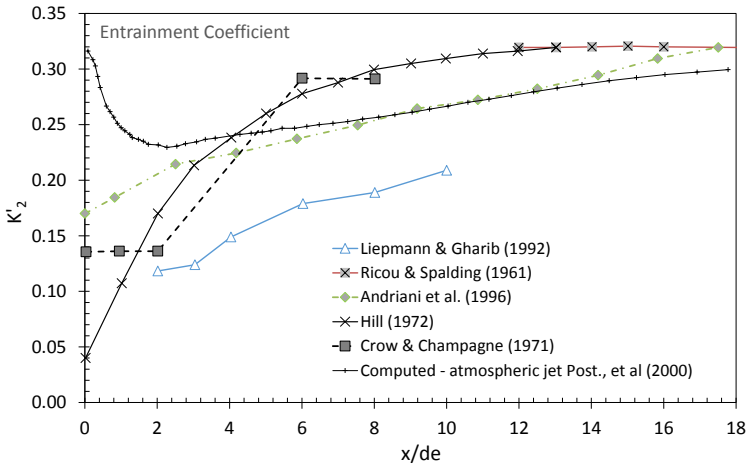

Figure 38, Entrainment coefficient, K_2' for nozzle-equivalent penetration lengths. Adapted from: (Post et al., 2000).

The variation in the reported entrainment coefficient and lack of highly resolved detail in the nearfield ($x/d \lesssim 10$) requires high spatial resolution across the entire field. To this end, the use of PIV appears an appropriate measurement technique but to date has been rarely applied.

Recent research has attempted to identify an appropriate measurement location for velocity in the determination of the entrainment rate. The uncertainties in using theoretical or root mean squared (rms) velocity-derived measurement surfaces hindered previous research (Cossali et al., 2001). Using a novel combining PLIF and PIV measurements simultaneously, Bruneaux et al., (2011) investigated the mean normal velocity, $\bar{u}_n$ (PIV), at a specified concentration boundary, x, r (LIF). The value for the entrainment rate was in turn calculated through the following control surface equation, derived from Equation 32.

Equation 39, Mass entrained through control surface. Source: (Bruneaux et al., 2011).

$$\dot{m}_e(x) = 2\pi\rho r \int \bar{u}_n(x,r) \frac{dx}{cos(\theta)}$$

Bruneaux et al's data on the effect of nozzle diameter on entrainment rate are shown in Figure 39. A decreased nozzle orifice size produced an increase in the entrainment rate.

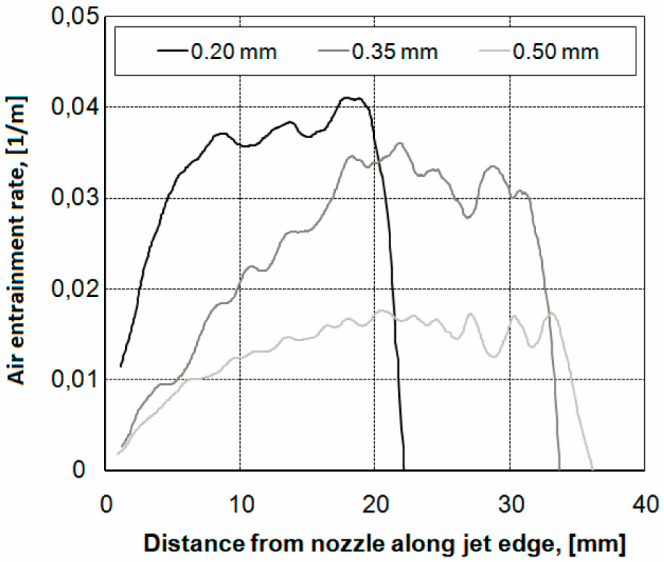

Figure 39, Normalised entrainment rate for various nozzle diameters of a Methane/Ethane jet issued at 200 bar. Source: (Bruneaux et al., 2011).

It has been shown that entrainment of ambient air plays a dominant role in the development of turbulent free jets. For example, the spreading rate (Lyogun and Birouk, 2009) and mixing (Turner, 1986) of jets are governed by the entrainment process. However, an approach incorporating physical jet structures is needed when studying entrainment as many of the physical process are interlinked, such as the underexpanded shock-structure size and development on entrainment (Otobe et al., 2008).

It is hypothesised that the flow region within the barrel length of highly underexpanded jets is influential in controlling the nearfield ambient entrainment rate. The two main influences are predicted.

- the convection of the ambient gas, where the jet core is substantially lower in temperature and pressure than the ambient region (induced by the large axial velocity), and;
- the entrainment rate is affected by the strength of turbulent shear layer

It is foreseeable that the compressible barrel-structures will influence the nearfield turbulent shear-layer. Studying the effects of the nearfield compressible behaviour on the incompressible nearfield regions (jet radial and axial penetration, and shear layer thickness) should enable accurate estimate of the entrainment rate. This is particularly important for transient jets, as little is currently known about the evolution of the nearfield compressible structures for fuel jets issued at high PR. Additionally, adequately resolving the entrainment rate spatially (x/d) will determine if there is a varying rate of entrainment along the transient highly underexpanded jet.

THIS PAGE IS INTENTIONALLY BLANK

3. Experimental Method

3.1 General Introduction

This chapter outlines the approach used to identify and quantify the attributes of gaseous jets which influence gaseous fuel delivery and mixture preparation. Fuel jets are issued into a quiescent medium where optical diagnostics are applied to measure the characteristics of the: targeting and dispersion behaviour of the gaseous fuel jet, transient jet behaviour near the nozzle exit region and the effects of the jets on the in-cylinder flow and turbulence. The broad quantities measured include; the incompressible and compressible geometric features of the jet, the centerline velocity profile of the jet and the velocity profile within the ambient region.

3.2 Natural Gas – Fuel Property Selection

The natural gas required for the gas jet experiments came from a commercial mains-supply compressed natural gas stock was used. This represents the stock that would be used for refuelling road vehicles and thus aligns experiments to end-user requirements. Natural gas consists in majority of Methane (80 – 100%) but can contain other gases based on the reservoir and method of recovery and conditioning of the gas. These other fractions can either be higher hydrocarbons or inert gases but for automotive use their maximum fraction is not always regulated. The most important other fractions are: ethane (max. 15%), propane (max. 5%), butane (max. 2%), CO2 (max. 2%) and N2 (max. 15%) with the values given in brackets being the maximum values proposed in Germany for automotive use (Elvers, 2008). Other gas fractions than methane change the characteristics of CNG and therefore a quality indicator for gaseous fuels was introduced namely the Wobbe index and is correlated to the stoichiometric air-fuel ratio (Owen and Coley, 1995). Thus, the Wobbe index of a given gaseous fuel is:

Equation 40, Wobbe Index. Source: (Owen and Coley, 1995).

$$WI = H/\sqrt{\rho}$$

where H is the volumetric heating value and ρ is the specific gravity of the gas.

For natural gas the Wobbe index can vary between 37.8 MJ/m^3 and 56.5 MJ/m^3 (Elvers, 2008, Owen and Coley, 1995). Because of this large range, extra engine management functions are required for the engine to guarantee performance and emissions. For example, knock and lambda control are obligatory on CNG engines (Pischinger et al., 2003). An overview of the effects of variation in CNG characteristics on engine operation was given by Ahmadi and Izanloo (2008) provided in Table 6.

Table 6, Natural gas characteristics: modes and effects of composition. Source: (Ahmadi and Izanloo, 2008).

Natural gas variation	**Fuel consequence**	**Engine consequence**
High methane level	Higher heating value	Higher engine performance
High ethane, propane and butane level	Liquid phase build-up in pressure regulator	Pressure regulator malfunction
	Lower knock resistance	Lower engine performance
High nitrogen level	Higher injection duration	Limited engine performance Higher fuel consumption
High unknown gas level	Loosing optimum control over air/fuel ratio	Weaker drivability and engine start

The composition of natural gas is quite varied in Australia, as it is across the globe. Seasonal data from several sources are outlined in Figure 40, with the five main constituents shown. Aside from methane the two largest remaining constituents; ethane and carbon dioxide also vary substantially, where carbon dioxide also typically exceeds the German automotive limits and is in consequence to the engine modal effects in Table 6.

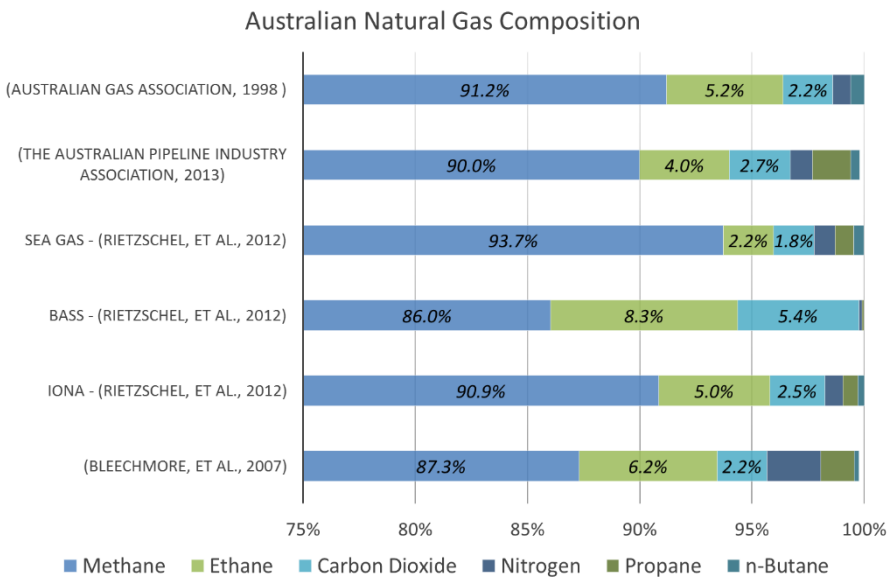

Figure 40, Australian natural gas composition of the six main constituents. Sources pared to data.

The exact composition of the town-supply natural gas used throughout this study is unknown. The sample used, however, was of the same stock for the entire experimental sequence. It was decided to assume the average composition values proposed by Rietzschel et al., (2012) as they represent a good cross section of the Australian market and are data obtained from the closest extraction sources. These average values are outlined in Table 7. The index assumed in this work is at the lower limit of previously defined Wobbe index range; ~37 MJ/m^3.

Table 7, Average composition of natural gas supplied locally. Source: (Rietzschel et al., 2012).

Constituent	% Volume	% Mass
Methane	90.37	81.84
Ethane	5.11	8.68
Carbon Dioxide	3.03	7.53
Nitrogen	0.66	0.52
Propane	0.57	1.42
Butane	0.25	0.82

3.3 Constant Volume Chamber

Constant volume chambers (CVC) are a widely used experimental apparatus for replicating engine-like conditions quiescently. The quiescent environment allows the injection, or in some cases combustion, phenomena to be removed from the dynamic processes found within typical engine operation. This decoupling allows a more fundamental approach to the analysis with complexity based on an addition hierarchy, as represented in Figure 41 below.

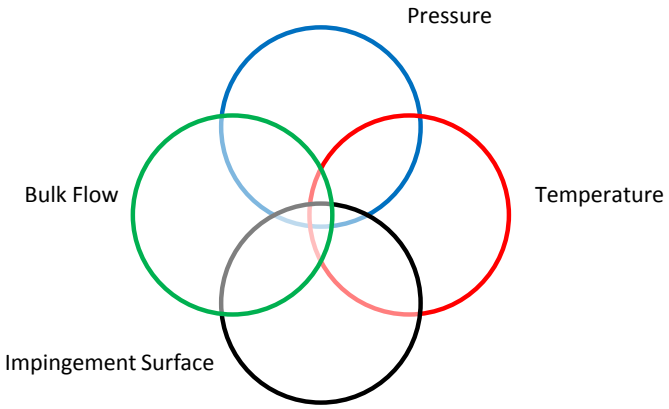

Figure 41, CVC Control Process Venn

Having independent control of each process offers wider control than would otherwise be restricted in a more thermodynamically changing process such as the induction and compression phase within the otto-cycle. The drawback is that it is not a fully representative environment but does allow decoupling of parameters for fundamental studies such as this work. Traditionally, most novel processes are evaluated within a CVC before engine tests, however, engine tests can ensue. CVC experiments, due to their inherent fundamentalism, are useful when validating computational (i.e. CFD) databases.

Two main variants of CVC exist, those suitable for combustion and those suitable to visualisation of non-combusting flows. The latter is employed for this work and will be discussed in the following section. The combustion CVC, colloquially known as a 'bomb' is significantly more complex in design and operation particularly for self-ignition units (à la compression ignition: Diesel and HCCI) due to the pressures and temperatures required. These units are designed to withstand high ambient (100 bar, 700+ K) and post combustion conditions (200 bar, 1500+ K) and hence require large support services and design requirements. For these reasons these are the less common of the two CVC types.

3.3.1 Constant Volume Chamber Design and Operation

The CVC employed for this work was constructed and modified from an existing OEM design which expedited the product delivery to fit within the framework of this research. Minor adaptations were made to suit the requirements of the current users. The design is intended to withstand an operational pressure and temperature of 25 bar abs and 573 K, respectively. These conditions allow for representation of a non-combusting fuel to be delivered into an SI engine-like environment; high-load, late injection conditions. Previous studies by the author have shown that a high degree of representativeness to engine conditions can be achieved (Marti-Aldaravi et al., 2012).

The CVC constructed consists of an internal volume of 7.023 L, with the injector orientated either on the top or side of the chamber for imaging in longitudinal and lateral planes, respectively. Services; air supply, air return, temperature measurement and safety venting were all configured from the bottom of the chamber to allow easy service access to the fuel injector. The air distribution ring was positioned above the injection plane and permitted a more complete purging of the internal volume. Purging is typically required once the ambient medium is no longer representative of the initial conditions. This configuration came at a cost as some of the image plane in the lateral direction was obscured. This was, however, no concern as the radial penetration never encroached on the outer lateral limits.

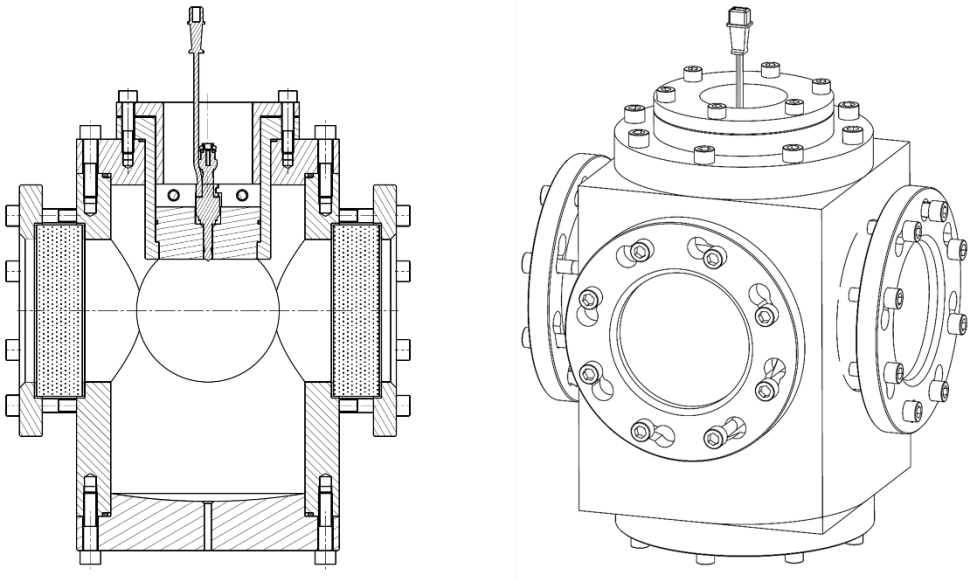

Figure 42, Constant Volume Chamber: cross-section (left) and isometric view (right)

A low flow rate can, when appropriate, be introduced through the chamber through the distribution ring as discussed above with the flow monitored manually through a rotameter. It was found experimentally and from previous work i.e. (Marti-Aldaravi et al., 2012)) that a flow of 30 LPM

or less was sufficient to not show any discernible flow pattern when imaged with a highly-sensitive schlieren imaging system. At ~40 LPM and above; strong gradients existed in the schlieren images indicating density inhomogeneity and hence a flow field present. These higher flow rates are still largely inconsequential to the gas jet studied and will in effect appear '*frozen*' in comparison due to the significant velocity magnitude differences between the injected and environment media. Typically, the ambient flowrate was held between 5 and 15 LPM for all experiments. The pressure and flowrate were controlled via inlet and outlet throttling valves and an upstream pressure regulator.

Great care was taken with the design to avoid any materials which could contaminate the CVC and generate spurious fluorescence signals[6] when the CVC is used for PLIF in future. Materials were generally limited to stainless steel, forged alloy-steel, graphite, aramid fibre (Novus 30 Supra), virgin PTFE (Teflon) and virgin Viton. Whilst the vessel does little in terms of reducing specular reflections, coating options were considered but were prohibitively expensive and there was uncertainty if they would withstand the corrosive tracers; toluene, benzene, triethylamine (TEA) or acetone.

The windows of the CVC were selected as fused-silica (Corning Code 7940) of 150 mm diameter by 40 mm thick, where the resultant viewing diameter was 124 mm after installation to body with flanges. The windows were free of any optical impurities and were selected for their performance in both laser diagnostics (transmittance including in the UV for PLIF) and schlieren/shadowgraphy imaging. With a relatively strong refractive index and thickness great care was taken to ensure windows were aligned in-plane and orthogonally to the imaging planes.

The CVC was filled with high purity (>98%) nitrogen for several reasons. Firstly for the case where laser illumination was used, the energy per/pulse supplied was above the threshold for the autoignition limits of fuels considered and hence the nitrogen environment would suppress any undesirable combustion. Secondly, nitrogen gas provides the most representative environment to air (assuming no combustion residuals for the charge) where the fluidic properties closely matched. Specifically the molecular weight, specific gravity, ratio of specific heats (γ), dynamic viscosity and thermal conductivity all fell within a 5% variance. Comparatively carbon dioxide has properties which are up to 50% different from air. For a constant temperature, a 3.14% variance in pressure exists between the nitrogen filled CVC and an air-filled engine cylinder. This density discrepancy is a result of the oxygen's influence on the gas constant for air.

[6] Laser induced fluorescence (LIF) was originally intended as the primary evaluation method. Considerations made for LIF are not necessarily transferable to the particle image velocimetry nor Schlieren methods used in this work.

3.3.2 Injector Mounting

A single fuel injector is mounted into an adapter and housing where it is either situated on the top or in replacement of any of the four CVC windows. This permits imaging in two planes without altering the optical and imaging apparatus. In all conditions presented the injector was mounted on the top of the vessel. For Figure 43 below, one can clearly see how the injector is mounted in housing. Orientation of the injector is dictated by the operator and is set by several means where components 1, 3 and 5 rotate freely allowing 360° positioning. This is particularly useful for non-symmetrical nozzles such as multi-hole injectors.

This arrangement was configured to allow any injection apparatus up to the envelope diameter of 78.0 mm set by the retaining flange ID. This proved to be more adequate than most designs yet in some cases the injector electrical-pin mount was needed to be trimmed back if it was without a pig-tail from the OEM.

One final consideration was that the injector tip needed to penetrate a minimum of 2.0 mm to ensure that the imaging plane is not interrupted by any other protrusion. The injector tip is shown in Figure 43 to protrude past both the injector adapter and retention housing.

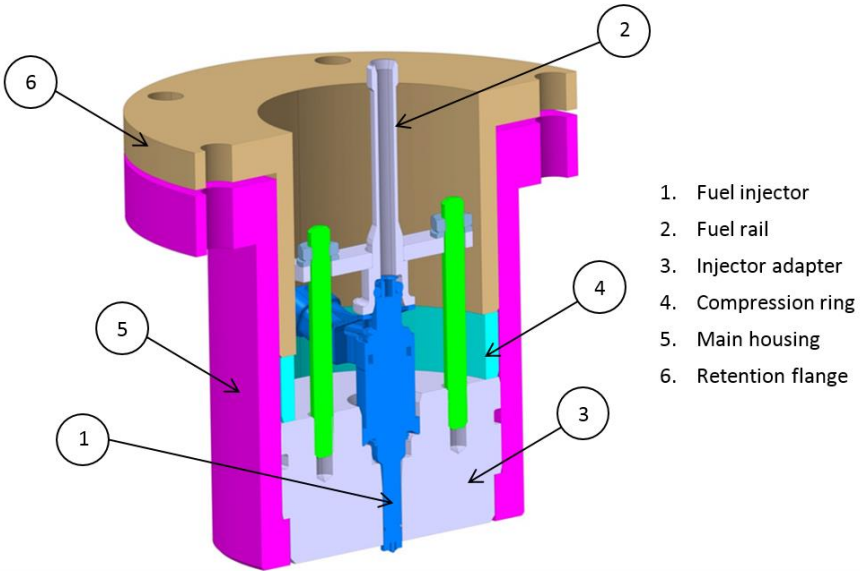

Figure 43, Fuel Injector mounting arrangement in the CVC.

3.4 Low Pressure Ratio Experimental Configuration

Three alternative automotive fuels were evaluated and compared against one another. Mains supply CNG (*town-gas*) was selected as the primary investigation fuel with discussions surrounding this fuel outlined in Chapter 3. Hydrogen and the blend gas are discussed as follows.

Hydrogen was selected for a variety of reasons including; the absence of any carbon-compound emissions when combusted, inverse Joule-Thompson effect and a low density. Moreover, its integration with natural gas as a standalone transport fuel is increasingly popularised at a research and industry level. Hydrogen has long been touted as the fuel for the 21st century and albeit with advancements in the R&D sector over the last 30 years, hydrogen ICE vehicles have failed to penetrate the market. Hydrogen is still a viable energy source for conventional passenger-vehicle powertrain but much of the focus in the Asia-pacific region is on pathway applications. An excellent review of the hydrogen fuelled ICE is given by (Verhelst and Wallner, 2009).

Combustion of gaseous hydrogen is not emissions free as it is often speculated by proponents but it does, however, provide an opportunity to reduce carbon based emissions: total hydrocarbons (THC), carbon dioxide (CO_2) and carbon monoxide (CO) alongside particulate matter (PM). NOx emissions are, however, a concern particularly within the operational band of $\lambda = 1.0$ to $2.2{\sim}2.5$ where after significant reductions occur (Berckmüller et al., 2003). Berckmüller et al. also show that nearing the lean limit ($\lambda \approx 4.8$) achieves very low NOx emissions (<5 ppm). At stoichiometric conditions it is possible to reduce NOx emissions with a conventional catalyst at a typical conversion rate; $>99\%$ (Rottengruber et al., 2004).

A blend gas composed of 25% hydrogen bathed in pure methane (mol/mol basis) is also employed. Hydrogen addition to CNG has proven to be a relatively simple method of reducing carbon based emissions proportional to its constitution. The industry has converged on a hydrogen addition value between 20-30% (volume) with commercial options available in the US and Korea (National Petroleum Council, 2012). This concentration level also reflects good environmental value at a net energy perspective (Villante and Genovese, 2012). The concentration ratio (0-100%) of H_2CNG has been widely studied with a positive response for 20-30% additions to CNG (Akansu et al., 2004). It has also been shown that additions of 10% hydrogen to high CO_2-concentration natural gas (land-fill gas) has substantial advantages (Porpatham et al., 2007).

This work considers supersonic jets of low to high delivery pressure ratios with a particular focus on the latter. Whilst the pressure ratios are quite high they are still representative of delivery conditions for an engine under various load points. PFI injection systems do not need substantially high pressures ($PR < 12$, typically $PR \approx 4$) due a large delivery time permissible and the ambient

pressure (intake manifold) is typically, $Pa < 1.5$. This work exclusively contains jets which have a higher pressure ratio than unity and thus are considered to be underexpanded.

The three key flow determinants are presented in Table 8, with the range for the experiments undertaken as shown. Refer to Appendix II for the full experimental schedule. The temperature conditions are assumed to be constant at ~293K for both the upstream and ambient stagnation conditions.

Table 8, Flow conditions for low PR PFI jet delivery.

	PR	*NPR*	*Density Ratio*
	P_o/P_a	P_e/P_a	ρ_o/ρ_a
CNG	2.8 - 12.0	1.53 - 6.57	1.60 - 6.85
Hydrogen	4.3 - 12.0	2.28 - 6.37	0.31 - 0.86
25% H_2/CH_4	2.8 - 12.0	1.52 - 6.49	0.58 - 2.50

A commercial port fuel injector (Keihin KN8 100cc) was employed which was driven by an in-house solenoid driver coupled to a BNC 575 signal generator for actuation and camera synchronisation. The injector is an inwardly opening unit which incorporates a small pre-chamber before the actual orifice-exit as shown in Figure 44. The nozzle exit has a diameter of $3.65\,mm$ with a length of $\sim 2.55\,mm$ (straight) and $4.83\,mm$ total. The orifice-exit edge has a very slight chamfer also. It should be noted that up to $x/d = 0.5$ was unable to be imaged due to the injector mounting arrangement, this offset (true nozzle exit location) was, however, accounted for in all processing.

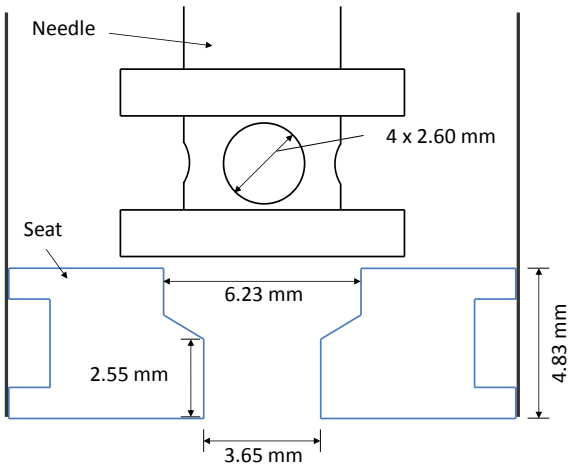

Figure 44, Port fuel injector internal and nozzle geometry.

The needle lift was measured in ambient conditions with no fuel pressure using a HSV technique. This is a somewhat arbitrary measurement but regardless, yields an indication of the lift profile even if measured in non-operationally realistic conditions. The needle lift profile gives an indication of the

transient nature of gaseous PFI conditions which drive the jet delivery process. It can be seen that a substantial needle rise-time exists, before steady operation.

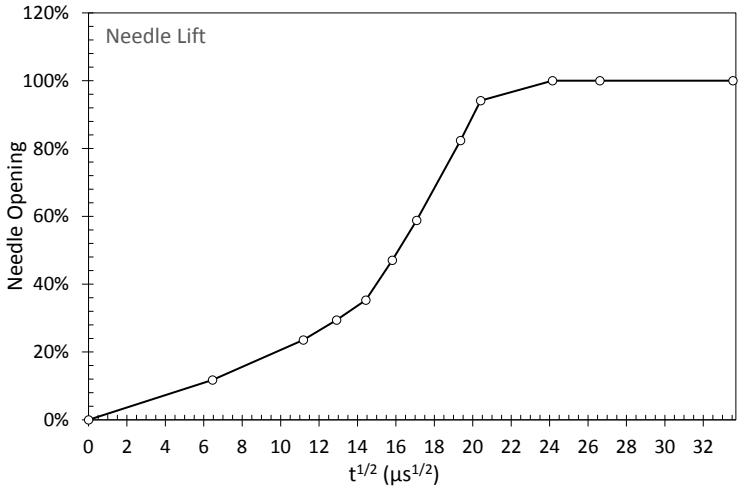

Figure 45, PFI needle lift displacement profile in the transient-rising to steady-state region.

It should be noted that no dampening reservoir (i.e. accumulator) was employed in the fuel feed line, which was consciously decided to achieve realistic in-vehicle conditions. Sufficient time was allowed between each injection repetition to ensure no reflected pressure pulses were residing from the previous event.

A constant injection signal duration of 5.7 ms was used which represents the conditions of a PFI CNG engine operating at 2000 rpm/2.0 bar BMEP. Combustion and emission performance under these conditions can be found in (Soanes and Koopmans, 2012). This duration corresponds to a total injection mass of 14.29 and 5.39 mg for 4.3 bar (abs) injection of CNG and Hydrogen, respectively.

Determination of the fuel quantity per injection duration event was performed using a mass balance. The mass flowrate delivered was evaluated by means of a Coriolis meter (Siemens Sitrans FC-300 DN4) with measurements taken every 100 injection events for a total of 1000 events per series. The series was otherwise repeated until a coefficient of variation of less than 5% was reached. The precision of the 100 shot-to-shot repeatability for CNG testing was quite high with an average (across total range) standard deviation found to be $\sigma = 0.221$ mg.

The relationship between mass and the selected signal duration time window (5-10 milliseconds) is linear hence allowing the use of linear -regression or -interpolation to determine the inter-time injection mass Figure 46 below depicts the mass flow rate of each of the fuels. It can be clearly seen that the effects of fundamental fuel properties, i.e. density and viscosity, heavily influence the mass delivered for a nominal duration, particularly at the higher injection durations.

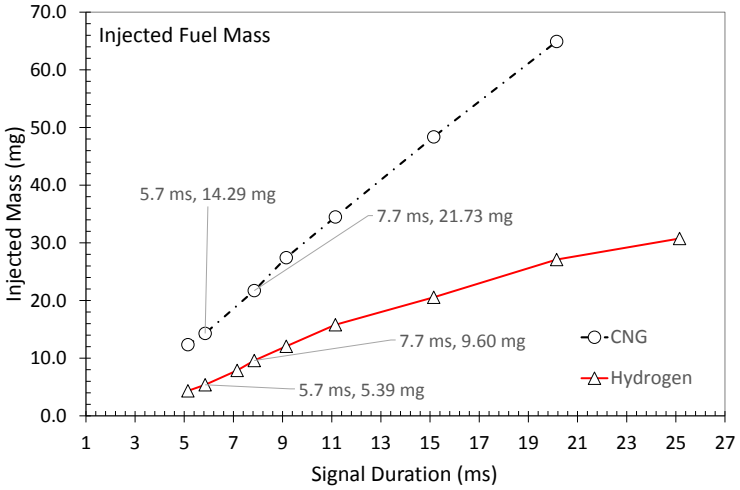

Figure 46, Fuel mass for CNG and H2 issued from a PFI injector for a supply pressure of 3.3 bar.

Interestingly, hydrogen testing proved to yield a lower shot-to-shot average standard deviation ($\sigma = 0.186$ mg) yet the linearity of the mass was lower than that of CNG where R^2 values were 97.84% and 99.89%, respectively.

Schlieren high speed photography was employed as the principal investigation tool with the generic configuration and arrangement detailed fully in 3.6.3 Experimental Set-Up. The particulars of this investigation are as follows.

The camera utilised in this work was a Vision Research Phantom v1610 coupled with a Schnieder-Kreuznach 210 mm or Symmar 480 mm lens for the freestream and impinging tests, respectively. This combination resulted in an imaging capacity of 0.2105 mm/pixel (640 x 640) at 30,000 fps (33.33 µs between frames) for the freestream conditions. As for the impinging scenarios, imaging capacity was performed at a higher resolution of 0.1027 mm/pixel (896 x 384) at 40,000 fps (25.00 µs between frames). This provided sufficient resolution to resolve the dynamic properties in adequate fidelity for the nozzle size. The exposure settings varyed between 10 and 30 µs depending on the light source luminosity, neutral density filter and fuel injected.

Two flow scenarios have been considered experimentally; freestream and impinging. The freestream conditions allow an uninhibited natural distribution of the gas. The impinging scenario, however, provides a comparative measure to freestream flow with respect to distribution, structure and mixing in a quasi- engine realistic configuration.

3.5 High Pressure Ratio Experimental Configuration

The range of flow conditions tested for the high pressure ratio experiments are summarised in Table 9 (refer to Appendix III for the full experimental outline). These conditions were selected to provide a wide range of conditions relevant to pressure ratios experienced within current and future engines. The energy and hence mass per fuel were held constant and thus injection duration shortened for an increasing upstream pressure. The use of sub-ambient environmental pressures allowed PR values exceeding the supply pressure ceiling value (100 bar). All experiments involved CNG issued from a $1.00\ mm\ \emptyset$ nozzle as discussed subsequently.

Table 9, High pressure ratio schlieren HSV testing range.

Upstream Pressure	*Downstream Pressure*	*Density Ratio*	*Condition*	*Number of Tests*
Po (Bar)	*Pa (Bar)*	*Po/Pa*		*#*
20 - 100	0.25 - 2.40	8.33 - 400.00	Freestream	14
20 - 100	0.25 - 2.45	4.56 - 219.07	Impinging	21

The impinging conditions represent the physical boundary conditions experienced in an engine (previously outlined) in which a square 'piston' was employed to represent $50°\ bTDC$ ($\sim 33.40\ mm$ injector orifice-to-surface). A square open-ended piston was required for optical access and whilst not fully geometrically realistic, it provided adequate insight into the effects of surface and wall impingement. The piston crown was aligned in a horizontal plane going through the camera axis. The camera base was also mounted horizontally.

The camera utilised in this work was a Vision Research Phantom v1610 coupled to either a Sinar Sinaron S 300mm or a Rodenstock Apo-Ronar 800 mm lens for the freestream and nearfield tests, respectively. This combination resulted in an imaging capacity of 0.157 mm/pixel (384 x 640) at 46,000 fps (*21.74 μs* between frames) for the freestream conditions. For the nearfield scenarios, imaging capacity was performed at a higher resolution of 0.087 mm/pixel (256 x 400) at 80,000 fps (*12.50 μs* between frames). This provided sufficient resolution to resolve the dynamic properties in adequate scale for the jet nozzle diameter.

3.5.1 Direct Injection Injector Tip Adaptation

To satisfy the main investigation of this thesis an appropriate high-pressure gaseous fuel injector was needed. No commercial gaseous direct-injection fuel injector was available for use. Instead an adaptation to a previous solenoid multi-hole gasoline unit was devised by means of a new tip which is illustrated in Figure 48. Although not a new concept (Baert et al., 2010, Bovo and Rojo, 2013) some detail was specific to this project. The high level design requirements were as stated below:

- Single orifice hole
- High pressure
- Largest possible orifice size
- Fast actuating
- Precise opening and closing control
- Cost effective

The adaptation of a new tip also required the donor gasoline multi-hole injector to have a ball-end needle as the sealing mechanism. This is in opposition to a conical needle where sealing is achieved on tapering surface. The ball seal allows an easier design and manufacturing processes and was seen to provide a significant reduction in tooling cost. For the injector selected (Bosch #261 500 056) the 3 mm diameter ball provided a sufficient working boundary for sealing. An image of the exposed needle is depicted in Figure 47 below.

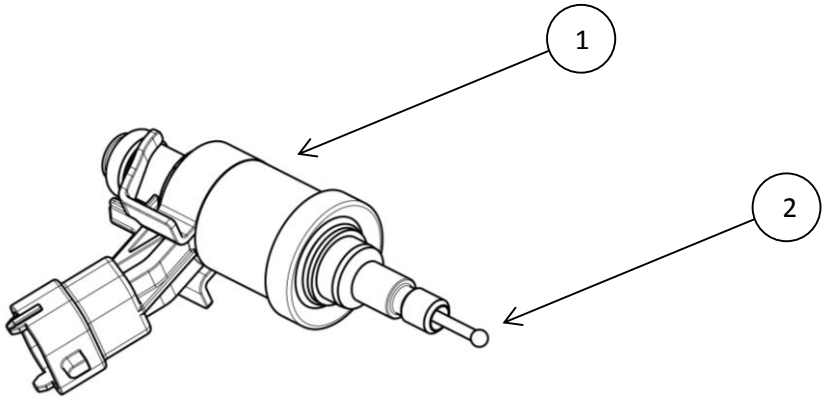

Figure 47, Exposed ball-needle on multi-hole injector. 1. Body and 2. Original tip removed exposing ball-end needle.

The tip design evolved according the base geometry of the donor injector which resulted in a maximum single orifice size of 2 mm diameter. A single round orifice provides a straightforward arrangement needed for fundamental studies. Two sealing options were trialled; one which allows a large surface contact along the cord of the ball and another which effectively had a point location. The latter was anticipated to deliver a higher mass flow due to a larger curtain area when the needle lifted but at a cost of sealing integrity. In practice this larger flow rate item proved to seal adequately and was used exclusively.

For semi-commercial DI gaseous injectors, a range of orifice sizes (single and multi-hole) have existed ranging from 0.38 mm to 0.80 mm and for previous research studies using in-house (non-commercial) nozzles a range of nozzle diameters also exist 0.52 mm to 1.4 mm. A full list of relevant nozzle geometries are shown in Table 10. The length-to-diameter ratio (l/d) is also shown where available. The nozzle used in the DI study is a 1.00 mm diameter orifice with a barrel length of 2.00 mm

Table 10, Summary of gaseous DI injector nozzles previously tested.

	Nozzle Diameter (mm)	*Nominal Area (mm^2)*	*l/d*	*Arrangement*
Current Work	1.00	0.785	2.00	non-commercial
Petersen, 2006	0.38 to 0.80	1.500	-	semi-commercial
Bruneaux et al., 2011	0.20 to 0.50	0.031 to 0.196	-	semi-commercial
Ouellette, 1996	0.50	1.178	-	semi-commercial
Johansen et al., 2013	1.00	0.785	6.00	non-commercial
Yu et al., 2012	1.40	1.539	-	non-commercial
Baert et al., 2010	0.212 and 1.300	0.212 to 1.327	1.54 to 7.69	non-commercial

It can be seen that the nozzle design used offers a realistic orifice effective-area whilst also employing a short and thus also realistic barrel length. A short barrel length, the distance between nozzle exit and sealing line, is crucial for accurate fuel metering and potential reduction of THC emissions. The needle lift is within typical OEM operation, where the most of the others in the literature are not reported. The complete configuration is a production-realistic design which allows fundamental characterisation of the fuel delivery.

The basic configuration of the modified gasoline injector is shown below in Figure 48. It was decided that brass (grade 385) was the most suitable metal due to the ductility of the material where it was intended that some deformation at the ball-to-tip interface (6) would ensure an appropriately mated interface for the high pressure sealing requirement. After several thousand cycles the internal lip would roll over ($\sim 200\ \mu m$) with obvious consequences on the flow behavior. In light of this, high copper content bronze (LG2) was selected where no lipping has occurred to date. The amount of sealing deformation could be governed by the thread-in distance when the new tip was wound on the injector body (5). Care had to be taken to not impart too much back-pressure on the spring-loaded needle as to induce bending along its shaft. Sealing of the needle to tip is crucial as any leakage would be detrimental to performing realistic, accurate and repeatable results, particularly the transient cases tested.

Due to the adjustability needed in the tip's position from the needle a parallel thread was employed which imposed concerns for gas leakage. In the design this was countered with the application of an o-ring (Viton N70 or PTFE) either side of the thread. This arrangement would effectively contain any escaped gas between the injector (1), tip (4) and adapter (2). This was confirmed through high sensitivity schlieren imaging of the configuring.

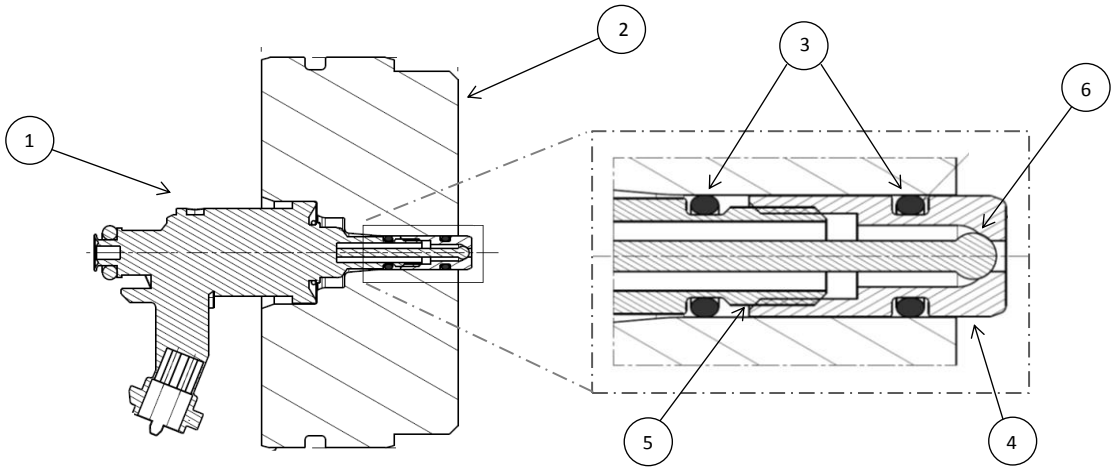

Figure 48, Modified gasoline fuel injector assembly and enlarged view of adapted tip where: 1. Fuel injector, 2. Injector adapter, 3. O-ring, 4. New tip, 5. Thread location and 6. Sealing surface.

The final assembly was constructed where the nozzle tip was threaded onto the injector shaft until physical hand rotation ceased. The injector was then actuated 100 times to ensure correct seating. The tip was tested again for hand rotation. The assembly of the unit is shown below in Figure 49 below. To test for sealing, a small volume (~0.5 mL) of leak detecting fluid was dabbed onto the orifice whilst under high-pressure static conditions, additionally schlieren imaging provided confirmation.

Figure 49, Modified gasoline fuel injector (left), alongside a new 2.0 mm ID brass nozzle with seals (middle) and visible sealing needle-ball.

Care was also taken to ensure that the chamfer at the orifice external edge was minimal/non-existent. The finish is intended to have as little effect as possible on the flow phenomena, as the orifice edge geometry determines the angle and propagation of the

Prandtl-Meyer expansion fans. Each nozzle was inspected under a microscope to ensure no large non-uniformities around the orifice edge or along the barrel surface. Each nozzle was imaged prior to use using a Leica optical light microscope (model: DM ILM) with micron scale resolution, where a subjective analysis was performed on nozzle quality and consistency. Sample microscope images of a rejected 2mm diameter orifice nozzle is presented below in Figure 50. This unit showed considerable surface quality variation along the outer orifice edge (rim).

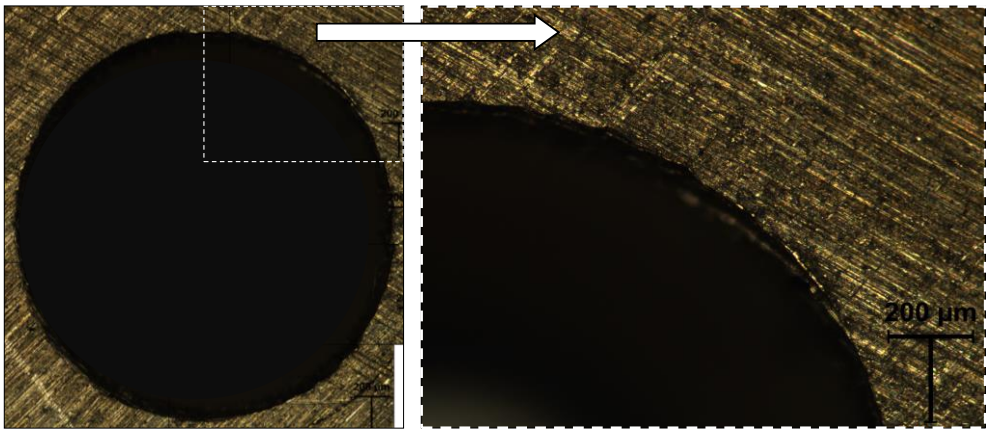

Figure 50, 2mm diameter nozzle imaged for edge quality, reconstructed (left) and individual (right).

The edge and surface finish is not expected to align with modern injection manufacturing standards however great care was taken as to reproduce a nozzle to a standard aligned with scientific inquiry. The precision on the inner orifice edge and the barrel, both depth accuracy and surface finish where of significantly high standard. Dimensional accuracy of the 1mm and 2 mm diameter orifices were, ±0.010 mm and +0.000/−0.002 mm respectively. No striations were visible along the surface of the orifice barrel.

The final injector selection is a 1.00 mm diameter orifice with a barrel length of 2.00 mm. The internal geometry used is based on Nozzle Design II, where the sealing geometry allows for maximum flow around the needle-ball. Further detail of the nozzle geometry and configuration are given in Appendix IV.

3.5.1 Flow Rate and Needle Operation

The needle lift was measured optically using a high speed camera. No fuel was delivered at the time of measurement, thus any dynamic or pre-load effects on the needle were not incorporated. This omission will have influence on the measurement but is anticipated to be minor due to the high driving force exerted when injecting higher pressure/viscosity liquid fuel; as the injector does in normal operation. Figure 51 shows the configuration of the measurement. The high speed camera (i.) measured the needle shaft displacement via optical access through the injector wall (ii.).

Illumination was provided by two Dedocool 250 Watt lamps (iii.) with a neutral density-filter steering some of the light directly onto the needle shaft (iv.). The neutral density filter provided light directly in plane to the camera.

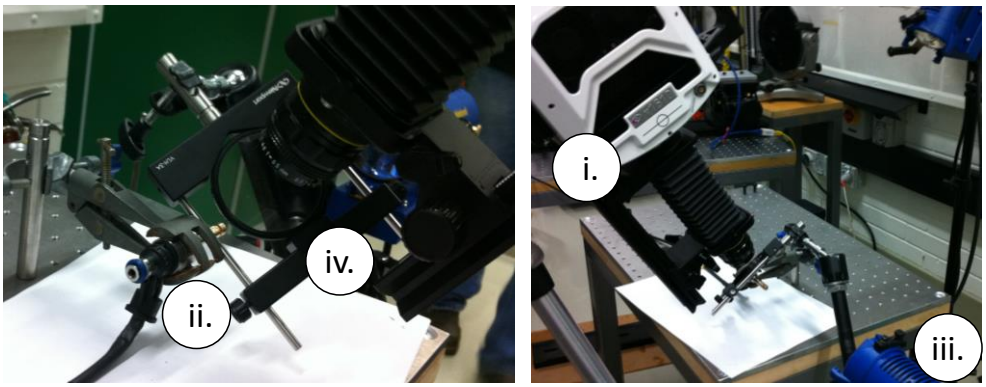

Figure 51, Imaging set-up of the injector needle lift.

The results of the test are presented in Figure 52. Coincidently the needle lift profile is consistent with the observed flow histories described in the results section. The steady-state, fully open (100%) needle lift (µm) is consistent with data obtained from the manufacturer. The use of square root-time as the base function is employed here (and throughout the thesis) provides a means for easier integration when mathematically modelling – derived from the velocity-time relationship discussed in Chapter 2.

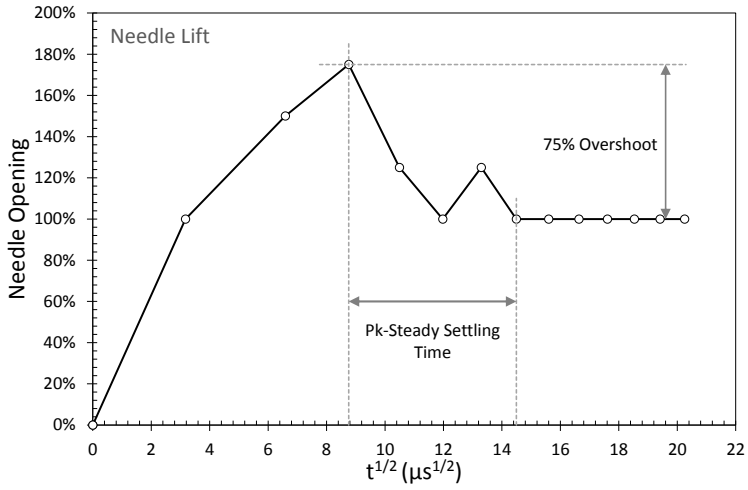

Figure 52, DI needle lift displacement profile in the transient-rising to steady-state region.

In addition to the vertical needle displacement there was significant rotation ($\pm \sim 15°$) up to $t \cong 15.0\ \mu s^{1/2}$. This is not an uncommon occurrence given the driving force exerted on the needle and any non-uniformity in the retention seating pressure on closure.

The injection mass quantity for the direct injection unit was determined through the accompanying pressure rise in the sealed CVC. This method was necessary as the short delivery time proved to incur a high uncertainty when more conventional methods were attempted (i.e. Coriolis meter as per the low pressure ratio – PFI experiments). The addition of high pressure fuel to the ambient closed volume environment raises the overall pressure in accordance with standard gas laws with an isothermal assumption. This method has been applied in similar circumstances i.e. (Baert et al., 2010, Johansen et al., 2013, Petersen, 2006). The mass per injection was calculated through the following relation:

Equation 41, Mass per injection.

$$mass\ of\ cng\ per\ injection\ event\ = \frac{n_{moles} M_{CNG}}{n_{injections}}$$

where M_{CNG} is calculated through the previously outlined fuel composition. The number of injected fuel moles , n_{moles} , is derived through the ideal gas law utilising the fixed volume and negligible temperature change:

Equation 42, Moles of CNG injected using adiabatic ideal gas law.

$$n_{moles} = \frac{dP\ V_{CVC}}{RT_{CVC}}$$

Several hundred tests were conducted (at various injection signal durations) with samples only considered where a coefficient of variation existed below 5%. This approach was also used in (Marti-Aldaravi et al., 2012). Figure 53 presents a section of the injected mass obtained. Using linear regression, line fits were applied and injection durations obtain for a constant mass of 12.05 mg (602.7 Joules). For each injection pressure tested (40, 60, 80 and 100 bar) the injection mass corresponds uniquely to the respective duration which can range between 2.32 to 6.21 ms (values are highlighted on Figure 53).

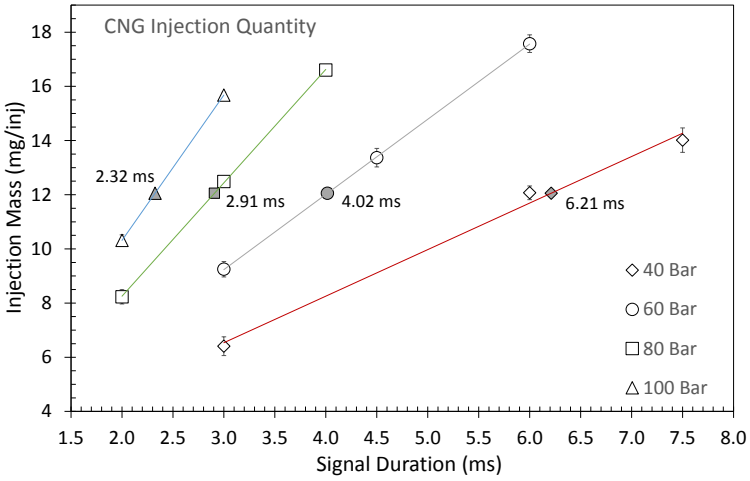

Figure 53, DI CNG injection quantity with values denoted at constant energy (602 J). 1mm orifice, Nozzle Design II.

As a direct measurement of the instantaneous flowrate was unavailable, an estimated rate of injected mass is proposed as illustrated in Figure 54. The calculated massflow rate is derived from a hybrid model employing the transient needle lift (Figure 52) and steady-state isentropic flow defined by Equation 12. The transient needle lift was considered through a changing the effective orifice area (A) as the needle ball rises, and the total mass injected (Figure 53).

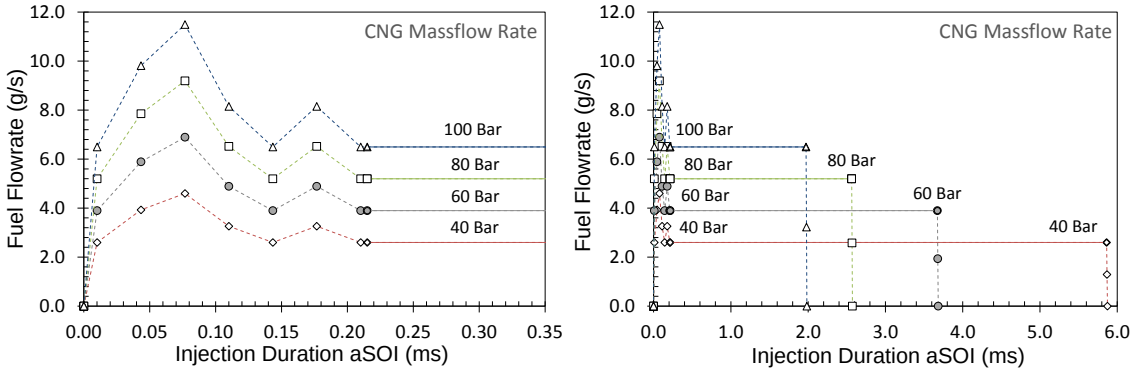

Figure 54, Isentropic DI CNG massflow rate, early (left) and whole (right).

For a discharge coefficient of one (C_d ideal) the discrepancy between measured and calculated injected mass ranges (fairly linearly) between 6% and 26%, for the 100bar to 40bar cases. This fits relatively well with the previous acknowledgement that the C_d is expected to be between 0.7 to 0.9.

3.6 Schlieren High-Speed Imaging

Schlieren and shadowgraphy are two largely similar methods of visualising a field of interest by means of highlighting and capturing light ray behaviour. Density changes in the visualisation media allow for imaging an otherwise 'invisible' flow. This *invisibility* may be due to the spatial, temporal and optical (transparency) variations of the flow under investigation, where high speed, highly resolved imaging is needed. Time scale and recognition of test object phenomena will most certainly be beyond the capacity of the human eye for quantitative (and qualitative) analysis. Most flow tests made for the present work will have flow structures that change within the time of an eyelid blinking. The *Devil* is most certainly in the detail*,* when it comes to visualising this flow behaviour.

3.6.1 Basic Optical Concepts

When parallel light rays transverse through non-homogeneous media they experience: displacement, deflection and a phase shift (retardation or acceleration) (Kleine, 2010, Kleine et al., 2005). These phenomena allow us to investigate the subject medium; whether it is the homogeneity of spectacle glass, characteristics of compressible shock waves or the two-phase flow occurring when injecting liquid fuel in an engine cylinder. The main principal is of a light ray shifting as it comes into contact with a medium (*background*) of different refractive index within the optical path (Pastor et al., 2007). The three phenomena, displacement, deflection and phase differences allow the use and distinction between three main optical methods; shadowgraphy, Schlieren and interferometry.

Refraction is the change in light ray direction when passing through a non-homogeneous medium or through varied media. This principal is based on Snell's law and is depicted in Figure 55, below. When a light ray enters an optically denser medium ($n_1 < n_2$) the ray will refract towards the normal plane and thus the angle of refraction; $\varepsilon = \varepsilon 2 < \varepsilon 1$ (Tavoularis, 2005).

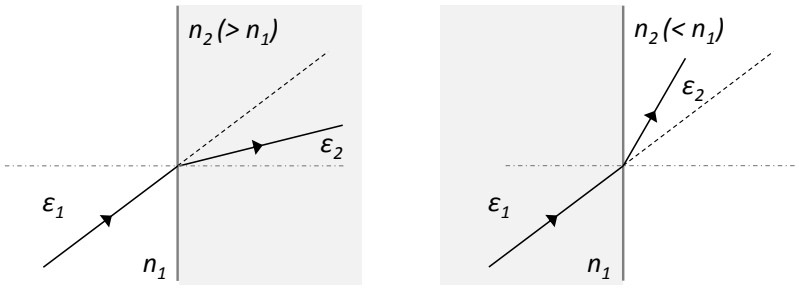

Figure 55, Refraction of light ray in two mediums. Adapted from (Tavoularis, 2005).

Snell's Law models the refraction of light as it passes through the interface of two media with different refractive indices n_1 and n_2.

Equation 43, Snell's Law. Source: (Tavoularis, 2005).

$$\frac{\sin \varepsilon_1}{\sin \varepsilon_2} = \frac{n_2}{n_1}$$

The refractive index, n, of a medium is defined as the ratio between the speed of light in a vacuum, C_o and the speed of light through the medium under observation, C.

Equation 44, Refractive index of a medium. Source: (Kleine, 2010).

$$n = \frac{C_o}{C}$$

For some gases including air a linear relationship exists between the refractive index and the density ρ, where k is the Gladstone-Dale coefficient (Settles, 2001). The Clausius-Mosotti relationship (Equation 45) can be employed, and simplified using the Gladstone-Dale coefficient, producing Equation 46. This assumes that the refractivity of the gas is $n \approx 1$.

Equation 45, Lorentz-Lorenz relationship. Source: (Panigrahi and Muralidhar, 2012).

$$\frac{n^2 - 1}{\rho(n^2 + 2)} = k$$

Equation 46, Gladstone-Dale index of refraction for gases. Source: (Panigrahi and Muralidhar, 2012).

$$\frac{n - 1}{\rho} = k$$

The refractivity of a medium depends on the composition of the gas; the temperature, pressure and thus density, and of the wavelength of the light source. It is frequently seen that for n of a given medium a multitude of corresponding illumination wavelengths are cited i.e. (Rollefson and Havens, 1940).

The ideal-gas law can also be incorporated into the determination of n, when pressure, temperature and density are not far from atmospheric, with R as the specific gas constant:

Equation 47, Ideal gas law. Source: (Settles, 2001).

$$\frac{p}{\rho} = RT$$

The determination of refractivity, n, is highly dependent on the density of the gas and unless experimentally measured for each test condition some approximation is needed. Equation 60 shows that the refractivity is indeed determined by the gradient change $\partial n/\partial y$ of the media, for a particular direction. It should be noted that the angle of refraction, ε, is typically given in

arcseconds[7]. The small angle approximation rule is typically employed where the change in ε is equal to dy/dz and dx/dz, resulting in Equation 48.

Equation 48, Refractive Curvature. Source: (Settles, 2001).

$$\frac{\partial^2 x}{\partial z^2} = \frac{1}{n}\frac{\partial n}{\partial x} \quad , \quad \frac{\partial^2 y}{\partial z^2} = \frac{1}{n}\frac{\partial n}{\partial y}$$

From Equation 48, integrating once yields the x and y coordinate deflections.

Equation 49, Third component refraction. Source: (Settles, 2001).

$$\varepsilon_x = \frac{1}{n}\int \frac{\partial n}{\partial x}\,\partial z \quad , \quad \varepsilon_y = \frac{1}{n}\int \frac{\partial n}{\partial y}\,\partial z$$

Whilst for two dimensional schlieren along the optical axis, L, where n_o is the background medium, Equation 49 transforms into:

Equation 50, Two-dimensional refraction. Source: (Settles, 2001).

$$\varepsilon_x = \frac{L}{n_o}\frac{\partial n}{\partial x} \quad , \quad \varepsilon_y = \frac{L}{n_o}\frac{\partial n}{\partial y}$$

The Cartesian-coordinates are thus represented within Figure 56 alongside a simple lens-type schlieren configuration.

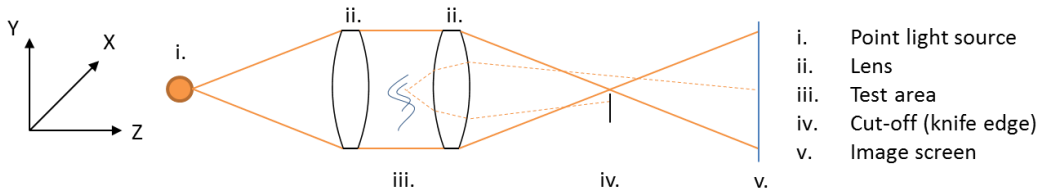

Figure 56, Coordinates and ray-tracing corresponding to a simple schlieren system. Adapted from: (Settles, 2001).

3.6.2 Visualisation Techniques

Although shadowgraphy has not been employed with the current work it is essential to briefly define the principals as schlieren is essentially an extension of the shadowgram. The defining

[7] One arc degree equals 3600 arcseconds with 1 radian equalling 206264.8 arcseconds.

mechanisms and specific techniques used for the qualitative high-speed schlieren are outlined in this section.

3.6.3.1 Shadowgraphy

Although both schlieren and shadowgraphy are line of sight imagining techniques which use changing refractive gradients to visualise density gradients in media, there is a clear distinction between the two. Both have interesting characteristics individually and if combined they will provide a more complete picture of the media, with minimal cost, setup and apparatus change. This is the most attractive prospect for the current work.

Shadowgraphy is a non-focused image where no cut-off is employed; this form simply produces a shadow on a background. Shadowgraphy requires only a few basic elements; a light source, imaging media and a reflective background. Shadowgraphy can be particularly valuable when visualising shock waves or turbulence as the sensitivity of a shadowgraph can be greater than schlieren techniques (Settles, 2001).

Variations in light intensity are produced when the light rays transverse across the non-homogeneous subject, which refract and displace from their initial position producing varying illumination intensities. This intensity variation; dark and light regions, produce the shadows which appear on the recording screen. The illumination intensity can be expressed by the following Equation 51, where Z is the distance along the optical plane using coordinate system shown in Figure 56:

Equation 51, Shadowgraph intensity profile. Adapted from (Kleine et al., 2005).

$$\frac{\Delta I}{I} \approx lk \int_o^L \left(\frac{\partial^2}{\partial x^2} + \frac{\partial^2}{\partial y^2} \right) (\rho) \; dz$$

The distance between the recording screen and the subject field, l greatly influences the intensity to the upper limit where image blurring sets in (Kleine et al., 2005). A 'focusing' lens can be employed to collimate the image according to the size of image required on the screen; this is preferably used in conjunction with a collimating lens prior to the subject field to ensure a uniform light ray, as depicted.

3.6.3.2 Schlieren

In comparison with shadowgraphy; schlieren requires the use of a greater defined light source, mirror(s) and/or lenses and a cut-off, for focusing. There are also more restrictive alignment requirements when setting up and focusing the image. Schlieren is generally more sensitive to

gradient changes and can provides quantitative data on the subject, hence its applicability to the current work. As discussed in Settles (2001) an imaged formed by shadowgraphy will display the light-ray displacement whilst contrastingly a schlieren image will display the deflection angle, previously denoted as ε and attributed to the introduction of the cut-off.

3.6.3 Experimental Set-Up

The experimental configuration of a '*folded Z-Type'* provided a layout yielding a reasonable amount of range to image within and fit within the constraints of the laboratory environment including other imaging/diagnostic apparatus. The folded Z-type, as shown in the schematic Figure 57 below, utilises an LED for continuous illumination at a plane-angle of ~7.50° which is replicated twice-over at the image-capturing end. This configuration proved complimentary to the laser-diagnostic arrangement whereby no apparatus needed to be reconfigured. A full component list and complete layout detail of the schlieren system used is available in Appendix V.

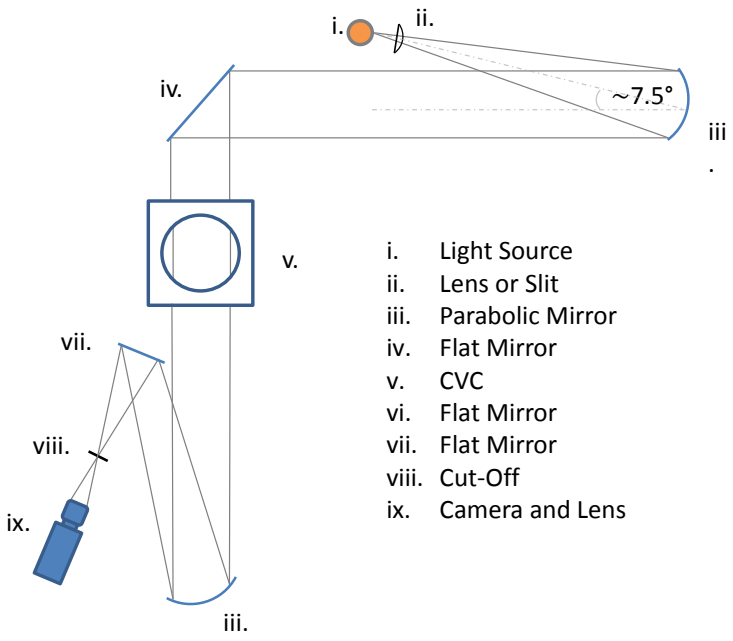

Figure 57, Folded Z-Type schlieren configuration.

It was proven advantageous to incorporate a slit at the light source to better shape illumination and in turn the image formation. Whilst controlling the image post-formation was handled by a rotatable knife-edge, for both horizontal and vertical 'cut-off' planes. A gradient filter also proved useful in lieu of a hard knife-edge for a gradual transition in image gradient. Typically both the knife edge and light-source slit were oriented vertically as this arrangement provided the easiest adjustability with the opto-mechanics employed.

The angle at which the light source was offset to the first parabolic mirror was selected primarily on packaging constrains but was minimised to reduce any comatic aberrations (Settles, 2001). The equal and opposite angle achieved at the second parabolic mirror will ideally cancel out any coma induced by the first parabolic steering. The other aberration to consider is astigmatism, which a rises when non-equal lengths are present between the optical centreline and mirror boundaries, even when small offset angles are employed and large focal-length mirrors are used some astigmatism will be present (Settles, 2001).

The total distance achieved between the two parabolic mirrors is greater than the twice their focal length, which was only made possible with the additional large 45° flat mirror; steering the parallel light laterally across the laboratory, and giving rise to the '*Folded-Z-Type'* name sake.

The light source selected was an affordable unit and provided only a modest output yet was sufficient in marking the transitional effects of the jets studied. The selection of a white continuously operating LED over the various laser generated visible wavelengths at hand (i.e. ~500nm and 532nm) was to reduce the diffraction effects induced with a coherent light source (Klein-Douwel et al., 2007).

3.6.4 Image Quality

Exposure durations, set solely by the camera in continuous lighting arrangements, were determined qualitatively by: 1) the velocity of the flow expected and 2) from examining the phenomena exhibited in an acquisition image. Typically, one sets the exposure to a low duration in the order of several micro-seconds for the supersonic flow considered. Judgement was made on the sharpness of each frame as to not produce 'smeared' or 'smudged' pixels in the interrogation ROI. This consideration was also made with respect to the quality of the background and whether the image was of appropriate post-processing quality.

The case of too short an exposure duration is shown on the left in Figure 58, where the shock and acoustic waves induced by the expansion of the jet are captured. The waves propagate from the nozzle and expand as spheres to the point of boundary reflection. The 'noise' associated from these wave are compounded on reflection where some waves were acoustically amplified. Because of background inhomogeneity the waves are seen to be unfavourable when considering the digital segmentation (image object identification (Gonzalez et al., 2004)) of the gas jet from the background. Consequently, when a greater exposure duration is chosen (as per Figure 58, right) the flow phenomena of interest, which are still moving slower than the exposure duration, will continue to appear whilst the faster events (shock/acoustic waves) will now appear as a smeared to spatial uniformity.

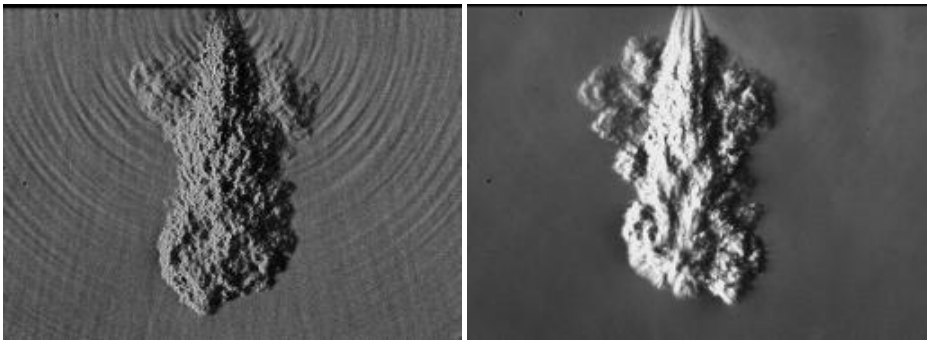

Figure 58, Schlieren exposure duration sensitivity; 3.7 µ s (left) and 29.8 µs(right).[8]

For experiments where the ease of accurate segmentation is deemed a priority the exposure duration is increased to a time where: the acoustic shockwaves are removed and the region of interest is sufficiently 'frozen' to contain the desired level of detail. For this example, a ~30µs exposure duration attained this requirement.

The schlieren sensitivity of imaging gaseous density gradients is of key importance in quantifying individual flow behaviour. Thus for appropriate schlieren imaging, the knife edge cut-off is a central factor in providing a high raw contrast level in order to distinguish the jet from the quiescent media. As no correlation between density (and hence mass) is required between the various fuels tested, the cut-off was altered between experimental set-ups. This variation in image contrast was required for a more comparative post-processing analysis. The cut-off level was varied based on the refractivity of the visualised media (fuel typically).

The variation in refractive index between CH_4 and H_2 relative to N_2 is small; $\pm 0.015\%$, respectively. This small change in refractivity is, however still apparent in a highly sensitive, appropriately tuned schlieren imaging system. The sensitivity of the image is adjusted through the cut-off (Figure 57 viii.) where, the set-point was typically between 40-60% transmittance. The variation in this range was needed to accommodate differing fluid density ratios over the conditions tested.

This is further illustrated in Figure 59 below where the effects of decreasing refractive index are practically shown. Interestingly an almost bathtub curve was apparent with the mid-range refractive fuel, $50\%H_2/CH_4$, consistently produced the lowest contrast results. This is, however, notwithstanding the fact that the pure Hydrogen sample were at lower contrast than the CNG (90+% CH_4). The figure segments below were all captured under identical conditions.

[8] The image was captured under identical physical and imaging conditions albeit from exposure duration. The difference in image presentation is solely due to image adjustments; Brightness, Gain, Gamma and sensitivity.

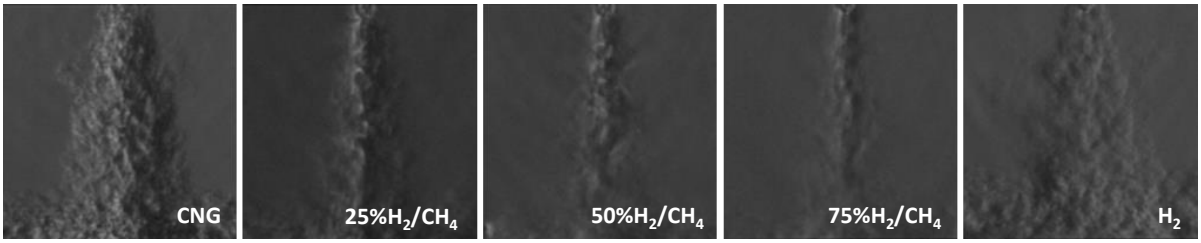

Figure 59, Effect of refractivity on schlieren image quality. Left to right: CNG, 25%H_2/CH_4, 50%H_2/CH_4, 75%H_2/CH_4 and H_2.

3.6.5 Schlieren Image Processing

For the high speed images captured using the method outlined in Section 3.6 an in-house processing technique using Matlab was applied. Matlab is commonly used for such an application, for example: (Petersen, 2006) and (Marti-Aldaravi et al., 2012), and is regularly employed due to its existing image processing database with a relatively intuitive work environment. At a simplistic level, the processing hierarchy is as follows in Figure 60.

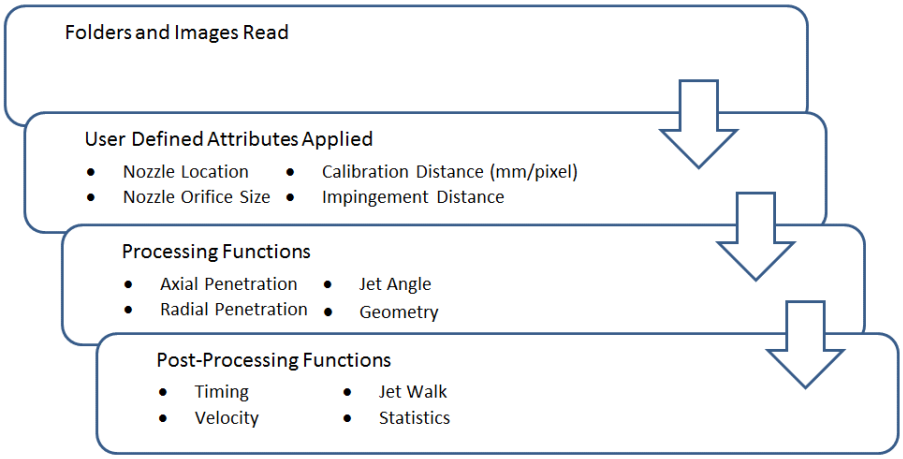

Figure 60, Schlieren HSV processing flowchart.

The most crucial of these steps is the 'Processing Functions' as this is where the image is segmented into two components; the foreground and background. The foreground is the actual jet whilst the background is the remainder of the image.

Before this can occur some definition of the active area is assigned. A background mask is crucial in defining where the region of active interrogation lies. As the processing of images works at a pixel level division, any slight mal-alignment of the optical or physical system i.e. plane not absolutely level, may result in flow which extends past the seemingly physical boundary. This is to say that the flow extends past what appears visually to be a boundary whilst in reality it is not. This coupled with the camera and lens' inability to sufficiently resolve all spatial detail results in some ambiguity to

where the boundaries actually exist. These sources of discrepancy are usually 1-2 pixels or 0.2-0.4 mm (typically) in '*real terms*', but exist in areas which are usually inconsequential to data output. To regulate this discrepancy a background mask derived on the same segmentation process in Step 6. below is applied to all like images; same physical CVC and optical set-up to ensure uniformity and remove uncertainty. The background mask sets all pixels within the segmentation threshold as active (binary = 1 = white) hence eliminating everything that exists outside of the threshold; be it background or flow. A figure of this mask is shown for a typically image below. Of note in Figure 61 is the processes ability to deal with ambiguous areas such as the dark region in the top-right corner of the CVC. The performance of the segmentation is based on the algorithm and threshold value(s) selected.

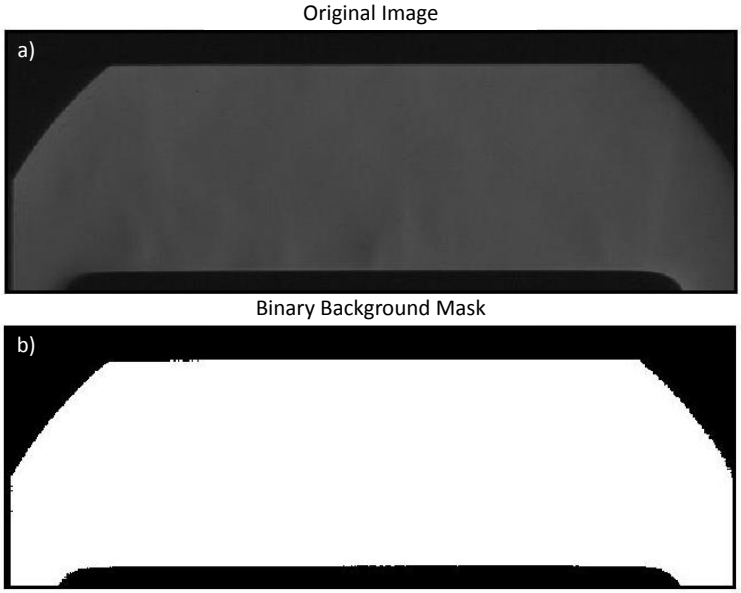

Figure 61, Original image top a), and segmented binary mask image (below, b).

The main steps in which the processing functions are undertaken is roughly as follows and are depicted in Figure 62 below.

1. A synthetic border of zero-intensity (black pixels) is added to all images
2. A mask is created from a background image
3. The mask is applied to the interrogation image.
    a. This leaves only the pixels within the region of interest open for processing.
    b. This removes any areas not intended for analysis – i.e. impingement objects or injector tips
4. The masked interrogation image is compared to the masked background image
5. The absolute difference in pixel intensity is calculated
    a. This leaves only pixels that have had an intensity shift; flow.
6. The absolute difference is then segmented using a segmentation algorithm of either:

a. Prewitt
b. Sobel
c. Canny

7. Once defined, the pixels are dilated and eroded (equally) to fill in any pixels within the boundaries
8. Erroneous segmented areas outside of the main jet are removed
9. The boundary perimeter is then applied back to the original image for visual inspection.

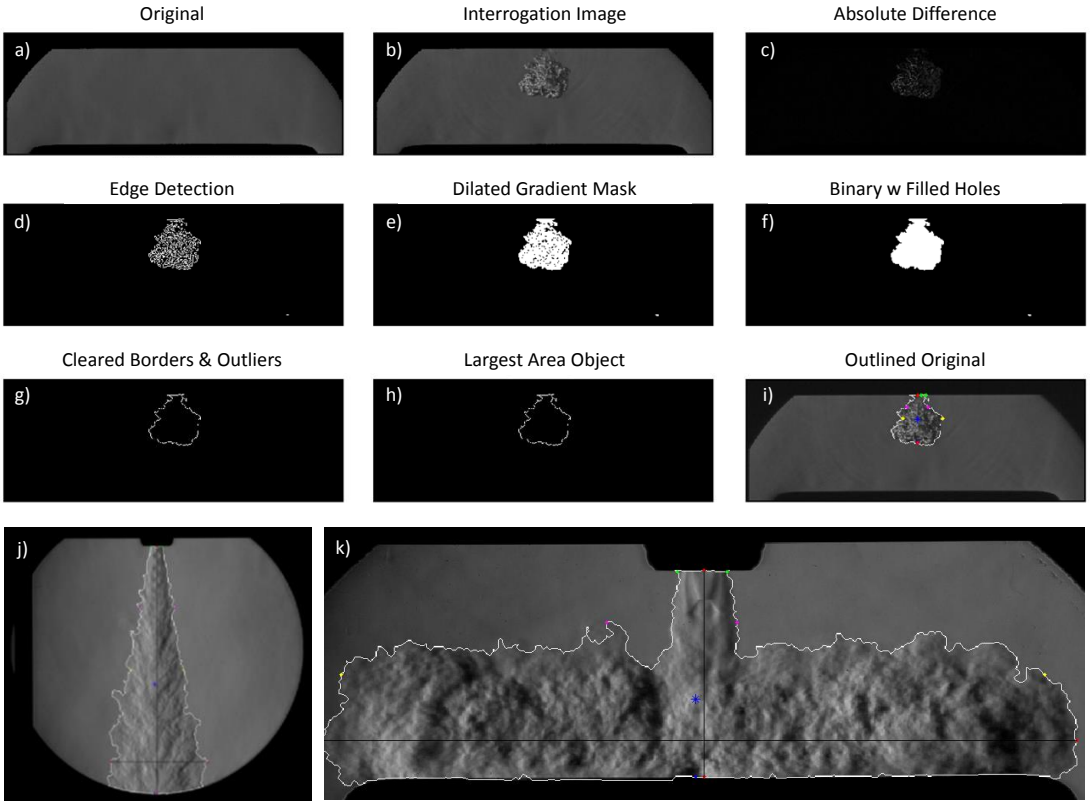

Figure 62, Basic image segmentation steps (a-i) for image processing and a freestream (j) and impinging example (k).

It should also be noted that for the first n images aSOI an additional mask is applied as an ROI for the nearfield. This additional mask (approx. 40 x 60 pixels) affords increased processing capacity closer to SOI where a high subtlety exists between the foreground and background. The ROI size is determined for the higher velocity gases such as hydrogen to ensure the jet in the n^{th} image doesn't exceed the mask boundaries.

Once the jet is defined the value-adding functions are then applied, producing numerical quantification of the following main attributes:

- Axial Penetration
- Radial Penetration
- Spread Angle

- Geometry: Area, Symmetry and Centroid Location
- Location, spacing and number of shock diamonds or triple point locations for the highly underexpanded (NPR>4) flows.

As these parameters hinge on the location of the boundary or boundaries (i.e. shock-diamonds) it is again, crucial to visually check that the original image segmentation process is as it should be. Coupled to the injector nozzle location and the angle at which the jet exists the axial and radial penetration are defined. The overall macro-geometry of the jet is defined using the parameters shown in Figure 63.

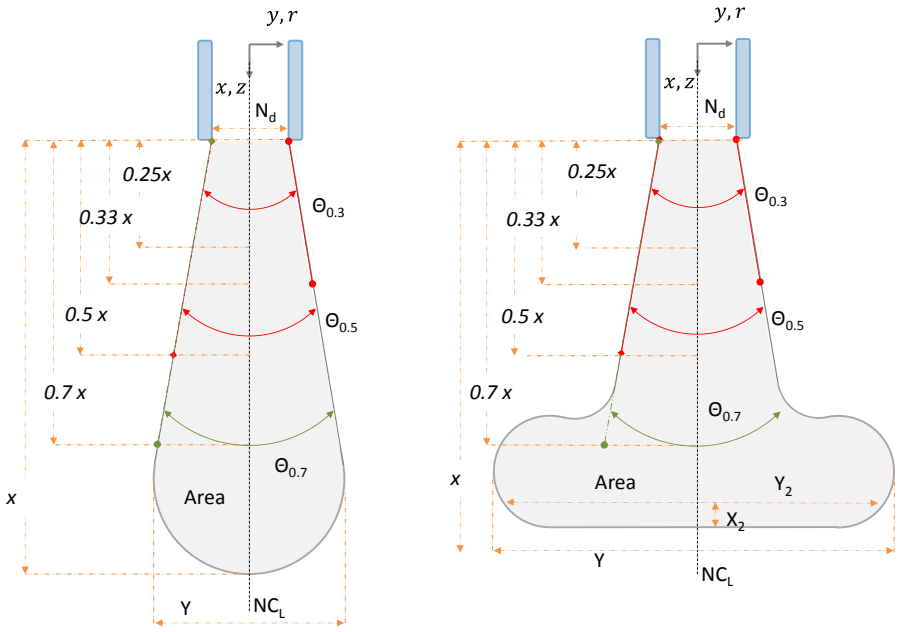

Figure 63, Jet geometric definition.

3.7.6.1 Axial and Radial Penetration

Axial penetration is based on a maximum length calculation from the nozzle centre line taking into account any jet angle deviation (user defined and or centroid location). Sweeping n number of pixels either side of this preliminary location, and averaging across this radial collection gives further resolution on the jet-tip location. This radial sweep was typically ± 5 pixels and was shown to remove any minor boundary perturbations. The axial penetration is defined in this work as a normalised quantity, with respect to the nozzle diameter; x/d.

A similar principal is applied to in defining radial penetration, defined as the normalised quantity; y/d. The radial penetration is defined as the maximum width across the entire jet and is represented as; y. It should be noted that anywhere in this text where y is referred to as a measurement, and not a coordinate, it is given as the total radial dimension across both halves of

the axisymmetric jet. In the case of the maximum radial penetration; the jet was scanned for all pixel rows between 30 and 100% of the maximum axial penetration. The first 30% of the jet is omitted to speed up the interrogation. It was found advantageous that once the maximum radial penetration location was found, that an axial sweep of ± 10 pixels of this location was performed. This is akin to the axial penetration method, however, the radial location was invariably more difficult to accurately resolve – stemming from the turbulent structures at the jet-to-ambient shear-layer. Thus, the maximum radial penetration was employed as a mean value from the ± 10 pixel interrogation.

The velocity of the jet boundary is calculated from the respective axial and radial penetration lengths for a given delivery time. The velocity is an instantaneous insight into the outermost locations of the jet. Additionally, for jets under impinging conditions an additional radial penetration and velocity is computed for a physical location above the impingement surface. This output provides a measure to analyse the boundary layer effects as the fluid shears across the surface. The velocity is prepared as an absolute rate (total growth) and as left and right measurements from the NCL. If the jet is symmetrical (pre-impinging flow centroid located at NCL) one can conclude on any invariance in fluid movements i.e.; effects of non-symmetrical impingement surface, non-zero impingent angle et cetera.

3.7.6.2 Spread Angle

The jet angle has traditionally proved to be the most non-standardised geometric measurement with most researchers having slightly different approaches. The spreading rate is key feature analysed when comparing between experimental and numerical work, hence clarity on its derivation is important. Ouellette (1996) report that for their standard $k-\varepsilon$ turbulence model employed, discrepancies were present between the spreading rate input of 0.11 where their experimental analysis showed this value to be in the order of 0.085 to 0.090.

Traditionally, the spread angle is calculated from a single axial location with reference to either the nozzle exit, a virtual origin preceding the exit or another axial location. This method comes at a cost of a narrowed interrogation where any localised non- uniformities may affect the measurement precision. Single point estimations were employed at half the penetration length which has reoccurred in several works i.e. (Naber and Siebers, 1996, Petersen, 2006). A more complete summary of the jet angle calculations employed by researchers is listed in Appendix VI.

The approached employed in this work utilises a multi-point averaging method whereby all radial locations of the jet boundary are considered for locations up to: $0.33x$, $0.5x$ and $0.7x$ from the nozzle exit. Performing this operation in post-processing; the true values of the column vectors $,j$, are sought at the jet boundary where the lower value is subtracted from the maximum, hence

giving a width for each row (i) location. The row vectors are first summed and the mean angle calculated for each of the three x locations as per Equation 52 and Equation 53 below.

Equation 52, Row vector calculation for jet width

$$i_{a\to x} = [i_1, j_{2\to x}] - \left[i_1, j_{1\to(x-1)}\right]$$

Equation 53, Mean spread angle calculation

$$\theta_x = \frac{\sum \tan^{-1}\left(\frac{i_{a\to x} - d_e}{a \to x}\right)}{i_x - i_a}$$

where, d_e is either the nozzle diameter in pixels or the actual jet exit width at the nozzle (where jet exit is $< d_e$).

The mean angle calculation across a multitude of locations (i.e. $i_{x-a} = \sim 165\ to\ 350$) affords greater certainty in the absence of localised anomaly and provides a highly probably trend in spread angle development when compared to the other x locations computed. This method was compared to single point interrogation where a discernible increase in precision and reliability was observed.

The three locations of x; 0.33, 0.5 and 0.7 were chosen from the heuristics of jet interrogation of both single and multiple jets. They were also chosen to give a somewhat equal segmentation of the jet in the near, mid and far fields whilst conforming to previously measure results. $0.7x$ has also been identified previously a an interrogation location for jet velocity.

Recently, and unknown to the author at the time a similar approach was employed by (Johansen et al., 2013) whom also had success with this multi-point approach.

Additionally, other approaches have shown the discrepancy in single-point angle calculations at various positions along the jet (x/d) for diesel jets, where as expected for narrow largely uniform liquid jets the angle decreases for an increasing x/d (Benito, 2010). This method gives good indication of the trend in spread angle across multiple cross-sections it, however, is still limited to localised uncertainty.

3.7.6.3 Other Geometrical Features

The area of the jet is defined from a binary image post thresholding and segmentation. This area is the area which occupies all pixels within and including the jet boundary. Each pixel is counted as an individual element with no connectivity inclusions. The area is then converted to a mm^2 via the calibration constant mm/pixel. This area is the projected area of the jet as it is taken from the

schlieren image, and hence it is an integrated image of all cross-sections orthogonal to the image plane. The rate of growth is also calculated much the same as the penetration velocity.

Matlab's Image Processing Toolbox offers several useful algorithms for calculating geometric features, the centroid function was employed here on the same binary image as used previously. The radial location (i) of the jet centroid when compared to the NCL gives indication to how asymmetrical the jet is about the centreline. If the jet delivery angle is zero (90˚ to the y,r plane) then integrating against time will yield the 'walk' characteristic. The radial fluctuations can then employed in calculating the jet oscillation frequency.

Symmetry or asymmetry is presented in three variants; left, right and total all presented as a percentage of one hundred. The left and right conditions taken about the NCL are determined from half the total area and thus represent a left and right proportion of a perfectly axis-symmetrical jet. The total symmetry is a proportion of the left and right symmetry and thus it represents the overall jet NCL symmetry. For the jets considered in this work, where the delivery angle is set to zero and there is no cross-flow the symmetry is acceptably taken about the NCL.

The centroid function is employed again in the determination of the spatial locations of shock diamonds as well as their total number. The determination of shock diamonds is approached in a similar way to the overall jet boundary. The process is applicable conditions where shock diamonds/cells have a propensity to form as commonly seen in low-to moderately underexpanded jets.

For a vertical knife-edge orientation, gradients of high and low intensity (white and black) form about the X-plane, and ordered from the cut-off insertion edge; left-to-right or right-to-left. As such, determination of features which contain a range of both high and low intensity requires a more thought out segmentation approach. Figure 64 depicts the shock diamond formation with temporal and spatial evolution highlighted alongside the contrast affects due to the vertical knife edge and inverse effects within the shock diamonds themselves.

The process of this feature extraction is as follows post aforementioned processing;

1. Image is halved about the NCL using a ROI mask, leaving the dark-side in tact
2. Threshold segmentation is applied to leave only the brighter object(s)
3. The binarised image is dilated and eroded leaving islands representing half of the apparent shock diamond(s)
4. The half shock diamond(s) are mirrored about the NCL axis
5. Geometric properties are calculated; area and location of each shock diamond
6. The shock diamond boundaries are defined as an integer border
7. The borders are added to the original image for visual inspection and representation.

The result of shock-diamond extraction is shown in Figure 64 where the far right image displays a black border surrounding the first two shock-diamonds within the jet core. These would be numbered as the 1st and 2nd accordingly and can be tracked throughout their presence within the jet delivery period. Their size and location evolution can then be attributed back to the flow conditions.

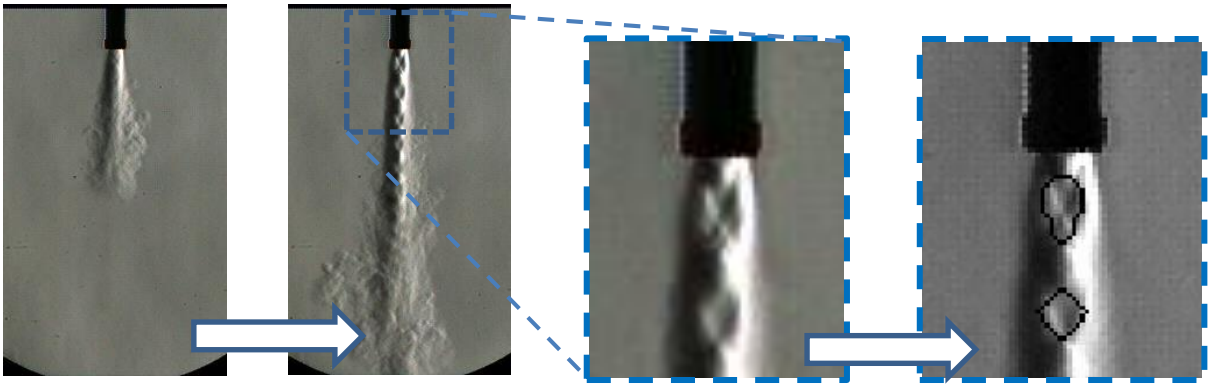

Figure 64, Jet shock cell highlight and contrast due to vertical knife-edge. Far right image depicts the boundary trace of the first two shock diamonds. 0.6ms increments between first two images.

This feature detection accuracy is highly dependent on the pixel resolution with the ROI and for high-accuracy results where absolute values are desired then partitioning of the image via camera zoom/lens configuration would be required. However, a more meaningful analysis of these features would further employ alternative quantitative techniques i.e. Raman scattering (Panda and Seasholtz, 1999). For this work, it was decided that such measures were not necessary for schlieren HSV and thus the trends in shock diamond behaviour are focused on exclusively. The above image gives a good level of accuracy without divergence of experimental set-up.

Using the outlined shock cell, the centroid for each area is positioned from which the distance from the nozzle exit is calculated and where there is shock cell repetition the distance between the cells are also computed. This measure gives a good indication of flow stability when considering transient jets, hence the evolution and growth of shock phenomena can be studied. Again, whilst not a very accurate absolute measurement the relative information gives good detail on the structures.

This feature of shock-cell outlining was seldom employed due to high processing sensitivity. More specifically it was rarely needed due to the highly underexpanded nature of the vast majority of jets considered herein. In light of the large range of cut-off sensitivities produced through the experimental course, due to varying investigation media and set-up configuration, a more user centred approached was developed. For NPR>2.0, and for the first 30 to 80 images aSOI (750 to 1000 µs), the user would select four features within the nearfield corresponding to the coordinates of the shock boundary at the nozzle exit and the triple point(s) for the first shock wave. This selection is shown as points 1. and 2. in Figure 65 below.

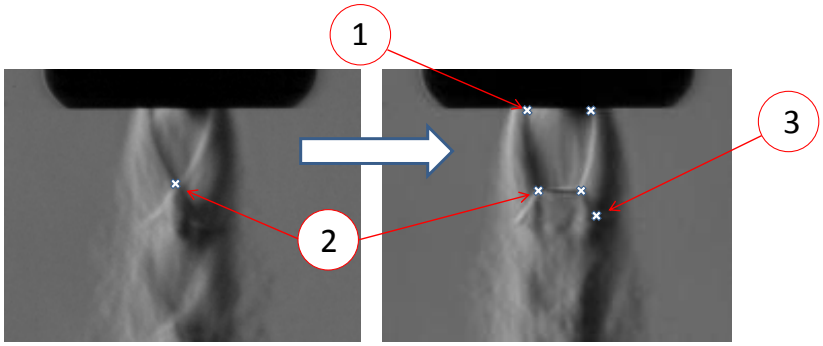

Figure 65, Nearfield shock formation development; with 1. nozzle exit boundary, 2. triple point coordinate(s) and 3. location for reflection angle, for a CNG jet at NPR = 10. Right image depicts formation of classical barrel shock some 375 µs after the left image.

From these selected coordinates the barrel length and Mach disc diameter are presented. The barrel length is defined as the axial distance from the nozzle exit to the triple-point whilst the Mach disc height is the radial distance between the two triple points where appropriate. This representation gives quantification to the evolution of the classical shock propagation for highly underexpanded jets. The regression of the shock wave propagation was deemed to be of no consequence for the current study.

For instances where the Mach disc diameter is greater than 0.5 mm, a third set of coordinates were tagged onto the image. Two coordinates were represented at appropriate positions along the left and right reflection lines. The reflection angle is calculated from these location alongside the previously selected triple points. The reflection angle presented in this work is the average of the two angle calculations. A typical location selection for the right side reflection angle is annotated as 3. in Figure 65 above.

As a supplementary measure, the average width of the jet for x/d distances of 1 and 2, and at the triple point (Mach Disc) location are calculated to and matched to the evolution of the nearfield structures. The nearfield shock propagation can hence be presented cooperatively with these metrics at the outer boundary shear-layer. The locations of nearfield compressible flow features; Barrel length, Mach disc diameter, Triple Point and the Mach disc reflection angle are shown below:

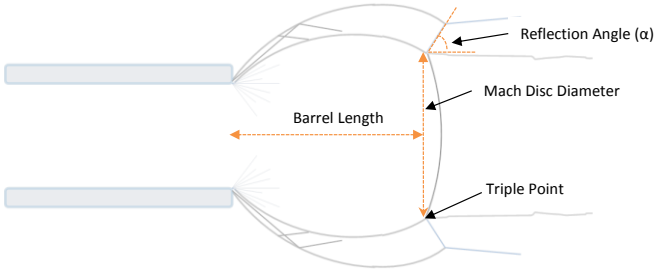

Figure 66, Barrel Length and Mach disc profile for highly underexpanded jets.

3.7 Particle Image Velocimetry

Particle Image Velocimetry (PIV) is employed in this work to quantify the instantaneous jet and bulk air velocity flow fields. This technique was facilitated through the use of a dual cavity Nd:YAG laser, individual sheet optics and a CCD frame grabbing camera. PIV has long served as a useful unobtrusive method of analysing fluid motion and has been developed significantly in the last twenty years.

PIV as it namesake suggests is reliant on a media seeded with particles that faithfully follow a corresponding fluid motion. Illumination of such particles causes Mie-scatter, captured digitally on an optical sensor. Imaging two sequential instantaneous events allows the inference of velocity through the matching of particle constellation with the use of a cross-correlation algorithm. Several works cover the theory and application of PIV to similar underexpanded jet studies (Mitchell et al., 2005) (Chauveau et al., 2006) and the technique as a whole is well documented (i.e. (Raffel et al., 2007)). This chapter will detail the experimental conditions and considerations related specifically to this work. Further discussions are held within individual results chapters.

3.7.1 Illumination and Imaging

A Nd:YAG laser was pulsed at a specific frequency where the separation time between pulse was assigned according to the experimental flow velocities. Solid titanium dioxide particles were introduced into the CVC via a purpose build seeding device or via the fuel delivered. These particles are illuminated by a planar sheet up to 55 mm tall and 1.0 mm thick, formed via two potential configurations (see Appendix VII for full specifications). The in-house system is described in detail below, and are shown ideally in Figure 67 below.

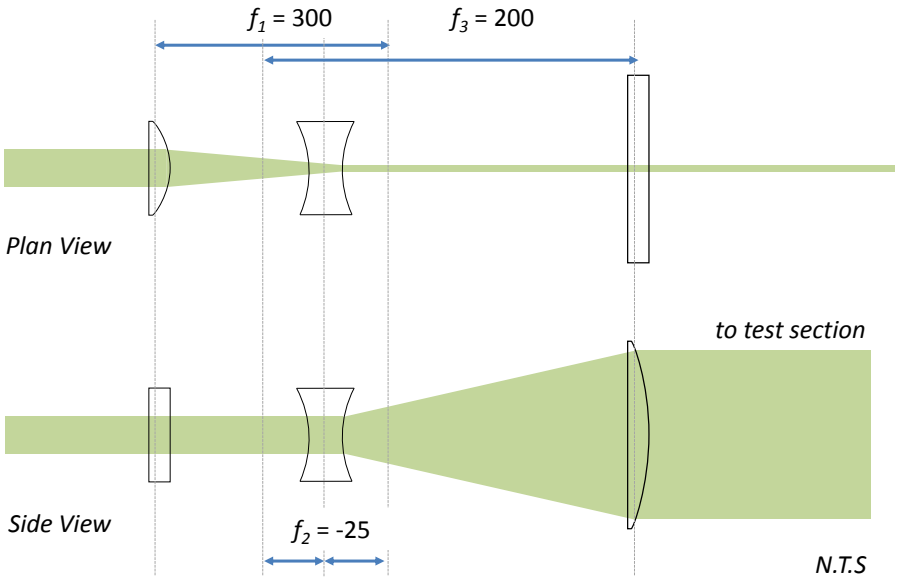

Figure 67, PIV Planar light sheet optics.

The initial output beam of ~9 mm Ø is reshaped using; a plano-convex lens (f_1 = 300) to reduce the plan thickness followed by a spherical bi-concave lens (whose focal point is f_2 = -25) positioned at f_1, and then a third lens; a plano-convex (f_3 = 200) to shape the now height-expanding sheet into a co-planar form. In practical terms the final lens was positioned ahead of it's focal length, due to the high divergence angle of the bi-concave lens, thus in reality the output sheet continued to expand slightly throughout the test section. This was despite the third lens which was employed to control the planar sheet irradiance. This situation was imposed by the space available on the optics bench and lenses available in the laboratory. Sheet forming calculations were employed from optical ray tracing relationships as per below:

Equation 54, Sheet thickness. Source: (Lappas, 2003).

$$W = \left| d\frac{f_2}{f_1} \right| = 0.75\ mm$$

Equation 55, Sheet half-divergence angle. Source: (Lappas, 2003).

$$\theta_d = \tan^{-1}\left(\frac{d}{2f_2}\right) = 10.2°$$

where, W is the ideal sheet thickness and θ_d is the sheet half divergence angle in degrees.

The laser and sheet optics, CVC and camera were mounted independently from one another where the laser and sheet optics were stabilised on a pneumatic table. Great care was taken to ensure the light sheet aligned perfectly under the nozzle orifice centre whilst passing orthogonally to the CVC and camera. All extraneous reflections were dealt with using optical blocks, and the CVC

itself was darkened using black shielding or a black-oxide process (gun bluing). The beam was terminated post- test-section but still within the CVC where a series of blackened razor blades were stacked vertically to form a highly efficient beam dump, 80 x 8 mm. The top of the light sheet was positioned some ~0.3 mm under the nozzle orifice; as needed to reduce the specular reflections emanating from the bronze/brass nozzle tip, even once the tip was blackened. All images were taken in a dark room with all other light sources removed. An example of the illumination exhibited at low laser energy levels is presented in Figure 68 where the particle seeding distribution nozzle is also in view on the right. Illumination energy was held constant for ambient and in-jet seeding configurations at 164 and 110 mJ/pulse respectively.

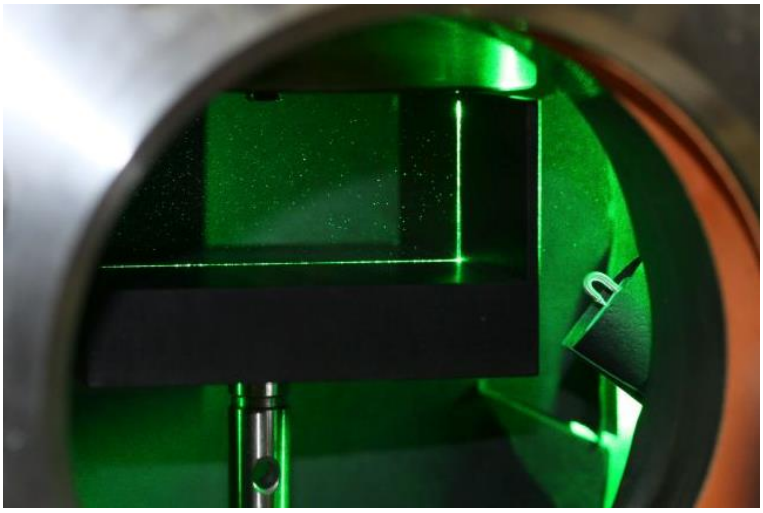

Figure 68, Particle illumination for impinging conditions.

3.7.2 Imaging and Calibration

Images were captured with a Hisense 620 MK II camera (2000 x 2000 px) coupled to a 60 mm lens (Nikon AF Micro-Nikkor f/2.8D). The aperture was set according to the experimental condition in balance between the illumination quality and particle resolution, typically f/8. The lens was set approximately 380 mm from the illumination plane with the set-up depicted in Figure 69 The depth of field for the configuration was greater than the light-sheet thickness; enhancing the acquisition quality (Peterson, 2010). No light filtration was needed as all peripheral illumination sources were removed from the test area.

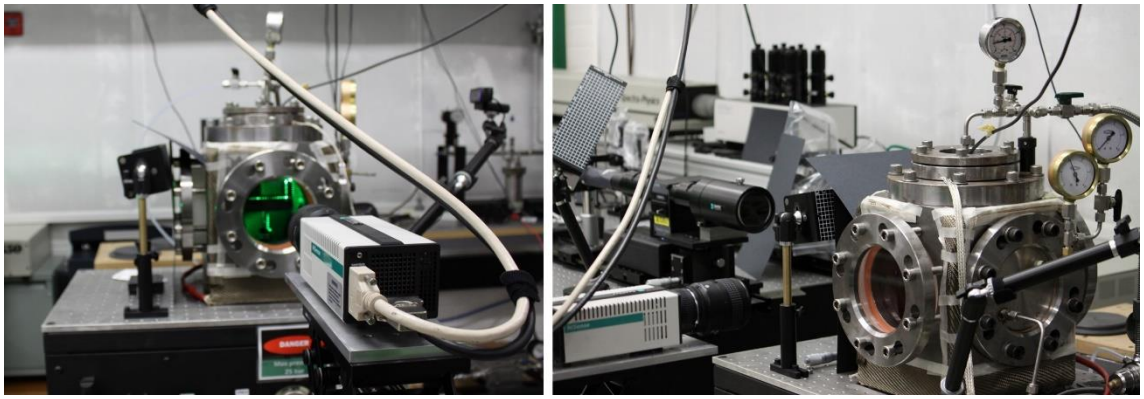

Figure 69, PIV imaging configuration.

Correct calibration of the image is of crucial importance to the accuracy of the PIV results. To ensure correct alignment and image scaling the following took place. A magnetized square bar with the exact nozzle radius cut into the center was placed inline to the nozzle orifice. Along the face of this square surface, a high-precision ruler was placed. The angle at which the ruler and square bar was placed was set in accordance to the laser sheet plane, through care rotation of the pair. This method effectively constraint two degrees of alignment freedom whilst rotation about the orifice center allowed alignment to the laser plane. The camera was then focused on the surface of the ruler from an orthogonal angle. Several fine scratches were cut into the surface of the rule to ensure as precise focus as possible; the existing large ruler features did not allow this otherwise. The ruler was aligned to fall at the horizontal pixel alignment. Calibration is based on a three point method; the intersection of the ruler and the nozzle marked the orifice location origin and two points in the far left and right of the image marked the calibration distance (i.e. 0.0475 mm/pixel), as depicted in Figure 70. The calibration distance was also check in Matlab using a triangulation method as a cross-check.

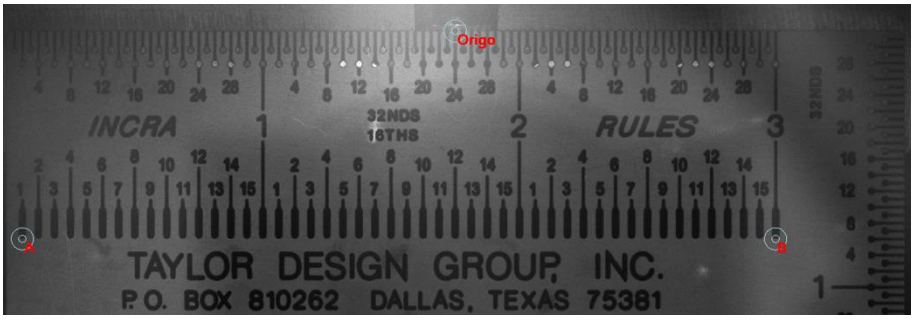

Figure 70, PIV calibration target.

In pre-configuration testing the accuracy of the focus was checked against how well the particles were in focus. It was found that no additional focussing was required to enhance the particles, confirming that target was correctly lined against the laser sheet and that the focus was at the correct depth when aimed at the fine target surface scratches.

3.7.3 Particle Seeding

Two particle seeding configurations were employed in this work for ambient and in-jet seeding. For both cases titanium dioxide (TiO_2) solid particles were used. TiO_2 particles were selected for the seeding medium as their properties provided the best fit to the entire selection criteria:

1. Sized according to:
    a. Flow velocity
    b. Light scattering energy
    c. Turbulence intensity and scale
2. Health and Safety
3. Cost and Accessibility

Two experimental seeding conditions were performed in accordance with the objectives and flow-feature enquiry. The bulk ambient seeding arrangement resolves the features of the region external to the jet but also provides information of the mixture formation where ambient particles are entrained into and mixed with the fuel jet. For example; tracking the 'ambient' flow permits investigations into rate of entrainment in the nearfield region or on the influence the high PR jet has on the initially quiescent in-cylinder fluid. The second experimental condition, where the seeding particles are pre-mixed with the fuel (CNG) provide information on the internal jet flow features. This second condition was primarily aimed at deriving the location of the normal shock, where resolving the in-jet flow velocities (and turbulent structures) are outside of the scope of this work. Whilst accurate in-jet velocity profiles would be useful, accurately tracking the jet core region is not trivial – numerical studies have shown the velocity in the expanding region can reach $M \approx 4.5 \,\&\, 10$ for jets of $NPR\ 10 \,\&\, 166$ respectively (Bonelli et al., 2013, Dubs et al., 2011). However, lower velocity regions such as the jet-to-air shear-layer and jet mixing region downstream of the normal shock (i.e. radial velocity profile of v) did help in confirming the jet boundary locations and the large, sustained velocities (v) expected outside of jet-core region. The following sections will discuss the techniques and applicability of both seeding investigations.

3.7.3.1 Bulk Ambient Seeding

For the ambient bulk-flow seeded scenarios, $1\ \mu m$ amorphous TiO_2 particles (SunChemical) were selected. Particles of this size ($1{\sim}2\ \mu m$) are typically employed when studying in-cylinder flow as either liquid (i.e. (Zentgraf et al., 2014)) or solid (i.e.(Salazar and Kaiser, 2011)). Larger particles, $30 - 55\ \mu m$, have been shown to adequately resolve the larger scale flow motions too (Bevan and Ghandhi, 2004). The density of the particle is equally important for inertial response reasons, as discussed subsequently. Additionally, oil particles of $3\ \mu m$ have been employed in quiescent high pressure gas-jet and liquid-spray studies when resolving the air entrainment and ambient flow-field

(Bruneaux et al., 2011, Arbeau et al., 2004). The type of investigation, however, dictates the requirements of the particle, thus an understanding of a particle's ability to follow the flow is necessary.

A particle which is not a molecule of the measured flow will inevitable have a varied behaviour to the flow it is immersed. The characteristics of such a free-flowing particle are limited by its physical characteristics and the flow conditions. The physical particle is discussed in terms of resistance to flow thus the particle size, shape and mass. For these reasons the aerodynamic drag force becomes important. Other potentially influential terms such as electrostatic or gravitational are ignored given the circumstances of the investigations (Lappas, 2003). For incompressible flow at low particle seeding densities; the molecule-to-particle and particle-to-particle (i.e. agglomeration) interactions are also ignored. The inertial and aerodynamic drag acting on a particle in accelerating flow can be expressed as:

Equation 56, Particle velocity according to the forces acting it. Source: (Lappas, 2003).

$$\frac{\pi d_p^3 \rho_p}{6}\frac{dU_p}{dt} = \frac{6\pi d_p}{2}\mu\left(U_p - U_f\right) + \frac{\pi d_p^3 \rho_f}{6}\frac{dU_f}{dt}$$

where, μ, ρ_f and U_f are the fluid's dynamic viscosity, density and velocity and d_p, ρ_p and U_p are the particle's diameter, density and velocity.

Stokes' law of viscous resistance can be used when the particle Reynolds number (Re_p) is less than one. The particle Reynolds number can be defined as:

Equation 57, Reynolds number for particle flow. Source: (Mei, 1996).

$$Re_p = \frac{(U_f - U_p)\rho_f d_p}{\mu}$$

In such a case, the velocity lag or particle slip, U_s, can be defined as

Equation 58, Velocity lag of a particle where $Re_p \leq 1$.Source: (Raffel et al., 2007).

$$U_s = U_p - U_f = d_p^3 \frac{\rho_p - \rho_f}{18\mu}\frac{dU_f}{dt}$$

The most commonly used metric in defining whether a particle will adequately follow the fluid is the Stokes number, St, which incorporates the particle response time, τ_p and the fluid time-scale τ_f.

Equation 59, Stokes Law.

$$St = \tau_p / \tau_f$$

Equation 60, Particle response time. (Raffel et al., 2007).

$$\tau_p = d_p^2 \frac{\rho_p}{18\mu}$$

For the $1\ \mu m$ TiO2 particles, with a density of 4239 kg/m^3 immersed in nitrogen of $\mu = 1.69 \times 10^{-5}$ Pa.S, the response time is $\tau_p = 13.9\ \mu s$. Viscosity will remain constant as the main areas of interest (nearfield entrainment and the ignition-region) are seen to be areas where no (or insignificant) mixing occurs and where the temperature should remain close to ambient (293 K).

To define the fluid time-scale of the in-cylinder motion the third and fourth considerations used by (Cosadia et al., 2006), have been studied. This approach has also been applied by Alharbi (2010) and Salazar and Kaiser (2011) with similar objectives to this work. The relevant fluid time-scales are the turbulent turn-over time which represents the largest scale of turbulent-eddies within the confines of the 'cylinder' (τ_t) and limited to the largest PIV interrogation window (τ_Δ). (Alharbi, 2010)

Equation 61,Fluid time-scale limited for the largest eddies. Source: (Cosadia et al., 2006).

$$\tau_t = \frac{L}{u_{rms}}$$

where L is the length scale of the large-eddy and u_{rms} (or v_{rms}) is the instantaneous root-mean squared velocity fluctuation. Under the impinging jet scenarios L is limited by the piston clearance height at 50° bTDC, which is ~33 mm. The fluid time-scale limited by the resolution of the PIV system is defined as:

Equation 62, Fluid time-scale limited for the smallest eddies limited by the interrogation window. Source: (Cosadia et al., 2006).

$$\tau_\Delta = \tau_t \left(\frac{\Delta}{L}\right)^{2/3}$$

where Δ for the measurements where the smaller scale structures are most important, in order to appropriately resolve the turbulent kinetic energy, is bound by a maximum interrogation window of ~3.74 mm (128x128 pixels). It is believed however that a length-scale of ~1.00 mm could be achieved if the expected interrogation window is assumed. Further discussion on the image processing is found in the Section 3.7.5.

As an estimate of the particles ability to track the flow, a worst case scenario is demonstrated. For a highly turbulent flow of turbulence intensity (TI) of 5 & 10%, with the mean flow velocities set

20 m/s and 50 m/s, the maximums expected within the ambient regions of the ignition zone and jet boundary respectively, the following table is prepared:

Table 11, Comparison of Stokes numbers for varying turbulence intensity and mean flow velocity.

T.I (%)	*U*	τ_t	τ_Δ	St_t	St_Δ
5	20	3.30×10^{-2}	1.41×10^{-4}	4.21×10^{-4}	9.84×10^{-2}
10	50	1.32×10^{-2}	5.65×10^{-5}	1.05×10^{-3}	2.46×10^{-1}
5	20	1.65×10^{-2}	7.06×10^{-5}	8.43×10^{-4}	1.97×10^{-1}
10	50	6.60×10^{-3}	2.83×10^{-5}	2.11×10^{-3}	4.92×10^{-1}

Form Table 11 it can be seen that only the lowest velocity and TI case result in a condition where the smallest eddies are sufficiently captured. The remaining cases present varying degrees of Stokes numbers > 0.1, thus will show discrepancy from the flow (Ouellette et al., 2008). The results of the above assume significantly large velocities (higher than any individual velocity component; u, v) and large turbulence intensity values where for actual measurements the $1\,\mu m$ are expected to resolve the rms fluctuations with reasonable accuracy.

Moreover, for a 10 kHz oscillating flow, a high order in-cylinder turbulence frequency (Tabaczynski, 1990) and within the practical turbulence range suggested by Melling (1996), the Stokes number is calculated to be 0.0652. The in-cylinder profile used by Lappas (2003) has been adapted to show the response profile of a $1\,\mu m$ TiO2 particle, which can be observed in Figure 71 to remain faithful to the fluid motion.

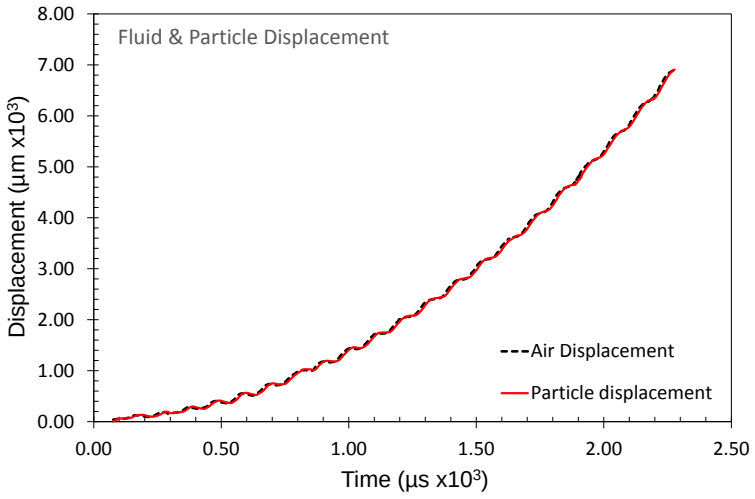

Figure 71, Particle response to a fluctuating air flow, modelled for in-cylinder conditions and a 1 µm TiO_2 particle.

For the ambient, bulk-flow seeded scenarios the following seeding approach was used to deliver the $1\,\mu m$ particles. The seeding device took the form of a typical fluidised bed approach where a canister containing the particles is bottom-fed dry high-purity nitrogen after which a particle laden aerosol is issued. All but the final recommendation by Raffel et al., (2007) on fluidised bed seeding considerations were carried applied to the current method. A unique arrangement was devised in-house to better meet the experimental objectives and further the typical fluidised bed arrangement. A commercial multi-hole gasoline fuel injector (Bosch #261 500 056) was fitted to the underside of the reservoir (Parker Hannifin #33S6 body and filter 100-12-05M) and controlled by an in-house low-voltage MOSFET driver. The injector could be driven up to feed pressures of 50 bar without a high-voltage powerstage driver, which kept cost and resource allocation down. It was found that a 15 bar nitrogen supply pressure provided sufficient aerosol delivery without substantial ambient disturbance.

On the delivery side, a distribution tube ($1/4$ in. Ø) was fitted to bridge the fluidised bed canister and the CVC, the length of this tube was kept as short as possible to reduce the transient delay times (and acoustic feedback flow effects) but a 230 mm length was unavoidable. Furthermore, to ensure a homogeneous mixture within the CVC a distribution nozzle (Bete PJ20) was fitted. This impingement style nozzle, offers a small orifice size (508 µm) which speeds up the flow and a large $90°$, cone angle. Moreover the use of a nozzle facilitated better aerosol targeting which aided in have a rich core of homogeneous particles in the centre of the CVC where the outer regions i.e. glass surface were largely baron of particles.

The combination of a fluidised bed, multi-hole fuel injector and distribution nozzle provided to be a very successful method of delivering particles to the ambient CVC environment. The flexibility in the system provided a consistent seeding density ratios based on the injector pulsation timing. Typically, twenty 5 ms pulsations at 15 bar supply pressures provided adequate particle density concentrations. Post seeding, a minimum of several seconds was required for ambient flow stabilisation which proved convenient to reduce experimentation times. Also, through using nitrogen as the aerosol gas and small (several mg at most) injection amounts did not influence the CVC pressure and density. Through the use of a low ambient flow, $\sim$2 LPM, the particles would remain suspended in a desirable concentration for several minutes. The homogeneity and density of particles was visually inspected prior to each test, an example of the particle distribution during injection of particles is shown in Figure 72 where clearly inadequacies in both are present. The particle density selected for an interrogation region of 16 x 16 pixels was typically 10 to 25 particles which provided adequate tracking resolution and confers to expectations i.e. (Melling, 1997).

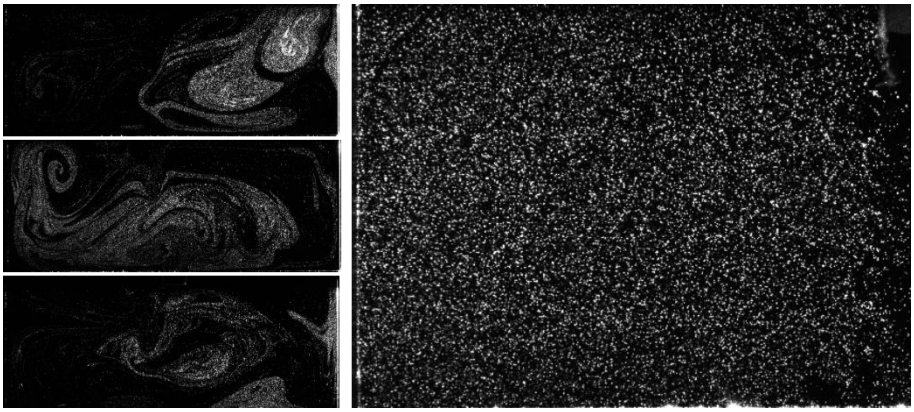

Figure 72, Particle distribution pre-settling time (left column of three) and acquisition image half including a PR60 jet impinging on the far right.

3.7.3.2 Jet Seeding

For experiments requiring in-jet seeding, $0.10\ \mu m$ near-spherical TiO_2 particles (US Research Nanomaterials, #US3535) were employed. These substantially smaller particles were required to more adequately track and hence resolve the large jet velocities. As already introduced, resolving the velocities in the expanding-supersonic region is difficult due to the collisional effects of the highly compressed gas. Resolving the supersonic in-jet velocities is not an objective of the current work but some of the limitations in tracking the nearfield flow are worth briefly explaining as is an estimated particle-slip (displacement) since the in-jet PIV results were used to measure the location of the Mach disc.

With the thickness of a normal shock is much smaller than the imaging interrogation area, resolving velocity information across the shock is largely unfeasible. Additionally, the velocity immediately downstream of a shock is notoriously difficult to resolve due to the near-instantaneous deceleration in fluid velocity (and the associated density change accompanying the shock-heating) with many studies focusing on this topic (i.e.(Tedeschi et al., 1999, Ragni et al., 2011)).

The response of a particle to a step change in flow velocity, as seen as a particle attempts to traverse a shock, can be estimated by an exponential function for particles with a large density ($\rho_p \gg \rho_f$).

Equation 63, Particle velocity. Source: (Raffel et al., 2007).

$$U_p(t) = U_f\left[1 - \exp\left(-\frac{t}{\tau_p}\right)\right]$$

Equation 63 is a simplification and is dependent on the upstream velocity and the particle's ability to follow Stokes' law within this region (Raffel et al., 2007). Tedeschi (1999) provides a

thorough discussion on the variables affecting a particle's ability to follow high-speed, accelerating flows. Under such conditions the Stokes, and thus particle response time, are modified accordingly (Melling, 1997), with the expression as:

Equation 64, Particle motion across a shock according to Stokes drag law. Source: (Melling, 1997).

$$\frac{dU_p}{dt} = -\frac{3}{4} C_D Re_p \frac{\mu}{\rho_p d_p^2}\left(U_p - U_f\right)$$

where modification to the Stokes drag law and corresponding particle response time as:

Equation 65, Particle drag coefficient with Knudsen number. Source: (Melling, 1997).

$$C_D = 24/\, Re_p\left(1 + Kn_p\right)$$

Equation 66, Particle response time with Knudsen modifier.

$$\tau_p = d_p^2 \frac{\rho_p}{18\mu}(1 + 2.7Kn_p)$$

where the Kn_p is defined in Equation 67 and the mean free path length (l) of the gaseous medium is defined from classical ideal kinetic theory in Equation 68.

Equation 67, Knudsen particle number.

$$Kn_p = l/d_p$$

Equation 68, Mean free length for a gas.

$$l = \frac{\mu}{\rho}\sqrt{\frac{\pi m}{2k_B T}} = \frac{RT}{\sqrt{2}\pi d^3 N_A P}$$

where m, k_B and T are the molecular mass, Boltzmann constant and the thermodynamic temperature alongside N_A defined as Avogadro's number. The mean free length for a Methane at upstream stagnation conditions of 60 bar and 293 K is therefore approximated at $8.85 \times 10^{-10}\, m$. The Knudsen number is therefore calculated to be 8.85×10^{-3} under these gas and particle conditions. The resultant particle response time, τ_p, for standard and Knudsen adjusted conditions is estimated as 0.142 and $0.146\, \mu s$, respectively. These are of course idealised response times and are shown to vary under measurement conditions (Mitchell, 2012). Additionally, the agglomeration of nano-size particles is said to increase the particle size by a factor of 10 (Urban and Mungal, 2001) with obvious consequences on flow tracking ability.

For nozzle exit conditions we define the fluid time (τ_f) using the characteristic length, L; the nozzle diameter ($1.00\, mm$) and the methane exit velocity is $\sim 446\, m/s$, as $\tau_f = 2.24\, \mu s$. At sonic

exit conditions $St \approx 0.065$ satisfying the relationship where if $St \ll 1$ the particle will behave like a tracer.

The Mach disc location is defined as the instance where the particles attempt to traverse across the shock and thus is represented by the largest velocity immediately prior to doing so. For the conditions expected the particle-slip at the location of the Mach disc is estimated up to $\sim 300\ \mu m$. It is shown in Section 5.3.1.1 that the Mach disc location defined by the PIV centerline velocity profile is in close accord ($< 300\ \mu m$) with schlieren measurements (~7% on average). This uncertainty is also shown to represent a fraction (<20%) of the change when Mach disc location variables are studied. This gives confidence in the particles ability to profile the jet in the nearfield region for the purpose of defining the Mach disc location.

The in-jet particles were delivered in a less-controlled fashion to the bulk-flow experiments where a small volume of particles were placed within a porous filter housing connected in-line to the fuel supply rail. The actual particle distribution was largely governed by the flow where the highly compressible nature dictating particle placement. Since the particles were delivered instantaneously with the fuel, the first image of the series depicted the jet outline with substantial detail. For subsequent injections, the particles would be distributed throughout the test section. A comparison of the first and third injection event (same image intensity) is shown in Figure 73.

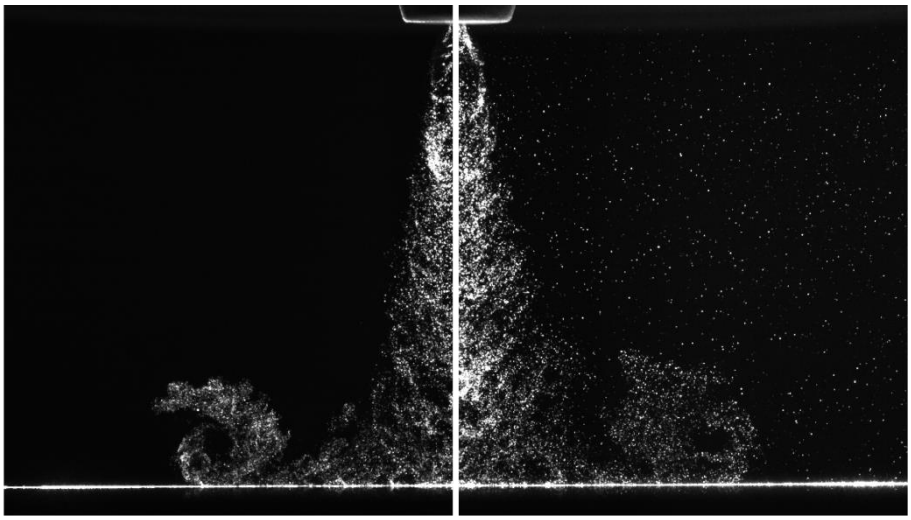

Figure 73, Internal jet seeding distribution of a PR60 jet 415µs aSOI; first (left) and third (right) acquisition.

3.7.4 Event Timing

Timing and synchronisation was handled by two BNC 575 digital delay generators, the primary unit operating all optical systems whilst the second acting as a slave, controlling the injection seeder and fuel injectors. The primary unit is controlled through the Dantec Dynamics StudioDynamics (v4.00) software, whose parameters were set and monitored and through a digital oscilloscope (Tektronix TDS 3012C). Timing confirmation was provided with a silicon photodiode (Centronic BPW 21) which at had a rise time of 1 µs; corresponding to less than 0.4% of the measured delay between injector signal and Q-switch 1. Figure 74 shows a simplified acquisition arrangement with Figure 75 providing an overview of a generic timing arrangement.

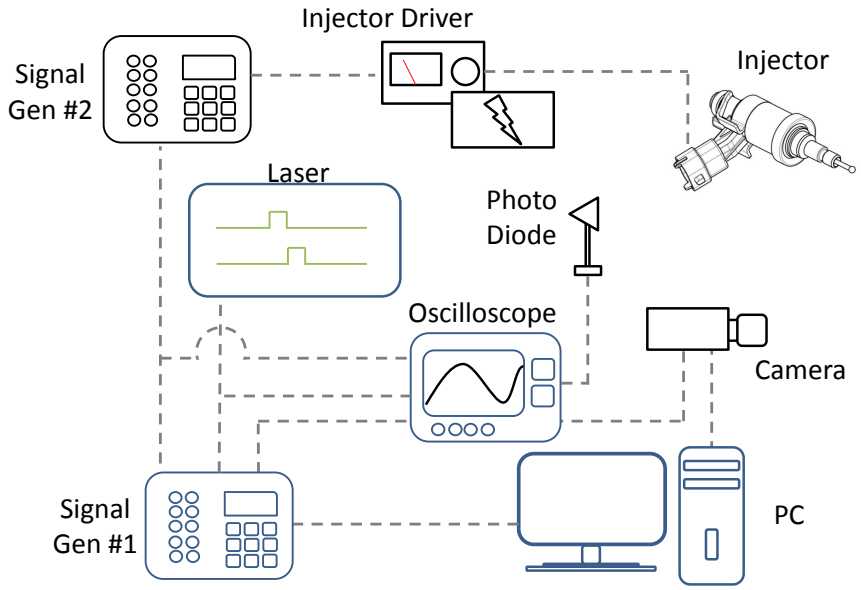

Figure 74, Schematic of PIV acquisition arrangement.

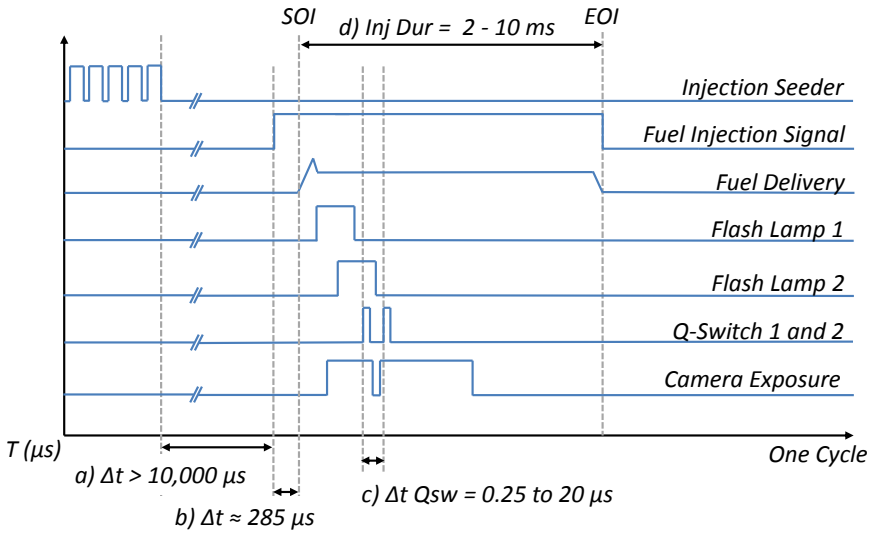

Figure 75, Timing diagram of PIV acquisition system.

During experimentation the laser and camera system would operate on a 1 and 0.5 Hz cycles respectively, producing approximately 100-200 image pairs. The laser however would operate at its ideal rate of 10Hz to maintain consistent laser power and to reduce thermal losses in the lenses. At the beginning of each test period the laser and optics were operated to a constant temperature with the laser operated at full then operation level for 2 hours. Additionally, fifty preceding 'warm-up' executions would occur before first image acquisition.

The fuel injector, however, operated every second laser event; a 0.5 Hz cycle. This frequency offset provides a several second delay between event acquisitions and was done intentionally for two reasons:

1. The input signal for fuel injection comes from the flash lamp 1 (FL_1) signal and due to the short time between FL_1 and Q-switch 1 (QSw_1), some 165 µs, the injection event can only be capture in the following sequence.
2. The two second delay allows sufficient time for the fuel delivered to disperse and exit and the CVC. The fuel is removed from the CVC via the continuous low-flow N_2 purge. The quiescent nature was confirmed by processing the PIV images between the injection events.

This acquisition method yielded ca. $50\text{-}100$ usable image pairs per test and proved to be a relatively quick and reliable method. The repetition of each test condition was at the discretion of the experiment and validity of the output data.

Prior to establishing the synchronisation timing, high speed schlieren photography was used to ascertain the delay time between injector signal, injector energisation and flow delivery. Typically for the combination of the DI injector (Bosch #261 500 056) and power stage (Bosch ES-HDEV1) the delay incurred was $\sim 285\ \mu s$. This delay is considered in event timing as per Figure 75. The flow delivery delay range is estimated between 10 and $25\ \mu s$, at a maximum, where the relatively large sample size would resemble a statistically representative jet. Much higher sample rates were employed in pre-configuration tested where no data uncertainty reductions were seen for increased acquisition sizes.

The pulse separation time Q-switch 1 to Q-switch 2, is set according to the flow velocity conditions where for the region and resolution of interest, the particles should move approximately $20\text{-}25\%$ of the interrogation size; typically $16\ \mathrm{x}\ 16$ or $32\ \mathrm{x}\ 32$ pixels. Due to the large dynamic range in flow velocity, a "*give-and-take*" approach was necessary. The resultant pulse separation time varied between ($0.25\ to\ \sim 20\ \mu s$) (which is similar to the hydrogen-injection in-cylinder study of (Salazar and Kaiser, 2011)). It was found that even at moderately high and low PR, and thus high and low velocity $1\mu s$ separation times provided adequate resolution for the bulk flow tests across the entire region of interest. For the internally seeded jet tests, pulse separation time was reduced to 0.25 to $0.50\ \mu s$ in order to resolve the high in-jet velocities. Similar separation times have been

employed for high PR jets, in which the compressible shock structures were investigated (i.e. (Chauveau et al., 2006)). The optimal timing for the flow velocity within the region of interest were compared to those obtained at across a range of separation times; the optimal separation time was set in accordance to the maximum flow velocity and the dynamic range needed. Additionally, the determination of the true rms values is discussed in Section 3.8.

The 1 µs separation times provided the greatest amount of in-jet and shear-layer detail. For the ambient seeded cases, the clear definition of the nearfield shear-layer was essential. This is discussed at length in Section 6.3. For these ambient-seeded experiments, the particles resolved in the jet are a direct result of air entrainment. An example of the criticality of pulse separation time is highlighted in the highest PR case considered; $\mathrm{PR}400$. As observed in Figure 76, the difference of decreasing the separation time two-fold ($1\ versus\ 2\ \mu s$) is substantial. Whilst the ambient flow velocity is largely the same, the 2 µs scenario fails to capture the particles entrained into the jet and also leaves a less clear indication of the boundary at the shear-layer.

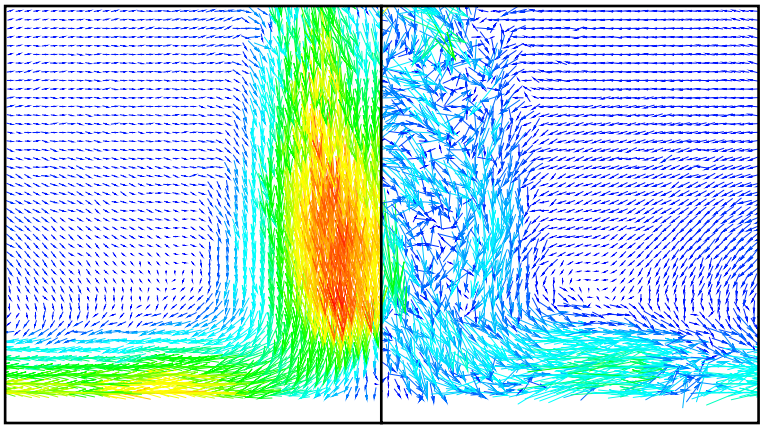

Figure 76, Pulse separation example for an ambient seeded, impinging jet. Left; 1µs and Right 2 µs. Note: particles within the jet are those which have been entrained.

3.7.5 Particle Image Velocimetry Processing

All initial processing was performed in Dantec Dynamic Studio (v 4.00) where the ensemble data was collected alongside the root mean square (rms) values for each $2\mathrm{D}$ velocity component; u and v. Vectorisation of the two 'particle constellation' images was performed using the AdaptivePIV method where individual interrogation areas were selected based on the local flow gradients (Dantec Dynamics, 2013). The interrogation bounds were set fairly broad at the cost of computational time but ensured a best fit for the high dynamic range experienced. This option was set to minimum of $16\ \mathrm{x}\ 16$ and a maximum of $128\ \mathrm{x}\ 128$ pixels, with outputs (scalar or vector) every $5\ \mathrm{x}\ 5$ pixels (grid step size). Depending on the final imaging configuration each pixel approximately represented between 0.029 to 0.047 mm in the image plane.

Prior to processing, a region of interest mask was placed on the original $2\mathrm{k}\ \mathrm{x}\ 2\mathrm{k}$ image; reducing processing time significantly and removing any erroneous artefacts outside the illumination plane. Cross-correlation was bounded though a coefficient minimum of 0.25 and a peak-to-peak height ratio of 1.25. This yields a greater degree of accuracy and all data were considered for "*true*" vectors produced under these conditions, with no replacement or integrated vectors permitted. The adaptivity of the interrogation areas were bounded by the default settings under the two velocity gradient conditions:

Equation 69, Velocity component considerations for gradient based adaptivity.

$$|U_x|, |V_x|, |U_y|, |V_y| \leq 0.10 \; and \; \sqrt{U_x^2 + V_x^2 + U_y^2 + V_y^2} \leq 0.20$$

The output data from the AdaptivePIV were ensemble averaged for the sample set where post processing was handled via an in-house Matlab script. Matlab was used to perform numerous data processing activities including statistical analysis. This aspect is further covered in the individual results chapters.

3.8 Measurement Uncertainty and Error Sources

Whilst all experiments were treated with care, as with any measurement, a level of uncertainty exists. A brief summary of the uncertainty approximation is provided below with the main error sources described.

The pressure within the CVC and the fuel lines were measured using standard industrial and laboratory gauges. Each measurement was made using two concurrent devices. The accuracy of each gauge is reported in the range of ±1.0 to ±1.6% of full scale deflection (FSD). This corresponds to a maximum uncertainty of 8% in fuel supply pressure. This is, however, expected to be typically below 5% with the cross-correlation of multiple gauges which had individual FSD ranges. This uncertainty is applicable to all experiments considered.

For the schlieren high-speed measurements several errors sources were present. These may include discrepancy with the injector SOI time, repeatability of the jet-to-jet phenomena, and the post-processing detection methods. The SOI time accuracy was limited to the resolution of the camera, where the maximum interframe times were 33.33 and 23.24 µs for the PFI and DI conditions, respectively. For conditions where more accurate timing references were needed (i.e. transient compressible features such as the Mach Disc evolution), shorter interframe times were used 12.50 and 25.00 µs (PFI and DI, respectively). It was observed, however, that the appearance of the jet (length penetrated in the frame "*aSOI*") remained largely constant for the samples taken.

The jet-to-jet repeatability was deemed to be sufficient where, although a small sample was obtained for each condition, the coefficient of variation for the measured features was typically less than 5%. The actual uncertainty for the measurement of jet features, i.e. penetration length, is estimated at 1-2 pixels (0.2 to 0.4 mm). Moreover, independently measured features showed significant correlation even between the highest and lowest spatial, and temporal resolutions (refer: Figure 140). All schlieren measurements are shown as mean values with error bars depicting the sample standard deviation. Any statistically significant discrepancies are discussed where relevant.

Regarding the PIV measurements, the deviation in SOI timing to acquisition time is at most 5%. This maximum potential uncertainty occurs for the earliest instantaneous PIV acquisition; 215 µs aSOI. For the later acquisition points the uncertainty in event timing is deemed negligible, particularly as the sample size was sufficiently large. The actual acquisition event was synchronised using a high frequency oscilloscope (500 Mhz, 5 GS/s), as previously discussed.

In order to apply statistical methods which are dependent on the sample distribution profile, the skewness and kurtosis were measured. This task was performed on the PIV data. Skewness represents the lateral shift in the mean with positive and negatives values indicating the level of

"*skew*", relative to a normal distribution whose mean is at the lateral centre. In short, for statistical terms reliant on a normal distribution the skewness of the sample must be near-zero. Kurtosis provides a measure of the shape of the distribution curve and as such is often described as a measure of "*peakedness*". The higher the kurtosis the sharper (and steeper) the distribution about the sample mean. Heavier distribution tails are thus inherent. A standard normal distribution will have a profile with a kurtosis value of three. High levels of kurtosis are said to be generally indicative of more coherent flow structures (Mitchell, 2012) and is therefore a quantity used outside of pure statistical terms for jet flows.

As an example for the statistical quantities, the ignition region PIV data is presented in Figure 77. This single experimental acquisition is a fair representation of typical data sets. The spatial concentration (contour) profiles are presented inset to the frequency distribution of the skewness and kurtosis for both velocity components (u, v). For all cases considered, it is observed that the skewness is most frequently near-zero, indicating good normality. Most cases do, however, depict sample locations where the skewness can vary substantially. This spatially-discrete data will undoubtedly effect the accuracy of standard normal-distribution statistical approaches but are expected to be of little- to no- consequence when considering the spatial average. These represent only minor excursions from the mean data. The mean skewness quantities across the ignition region for u and v are 0.117 and 0.050 respectively. Moreover, the kurtosis levels were typically consistent across each test sample and were shown to have a leptokurtic (high positive values) profile where the mean kurtosis quantities across the ignition region for u and v are 13.981 and 10.702 respectively. As with the skewness, the highest frequency within a spatial region was shown to indicate a generally high level of distribution normality.

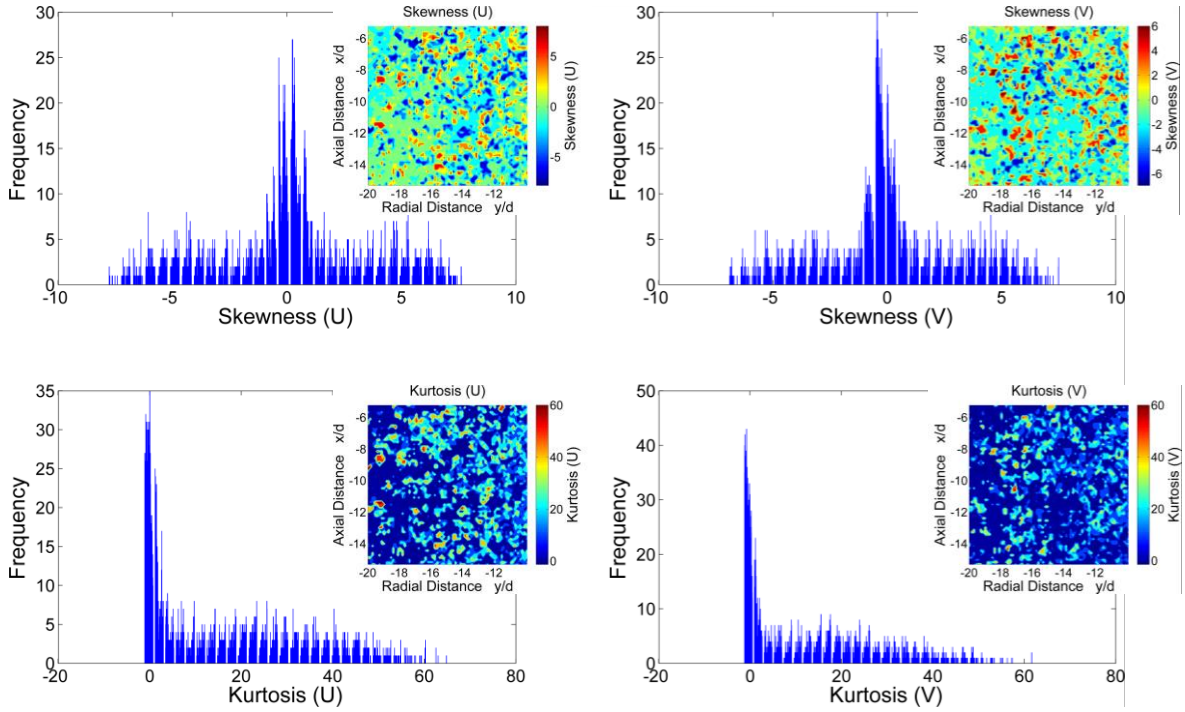

Figure 77, Normality distributions of skewness and kurtosis for U, V (m/s) ignition region components with contour inset. PR60, 415 µs aSOI.

With a satisfactory indication of data normality, the probability of mean values can now be represented through uncertainty analysis. A 95% confidence interval (C.I) is selected as the probability metric, with the approach defined as follows:

Equation 70, Probability statement for sample distribution.

$$Pr\left[\bar{u} \pm Z_{\alpha/2} \times \frac{u_{rms}}{\sqrt{N}}\right] = 95\%$$

where, $\bar{u}$ and u_{rms} are the sample mean and standard deviation of a velocity component, N is the sample size and $Z_{\alpha/2}$ is the critical value. Since the population size is sufficiently large, $N \geq 30$, the critical value for a 95% C.I is given as 1.960. Since the standard deviation is represented as the rms velocity fluctuation, a high level of turbulence will yield a higher margin of error for a particular sample. For this reason, some degree of relativeness of the actual quantities needs to be accounted for.

As a snapshot of the PIV uncertainty expectations Figure 78 is presented for several key cases. It can be seen that there is a higher mean margin of error for the nearfield region. This is proposed for several reasons but are anticipated to be largely due to the; turbulence levels, lower sample size and spatial resolution. Regardless, the values are seen to be largely indicative of expectations in both magnitude and trend. The location of the nearfield and ignition regions are discussed in Section 6.3.

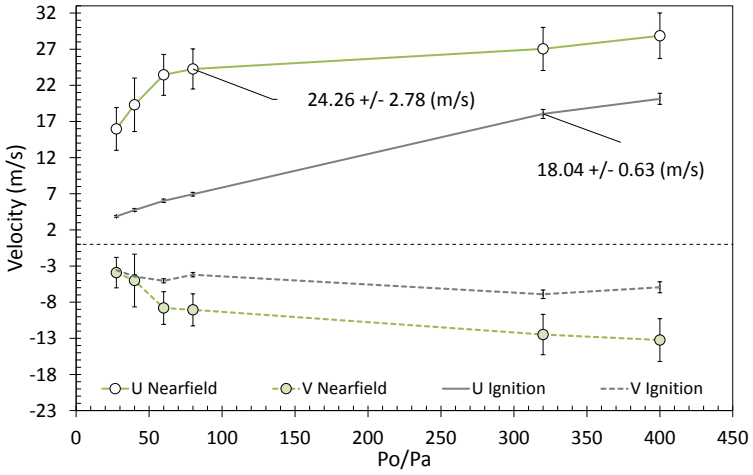

Figure 78, Statistic representation (95% C.I) for nearfield and ignition zone, u and v components. Values represent data obtained at 50% fill level.

One of the key objectives in this work was to resolve the turbulence levels within the ignition region. It can be seen from Figure 78, that the level of uncertainty is relatively small for the ignition region experiments. This was not achieved coincidently and as such a brief outline of how the acquisition was optimised is as follows.

In order to achieve representative velocity fluctuations (turbulence) in the ignition region, the mean TKE values were studied for varying pulse separation times (dT). It was observed that the mean TKE values, and thus the sum of the rms components, would asymptote to a minimum beyond a particular dT[9]. Utilising such a method removes or reduces the larger velocity measurement uncertainties when using small pulse separation times (Adrian and Westerweel, 2011). The minimum TKE values were achieved for most PR series (at an acquisition instance) at a mean pixel displacement of $\sim 2.5\, mm$. Seeding density levels were held approximately constant throughout each experiment series. As expected the pixel displacement followed a linear relationship for an increasing dT with velocity remaining unchanged throughout; this is provided that the dT is still within an appropriate range for the expected flow velocity. Consequently, a power-law relationship was devised for dT and PR and all remaining experimental series dT values calculated.

In addition to the above, the spatial resolution was increased nearly twofold (to $0.0294\, mm/pix$). The sample size was also increased to achieve ~ 100 usable image pairs. The combination of these outcomes have resulted in adequate depiction of the true velocity and velocity fluctuations within the ignition region.

[9] The velocity data obtained from the maximum pulse separation time must still reflect the flow velocity being captured. That is the pulse separation time must still represent a quasi-instantaneous velocity measurement.

3.9 Chapter Summary

The experimental method chapter has outlined the approaches, techniques and processing steps involved in conducting the quiescent experiments and processing the resultant data. The two analysis methods; schlieren high speed photography and instantaneous particle image velocimetry have been outlined alongside any non-standard or novel approaches applied to them.

The primary fuel used, compressed natural gas, has been defined with an estimation of its constituents. Delivering this fuel for the high pressure ratios considered is a largely novel gaseous fuel injector, adapted from a typical direct injection multi-hole gasoline unit. The mass per injection and approximated instantaneous mass flowrate has also been detailed.

Error sources and uncertainty are discussed where all (potential) discrepancies outlined with full disclosure. It is believed that the relative error and uncertainty is below statistical significance for individual analysis contained herein. An uncertainty approximation has been provided for the PIV data where uncertainties are dependent on measurement region and type. The dominant velocity component, u, is shown to have a mean uncertainty in the order of 13.9 and 4.7% in the nearfield and ignition regions, respectively.

4. Low Pressure Ratio Results & Analysis

This chapter focuses exclusively on port fuel injection (PFI) conditions, with objectives set to understanding the effects that pressure and density ratio variables have on fuel delivery. Specifically the objectives of characterising the: *targeting and dispersion behaviour of the gaseous fuel jet* and *the transient jet behaviour near the nozzle exit region*. This work utilises an industry standard port fuel injection (PFI) injector and assesses the delivery characteristics for three fuels: compressed natural gas (CNG), hydrogen (H_2) and a 25% Hydrogen/Methane blend (25%CH_4/H_2). A range of delivery conditions including an impinging jet condition were experimentally investigated using schlieren high-speed photography. Results conclude on the fundamental delivery characteristics i.e. jet spreading and targeting profile tied to other more complex phenomena due to the compressible underexpanded flow i.e. transient Mach disc evolution, barrel length and reflection angle. The relationship between the macro-geometric jet parameters and the internal structures give a more thorough insight to transient gaseous fuel delivery and the flow structure dependencies.

The objectives are guided by the first two research questions:

1. *Can highly resolved imaging provided quantitative insight into transient turbulent jet structures and characteristics?*
2. *What influence does the density ratio have on the jet flow-characteristics and on the mixture process?*

4.1 General Results Introduction

The results of experimentation will be presented with three abscissa references, representing the temporal ($t^{1/2}$) and spatial domains ($i.e. x/d \; and \; y/d$) and lastly the flow variable of interest ($i.e. PR$).

The time $aSOI$ is measured from the frame before the first instance of jet visibility. The first visible instance of flow is considered $0 + t$ where t is the inter-frame time; 25.00 or 33.33 µs (5.00 and 5.77 $\mu s^{1/2}$ respectively). This method accommodates for any variance in the solenoid actuation or fluidic differences between the fuels as it passes through the short internal nozzle geometry. Given the interframe duration is relatively small; 0.44% or 0.58% of the total injection duration, any source of error synchronizing the start of injection between scenarios is expected to be minor.

The pressure ratio (PR) is here defined as the ratio of upstream supply pressure (P_o) to ambient pressure (P_a). Figure 79 through Figure 82 present typical conditions studied, giving examples of nearfield, freestream, impinging and multiple fuel scenarios. These figures are used as general reference throughout the discussion of results.

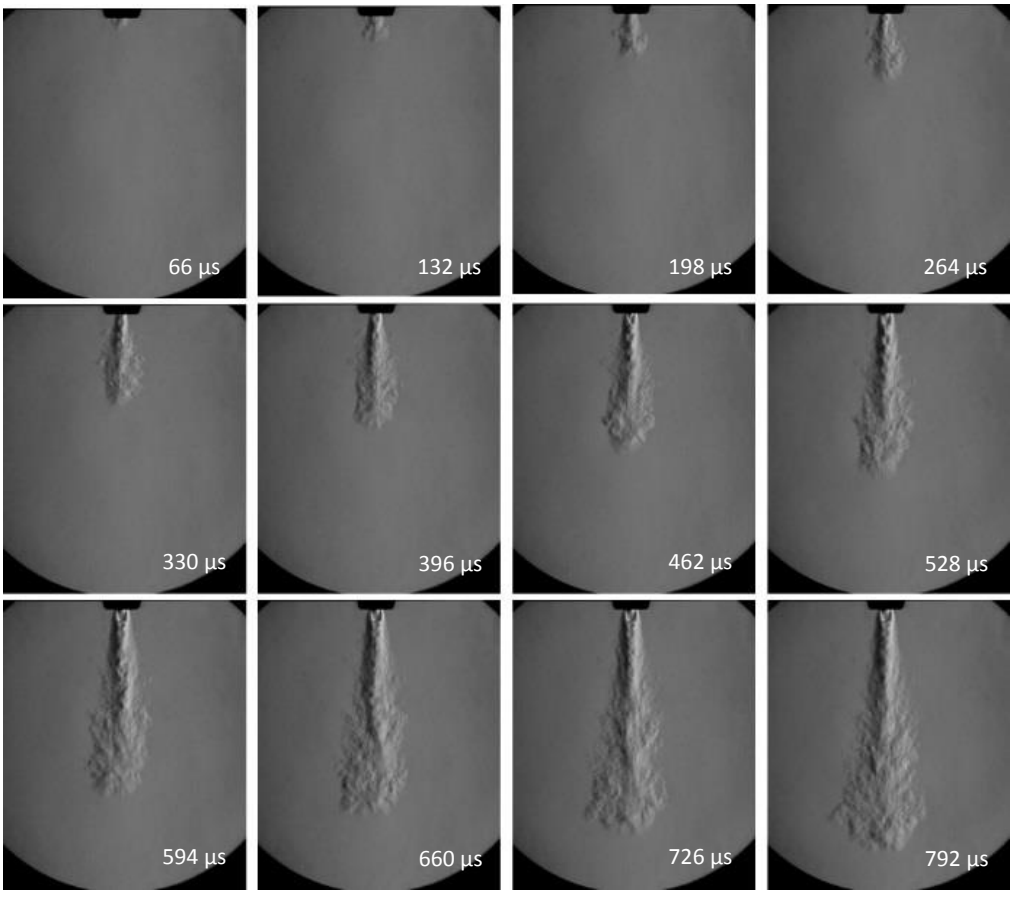

Figure 79, Freestream conditions for a CNG jet issued at PR = 12.0 and NPR = 6.57. Frames at an interval of 66µs ($t^{1/2}$ =8.12 $\mu s^{1/2}$).

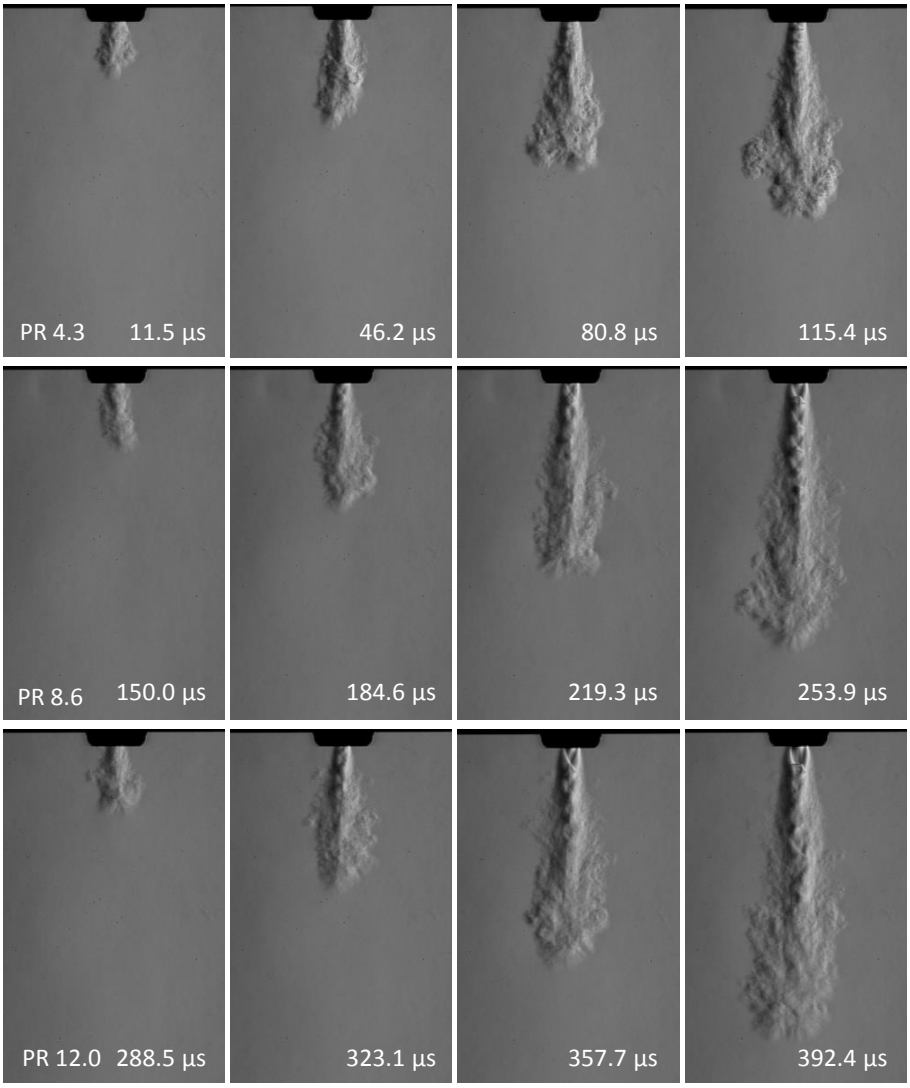

Figure 80, Freestream CNG jet evolution for three pressure ratios from $t^{1/2}$ = 11.54 $\mu s^{1/2}$ aSOI at displayed intervals of 11.54 $\mu s^{1/2}$ (every forth image).

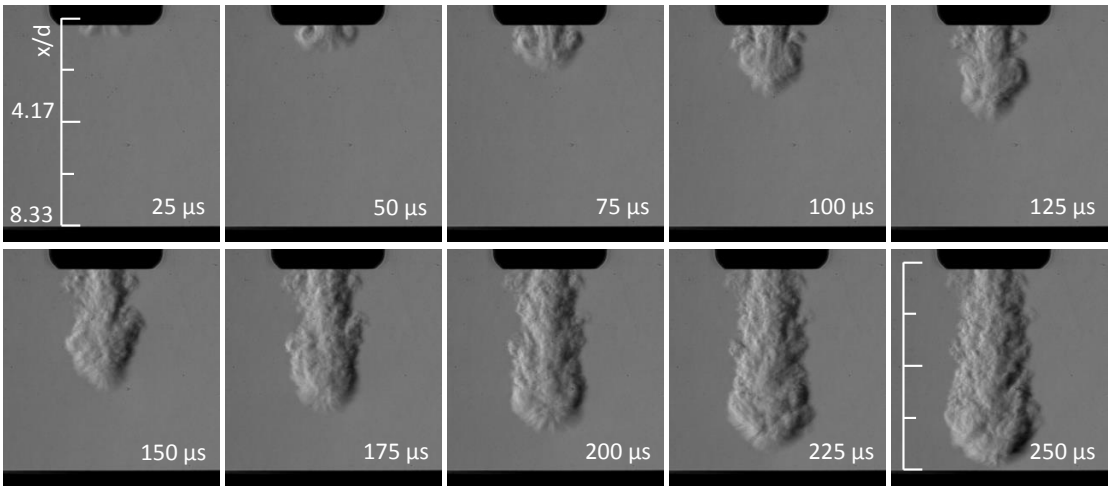

Figure 81, Evolution of a Hydrogen jet at a PR = 4.3 and NPR = 2.28 for the first 250µs ($t^{1/2}$ =15.81 $\mu s^{1/2}$) of image capture.

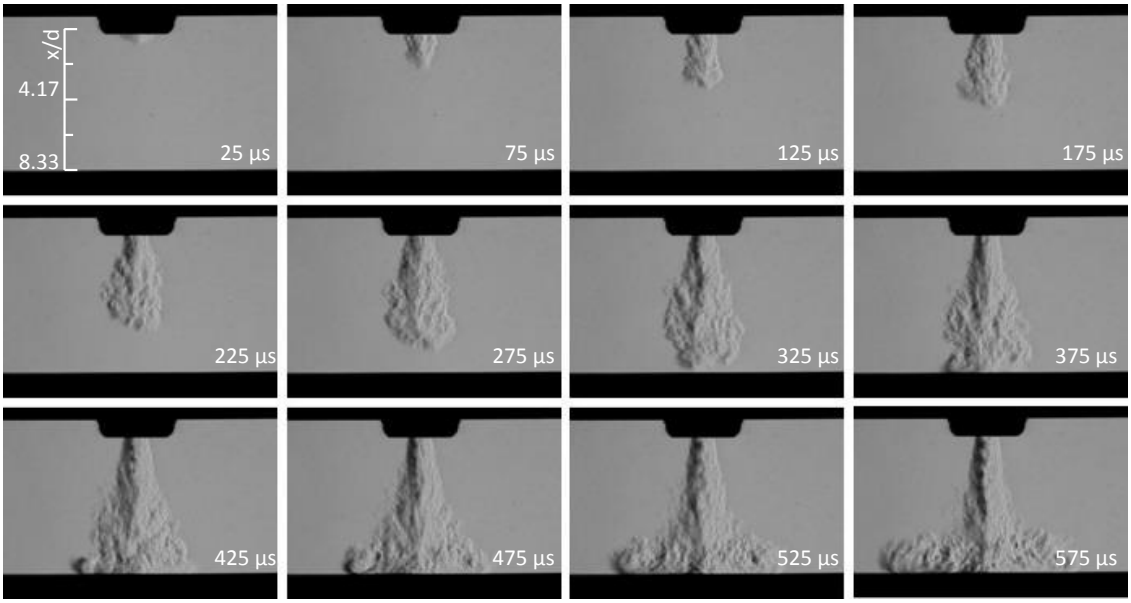

Figure 82, Typical impingement conditions for a CNG jet issued at a PR = 4.3 and NPR = 2.36. Frames at an interval of 50 µs ($t^{1/2}$ =7.07 $\mu s^{1/2}$).

4.2 Macro Structures

This section provides discussion on the interplay between the various parameters with respect to the macro jet structures for both freestream and impinging jets. For example, the macro structure measurements incorporate: axial and radial penetration, spread angle and self-similarity whereas the parameters being changed include fuel type and pressure ratio.

4.2.1 Axial Penetration

It can be seen in Figure 83 that two distinct modes of penetration occur for the freestream jets; initially the development rate up to ~ 15 $\mu s^{1/2}$ is slow where after the penetration rate increases almost two fold. This is observed by the change in gradient at ~ 15 $\mu s^{1/2}$. This mode change is coincident with the sharp decreases in both the jet boundary axial and radial velocities which is counter intuitive to what is expected for constant mass flux jets. Thus is proposed that the jets under consideration do not have a constant delivery mass flux and flow conditions are highly dependent on solenoid operation. Recalling the needle lift profile (Figure 45), a sharp rise in needle lift occurs from 14 $\mu s^{1/2}$.

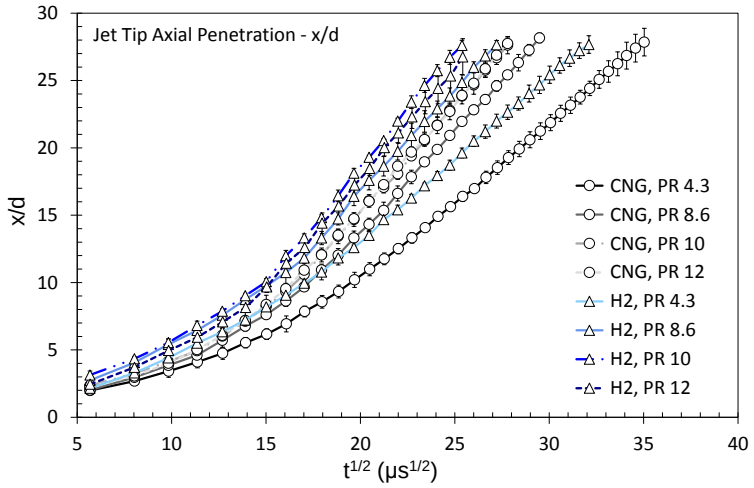

Figure 83, Freestream jet tip axial penetration for low pressure ratio CNG and Hydrogen jets.

Pre-existing scaling laws can be applied to collapse the penetration data set to reflect constant density profiles and attempt to remove the expansion effects occurring in the nearfield. This is achieved through the implementation of the equivalent nozzle diameter (density) scaling expression as introduced in Equation 23. Figure 85 depicts the implementation of the scaling law where two distinct penetration (x/d_{eq}) profiles can be distinguished for CNG and H2 jets. Whilst the scaled penetration rate is somewhat similar ($\Gamma = 3.77 \; and \; 4.01$, respectively) an offset in the scaled time

is present. A similar outcome is also observed in the high PR cases (i.e. Figure 111). Other attempts to collapse hydrogen jets with a higher density gas (Ethylene, C_3H_8) do not collapse ideally either, but show less of a deviation (Owston et al., 2008). It is believed, however, that Owston's numerical models may exhibit insufficient resolution in the nearfield region for $NPR \geq 5.56$. Owston did bring up the affect the nearfield temperature has on scaling – where for hydrogen; heating in the expanding region occurs due to the inverse Joule-Thompson effect which is not incorporated in the current scaling methods (Owston, 2010).

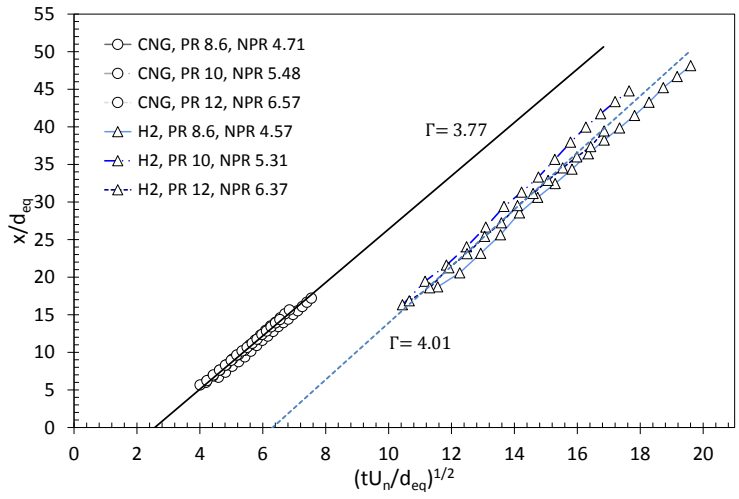

Figure 84, Diameter equivalent scaling of freestream CNG and Hydrogen jets at low PRs (8.6, 10 and 12) and developed beyond 10x/d.

Inclusion of the early development times, where the jet tip is located $x/d < 10$, ($t^{1/2} \cong 13.90 < 18.85\ \mu s^{1/2}$), shows a non-linear trend. This is coincident with the previous indication that prior to $\sim 15 \mu s^{1/2}$ the fuel delivery mass flux is not constant.

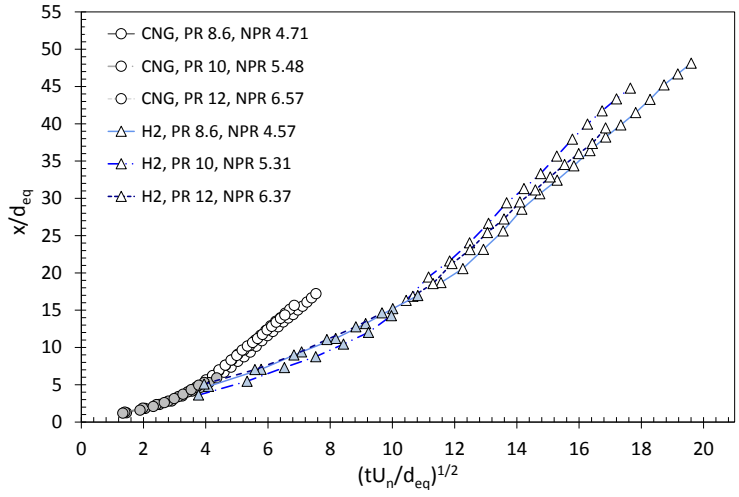

Figure 85, Diameter equivalent scaling of freestream CNG and Hydrogen jets at low PRs (8.6, 10 and 12). Jet Development earlier than $10x/d$ indicated by grey filled markers.

Considering a range of scaled CNG jets between $1.53 < NPR < 6.55$ three distinct development bands exist. These bands, exist in groups approximately according to the classical underexpansion regimes (Table 5). The three distinctive groups are defined by $NPR < 2$, $2 < NPR < 4$ and $NPR > 4$, as observed in Figure 86. For an increasing NPR the scaled penetration rate (Γ) increases, as does the lateral shift toward the origin. To the author's knowledge this is the first example of underexpanded jets showing transitional groupings for scaled penetration rate.

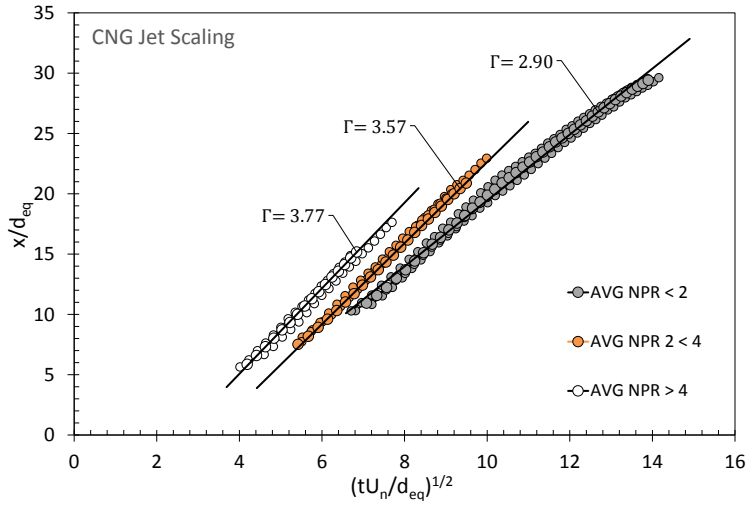

Figure 86, Density-scaled freestream CNG jets for NPR $1 < 2$ (PR 2.6, 3.0 and 3.2), NPR $2 < 4$ (PR 4.3, 5.0 and 6.0) and NPR > 4 (PR 8.6, 10 and 12) developed beyond $10\mathrm{x/d}$.

Whilst the data presented exhibits a deviation from classical regime groupings, regardless it is evident that either the nearfield expansion region (barrel length) does not scale linearly and are of influence to the developed penetration length or that secondary factors outside of the scaling term, such as nozzle exit and Mach disc temperature, affect the penetration length. Temperature ratio is commonly removed where it is assumed that the upstream stagnation temperature is equal to the ambient temperature (Birch et al., 1984), and that the temperature behind the Mach disc is equal to the ambient temperature where the jet and the ambient gas have mixed (Young, 1975). With transient jets, however, insufficient mixing time is available thus a temperature change will exist which creates uncertainties when using the simplified diameter-equivalent model.

The results presented in Figure 86 are for jets which have developed beyond $x/d > 10$ and are shown to exhibit a high linearity for development length well into the constant mass flux and self-similar (Figure 93) region. The barrel length for these fully-developed jets are shown to scale linearly with PR, they are however increasing at a rate of about half of what is proposed in the literature (Section 4.3). Additionally, for the high PR CNG jets (Section 5.2.1) where the barrel length can be a large proportion of the jet, no barrel length affects where observed on the scaled axial penetration. The rate of penetration ($\Gamma = 3.24$) is however lower. It is therefore suggested that the

nearfield process is far from ideal where the nozzle exit density is influenced by the level of expansion, which as shown later in this work is strongly influenced by the in-nozzle geometry.

4.2.2 Radial Penetration

The radial penetration trends do not clearly show any distinct modal change where the penetration (y/d) remains largely linear. Unlike the axial penetration the flow conditions in the time immediately after SOI greatly affect the radial penetration where the highly turbulent developing flow undergoes substantial radial change. The jet (as previously seen in Figure 81– jet images) is far from classical depiction where the geometry can even appear as a *cross-shape* rather than a cone-like shape, hence the lack of correlation in radial penetration (nor spreading rate) immediately aSOI.

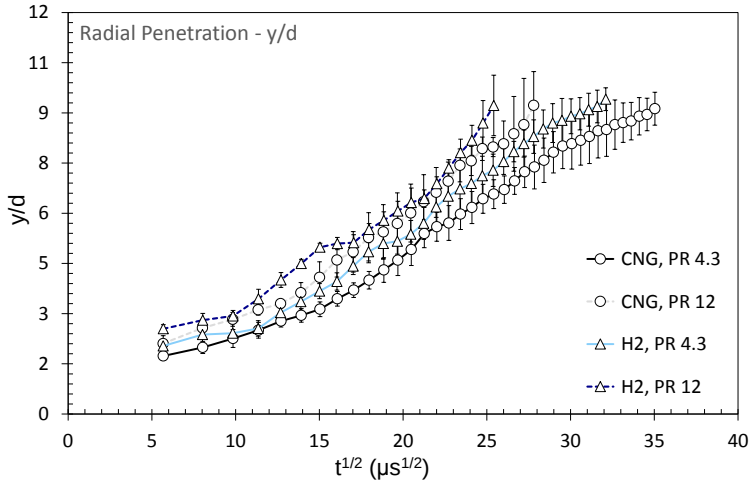

Figure 87, Low PR freestream radial penetration issued from a PFI injector.

The spreading rate increases with an increasing PR and also with a decreasing density ratio; that is a lower density fuel at a high PR will spread substantially more than its counterparts. This is consistent with the overall jet area (Figure 88) where it can be seen that the highest-density fuel with the lowest PR achieves the smallest projected area and at the slowest rate. The actual spread angle is discussed in the following Section 4.2.3.

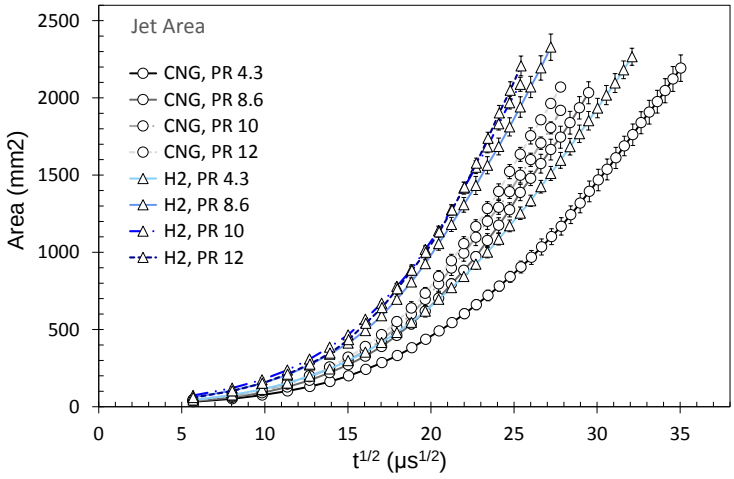

Figure 88, Low PR freestream jet area issued from a PFI injector.

A measurement of radial penetration was also taken 2 mm from the flat impingement surface. The distance of 2 mm was selected to provide information within the surface boundary layer as the jet traverses across the flat surface. Radial penetration at moderate and high NPR conditions are shown in Figure 89. It can be seen that there are two distinct clusters of test series corresponding to the low and high NPR jets. Similar trends were seen across all fuel compositions.

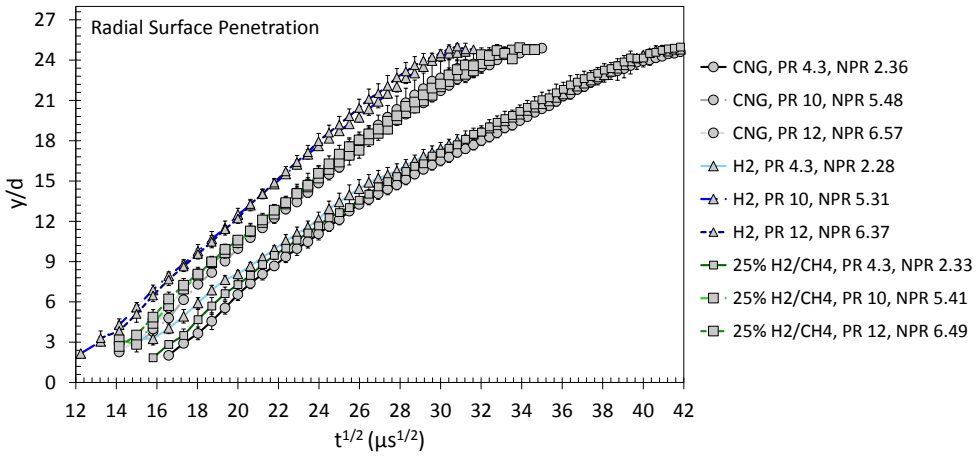

Figure 89, Low PR radial penetration measured 2 mm above the impingement surface location.

Comparing the NPR transitional effects, Figure 90 depicts a range of scenarios for an impinging 25%H_2/CH_4 jet. The high NPR jets are denoted with green-coloured plot-lines. It can be seen that for jets of constant momentum flux (injector is quasi-constant in this time period), that the NPR and thus speed at which the jet is initially accelerated has a considerable effect on flow conditions in the far-downstream. Similarly to Figure 89 a distinct modal separation exists between pressure ratios.

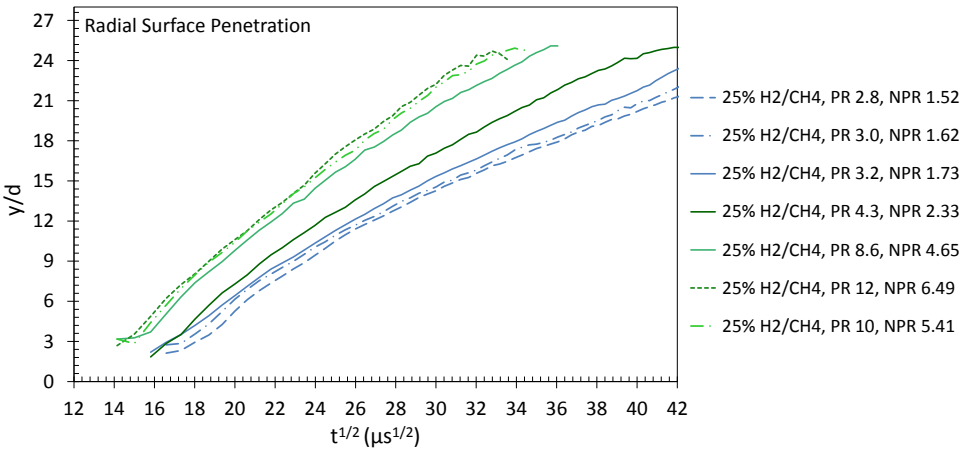

Figure 90, Low PR radial penetration 2 mm above the impingement surface location for 25%H_2/CH_4 jets.

It is observed that the PR = 12 jet arrived some $8.66\ \mu s^{1/2}$ earlier to the impingement surface than the PR2.8 jet. This separation time is of course limited to the interframe resolution ($5\ \mu s^{1/2}$ for 40k fps), where an increase in this resolution would likely yield a more accurate arrival time. Predicting *time-of-arrival* provides an increased understanding of impingement induced mixing. Moreover, the axial tip development profiles provide a means to estimate the *time-of-arrival* to any impingement distance (CAD a/bTDC) for jets under these conditions. This aids in more accurate determination of jet-targeting objectives.

4.2.3 Spread Angle

The spread angle was measured at three locations where mean cumulative measurements up to one-third ($0.33x$), one-half ($0.50x$) and 70% ($0.70x$) of the axial penetration are used. The difference between the measurement types are shown in Figure 91, where it can be clearly observed that during the first few instances aSOI the spread angle (and variability in measurement) is high. Whilst the $0.33x$ and $0.50x$ angles were closely related across the entire range; largely within statistical uncertainty. The $0.70x$ angle in this case produced a somewhat lower reading.

The mean $0.33x$ and $0.50x$ measurements conformed to within 6.7% of one another across the range $6 < x/d < 28$, whereas the $0.33x$ and $0.70x$ jets were separated with an average deviation of 23.7%. It is still largely undecided which of the three techniques yield the greatest overall predictability, but the uncertainty largely comes from the type of measurement which is prone to a high range of jet-to-jet variability, particularly due to their turbulent, transient nature.

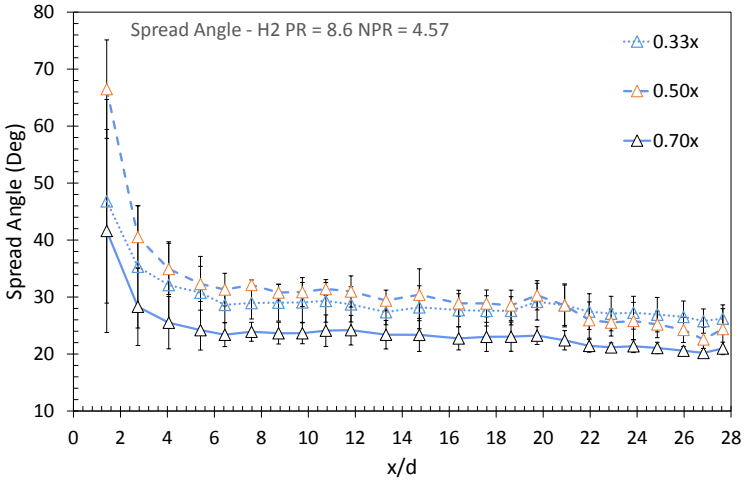

Figure 91, Spread angle measurement techniques exemplified for a Hydrogen NPR 4.57 jet.

To ensure a 'clean' measurement for comparison, the spread angle which is a combination of the three techniques is presented in Figure 92. The freestream spread angle for fully developed jets ($x/d > 20$) is also compared to the mean spread angle for impinging jets prior to surface contact ($x/d \leq 7.3$). There is also an observable trend that the fuel type also has a minor bearing on the spread angle where, on average, the lowest density fuel had the highest spread angle. This is consistent with the previous observations on jet growth. The impinging jet experiments were used for the early freestream spread angle measurements, where the increased temporal and spatial resolution was utilised for an increased processing accuracy. Likewise with the axial penetration (Figure 94), the radial penetration values between the freestream and impinging measurements remain the same whilst both are under freestream conditions. This 'freestream treatment' of impinging jets also valid for high pressure injection (Figure 140).

The average jet angle for a freestream CNG jet where it has developed beyond $x/d > 20$, is $22.63°$ whereas in the early flow development phase of $x/d \leq 7.3$ the average angle is considerable higher at $48.78°$. This is expected, as during the development region, particularly for $x/d < 6$, the jet is more representative of a 'mushroom-like' shape and as such has a considerable high spread angle. This behaviour is most clearly observed in the first 5 images of Figure 81. As the jet momentum increases for the transient flow, the jet narrows with the stronger delivery mass overcoming the surrounding ambient forces and hence assumes the more classic conical shape. The start of a low NPR jet is shown in Figure 81 where the initial vortices are toroidal in nature giving a mushroom cap appearance. Again, the asymptote behaviour of the spread angle is captured in the previous Figure 91.

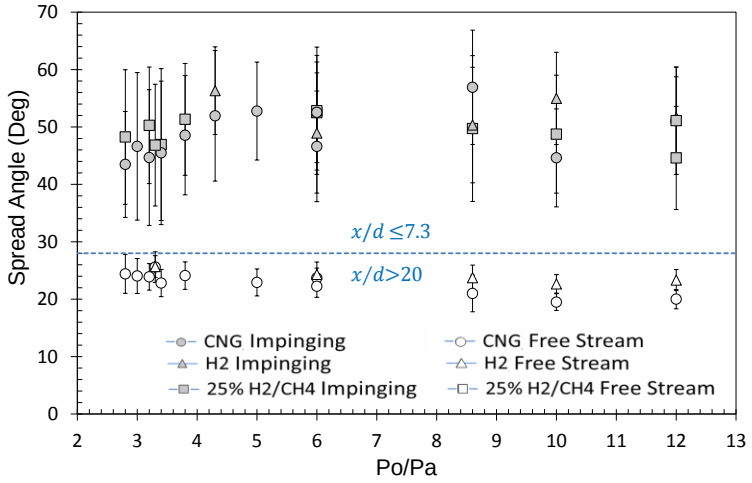

Figure 92, Freestream and Impinging mean jet angle for x/d >20 for low PR jets.

Table 12 provides a brief snapshot of variation in mean jet angle for the three angle measurement calculations, as taken for a high NPR condition. This sample is typical of the freestream jet measurements. In the nearfield the $0.70x$ measurement skews the mean measurement by around 10%, whilst in the developed jets the $0.70x$ measurement conforms well to the two other measurement types.

Table 12, Sample low PR impinging CNG jet angle calculation comparison.

CNG PR 12	*Jet Spread Angle (θ)*		
	$0.33x$	$0.50x$	$0.70x$
x/d < 7.3	39.27°	38.73°	55.83°
x/d > 20.0	19.99°	19.88°	20.13°

4.2.4 Self-Similarity

Self-similarity of the flow is a good indicator the jet has fully developed and the delivery conditions are constant. It is also an indication of the initial turbulence levels upon impulsive starting and hence the interaction of the jet with the surrounding fluid. For freestream conditions the macro jet self-similarity is achieved from $\sim 16\ \mu s^{1/2}$ or between $10 < x/d < 12$ for all cases considered. Geometrically, once the relationship between axial and radial extents is constantly proportional then

self-similarity is said to be achieved. This constant is achieved through the relationship, given in Equation 20.

This behaviour is observed in Figure 93 below where jet proportionality is achieved where the plots asymptote. It is evident that from $x/d \gtrsim 12$ a high level of self-similarity exists for all conditions presented. It is also apparent that the higher NPR conditions approach self-similarity at a greater axial penetration distance, though the effect is minor.

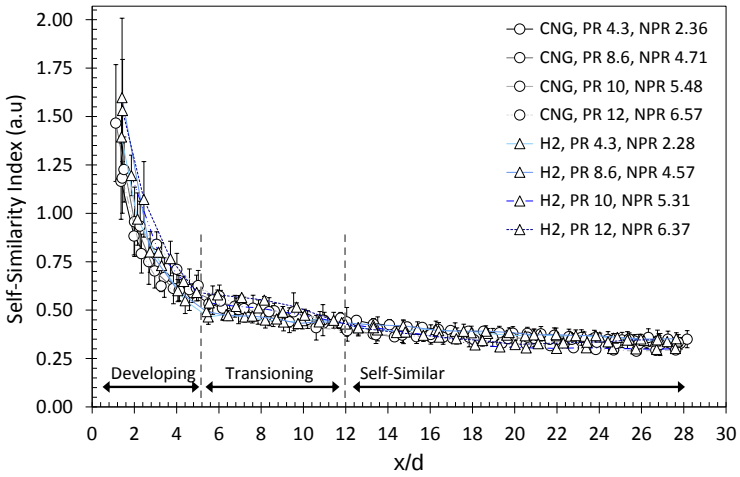

Figure 93, Self-similarity profile of CNG and Hydrogen low PR freestream jets.

4.2.5 Impinging Surface Effects

The impingement surface is positioned at a sufficient distance downstream of the nozzle exit where the surface was anticipated to have minimal to no influence on the nearfield flow conditions. This has already been validated through previous discussion regarding penetration development. This section provides further clarity to the previous arguments.

The impingement surface is located at approximately $x/d \cong 7.3$ and as such the flow preceding impingement should have sufficient time to develop that is the radial profile will have fully or nearly fully developed (i.e. (Zuckerman and Lior, 2006)) and the axial self-similarity has nearly or fully become asymptotic.

The normalised axial penetration is shown to deviate slightly when the impingement surface is introduced. The deviation, however, is mostly within measured sample standard deviation. Some variation in the penetration length is anticipated as the preceding ambient pressure profile extending downstream from the vortex head is expected to be influenced by the jet itself. If the jet is considered geometrically classical, then the maximum axial penetration will be located at the center most point of the vortex head tip where the velocity component is purely axial, v. Immediately to

the left or right of this location the velocity component will extend into the respective radial components, u, thus creating a local change in pressure. The extent of this process and variation of real to ideal jet will undoubtedly have an influence on the penetration length, x/d and thus the imposition of a solid boundary will change the flow behavior immediately before contact. The actual variation measured is hard to distinguish, as the measurements shown here are within one-standard deviation of each other. The highest pressure ratio conditions are presented in Figure 94, where the minor deviations between impinging and freestream flow are shown, particularly from $\sim 10\ \mu s^{1/2}$.

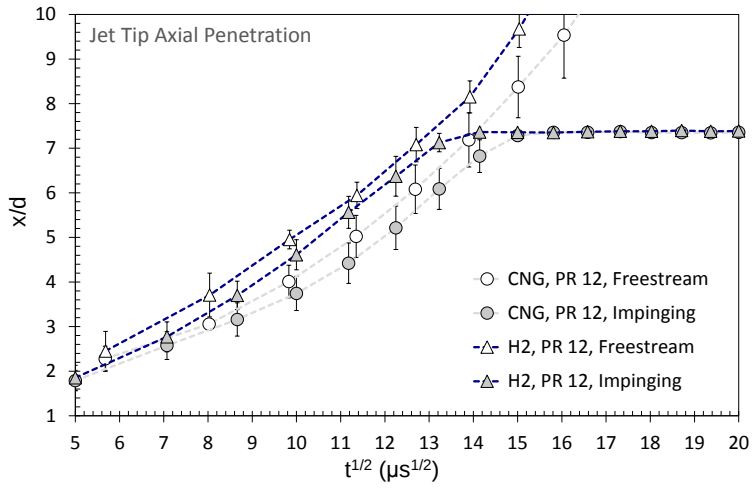

Figure 94, Freestream versus impinging conditions for axial penetration of CNG and H_2 jets at PR12.

The deviation for the lower pressure ratios (i.e. $PR4.3$) decreased to approximately ¼ to ½ of the higher pressure ratio ($PR12.0$) case presented above with similar trends for either fuel employed.

4.3 Nearfield Structures

The nearfield jet profile is discussed throughout this section, which comprises the jet core structure and any corresponding macro-properties within the first few downstream nozzle diameters. It should be noted that the PR8.6 experiments for hydrogen have been omitted where the near field compressible structures were indiscernible at the imaging conditions. Measurement of these features produce too large a statistical deviation to merit inclusion. The evolution of the core structures for a compressible, supersonic highly-underexpanded jet are depicted in Figure 95 below. These sequential images of a 25%H_2/CH_4 jet clearly show the evolution of the barrel length and Mach disc with a reasonable level of imaging detail.

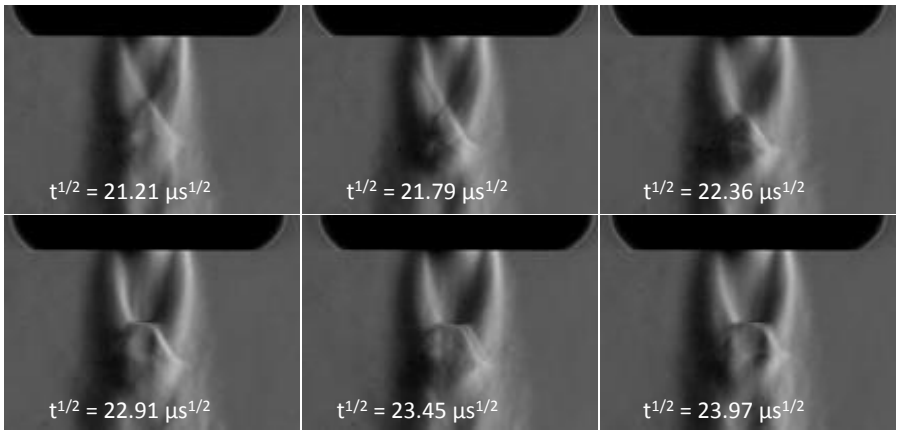

Figure 95, Evolution of Mach disc and barrel length within the nearfield region of a highly expanded 25%H2/CH4 Jet (PR = 12 and NPR = 6.49).

4.3.1 Barrel Length

The Mach disc barrel length has been measured during and after the initial jet development. For all gases the fully developed location occurs at 21.21 $\mu s^{1/2}$ aSOI, some 10 $\mu s^{1/2}$ after the initial triple point 'sighting'. Figure 96 depicts the transition of growing to fully developed barrels, which corresponds to the Mach disc formation from $t^{1/2} = 20.61\ \mu s^{1/2}$.

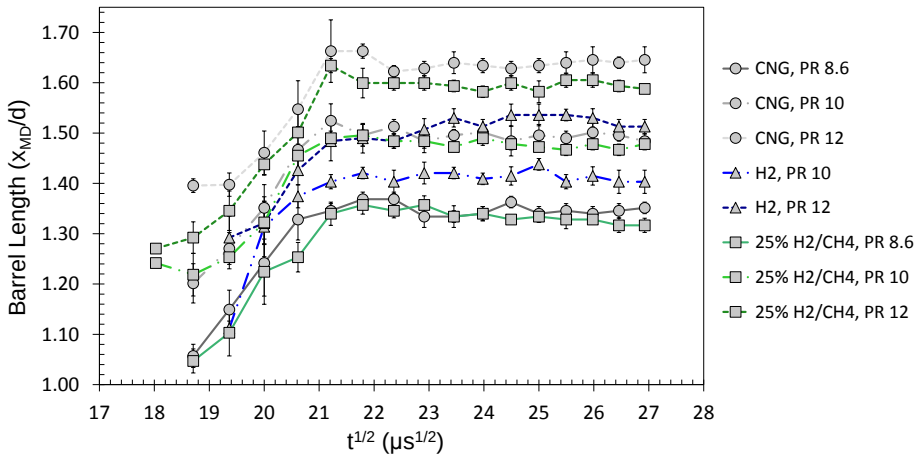

Figure 96, Mach barrel length evolution for low PR jets of CNG, H_2 and 25%H_2/CH_4.

The onset of the fully developed barrel length occurs at a freestream jet length between x/d = 15.33 and 20.02. As the blend gas (25%H_2/CH_4) was not studied for these freestream conditions an exact location cannot be given but is anticipated to align closely with the CNG locations as per the other results presented here. Table 13 presents the initial freestream length locations of the fully developed structures. It is also observed that there is a step-change in Mach disc between $PR8.6\ and\ PR10.0$. This step change is also observed for other related shock induced structures as seen in mean Mach disc reflection angle (Table 16).

Table 13, Jet Axial location (x/d) for the fully developed barrel length of low PR CNG and H_2 jets.

	Freestream Length Location (x/d)		
	PR (P_o/P_a)		
	8.6	*10.0*	*12.0*
CNG	15.35	17.06	17.26
Hydrogen	-	20.54	20.02

Once the jet flow is fully developed, the barrel length is constant with no further growth, Figure 97 represents the value of the constant, C_x, derived from Equation 15. Once again, the barrel length also indicates the location at where the Mach disc occurs from the nozzle exit, along the jet longitudinally.

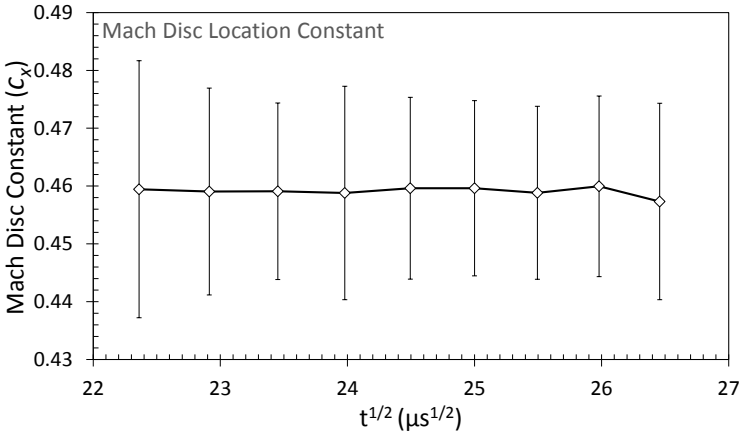

Figure 97, Mean steady-state Mach disc location constant, for the three fuel types for low PR delivery.

The mean barrel length constant is approximately represented as $C_x = 0.459$ for all fuel types considered. Where the average standard deviation across the barrel length for CNG, Hydrogen and 25%H_2/CH_4 is $\sigma_{mean} = 1.20\%$. However this comparison is unfaithful to the more discrete changes in barrel length for varying fuel density. Table 14 depicts the individual fuel Mach disc location constants were it observed that, indeed, the highest molecular weight fuel produces the greatest barrel length.

Table 14, Mean steady-state Mach disc location constant for low PR jets.

	Constant	*Mean Std Dev*
	C_x	σ_{mean} (%)
CNG	0.468	0.80
Hydrogen	0.443	0.60
25% H_2/CH_4	0.461	0.60
Combined	0.459	1.20

The location constants presented are not consistent with previous assignment where a range in the literature has been seen to occur between an average of $0.60\ to\ 0.67$ (Velikorodny and Kudriakov, 2012, Ewan and Moodie, 1986). The variance between the two C_x values is in the order of $0.5x/d$. It is believed that the main discrepancies from traditional C_x values reported for steady-jets are caused by the lack of an internally restricted nozzle geometry (i.e. injector needle). This aspect is discussed at length for the high pressure ratio jets, Section 5.3.1.

To conceptualise this variation, the nondimensional barrel length is plotted against the classical works of Ewan and Moodie, (1986) and Crist et al., (1966) where substantially large nozzles were employed, and also to current modelling efforts (Vuorinen et al., 2013) with a smaller nozzle diameter. The variation in barrel length between the fuel composition is minimally suppressed if the ratio of specific heats is accounted for - achieved using the square root NPR. This normalisation is shown in Figure 98. Attempts to collapse the barrel length further with the use of the square root nozzle exit density ratio was of no consequence suggesting that the barrel length is indeed a function of fuel composition.

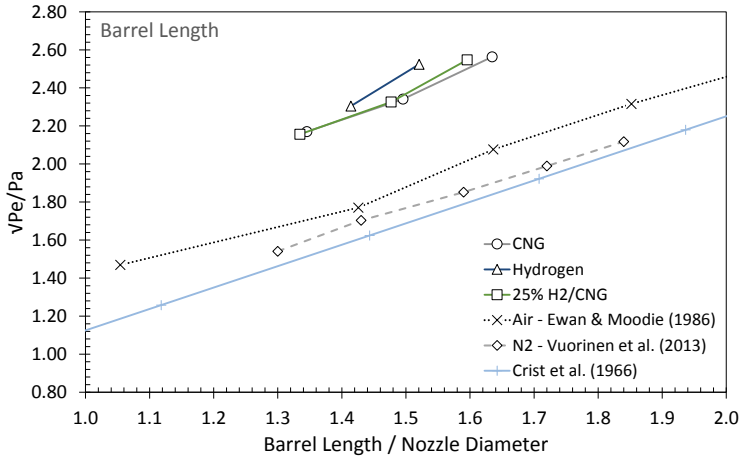

Figure 98, Square root NPR normalised, fully developed barrel length for low PR jets of CNG, H_2 and 25%H_2/CH_4.

To clarify the effects of pressure and density on barrel length Figure 99 and Figure 100 are presented, respectfully. It can be seen that for an increasing pressure ratio the Mach disc location will increase in location from the nozzle exit. The barrel length appears to be dependent on the density of the fuel where there is a trend for increased barrel length for an increasing fuel density (molecular mass). There is, however, only very minor differences between CNG and 25% H_2/CH_4 mixtures. Moreover an average 4.93% decrease is observed between the 25% H_2/CH_4 mixture and pure hydrogen.

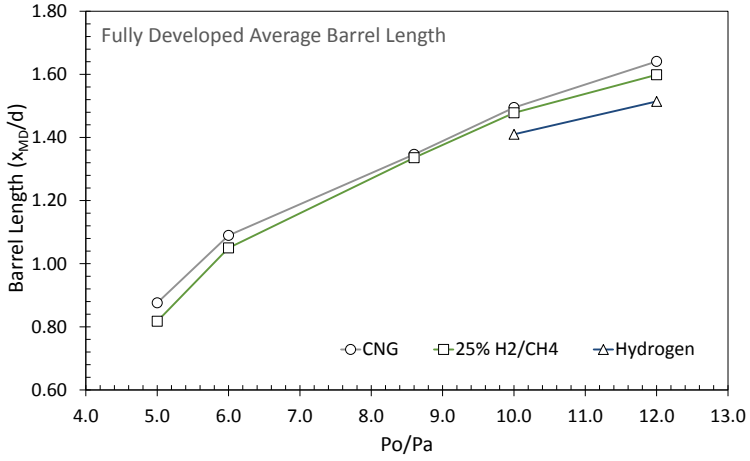

Figure 99, Fully developed Mach disc barrel Length for low PR jets of CNG, H_2 and 25%H_2/CH_4.

A strong correlation exists between the scale of pressure ratio (PR and NPR) and X_{MD} for the majority of the results presented. This adds to the consensus that compressible flow phenomena are primarily dependent on the pressure ratio. Secondary effects from density are minor but not negligible. There is a trend for an increased barrel length for an increasing fuel density (molecular mass). These effects are inconsequential between CNG and 25%H_2/CH_4 mixtures. On average, a 4.93% decrease is observed, however, between the 25%H_2/CH_4 mixture and pure hydrogen. These results are subtle when represented in a density normalised form as observed in Figure 100 for PR8.6, 10 and 12.

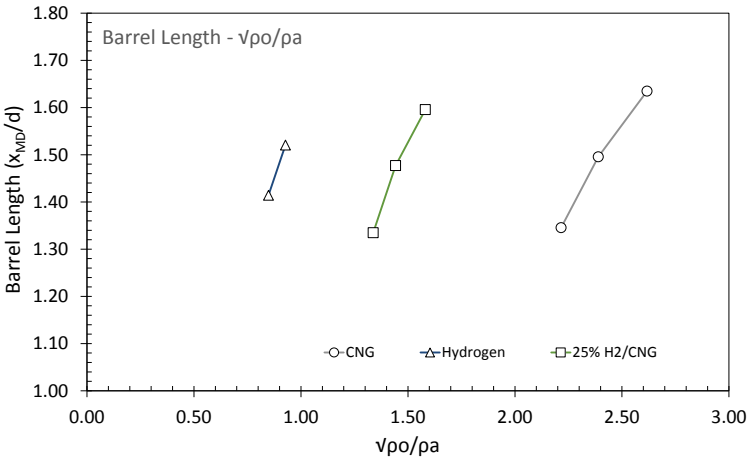

Figure 100, Density normalised Mach disc barrel length for low PR jets of CNG, H_2 and 25%H_2/CH_4 jets.

The core region between the nozzle exit and Mach disc location is wholly supersonic (expansion region), and thus by accounting for or predicting the length of this region further insights into jet development can be made. For example, this highly-supersonic region is impenetrable to ambient air-entrainment and is thus is a region where no mixing occurs (Owston et al., 2008). For a fixed axial penetration, a jet which has a longer barrel length, such is the case for the CNG jets, it can be

proposed that less jet-to-air mixing may take place. This in turn has consequences for air-fuel mixture preparation within an engine.

4.3.2 Mach Disc Diameter

The evolution of the Mach disc diameter has been tracked as a function of the injection time. Figure 101 shows this evolution for the highest pressure ratios. By $\sim 25.5\ \mu s^{1/2}$, the Mach disc diameter has fully developed for all fuels, some $12.3\ \mu s^{1/2}$ after the barrel length has fully developed to a constant size. This sequence is unsurprising due to the relationship between the shock formation and the pressure build up in the nozzle after the initial impulsive gas release.

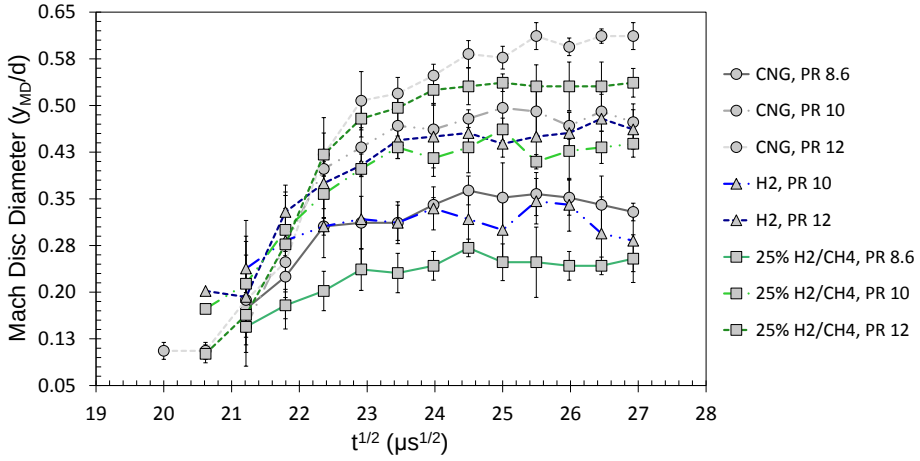

Figure 101, Mach disc diameter evolution for PR fuel jets of CNG, H_2 and 25%H_2/CH_4.

Although somewhat hard to distinguish in Figure 101 it is clear that the time at which a Mach disc fully develops is approximately the same regardless of PR. Moreover, and perhaps coincidently the transient stage of the Mach disc diameter formation falls within the transient needle lift period ($t^{1/2} \lesssim 24\ \mu s^{1/2}$). Once formed there appears to be little to no change in Mach disc profile which is in contrast to a recent work (Vuorinen et al., 2013) which suggests the diameter decrease as time increases whilst momentum flux of the jet through the nozzle is held constant.

Whilst correlations between for the Mach disc diameter and PR have been previously proposed (i.e. (Addy, 1981) and (Crist et al., 1966)) there appears to be little value in proposing an expression using only four $NPR > 2$ data sets. Instead Figure 102 depicts the normalised Mach disc diameter against some popular literature. There appears to be some reasonable fit for the CNG jets compared to (Addy, 1981) experimental data. There is limited value in such a Mach disc correlation, however, as the extent of the disc diameter is subject to individual fuel behaviour (not captured solely by incorporating γ in the use of NPR, P_e/P_a) and where the nozzle geometry is not consistent.

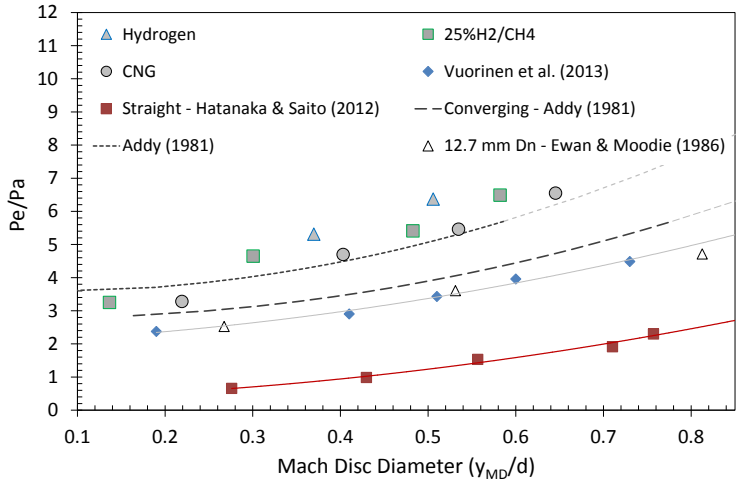

Figure 102, Mach Disc diameter of low PR of CNG, H_2 and 25%H_2/CH_4 jets, compared to popular literature.

Normalising the values according the square root of nozzle exit density ratio, Figure 103 depicts the trends in fully developed Mach disc diameter growth for a range of fuel densities. It can be clearly seen that the diameter of shock disc increases with an increasing fuel molecular mass, and in a somewhat proportional manner.

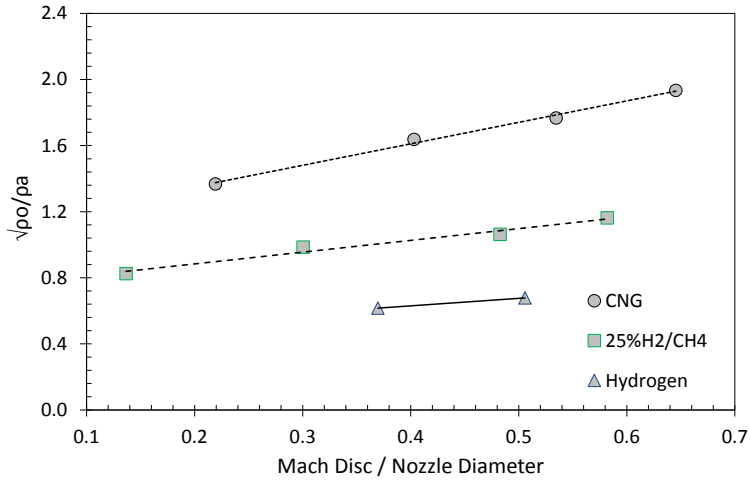

Figure 103, Density Normalised Mach Disc diameter for low PR jets of CNG, H_2 and 25%H_2/CH_4.

The barrel length and Mach disc diameter evolutionary processes are summed up in Figure 104 where the event time sequence is indicative of delivery conditions; $8.6 < PR < 12$, independent of fuel type. Of course the x/d location sequence will be dependent on the individual fluidic conditions.

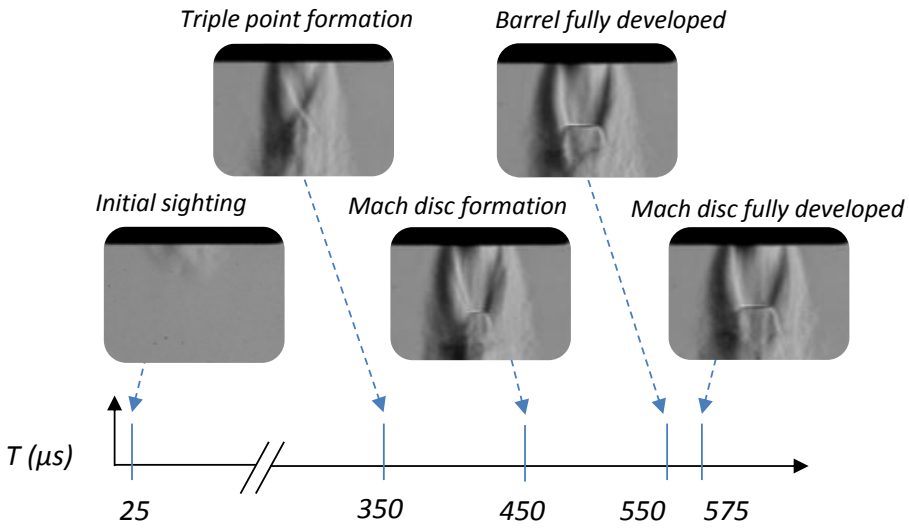

Figure 104, Event timing sequence for jets delivered at PR8.6, 10 and 12. Timing and feature resolution based on impinging imaging conditions.

The Mach disc diameter for the higher PR conditions are evidenced in Figure 105. As already shown there is an increasing Mach disc diameter proportional to the delivery PR, this is exemplified for in Figure 105 where the average size is shown for each variable.

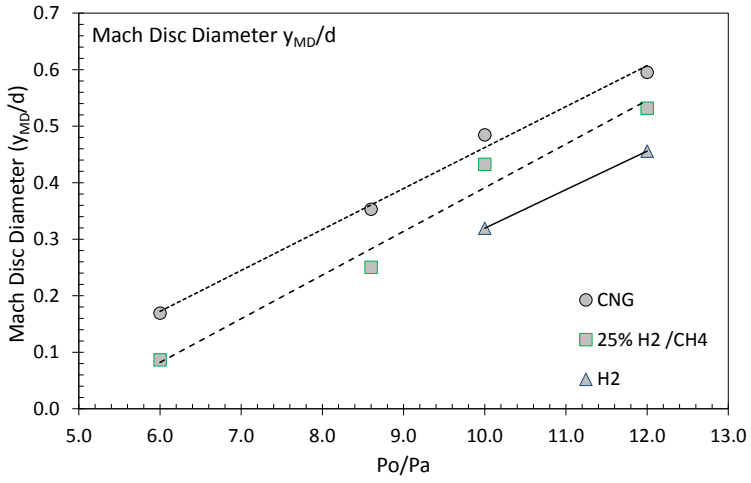

Figure 105, Mean steady-state Mach disc diameter for low PR jets of CNG, H_2 and 25%H_2/CH_4.

Likewise with the barrel length, understanding and predicting the size of the Mach disc diameter has consequences to fuel delivery and mixture preparation. The Mach disc diameter has been shown to govern the overall size (area/volume) of the compressible flow region, with it being the last compressible feature to fully develop to steady-state. Again as with the barrel length the nearfield (and overall) mixing processes will undoubtedly be effected by the evolution of the Mach disc diameter. Additionally, the Mach disc diameter influences the radial borders of the jet where substantial enlargement may lead to the jet encroaching on physical boundaries. Accurate

predication of the nearfield radial profile, including the Mach disc diameter, will aid in the positioning of the fuel injector. To this end, the jet width is analysed.

4.3.3 Jet Width at Triple Point

The Mach disc diameter also represents the separation width of the slip lines (see Figure 19). These slip lines continue to any subsequent normal shock location where they continue until the core region has dissipated through the engulfing turbulent flow. The downstream structure of the normal shock(s) with clear slip line definition has been represented in numerous experimental (e.g. (Panda and Seasholtz, 1999), (Donaldson and Snedeker, 1971) and (Yu et al., 2013b)) and numerical works (e.g. (Maté et al., 2001, Gorlé et al., 2010)).

The radial width of the jet was measured at the location of the triple point (and hence Mach disc location) and is denoted by: y_{TP}/d. This measurement was taken (in attempt) to determine the effects the evolution of the compressible flow structures have on the macro-jet properties.

Subtly it can be observed in Figure 106 that as the compressible flow structures develop the jet radial width also adjusts. The scaling of the width y_{TP}/d is proportional to the PR and NPR as seen with previous examples, but curiously the hydrogen jet, particularly at the highest jet PR, produced a substantial measurement range as shown by the large error bars. The measurement range decreases as the jet evolves as where a greater stability is present due to an increasing equilibrium state.

It should be briefly noted that the data sampling was extended to a greater downstream time, $t^{1/2} = 1175\ \mu s^{1/2}$, where no change in y_{TP}/d was observed thus the presented sequence identifies the critical evolutionary sequence.

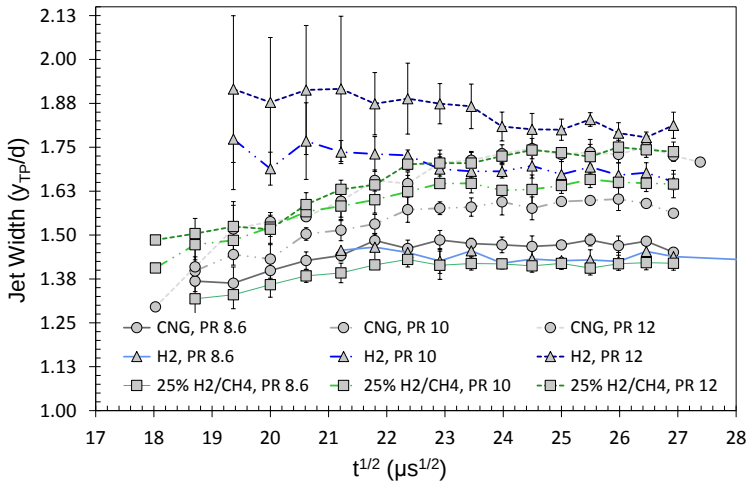

Figure 106, Jet width evolution measured at the triple point for low PR CNG, H_2 and 25%H_2/CH_4 jets.

Table 15 is presented to demonstrate the changes observed at the jet boundary for the developing and developed shock conditions. Again the developing region precedes $t^{1/2} = 21.21\ \mu s^{1/2}$ (450 µs aSOI) and is indicative of a jet extenting to between x/d = 15.33 and 20.02 for the NPR values considered.

Table 15, Developing and Developed Jet widths at the triple point location for low PR CNG, H_2 and 25%H_2/CH_4 jets.

		y_{TP}/d *Triple Point*			
		PR (Po/Pa)			*Combined PR*
		8.6	*10.0*	*12.0*	y_{TP}/d
CNG	*Developing*	1.40	1.46	1.48	1.45
	Developed	1.47	1.58	1.71	1.59
H_2	*Developing*	-	1.74	1.91	1.83
	Developed	-	1.69	1.83	1.76
25%H_2/CH_4	*Developing*	1.36	1.51	1.54	1.47
	Developed	1.42	1.64	1.72	1.59

It was observed that the jet width at the triple point location cumulatively grew 10% and 8% for the CNG and 25%H_2/CH_4 jets respectively, after the nearfield shock profile had fully developed ($t^{1/2} \approx 25\ \mu s^{1/2}$). This highlights the effect the core structure has on the macro jet properties. Moreover, the standard deviation in y_{TP}/d also grew (i.e. for 25%H_2/CH_4 0.59% to 2.89%) in accordance with an increasing pressure ratio potentially highlighting a rise in instability or a rise in turbulence or turbulence region; the shear-layer thickness. This is aspect is discussed for the high pressure ratio jets.

4.3.4 Mach Disc Reflection Angle

The Mach disc reflection angle shows a reasonable level of oscillation for all pressure ratios and fuel types but is well bounded between a $27°$ to $39°$ spread. This is evidenced in Figure 107, where it also seen that the angle is consistent between this boundary for a substantial period of time after the Mach disc formation; $\sim 15\ \mu s^{1/2}$ ($\sim 27.57\ \mu s^{1/2}$ aSOI). To the best of the author's knowledge this is believed to be the first such depiction of the transient nature of the reflection angle for the conditions presented and at such small measurement intervals. It is also observed that

for the conditions presented there is no identifiable trend between PR or NPR and reflection angle.

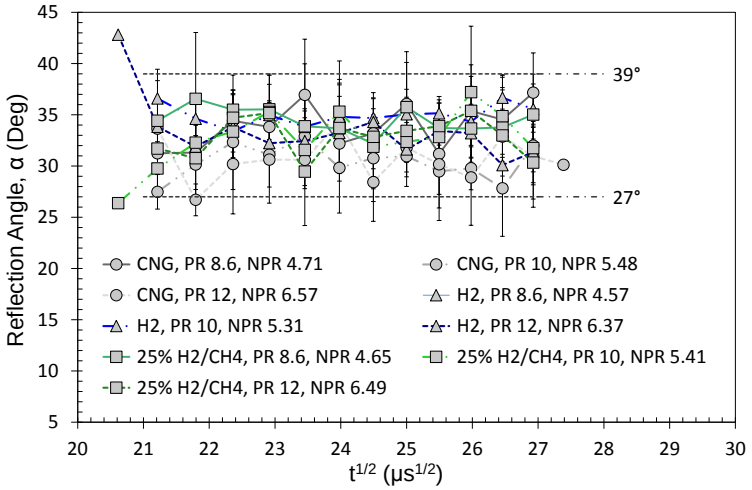

Figure 107, Mach Disc reflection angle for low PR CNG, H_2 and 25%H_2/CH_4 jets.

If mean values are assessed, the fully developed reflection angle does not appear to be affected by the gaseous fuel type whilst the PR does, however, the fuel type does have a small bearing on the mean angle as shown in Table 16. The exact nature of the changes could indeed be obscured by the oscillating nature of underexpanding supersonic jets, as described by other authors for larger nozzles (i.e.(Panda, 1998), (Mitchell et al., 2012) and (Buchmann et al., 2011)). The oscillating nature was apparent when viewing the continuous movie files of the jets tested in this work.

Table 16, Mach disc reflection angle for low PR CNG, H_2 and 25%H_2/CH_4 jets.

	CNG	*H_2*	*25% H_2/CH_4*	*PR (P_o/P_a)*		
				8.6	***10.0***	***12.0***
α_{mean}	31.70	33.80	33.52	34.22	32.86	32.09

4.4 Chapter Summary & Conclusions

This detailed characterisation of low pressure ratio fuel jets issued from an automotive PFI injector results in the following key conclusions:

i. The normalisation of jet axial penetration is shown to be an area in need of continuous development where non-uniformities in properties were highlighted for CNG jets which transition across low, moderate and high underexpanded regimes. These bands exist for $NPR < 2,\ 2 < NPR < 4$ and $NPR > 4$ whose penetration rates are 2.90, 3.57 and 3.77 respectively, which are believed to be a result of the exclusion of other terms (i.e. temperature) in the nozzle diameter equivalent scaling method. This is also highlighted as a potential cause of the abscissa shift between CNG and hydrogen penetration-scaled jets. The differing penetration scales indicate that the isentropic assumptions across the nozzle exit and pseudo-nozzle diameter (Mach disc) may not hold true.

ii. The freestream and impinging jet behaviour is near identical for conditions up to the impingement surface. This confirms the use of free-jet assumptions up to the instance where the jet impinges.

iii. A novel triple-point jet width measurement is presented. It is shown that jet radial width at the location of the Mach disc, and hence the shear-layer thickness and local spread angle, is tied to the development of the compressible flow features. The interplay between compressible and incompressible structures are shown for the three gas fuels tested.

iv. Three spread angle measurement techniques have been used, with clear characterization of the jet angle throughout the whole delivery process. Once self-similar development is achieved the jets achieve a consistent spread-angle of c.a. 22.63°. This mean value is in close approximation to fully-turbulent steady-state jet theory. Prior to self-similar development the mean jet spread angle is twice as large as the self-similar value.

v. The growth time for both Mach barrel length and Mach disc diameter was measured with high temporal and spatial resolution.
    a. The temporal evolution is independent of PR and NPR.
    b. The fully developed Mach disc reaches steady-state size ~150 µs after the location (barrel length) has fully developed. This delay is independent on the

fuel type or delivery pressure ratio.

vi. The density of the gas jet is shown to influence both the barrel length and Mach disc diameter. The highest density fuels exhibit the longest barrel length and largest Mach disc diameter.
Once normalised by density ratio, the effects on the barrel length are reduced to a minor change in length. The variation, however, is still largest for the highest density ratio, indicating that effects are not fully captured in classical dimensional analysis. For an increase in density ratio, be it through pressure ratio or molecular mass (gas fuel type) changes, the Mach disc diameter will inevitably be larger.

vii. The Mach disc reflection angle has been characterized at high resolution, where it is shown that even before the Mach disc has fully developed the reflection angle remains constant within its oscillation period (27° to 39°) with a mean value of 31.7° recorded.

THIS PAGE IS INTENTIONALLY BLANK

5. High Pressure Ratio Results & Analysis

In the previous chapter that deals with low PR jets, the composition of the fuel was shown to transform the nature of the jet structure. The flow structures are reliant on the fuel composition and pressure/density ratio where substantial deviation in targeting and mixture formation has been shown, even at relatively low pressure ratios. The previous chapter provided a foundation for the techniques used in characterising transient fuel delivery and answers the first three research questions.

In contrast with Chapter 4, which covered $PR < 12$ jets, high PR CNG jets ($PR > 8.3$), with a particular focus on the $40 < PR < 400$ range are studied in this chapter. This PR range is expected to be closely aligned with conditions experienced in direct-injection gaseous engines. Detailed analysis on the freestream and impinging jets is provided for a holistic understanding of transient high-pressure fuel jet behaviour experienced in direct-injection engines. Experimental investigation of CNG jets issued at high PR is needed to increase understanding of the delivery (targeting and mixing) characteristics such as spread angle et cetera. Knowledge of the transient behaviour of fuel jets (as opposed to steady behaviour which is relatively well know) is crucial in developing appropriate strategies for fuel delivery in internal combustion engines.

The time available for injection and mixing is limited in gaseous DI engines; this necessitates either a high fuel delivery pressure or a large orifice opening area (e.g. needle lift). The injection process is governed by the fuel rail pressure and to a greater extent the electro-mechanical operation of the fuel injector. For the typical solenoid units, the opening and closing actuations are fixed. The proportion of this transient opening/closing time is still quite low (5%-16% of the fully open period), but at late injection operation the ignition time occurs during the early delivery period. Thus knowledge of this period of flow development is crucial for engine operation.

In accordance with the research objectives of high-pressure CNG jet characterisation pertaining to; *the targeting and dispersion behaviour of the gaseous fuel jet* and *the transient jet behaviour in the nearfield.* Additionally general inference on the *effects of the jets on the in-cylinder flow and turbulence* is also provided – this third objective is covered at length in Chapter 6. Keeping with these objectives, Chapter 5 answers the following research questions:

3. *How do the shock phenomena affect the internal structure of the fuel jet and the surrounding regions immediately after jet delivery?*

4. *How does a high pressure-ratio influence the jet flow-characteristics and the mixture process?*

As in *Chapter 4: Low Pressure Ratio Experiments*, the results and discussion include separate sections on the macro and nearfield structures. This segmentation allows independent discussion of the global objectives around fuel delivery targeting and mixture preparation.

5.1 General Results Introduction

Representations of freestream and impinging jets are depicted in Figure 108 and Figure 109 respectively. General observations are made for both as an introduction to the images used in quantitative processing and discussion. The freestream jet is quite slender in nature and the nearfield underexpanded region appears to vary in size; the largest barrel-like structure is seen in the fourth image of Figure 108. The jet progresses at a very fast rate, extending to a substantial downstream distance in a short amount of time (the nozzle outer diameter is 7.87 y/d). The left side of an impinging CNG jet is shown in Figure 109 where for a fixed acquisition instance ($t = 976$ µs aSOI) the effects of an increasing ambient pressure are shown. The jet here disperses at a slower rate, at which a greater concentration is apparent for the lowest PR (far right image).

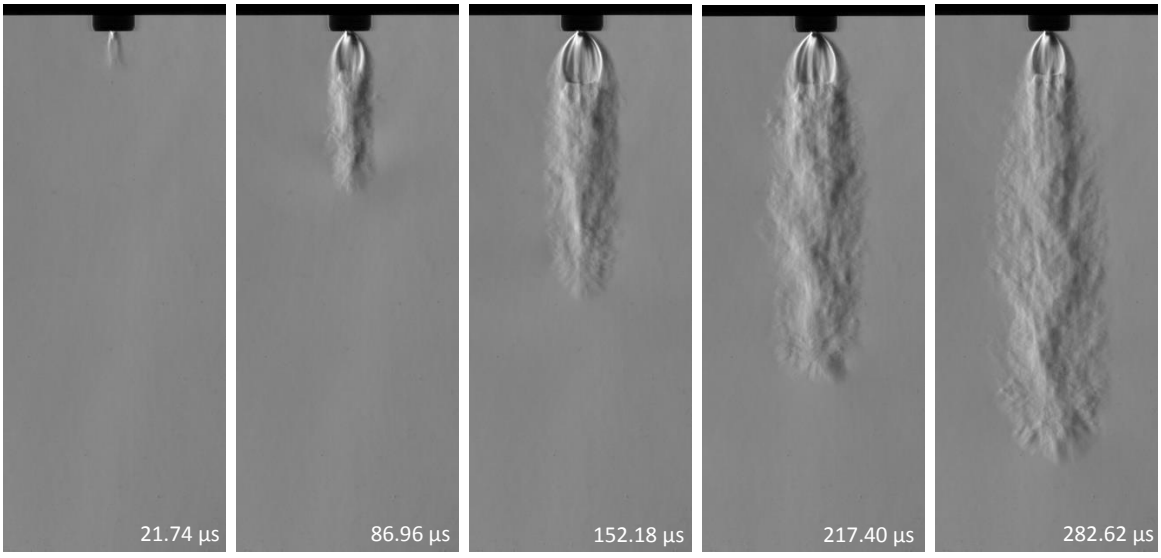

Figure 108, Freestream PR400 CNG jet sequence. Every forth image presented.

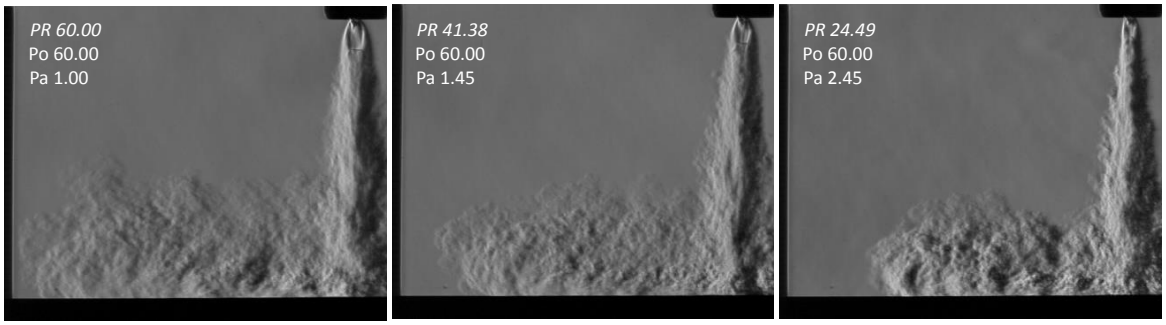

Figure 109, High PR CNG jets impinging at 976 µs aSOI for an increasing ambient pressure.

5.2 Macro Structures

5.2.1 Axial Penetration

Accurate prediction of the jet tip location at high PR is crucial to fuel delivery targeting. At high velocities, even a small change in delivery time can lead to substantial displacement of the fuel jet. Whilst the gradient change between PR scenarios, seen in Figure 110, does not appear dramatic, the consequence of even a small change in jet axial location can significantly affect the mixture formation process. The criticality is highlighted if a stratified combustion mode is operated, in which plumes of fuel are required to contact specific piston-bowl locations (not only for combustion but for flow processes, owing to the oxidization of soot).

Figure 110 shows that the penetration rate is proportional to the PR, as anticipated. The data at the lowest PR are also aligned, in scale, to the work of Johansen et al., (2013), who used a similar experimental configuration albeit with Helium. For the data presented, the early development region ($t^{1/2} < 12$), where the correlation between PR and x/d location is diminished is a potential concern for universal normalisation. The accuracy in defining the jet tip was not lost for these scenarios but considering the very high-speed nature of the jet immediately after release, some resolution would have certainly been lost due to the fixed imaging speed (FPS) and exposure duration. Similar trends regarding this discrepancy were also observed in the impinging scenario prior to contact ($x/d < 30$). Regardless, the effects of low outright PR correlation are largely inconsequential at these very early aSOI times. It should reiterated that the zero time instance is indeed defined from the image prior to when the jet is first present. This method produces the shift in abscissa as seen in the several following figures.

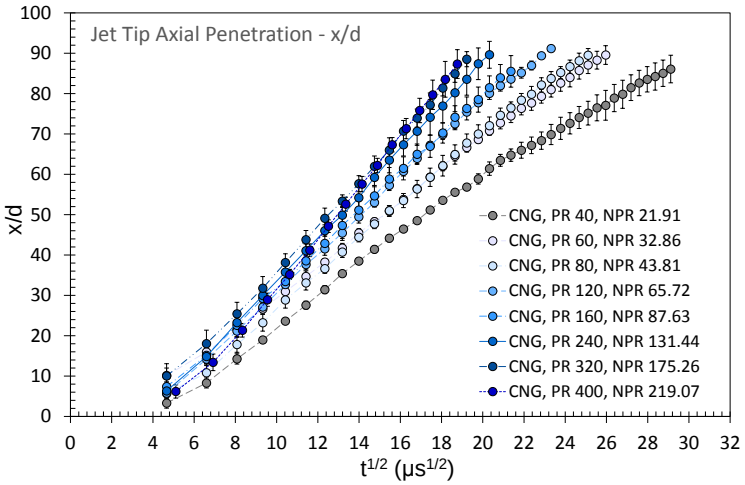

Figure 110, High PR freestream CNG jet tip axial penetration.

The diameter equivalent model defined in Equation 22 is employed in an attempt to collapse the wide range of upstream $(26 < \rho_o < 65)$ and ambient $(0.29 < \rho_a < 1.15)$ delivery conditions. With the exclusion of PR40, all other scenarios scale with good agreement as shown in Figure 111. It is seen that the PR40 case deviates from single line at the early stages of development. The remaining cases align linearly with the scaling law where a mean and median deviation of 2.78% and 2.12% were observed. This scaling provides good agreement that overall the nearfield structures (i.e. Mach disc location) play a normalised role in the overall penetration length. No deviation in scaling was observed indicating that once a highly underexpanded regime is formed ($NPR > 4$) no further changes in nearfield structure are observed and that any secondary effects not captured in the scaling term are in-proportion to the jet development and isentropic terms used. The accurate prediction of the jet penetration using fundamental parameters (nozzle diameter, sonic velocity and density) provides universal prediction of fuel delivery for most foreseeable single round orifice conditions. Most importantly, the angle of the slope ($\Gamma = 3.19$) is in agreement with the literature range reported previously (i.e. (Hill and Ouellette, 1999)).

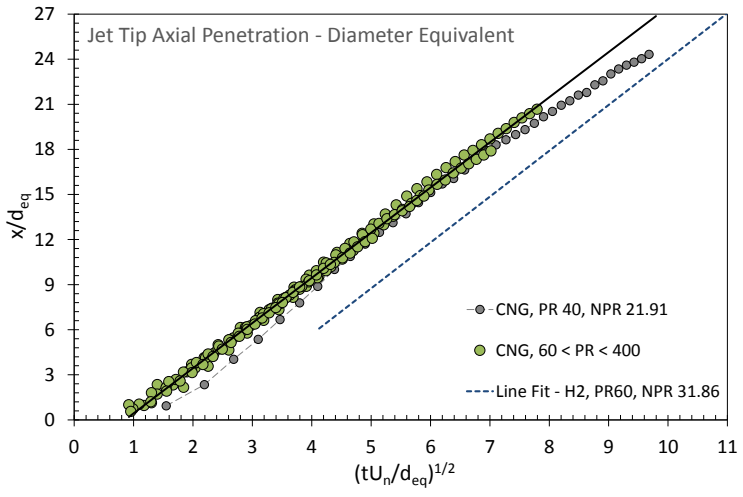

Figure 111, Diameter equivalent scaling of freestream high PR jets. *(Error bars withheld for visual clarity).*

A scaled hydrogen jet (PR60) is also included in Figure 129, where the penetration rate ($\Gamma = 3.24$) is approximately the same to the high density CNG jets albeit with a time (abscissa) offset. The time offset is predicted to be influenced in any misrepresentation through isentropic relationships in both the nozzle exit velocity (U_n) and the nozzle exit density (ρ_e). Similar observations were seen for the low PR cases.

The axial velocity, a function of the jet tip penetration, is calculated for each individual schlieren frame relative to its preceding frame. This is termed the integrated method and should yield a relatively close value to an instantaneous jet velocity but is limited by imaging frequency and actual jet velocity. These results coincide with the axial penetration characterisation shown below in Figure 112. It can be seen that a $\sim 100\, m/s$ band is present between the PRs tested for $9.32\ \mu s^{1/2} <$

$t^{1/2} < 19.22\ \mu s^{1/2}$. The overall high velocities are not unexpected given the extent of the jet pressure ratio and their respective core velocities immediately after exit.

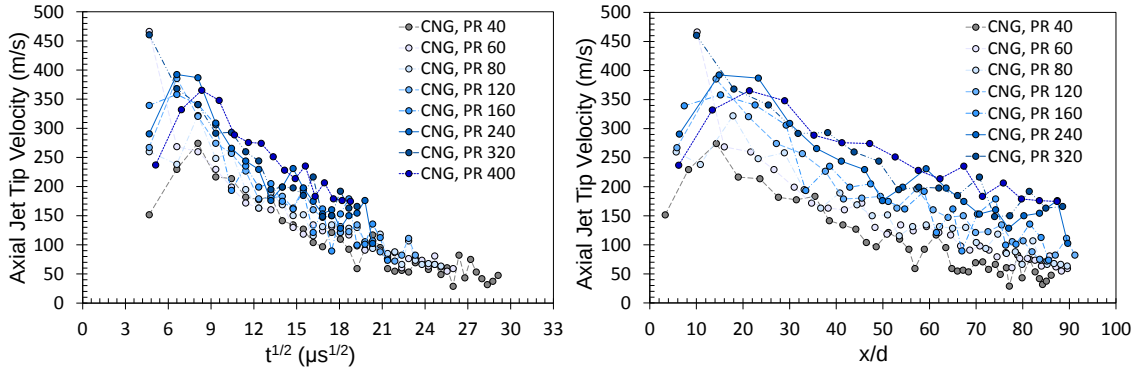

Figure 112, High PR Freestream CNG jet integrated axial velocity.

Whilst the trend in velocity decay is self-evident, the absolute values should be taken as largely indicative. The uncertainty in magnitude, particularly at early aSOI, is due to the absolute imaging scale, $x/d \approx 90$ and relative pixel resolution, for the fast-moving jets.

The increase in velocity in the early development region is a direct result of the impulsive momentum injection of the jet corresponding to the delivery profile of the injector. This initial increase has been observed in similar studies (Yu et al., 2013a). The initial change in velocity is reflected in the jet-tip acceleration, where there is the strongest positive acceleration component (Figure 113). After the initial period, all jets decelerate, in line with the decaying velocity. This is in line with the expectation that the jet tip, continuously moving further downstream from the orifice, is fed with less momentum from the supply and greater interaction with the ambient environment takes place.

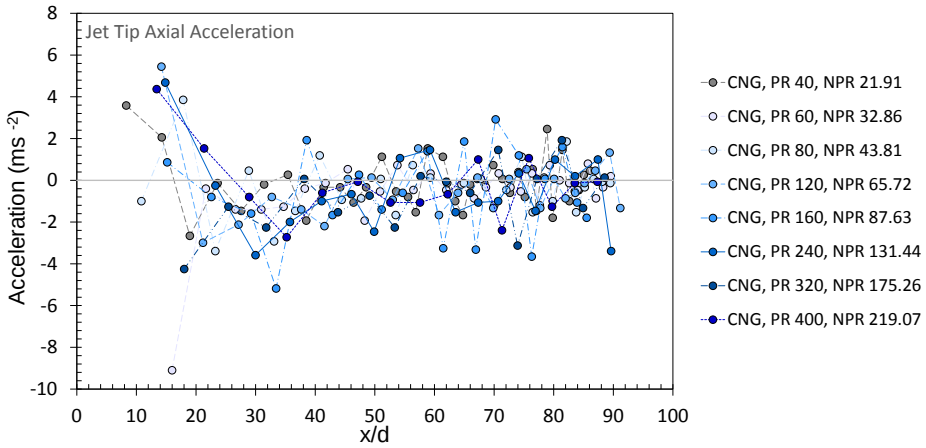

Figure 113, High PR CNG freestream jet tip acceleration.

In addition to the previous integrated velocity (and acceleration) methods, a global axial velocity profile is presented. This method takes no account of the preceding jet-tip location; instead, the

axial jet-tip location is divided by the total aSOI time. Again, all conditions show an initial increase in velocity except for the PR60 and PR320 scenarios.

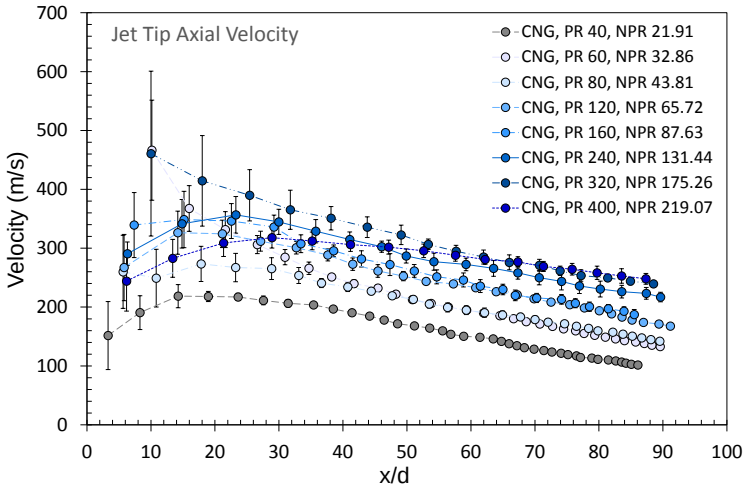

Figure 114, High PR CNG freestream global jet velocity.

Comparing the two velocity methods (Figure 115) for the lowest and highest PR scenarios, one can distinguish that for the first four measurement points the integrated velocity is substantially higher than for the global method; thereafter the profiles cross over, the inverse is true. The difference for the PR400 and PR40 cases between the two methods is 23% and 33%, respectively, a substantial variance considering the significance of the axial velocity in fuel targeting.

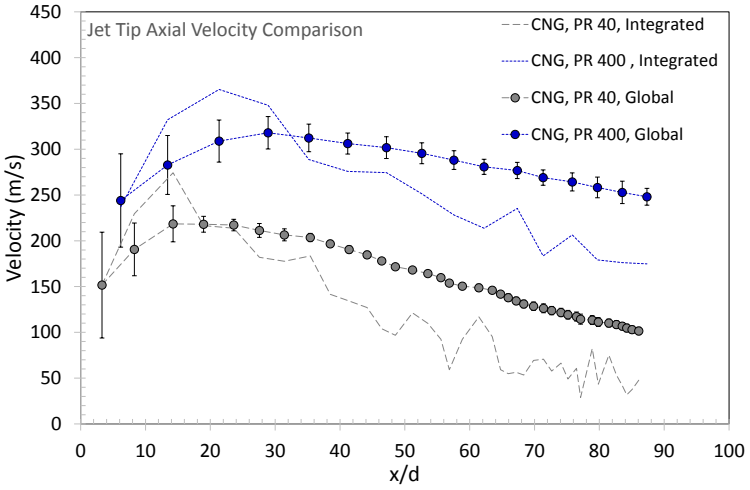

Figure 115, Freestream jet velocity measurement comparison for high PR40 & 400 CNG jets.

5.2.2 Radial Penetration

The radial jet profile is typically sidelined in fundamental studies which provide little information about geometric development. This aspect, however, is particularly useful for SI ICE considerations, where in stratified mode the fuel is ignited at the jet periphery. Through depiction of the radial penetration alongside other key radial areas (i.e. triple point jet width and spread angle) one can establish a reliable profile relative to physical engine geometries (i.e. spark plug electrode).

Here we find a similar scenario to the axial penetration where the higher PR cases don't necessarily equate to a greater radial penetration in the very early stages of jet development (Figure 116, left). Interestingly if the time domain is swapped for the spatial domain ($axial\ penetration$: x/d) the resultant order is fairly mixed. There is a strong correlation, however, between y/d and x/d, where a linear fit gives good representation for each of the PR cases, with the best agreement after $x/d > 30$ where self-similarity is realised (discussed subsequently).

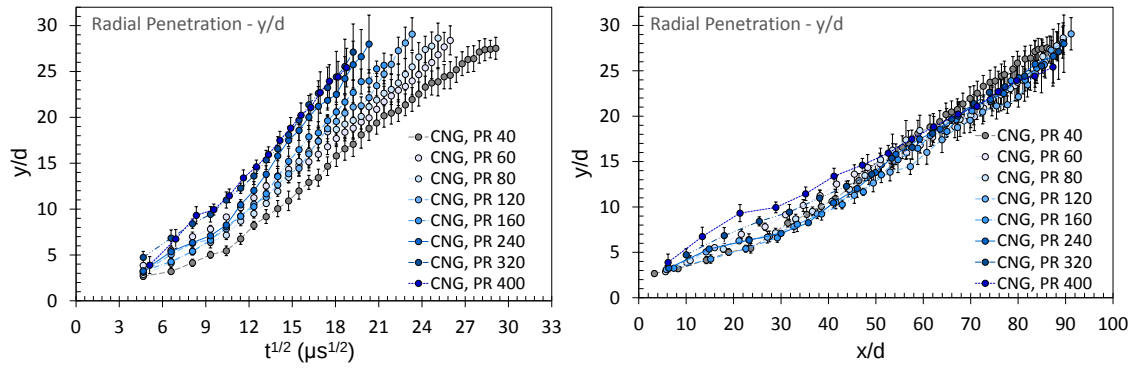

Figure 116, Freestream radial penetration for high PR CNG jets.

It can be seen that the maximum radial penetration appears to be function of axial penetration, and thus the injected mass delivery rate. In an attempt to collapse this relationship to an empirical term, the radial penetration is presented using the diameter equivalent model. Using the method the radial penetration is observed to develop non-linearly. However, if only the self-similar development locations are considered, than a linear profile is observed. These results are seen in Figure 117 left and right plots respectively.

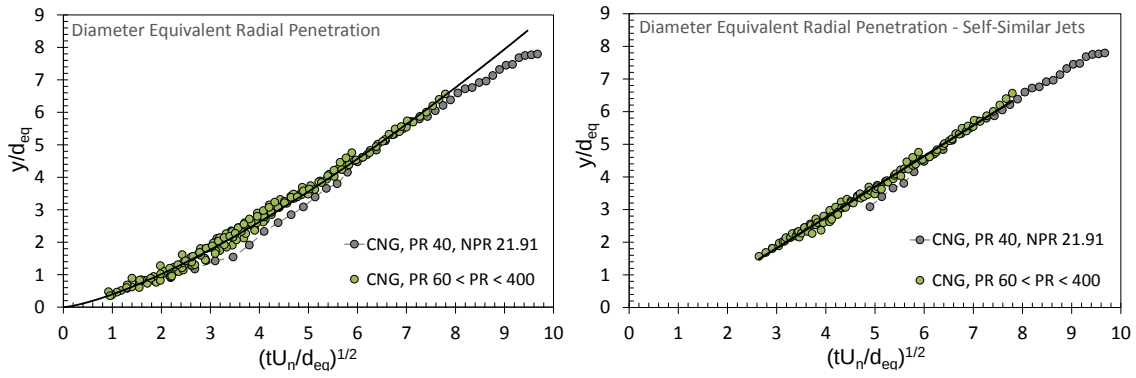

Figure 117, Diameter equivalent scaled radial penetration for high PR CNG jets (left) and for self-similar jets only (right).

The simplified power-law and linear relationships for the radial penetration are presented as the following expressions. The mean variance between measured and predicted values for the power-law and linear expressions are 6.64% and 5.51% respectively where an R^2 of 99.24% was also observed for the linear fit.

Equation 71, Power-law curve fit for high PR CNG jets.

$$\frac{y}{d_{eq}} = 0.39\left(\frac{tU_n}{d_{eq}}\right)^{1/2}$$

Equation 72, Linear fit for high PR self-similar CNG jets.

$$\frac{y}{d_{eq}} = 0.94\left(\frac{tU_n}{d_{eq}}\right) - 1$$

These results are not surprising given the dependencies of jet development on the PR and thus the massflow rate injected. The use of the diameter equivalent model, yet again for a single fuel type, provides a reasonable means to collapse the jets under consideration. As shown here and as discussed in subsequent sections (projected area, spread angle), the jet targeting behaviour is predictable and in line with classical theory of turbulent free jet development.

The radial velocity is presented as the mean of the two largely axisymmetric jet halves, thus the velocity is the total radial growth at the maximum jet width location. These values are presented in Figure 118, in the form of time (left) and jet axial location (right). Unsurprisingly, the velocity profile is largely asymptotic with largely consistent values when $x/d > 30$.

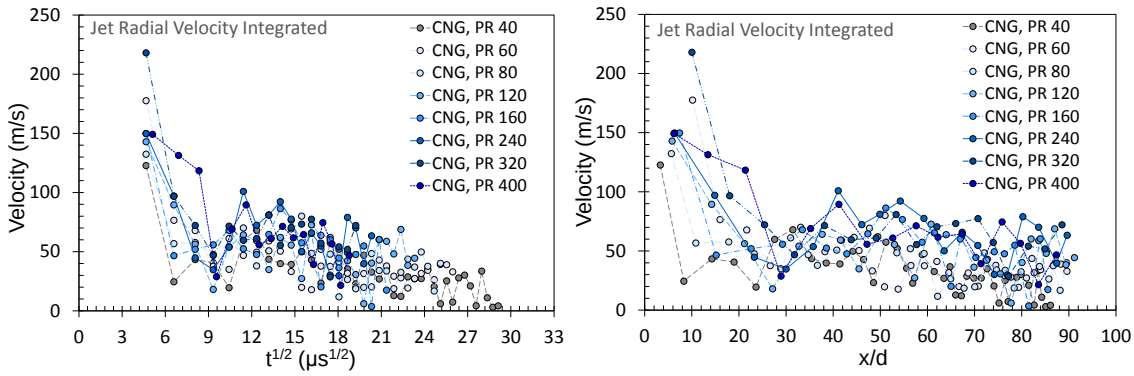

Figure 118, Freestream radial velocity for high PR CNG Jets.

5.2.3 Spread Angle

The difficulty in accurate spread angle measurement is further increased in the high PR cases. The nearfield compressible structures, involving several nozzle diameters downstream significantly shape the radial structure of the jets. Again, as with the low-PR experiments three measurement methods were employed (cumulative mean angle up to: 33%, 50% and 70% of axial penetration), with the intent to segment the jet for a clearer depiction of the geometric structure.

The 33% measurement ("Third Mean") method provides the clearest view of the role of PR where a uniform increase in spread angle is observed. Moreover, for this measurement location there is a high consistency in the measurement values across the jet development period ($6.3 \lesssim x/d \lesssim 90$). This method provides direct insight into nearfield spread which is derived from the accelerating gas and hence the barrel shock structure, which is PR-dependent. These trends are in contrast to those obtained using the 50% and 70% methods, where for the most part there is no clear dependency on PR and less consistent values across the measurement range. This is largely expected as these methods incorporate a large portion of the jet where excursions in larger spread angles (i.e. the angle up to the location of the Mach disc) are reduced once averaged. This is why PR dependency is non-existent for the 50% and 70% methods. Additionally, as the jets develop toward a self-similar, steady-state flow profile, the mean jet spread angle should converge to a stable value. The three methods are depicted in Figure 119:

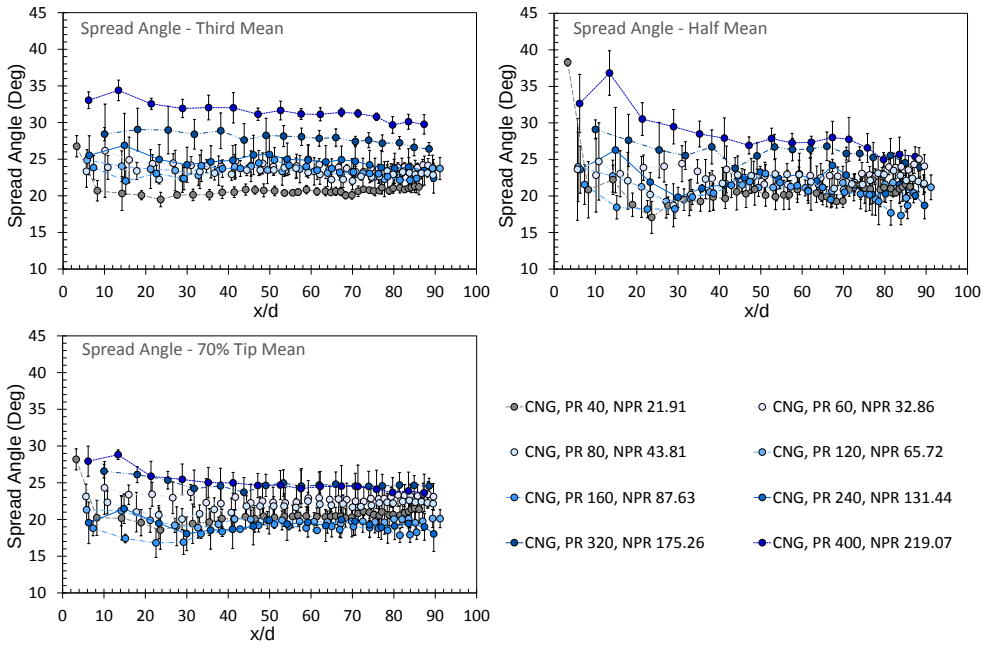

Figure 119, High PR freestream spread angle captured up to 33% (a), 50% (b) and 70% (c) of the jet tip.

Collapsing all three spread angle measurement methods ($33, 50\ and\ 70\%\ x/d$) and considering jets developed beyond $x/d > 20$ are presented in Figure 120. It is immediately evident that under these circumstances the spread angle does not strongly correlate with PR. There is generally good correlation, however, for the 33% (Third Mean) measurement. Whilst there is no consensus for gaseous spread angle measurement the absolute spread angle range on average for jets developed beyond $x/d > 20$ is a mere $6°$ over a ten-fold increase in PR. With the mean spread angle value for these freestream CNG jets equals $23.33°$, within the commonly reported range of circa $24°$ for gaseous jets (i.e. (Mohamad et al., 2010)). This is also in agreement with the previous discussions (Section 2.6.2.3) that the spread angle should not change once fully-turbulent conditions are reached – with the Re_{exit} value reaching a maximum of $\sim 9.91 \times 10^5$.

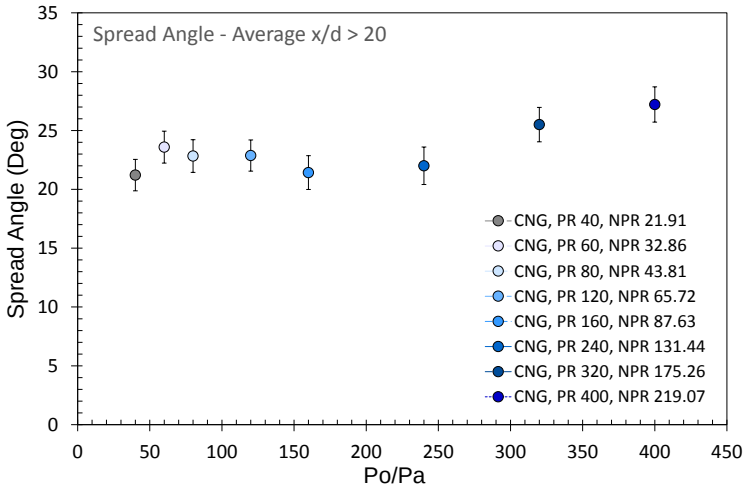

Figure 120, Mean spread angle for freestream high PR CNG jets.

5.2.4 Projected Area

The reporting of projected jet area is typically aligned to the axial and radial development profiles and is useful in determination of dispersion and fuel-to-cylinder occupancy. It can be seen in Figure 121 that the projected area growth rate is strongly correlated against PR when considering evolution for aSOI. The high-PR jets disperse and occupy a significantly greater footprint than their lower pressure ratio counterparts. A very different outcome is observed when the area is normalised to axial development. This indicates that the velocity of the jet (linked to the PR as discussed earlier) substantially influences the dispersion rate. Moreover, a clear collapse of the data is present once the velocity component (time base) is removed, as per the right-hand graph in Figure 121.

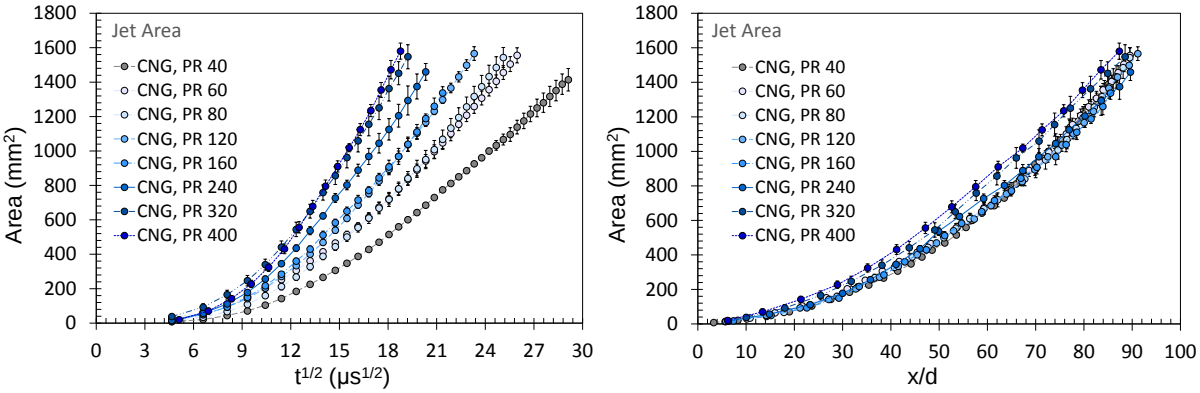

Figure 121, Projected jet area for freestream high PR CNG jets.

The profiles of jets excluding the two highest PR scenarios collapse to a good fit as expressed below in Figure 122. Currently it is not understood why this agreement doesn't fully extend across the entire range of experiments. The delay in achieving self-similarity may indicate why the PR320 and PR400 do not fit the proposed relationship.

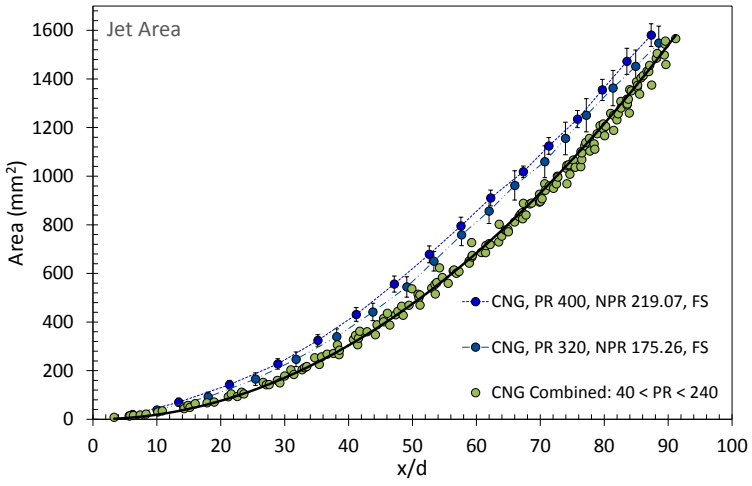

Figure 122, Projected area with polynomial curve for 40 <PR < 240 CNG jets.

The best fit for the combined series results in a polynomial fit with a mean and median variance in experimental data of 3.67% and 2.39% respectively, according to the following expression:

Equation 73, Projected Area for 40<PR<240 CNG Jets using best fit.

$$Projected\ Area_{40<PR<240} = 0.1866\left(\frac{x}{d}\right)^2 - 0.0613\left(\frac{x}{d}\right) + 11.544$$

A more succinct relationship is still appropriate and is provided in Equation 74. When considering the jet area for development beyond $10x/d$, the mean and median variance in experimental data of 4.61% and 2.42% respectively. This relationship is shown as the black solid-line in Figure 122.

Equation 74, Projected Area for 40<PR<240 CNG Jets using a generalised fit.

$$Projected\ Area_{40<PR<240} = 0.19\left(\frac{x}{d}\right)^2$$

A parabolic fit has previously been shown to correspond to the volumetric growth determined by air entrainment in subsonic transient jets (Cossali et al., 2001). Another meaningful and similar empirical relationship is derived for the growth and dispersion rate for impinging jets. This is discussed in Section 6.1.

5.2.5 Self-Similarity

Using the self-similarity expression (Equation 20), the point at which the jet becomes self-similar (a good indicator of flow development) was calculated; this is presented in Figure 123 below. A transition phase is present starting from $20 < x/d < 30$, with the self-similarity behaving asymptotically thereafter. This developmental position agrees with previous discussions on the geometric development trends (i.e. radial penetration velocity). It is interesting to note that the self-similarity for all series conforms around the same time aSOI; $t^{1/2} \cong 13\ \mu s^{1/2}$ regardless of the propagation speed (governed by PR and mixing rate). This was also observed for the low pressure ratio cases where self-similarity was achieved around $t^{1/2} \cong 15\ \mu s^{1/2}$, however the axial penetration length of the high PR cases is slightly greater by $< 12x/d$. The axial development length of the high PR CNG jets is in close agreement with previous studies (i.e. (Johansen et al., 2013).

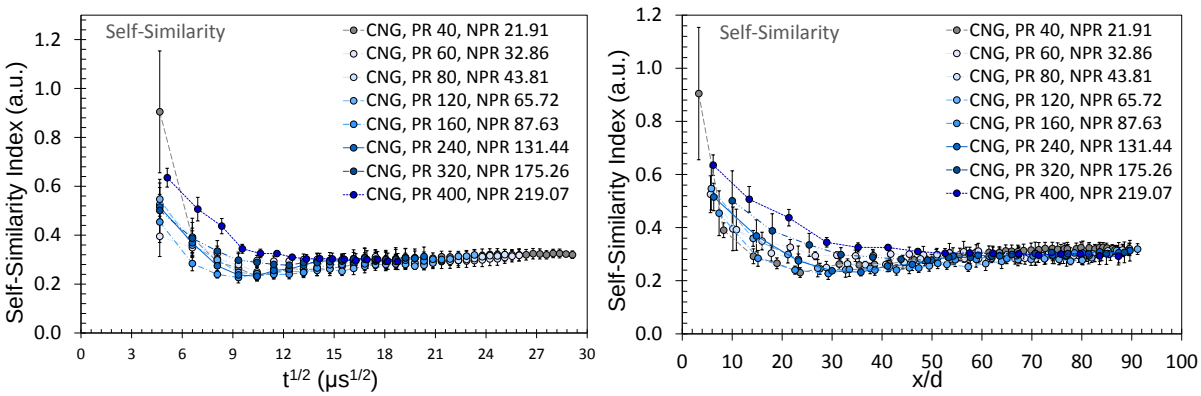

Figure 123, High pressure CNG self-similarity development; spatial (left) and temporal (right).

Moreover, the self-similarity index, s, is in good agreement with literature on transient-turbulent jets where a range of 0.25 ± 0.05 is given ((Hill and Ouellette, 1999) using the data of (Rizk, 1958)). Slightly greater values were observed by Johansen et al., (2013) where a mean range of 0.37 was presented. For the results presented in Figure 123 it can be observed that s asymptotes to a mean value of $0.29{\sim}0.30$ for $x/d > 20$ or $t^{1/2} \cong 13\,\mu s^{1/2}$, where the $0.7\% < \sigma_{Mean} < 1.3\%$. The agreement with self-similarity correlates to the previously discussed axial penetration scaling laws. This completes that physical dependence statement by Hill and Ouellette (1999) where the jet tip penetration is a function of; maximum radial development, time, exit momentum flow rate and fluid density.

5.3 Nearfield Structures

The importance of measuring and predicting the nearfield structures and geometry is exemplified when delivery PRs are substantially large. The larger compressible flow structures are a direct consequence of the high PR employed and accordingly the incompressible flow behaviour is also affected. Knowledge of the nearfield region processes is crucial for engine-based applications in which close-spaced geometries are employed. Moreover, the nearfield region plays a significant role in the spectrum of jet delivery and mixing behaviour. This section focuses on the nearfield structures, compressible or otherwise, and relates their influence back to the macro structures, with an emphasis on the transient domain.

Examples of the effects of varying delivery PR are shown qualitatively in Figure 124, which depicts marked differences in the region immediately after the nozzle. Typically, images of this nature are shown for much larger nozzle orifice diameters and even more seldom for transient flows. Additionally, Figure 125 depicts the early development region of a freestream jet. Several features are clearly visible. A strong bow shock leads the vortex head and is in fact in line with the jet tip for these early aSOI times. The transition between moderate and high underexpansion is also visible, where in the $t = 112.5\ \mu s$ from the repeated shock diamonds in the core have subsided from view. This is also in line with the physical dominance of the first Mach disc.

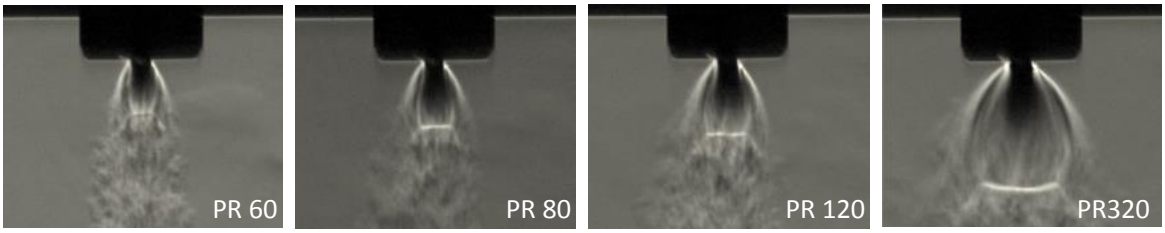

Figure 124, Nearfield high PR (60, 80, 120 and 320) shock structures at $t^{1/2}$=26.7 $\mu s^{1/2}\ aSOI$.

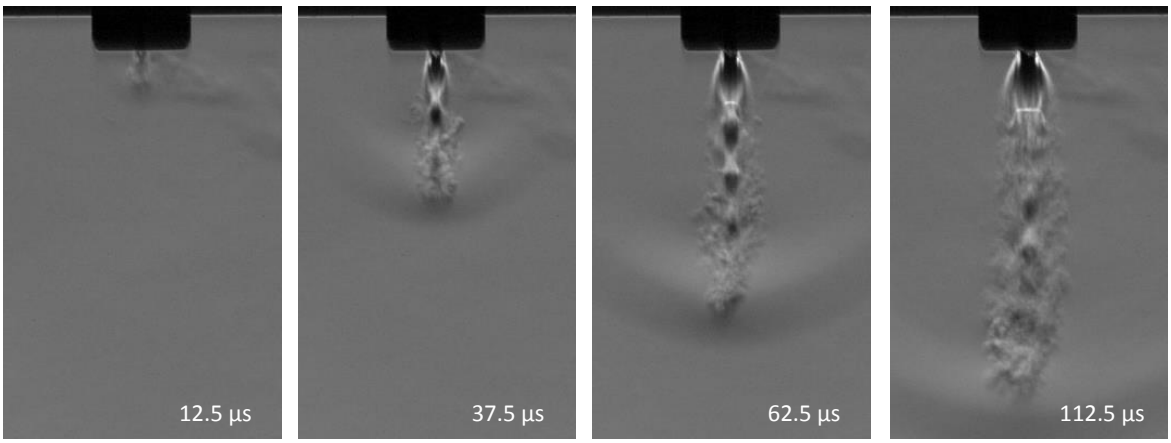

Figure 125, Freestream evolution of a PR120 CNG jet. Time stamp indicates aSOI.

5.3.1 Barrel Length

Through obtainment of the barrel length in conjunction with the Mach disc diameter (and other nearfield features, i.e. shear-layer thickness at the triple point) a fairly accurate depiction of nearfield conditions can be acquired. This information is not only useful in accurately identifying supersonic and subsonic flow velocity areas (before and after the normal shock, respectively), but also for spatial information needed for fuel delivery targeting. This spatial targeting information is needed to determine if the jet would encroach on the spark-plug and to this end may also determine the angle and orientation of the fuel injector.

The evolution of the Mach disc has rarely been analysed in modern literature, with very few investigations on the subject ((Lacerda, 1987, Maté et al., 2001)); the majority of the literature concerning steady-state jets. This work provides a highly resolved characterisation of the highly underexpanded compressible phenomena for a high-PR transient jets issued from a small nozzle.

The evolution of the barrel length is evidenced in Figure 126. The measurement of the barrel length was taken from the first appearance of the feature until a substantial downstream value, typically $t > 1600\ \mu s\ aSOI$. As with the low-PR experiments, the transient behaviour of the compressible flow features is captured in high resolution.

Interestingly, the compressible-flow formation process was not as predicted nor as seen per the low-PR scenario. The jet undergoes a process where the growth of the shock structure is normal: the normal shock increases with time and nozzle exit pressure stabilization but reaches a maximum at $t^{1/2} \cong 13.2\ \mu s^{1/2}$, after which a decrease or contraction occurs to $t^{1/2} \cong 17.2\ \mu s^{1/2}$, followed by a slow increase and then a largely stable period. The process is akin to a step-change response curve with a medium amplification overshoot and a moderate settling time. This process is seen for all experimental cases where an increase in magnitude is proportional to the PR.

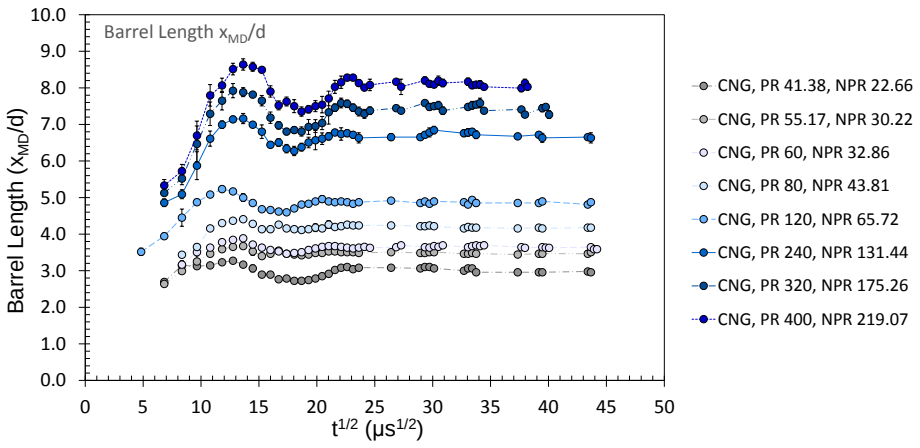

Figure 126, Barrel Length of high PR CNG jets.

It is not confirmed at this stage what the underlying factors are for the response-curve like behaviour. It is, however, likely that the needle lift is a key contributor. Recalling the injector needle lift measurement initially depicted in Figure 52, the profile of the needle lift is coincidental to that of the shock features. Whilst the lift profile shows no post-maximum undershoot, in fact the opposite is present: the remaining profile is indicative of the flow behaviour observed.

To illustrate the correlation between lift profile and barrel length, the average collapsed barrel length profile for a range of high-PR jets ($41.38 < PR < 400$) was plotted alongside the needle lift profile (see Figure 127). The average profile does give a good representation of the indicative barrel evolution, some minor perturbations are smoothed over. Two selected individual cases (PR55.17 & PR240), show exceptional correlation against the lift profile, albeit with a temporal phase shift of $t^{1/2} \approx 4.87\ \mu s^{1/2}$. This shows that whilst on average the smaller dependencies are potentially smoothed out in averaging (keeping in mind the needle lift profile is subject to case-by-case operation), there is enough evidence to suggest that the needle lift profile does strongly influence the nearfield Mach disc formation. The two individual cases indicate that the correlation applies in pressure conditions for both higher and lower than ambient P_a conditions.

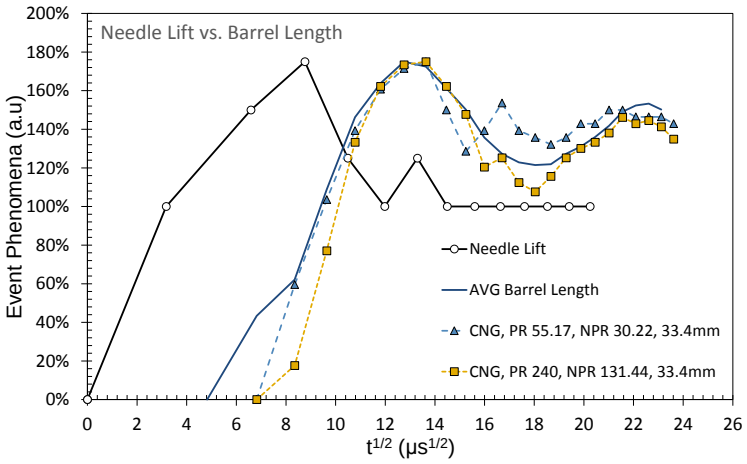

Figure 127, Needle lift profile versus averaged barrel length evolution in the unsteady region.

For all CNG cases presented, the barrel length appears to become settled for $t^{1/2} > 24.58\ \mu s^{1/2}$, with constant values thereafter. These values were averaged and compiled with normalisation to their respective $\sqrt{Po/Pa}$ values. Figure 128 presents a linear progression of barrel length against PR. A highly linear correlation exists, $R^2 = 0.996$ and a mean variance from the measured values and the linear fit of 2.17% (x_{MD}/d).

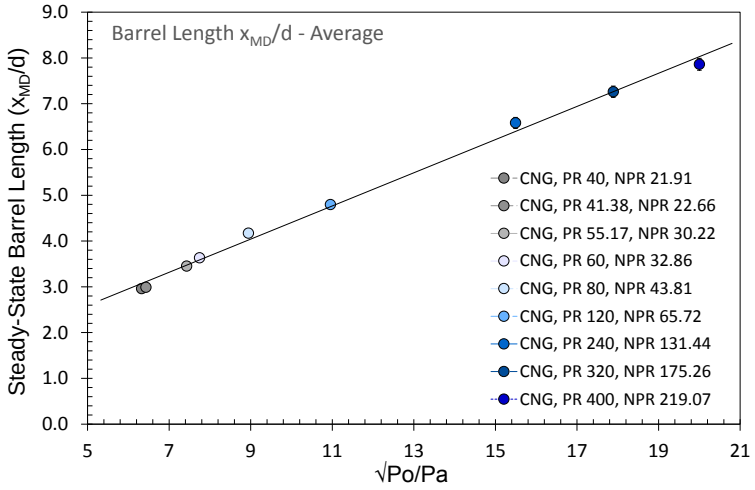

Figure 128, Average steady-state barrel length for PR normalised CNG jets.

The steady-state barrel length is thus represented by the following expression:

Equation 75, Steady-state barrel length expression for high PR CNG jets.

$$\frac{x_{MD}}{d} = 0.3625\sqrt{\frac{P_o}{P_a}} + 0.7788$$

From the above expression, it can be seen that the C_x term, the gradient, is approximately half of the commonly reported value for steady-state jets 0.60-0.65 (for example (Addy, 1981, Ewan and Moodie, 1986, Maté et al., 2001, Vuorinen et al., 2013)). Inspection of the developing and developed C_x values, (as expressed in Equation 15) reveals little where the values are inversely proportional to PR and follow the evolution of the barrel length. These trends are shown in Figure 129.

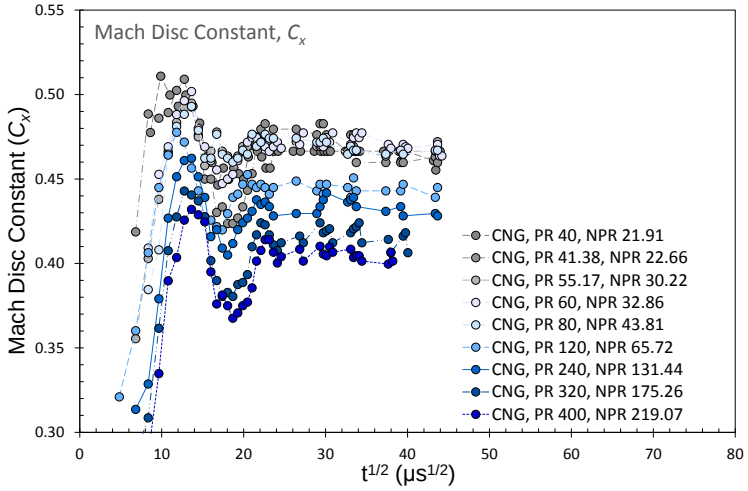

Figure 129, Individual Mach disc location constant (C_x) for high PR CNG jets.

As previously discussed, the temporal and spatial behaviour of the compressible structures is heavily influenced by the needle position and in turn the mass flow rate of fuel delivered. These effects were also in proportion to the delivery PR. To further understand the dependencies of barrel length formation, steady-state PIV images were acquired and compared to the schlieren measurements.

5.3.1.1 Barrel Length: Injector Needle and Internal Geometry Effects

To further substantiate the effects of the needle and thus the internal injector geometry on nearfield shock structure, in-jet velocity maps were measured using PIV. An identical DI injector was fitted with a similar (identical apart from any operational wear or manufacturing tolerance) $1\ mm\ \emptyset$ $(2l/d)$ brass nozzle. The needle-ball and needle-shaft were removed, allowing a constantly open orifice free of internal obstruction.

Experimentally, the arrangement consisted of a CNG fuel supply seeded with $0.100\ \mu m$ TiO_2 particles illuminated with two laser pulses separated in time by $0.250\ \mu s\ (dT)$. Through analysis of the axial centerline velocity profile, the location of the Mach disc (barrel length) is clearly discernible. The location of the Mach disc is situated at the centerline maximum peak velocity – the location at which the velocity starts to fall significantly as the particles pass through the normal shock. This method of defining the normal-shock location has been used in several experimental works for moderately and highly underexpanded jets (Mitchell et al., 2007, Chauveau et al., 2006) and recently as a comparative variable in numerical models with similar context to this work (Bonelli et al., 2013).

For three PRs the centreline velocity $(v, m/s)$ profile was extracted from an ensemble average of 150 PIV measurements. To aid in comparison, each velocity profile was normalised by its maximum velocity. This results in placing all maximum velocities on the same plane where the shift in axial location x_{MD}/d was then compared. It can be seen from Figure 130 that for the needle-less, steady-state operating conditions, x_{MD}/d increases with PR. This was of course expected due to the highly influential PR dependency discussed previously.

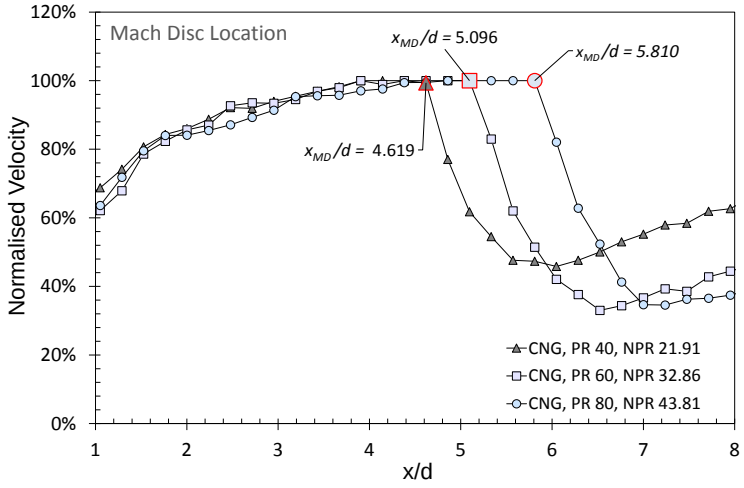

Figure 130, Mach disc location of needless steady-state DI CNG Jets using PIV centreline profile.

Studying x_{MD}/d for a fixed PR of 60 using PIV revealed that the location is indeed subject to operational phenomena (needle position or the actual massflow rate). As shown below in Figure 131, at various $aSOI$ times x_{MD}/d may differ. More importantly, for steady state conditions, $1141\ \mu s\ aSOI$ and the needle-less case ($aSOI > 2000\ \mu s$), a markedly different Mach disc location was observed. The needle-less steady-state condition is $1.56\ x_{MD}/d$ ($\sim 45\%$) greater than the regular steady-state condition - a significant change. This confirms that even during constant massflow other factors dictate the location of the Mach disc. Thus, the internal injector geometry is likely to influence these flow structures, be it through lowering the mass flux or where the internal upstream shock structure is influenced by the physical boundary (as seen in (Hatanaka and Saito, 2012) for numerical conditions and as discussed previously).

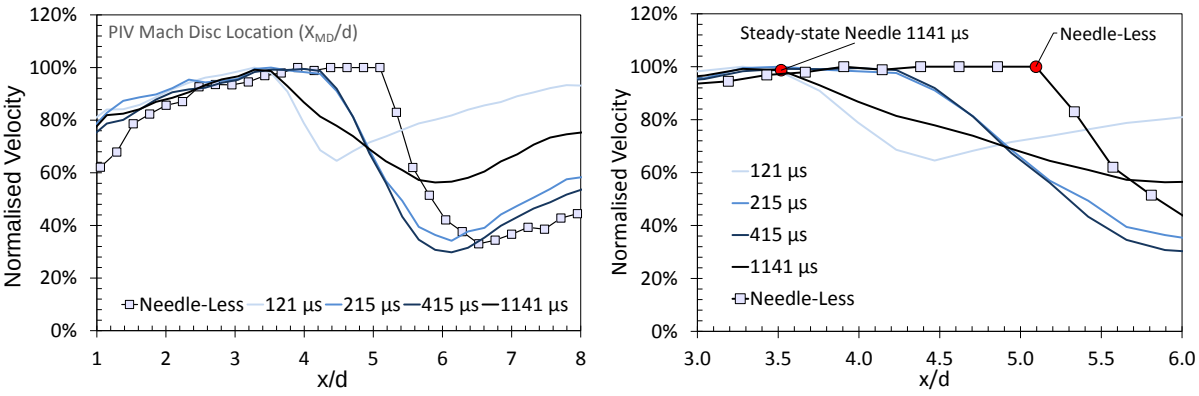

Figure 131, Comparison of PIV Mach disc location for PR 60, Needle and Needle-less injection. Right figure is an enlarged view of the left where red circle markers indicate Mach disc location for the needle and needless comparison.

The only condition which satisfies the classical Ashkenas and Sherman (1966) relationship is the needle-less scenario (within a previously reported range; $C_x \approx 0.67$). All other conditions, across the transient and steady-state period, show a significantly lower correlation. Since the experimental data reported in the literature represent a broad cross-section of massflow conditions with generally

good agreement to the Ashkenas and Sherman (1966) expression, with none expressing a restricted internal geometry, it is unlikely that the cause of the discrepancy reported here is solely massflow-based. Hence the physical influence of the needle ball imposed at nozzle entry is likely to be a key influence on Mach disc location.

The PR60, peak-velocity locations are displayed in Table 17 below. Whilst not perfectly aligned, the PIV results are highly comparable to the schlieren HSV measurements. For this example it is found that the mean variance between the two methods yields a 7.0% discrepancy or $243\ \mu m$ in real terms. Typically, it was found that the schlieren method led to longer barrel length measurements. This discrepancy in location is reasonable, as the thickness, curvature and oscillation of the Mach disc add to the measurement uncertainty. The schlieren processing accuracy ($\pm$ 2 pixels: $100\ to\ 200\ \mu m$), interpolation of location values between schlieren frames (refer Figure 175 and Appendix VIII) and of course any PIV particle relaxation effects induced at the onset of the high-velocity gradient increase uncertainty further.

Table 17, Mach disc location for a PR60 CNG jet at various aSOI times and a needle-less condition.

	Mach Disc Location PR60				
	121 µs	***215 µs***	***415 µs***	***1141 µs***	***Needle-less***
$PIV\ x_{MD}/d$	3.281	3.518	3.993	3.518	5.096
$PIV\ C_x$	0.424	0.454	0.515	0.454	0.658
$HSV\ x_{MD}/d$[10]	3.663	3.655	3.649	3.627	-
$HSV\ C_x$	0.479	0.472	0.471	0.468	-

Particle addition to underexpanded flows has been shown to influence the location of the Mach disc. It was found that the particle concentration decreased x_{MD}/d by up to $\sim 1 x_{MD}/d$, with the reduction also dependent on the particle diameter (Sommerfeld, 1994). The conditions investigated in Sommerfeld's work had some similarities to those in the current work (high-PR and relatively small nozzle diameter), however, particle size was substantially large (26 and 45 µm) and seeding concentrations ($\dot{m}_p$) for the maximum reduction in Mach disc location equalled or exceeded the gas mass flow ($\dot{m}_g$). Results presented here show no clear indicator of the effect of particle concentration, but effects are expected to lie outside of the imaging resolution used within this work. As stated, however, on average the schlieren barrel lengths were indeed longer than the

[10] The mean coefficient of variation for this variable was 1.48% and the mean standard deviation 4.99%.

particle-laden flows but the actual contribution of particle size and concentration effects are not easily decoupled from other variables. Quantitative particle seeding would need to be employed with studies limited to steady-state events within the nearfield and at high resolution.

5.3.2 Mach Disc Diameter

The Mach disc diameter was again defined through the selection of the triple point locations across the radial geometry from schlieren images. Whilst the profile shows the similar trends to the barrel length results, there is discrepancy in the period after the "response" region ($t^{1/2} < 24.58\ \mu s^{1/2}$). Instead of a consistent diameter, indicating stable fully-developed flow, there was a general decrease in Mach disc diameter for $PR > 120$ experiments and a higher oscillation between measurement locations.

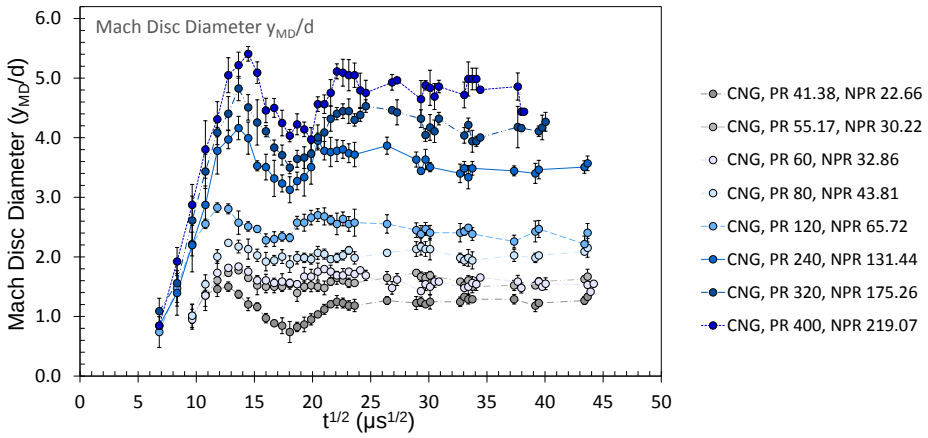

Figure 132, Mach disc diameter evolution for high PR CNG jets.

Despite the somewhat erratic Mach disc diameter for ($t^{1/2} > 24.58\ \mu s^{1/2}$), there is good linearity when collapsing the quasi-steady-state data above to single points as shown in Figure 133. It can be seen that there is a higher measurement range (error bars representing the standard deviation) for higher PR conditions. The data are highly linear, with an R^2 for the actual and linear fit of 0.997 and a mean variance between the actual and the linear fit of 2.82% (y_{MD}/d).

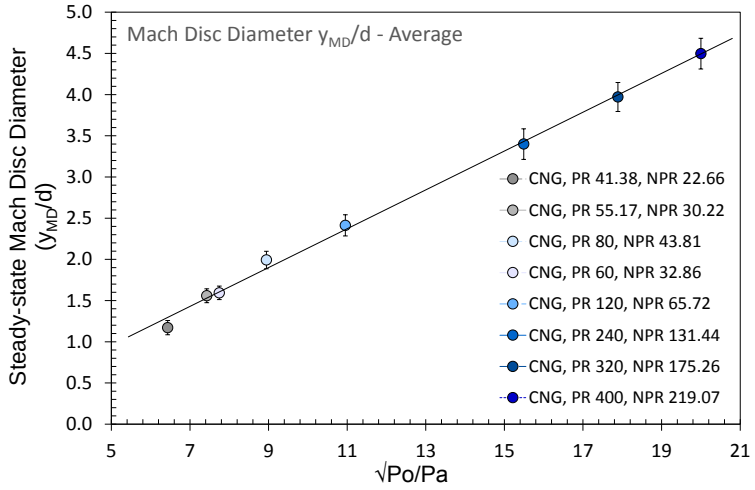

Figure 133, Mean steady-state Mach disc diameter for a range of high PR CNG jets.

The Mach disc diameter is represented through the following relationship:

Equation 76, Steady-state Mach disc diameter expression for high PR CNG jets.

$$\frac{y_{MD}}{d} = 0.2357\sqrt{\frac{P_o}{P_a}} - 0.2213$$

Whilst the correlation is similar in derivation to Addy (1981), the constants proposed are vastly different. The Mach disc diameters for these high-PR jets are significantly larger (~2-4 times Addy's). This indicates that a combination of the density ratio and the internal injector geometry significantly alter the Mach disc diameter.

5.3.3 Jet Width and Shear-Layer Thickness at Triple Point

Measuring the radial jet width at the location of the triple points (y_{TP}/d) provides an means to assess the influence of the Mach disc on the incompressible features – the radial penetration and the shear-layer thickness. The radial penetration, y_{TP}/d, is therefore measured at a dynamic downstream axial location (x_{MD}/d). It can be seen in Figure 134 that y_{TP}/d increases with PR, as was the case (for example) with the barrel length. The region presented in Figure 134, $13\ \mu s^{1/2} \lesssim t^{1/2} \lesssim 24\ \mu s^{1/2}$, was selected due to the large variability of measurement outside of this time domain. The variability for $t^{1/2} \gtrsim 24\ \mu s^{1/2}$ comes from the experimental condition in which the jet recirculates back onto itself in the nearfield region and thus affects the jet width.

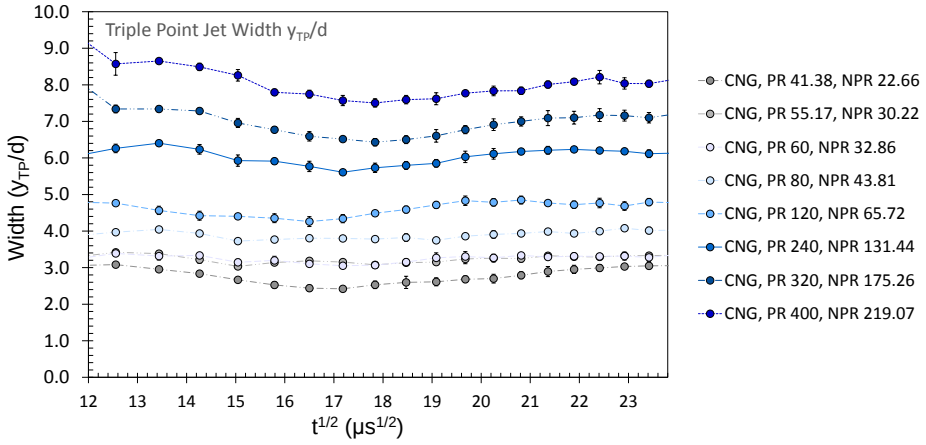

Figure 134, Jet width measured at the triple point location for high PR CNG jets.

Whilst y_{TP}/d apparently increases with PR, it does not show any immediate indication of the influence of the compressible flow behaviour. Scaling the data relative to the maximum and minimum values between the time interval for the triple point width and barrel length reveals that the changes are indeed in line with previous oscillating trends. Figure 135 depicts this scaled comparison for two selected PR cases. It is evident that the trends are aligned, albeit with a small timing-phase offset (one image frame) and the absolute difference is relatively small. The absolute variances for the PR41.38 and PR320 conditions averaged across the time domain is 16% and 12% respectively. This indicates that the compressible flow development influences the incompressible flow and thus the overall jet development.

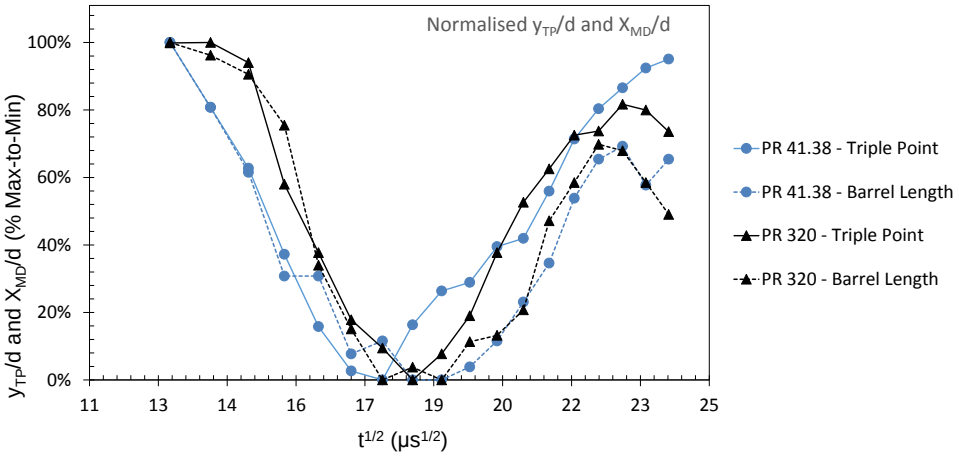

Figure 135, Normalised triple point width and barrel length for PR 41.38 and PR320 CNG jets.

The shear-layer thickness (width), y_{SL}/d, is calculated from the difference of the triple point jet width and the Mach Disc diameter, divided by two. With the trend and scale of y_{TP}/d aligning to the effects of PR and the resultant compressible flow structures, it is safe to conclude the same for the shear-layer thickness. The shear-layer thickness represents the transitional region where the

flow is bounded by the barrel shock and the ambient medium. The largest nearfield shear-layer thickness is measured at the triple point, and is shown in Figure 136.

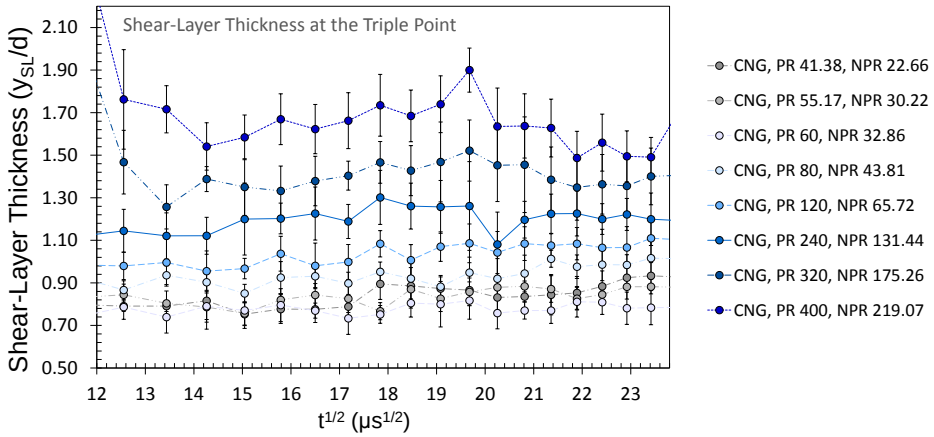

Figure 136, Mean shear-layer thickness measureed at the triple point for high PR CNG jets.

The shear-layer thickness for the time domain selected is typically half- to twice- the nozzle diameter and individually constitutes a moderate proportion of the overall y_{TP}/d. Again, this accountancy and dissection of geometric features aids in the fuller understanding of the processes within the nearfield region. In general terms, the greater the shear-layer thickness the greater the fuel-air mixing propensity. To help quantify the PR influence on shear-layer thickness, time-averaging ($12\ \mu s \lesssim t^{1/2} \lesssim 24\ \mu s$) is applied to the data in Figure 136 and arranged according to $\sqrt{PR}$. The resultant trend appears in Figure 137. An expression, Equation 77, is produced with reasonable fit to y_{SL}/d data, where the mean and median variation between the simplified expression and mean data values are; 4.4% and 2.6% respectively. The PR60 data, however, is omitted where it is observed to fall outside of the general fit.

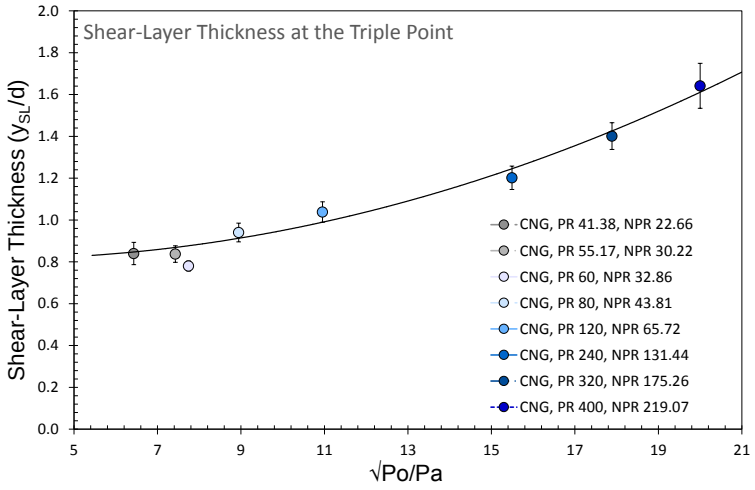

Figure 137, Time averaged ($12\ \mu s \lesssim t^{1/2} \lesssim 24\ \mu s$) shear-layer thickness normalised by the square-root PR, for high PR CNG jets.

Equation 77, Shear-layer thickness in the unsteady region of high PR CNG jets.

$$\frac{y_{SL}}{d} = 0.003\frac{P_o}{P_a} - 0.02\sqrt{\frac{P_o}{P_a}} + 0.8$$

There are two provisions that should be stated regarding the correlation of shear-layer thickness to the jet PR. Firstly, the shear-layer thickness was unfortunately only measured in the unsteady (developing) Mach disc diameter region. It is predicted that in the steady-state compressible flow region the shear-layer thickness would have a linear PR correlation where it has been previously shown that the steady-state features which affect the shear-layer thickness (barrel length, Mach disc diameter and jet spread angle) are linearly dependent on the PR. Secondly, the thickness of the shear-layer is highly dependent on the turbulence level. Whilst the Reynolds number remains in the fully-turbulent regime, secondary factors such as ambient-air entrainment will affect the turbulence levels and thus in turn the shear-layer thickness. The air-entrainment is discussed in Section 6.3.

5.3.4 Mach Disc Reflection Angle

The Mach disc reflection angle (α) shows no signs of evolutionary development. Once the reflection shock is present, an oscillation is the only discernible transient behaviour. This is indicated in Figure 138. The period of oscillation is undefinable in the present circumstance where the frequency is expected to exceed acquisition frequency. Moreover, the reflection angle does not change in accordance with the evolving large-scale compressible flow features (the Mach disc location, size and the angle of shock incidence). Another indicator of α independence is where PR, a strong determinant of other compressible features, has no clear effect. The oscillation or instability in α is most likely due to the formation of helical instabilities downstream from the triple point location and the radial pressure and velocity transitions across the α region. The reflection angle is also subject to the oscillation of the Mach disc and hence triple point location where turbulent boundary effects impose mixing-induced instability.

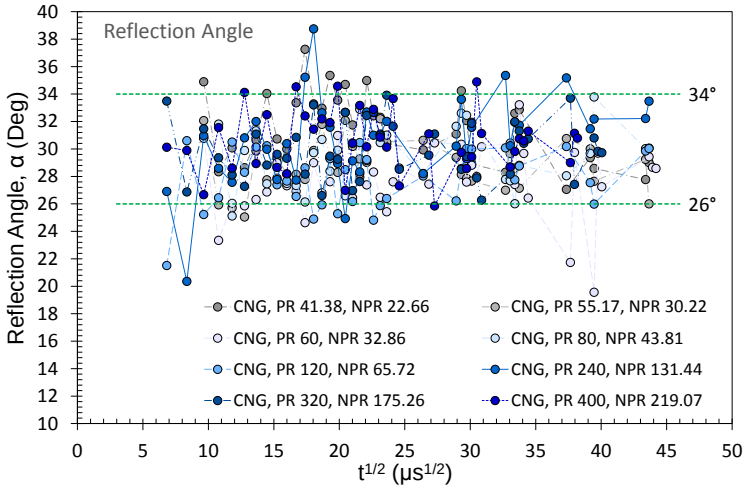

Figure 138, Mach disc reflection angle evolution for high PR CNG jets. *Error bars withheld for clarity*.

The average Mach disc reflection angle shows no discernible change across the PR range, with the values (once compressible features are stabilised as per Figure 128 and Figure 133) presented in Figure 139 below. Whilst the uncertainty is high (several degrees), no discernible NPR trends are present. This contradicts previous statements by (Yu et al., 2013b, Vuorinen et al., 2013). Both the actual average figures and their respective range were consistent, highlighting the quasi-stable nature of reflection angle when viewed generally. The average reflection angle for all scenarios presented is $\alpha_{mean} = 29.75°$. This agrees well with the low-PR measurements (Table 16) where the CNG jets yield $\alpha_{mean} = 31.70°$.

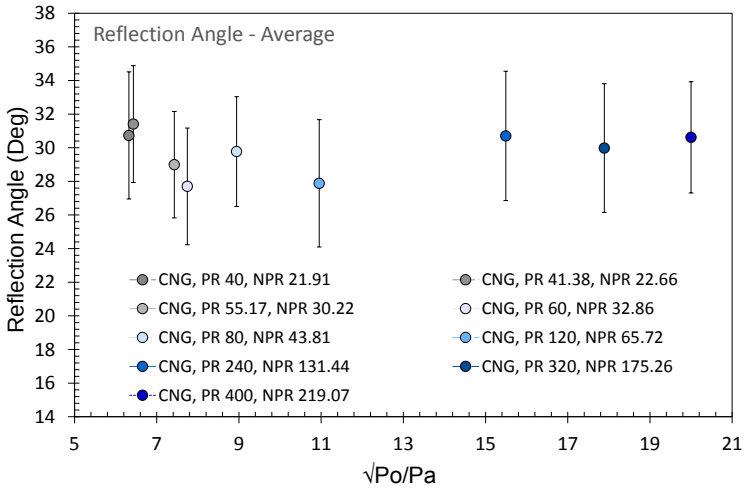

Figure 139, Mean Mach disc reflection angle for high PR CNG jets.

5.4 The Dimensionless numbers Pressure and Density Ratio

Two examples are provided and discussed to support the use of pressure and density ratio as dimensionless numbers. Although several scaling factors have been employed, showing the relationship between a vast range of delivery pressure and density conditions, it is worth highlighting this further. Two simple but key examples are given.

For the macro properties, the most all-encompassing condition is the projected area. The projected area incorporates the individual jets' growth rate, including velocity, spread angle and axial and radial penetration. To this end, a PR 80 jet delivered at equivalent density ratio is depicted in Figure 140. The upstream density is twice that of the ambient density, resulting in a large comparative change for the individual density values ρ_o and ρ_a. Additionally, the cases presented were obtained under different optical and physical configurations, with a freestream and impinging scenario compared. As Figure 140 indicates, the correlation between density variation and projected area is excellent. Both independent cases show very close agreement for the measured length scale ($x/d < 27$). Thus the arrangements of the two different optical configurations are also strongly correlated.

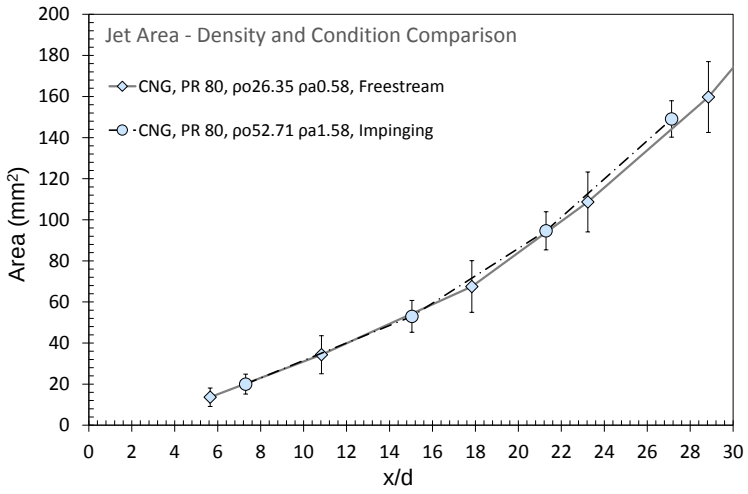

Figure 140, Jet area comparison of two, differently-derived PR80 jets, at freestream and impinging conditions.

As for the macro comparison, a PR equivalent examination of the internal compressible structures was carried out. The transient region of the barrel length was compared for near-similar pressure conditions of 40:1 and 60:1.45 (bar). The local variance in measurement is shown against the absolute values in Figure 141. The average barrel length variance was coincidentally very much aligned to the variation in PR with values in the order of 3.16% and 3.45% respectively. Again, this corroborates previous expectations that comparing such features to various PRs is appropriate.

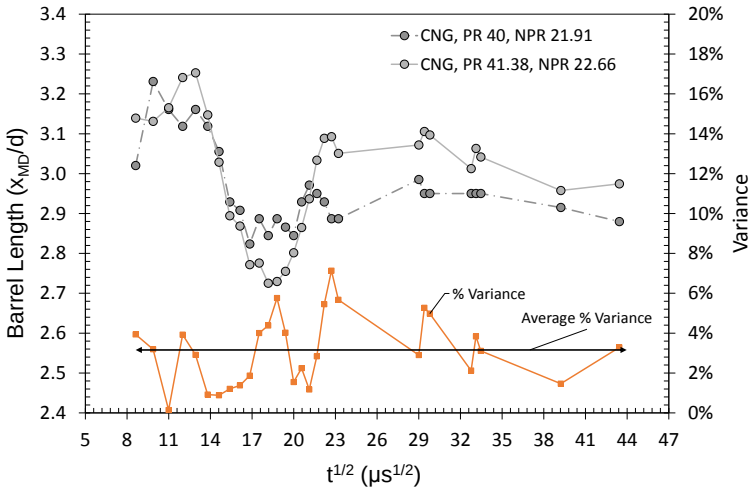

Figure 141, Barrel length variation for two $PR \approx 40$ CNG jets.

Further analysis reveals that the use of PR as an absolute normalisation term, is in fact, not acceptable for some flow characteristics. This becomes apparent when secondary flow influences such as the physical boundary interaction in impinging flows, are introduced. Specifically, the nearfield ambient velocity component $\bar{u}$ and the entrainment into the jet do not correlate wholly to PR normalisation. Discussion on this topic is presented in section 6.3.1 and section 6.3.2.

5.5 Chapter Summary & Conclusions

This detailed characterisation of CNG fuel jets issued from a purpose-built direct injector resulted in the following key conclusions:

i. The pressure and density ratio are meaningful factors influencing both macro and compressible flow structures. Existing scaling laws can be applied with good certainty indicating their usefulness in predicting transient highly underexpanded jets issued from an automotive fuel injector. The compressible structure size appears to have little or no bearing on the macro jet development once normalised. The rate of penetration for CNG jets issued between $60 < PR < 400$ is $\Gamma = 3.19$.

ii. The growth histories for both Mach barrel length and Mach disc diameter were characterised with high-resolution showing:
   a. The fully developed barrel length scales linearly ($R^2 = 99.6\%$) with PR. The relationship derived for this function shows a constant, C_x, in the order of nearly half compared to steady-state empirical relationships found in the literature. The steady-state barrel length expression is provided in Equation 75.
   b. The fully developed Mach disc diameter scales linearly ($R^2 = 99.7\%$) with PR. The CNG Mach disc diameters are $\sim$2-4 times larger than existing literature suggests. It is expected that both the density ratio and the internal geometry are dictating such differences. The steady-state Mach disc diameter expression is provided in Equation 76.
   c. The temporal evolution of the Mach disc diameter and location (barrel length) is largely independent of PR but highly dependent on the PR specific injection momentum/mass flux, hence the needle lift in velocity-choked conditions.
   d. For complex, highly restrictive nozzle geometries, as found in DI injectors, classical relationships will not adequately capture the transient or steady-state Mach disc structure.
   e. The barrel length is shown to be substantially influenced by the internal injector geometry. PIV measurements corroborate the schlieren defined x_{MD}/d location with reasonable certainty. PIV centreline velocity results indicate that in steady-state conditions the removal of the injector needle shifts the Mach disc location $\sim 45\%$ further downstream. It is proposed that the internal geometry influences the internal shock development or varies the in-nozzle pressure profile substantially.

iii. The geometric properties in the nearfield are tied to the effects of the compressible flow behaviour; the jet width (y_{TP}/d) evolves with the same relative magnitude and temporal phase with x_{MD}/d. This in turn is a function of the needle-lift profile and hence can be controlled using needle-lift/mass flow rate shaping.

iv. The shear-layer thickness, as measured at the triple point location, is shown to develop in proportion to the jet PR, even within the largely unsteady jet delivery region ($12\ \mu s \lesssim t^{1/2} \lesssim 24\ \mu s$). This proportionality was shown in polynomial form (Equation 77) where a mean variance of 4.4% was observed against measurements.

v. The Mach disc reflection angle was characterised at high resolution; even before the Mach disc and barrel length has fully developed the reflection angle remains constant within its oscillation period (26° to 34°). The mean angle of 29.75° and oscillation period for these high PR jets is in close agreement to the low PR tests, confirming this feature is independent of PR and injection momentum/mass flux.

vi. Self-similar CNG jets have a largely consistent spread angle. This is despite the large change in PR and therefore Re_{exit} magnitude. Thus the spread angle correlates well with classical fully-turbulent jet theory. The absolute value is also in line with theory and the low-PR results, where a mean spread angle of $23.33°$ was achieved.

THIS PAGE IS INTENTIONALLY BLANK

6. High Pressure Ratio Mixture Formation

In the previous chapter, high-pressure CNG jets were shown to evolve according to physical flow interactions. It was shown that the compressible flow structures take shape depending on the injector needle motion and the pressure ratio. More importantly the nearfield jet structure substantially changes according to these processes and thus spatial targeting and mixture preparation are potentially affected. This chapter describes the delivery properties and measurements of them associated with mixture preparation. To this end, DI CNG fuel jets were issued into a quiescent in-cylinder environment with realistic conditions.

This chapter describes measurements of impinging CNG jets using schlieren and PIV imaging. Measurements are Analysis and discussion centres on the implications of high-pressure fuel injection on mixture formation, including cylinder filling, air-fuel mixing and ignition probability. Investigation of these topics was aimed at revealing the consequences of high-pressure fuel jets issued transiently. In accordance with the research objectives of high-pressure CNG jet characterisation pertaining to; *the targeting and dispersion behaviour of the gaseous fuel jet*, *transient jet behaviour in the nearfield* and the *effects of the jets on the in-cylinder flow and turbulence*, this chapter answers the following research questions:

4. *How does a high pressure-ratio influence the jet flow-characteristics and the mixture process?*
5. *Can the nearfield entrainment rate be quantified using current particle image velocimetry methods for early stages of transient jet development?*
6. *How do non-dynamic physical boundaries influence mixture formation (i.e. impingement)?*

The experimental schedules utilise the same methods outlined in Chapter 3 and Chapter 5 unless stated otherwise.

6.1 Cylinder Filling

Using the projected jet area and the cylinder area, the percentage of cylinder filling (the ratio of fuel jet area per cylinder[11] area) was calculated. This metric is valuable when plotting key jet development positions (i.e. 30%, 50% and 80% filled) against jet delivery variables. Figure 142 presents the paths of constant filling between 10% and 80% at 10% intervals. The constant fill lines show a clear correlation between filling time and PR. This is largely unsurprising given the previous relations depicting the jet project area. There is, however, value in defining the filling-rate at specific locations; where an inherent level of mixing has occurred, as captured when defining the jet boundary. As stated earlier, the fuel jet is not entirely fuel. Due to ambient air entrainment and mixing, the "fuel jet" is in fact a mixture. Thus a more accurate definition of the cylinder filling rate is the jet dispersion rate.

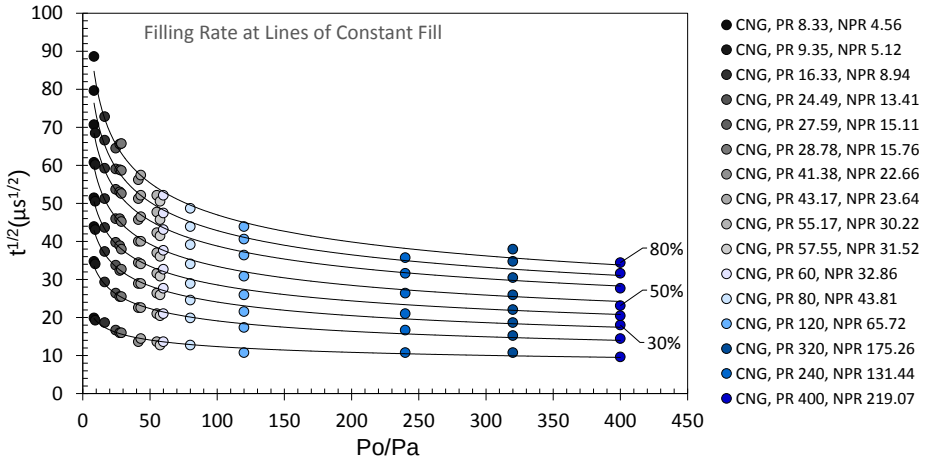

Figure 142, DI CNG (8.33<PR<400) cylinder filling rates with fill-level isolines

For the entire series of impinging jets ($8.33 < PR < 400$) issued from the 1mm Ø nozzle (excluding the PR240 case), a relationship between PR and filling time was semi-empirically derived. The power-law curve fits (as per Figure 142) for each percentage fill series were collapsed to one governing relationship, based on the assumption that the power-law coefficient (-0.234) is constant for all fill series. Sensitivity analysis on the power-law coefficient selection is provided in Appendix IX.

Equation 78, CNG filling times normalised for pressure ratio.

$$\sqrt{t_{\%Filled}} = m_{fill}\left(\frac{P_o}{P_a}\right)^{-0.234}$$

[11] The 'cylinder' referenced is the square-pseudo-cylinder defined in Chapter 3.

where, m_{fill}, the coefficient assigned to a nominal filled percentage (f) is defined as:

Equation 79, Cylinder filling coefficient for DI, 8.33<PR<400, CNG Jets.

$$m_{fill} = 167f^{11/15}$$

Using Equation 78, the time taken to reach a desired fill level was estimated to within an average uncertainty of 6.58% across a range of $f = 10 - 80\%$. The calculated values typically underestimated the measured values. With the exclusion of the 10% fill line, the statistical certainty of the average increases one full percentage point (5.31%). This is most likely due to small variability in jet delivery (i.e. mixing levels associated with the high-PR scenarios) and the relatively small jet volume at this early delivery time. For the remaining series, the deviations between predicted and measured values are shown in Figure 143.

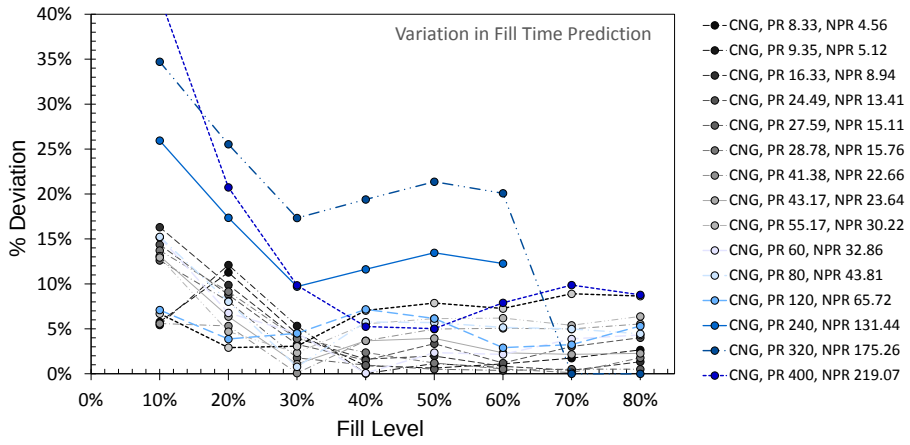

Figure 143, Fill time variation for prediction of 8.33<PR<400 CNG Jets.

A PR above 60 ($\sqrt{P_o/P_a}$ ~7.75) substantially reduces the time in which the jet propagates through the fixed cylinder volume. The filling rates relative to the PR60 case are presented in Figure 144, where losses (>100%) and gains (<100%) are shown. This type of normalisation provides an insight to the relative gains when selecting a fuel delivery PR – a key consideration in base engine calibration and architecture design.

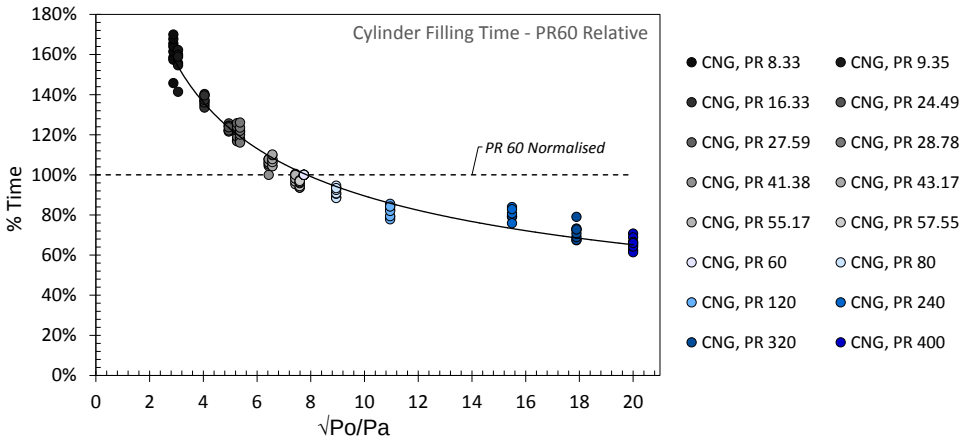

Figure 144, PR60 Relative cylinder filling time for DI 8.33<PR<400 CNG jets.

Considering the fuel supply pressure for a gaseous vehicle has substantial bearing on the fuel system cost and usable tank range (where no subsequent fuel pump is used), optimising the delivery pressure is a worthwhile pursuit. Figure 144 provides some justification for the asserted importance of delivery pressure to dispersion and mixing time. This can be used to define an optimal pressure ratio and justify if additional pumping is necessary. It could also be used to identify dispersion rates if the pressure ratio is variable in engine operation. With the losses associated with increasing pumping pressure are seldom linear, the above data have been left without any form of energy balance normalisation. For the PR60 reference case, it is evident that varying the PR below 30 or above 120, will not achieve a good balance of dispersion to PR.

6.2 Nearfield Condensation

The in-jet nearfield region for the CNG jets was partially characterised through the illumination of condensate (without seed particles) found within the fuel. A moderate and very high-PR case is presented in Figure 145. The illumination is caused by the Mie-scatter from by the liquid (or solid, i.e. ice) surfaces. The condensation-induced reflection theory was tested against gases with a lower liquefaction point: high-purity nitrogen and hydrogen. For both gas no such illumination was present, even under higher illumination energies. Aside from Methane, it is envisaged that for the CNG composition used, that either the ethane and/or carbon dioxide constituents are the most likely perpetrators of the nearfield condensation. This is due to their critical pressure and temperature, and their composition amount within the CNG used.

The illuminated nearfield region over-represents the HSV barrel length (Mach disc location) substantially, but is generally a good indicator of the Mach disc diameter. Additionally, the jet-to-air shear-layers are illuminated providing a qualitative insight into their turbulent structures. These highlighted shear-layers are carried along the high-velocity slip lines and extend several nozzle-diameters downstream beyond the Mach disc location. The shear-layer illumination is particularly interesting to view from a turbulent boundary layer perspective, where the small flow perturbations are highly resolved (best viewed in Figure 146).

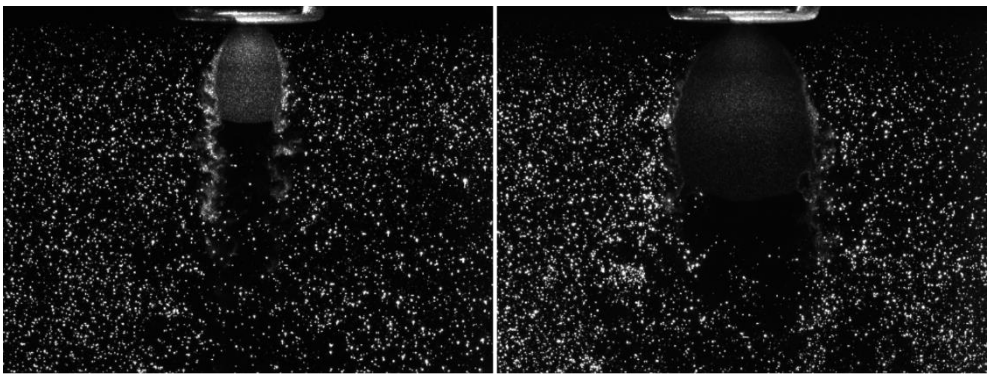

Figure 145, Nearfield particle entrainment, for developed PR80 (left) and PR400 (right) CNG Jets. Contrast adjusted.

The actual Mach disc location can be approximated by the entry location of turbulent swirls detached from the shear-layer. This landmark appears in several image sets for the total condition sample. The higher PR conditions gave the highest resolution to this feature, as exemplified in Figure 146. One potential explanation for this occurrence is that the jet-core gas downstream of the Mach disc is drawing in peripheral fluid as it begins to accelerate, hence a simultaneous pressure differential occurs. Shock heating after the Mach disc will also contribute to a lower density in the downstream core region. The shock heating associated with the normal Mach shock is expected to be the main contributor in the evaporation of the condensate. Since the in-jet gas velocity is large,

the evaporation is not instantaneous where illumination is apparent for a distance downstream of the Mach disc. The evaporation is thus dependent on time, temperature and pressure.

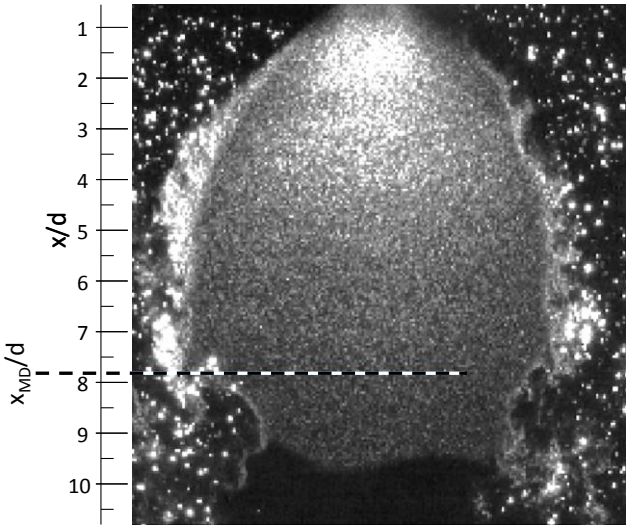

Figure 146, Nearfield condensate imaging. Shear-layer entry point with Mach disc location overlay (*x/d ~7.82*). PR320 CNG jet, 215µs aSOI. Contrast adjusted.

Depiction of the condensate illuminated regions also provides a useful landmark to assess the particle distribution. Figure 145 depicts the particles hugging the very edges of the shear-layer interface, but not penetrating it. Particles first appear $\sim 1x/d$ downstream of the illuminated edge and $2\sim 3x/d$ downstream of the actual Mach disc. As the particles are ambiently seeded, any particles contained within the jet section are a direct result of the ambient air entrainment. The particle density in the jet region will be dependent on the time $aSOI$, the entrainment rate and level of mixing. To accurately determine the level of mixing, measurements using quantitative acetone-LIF would be recommended.

6.3 Nearfield Flow

Two main areas of the nearfield jet region were analysed: the ambient flowfield extending around the highly underexpanded nearfield region and the entrainment at the jet-to-air shear-layer interface. The first offers an extended view of how the jet influences the broader ambient region for developing, stable and enveloping (self-entrainment at late aSOI) instances. This links the transitional effects discussed in Section 5.3 to the corresponding flow conditions. The second investigation area was the ambient air entrainment along the shear-layer interface. Analysis involved attempts to quantify the jet's miscibility for the corresponding pressure ratio and temporal location.

A nearfield region of interest (ROI) was created to isolate and compare nearfield ambient behaviour under different PRs. An adaptive ROI provided the best fit for the changing nature of the jet (temporally and spatially relative to jet PR) within the nearfield. The ROI was defined as follows, based on the schlieren imaging outputs:

Equation 80, Nearfield PIV ROI.

$$1.3\frac{x_{MD}}{d} \times (\frac{y_{TP}}{d} + 4\frac{y_{MD}}{d})$$

This dynamic spatial region of interest was selected for several reasons. The investigation covered a large range of PRs, and as seen previously the geometric behaviour of the jet is correlated to the individual PR for a particular delivery time. This ROI therefore sets an appropriate and most importantly a spatially consistent area for assessment, independent of PR. If a fixed spatial region were to be used it would need to compensate for the largest PR and geometric condition PR400, $t^{1/2} \cong 14\ \mu s^{1/2}$ (Figure 126 and Figure 132). This large ROI would over-represent the nearfield in the lowest PR cases. The actual spatial representation of Equation 80 allows several interrogation areas alongside each jet radially at their widest point, consistently for all jet development conditions. Axially, the ROI provides appropriate interrogation areas after the Mach disc ($+30\%\ x/d$) where any discrete changes induced from the Mach disc, reflection angle or slip lines should be discernible.

The interior of the jet was removed through the exclusion of the jet boundary. The jet boundary is defined through a process where for each individual case a gradient filter was constructed based on the changes in:

Equation 81, Boundary segmentation control variables.

$$\frac{d\bar{u}}{dx}, \frac{d\bar{v}}{dx} and \frac{du_{rms}}{dx}$$

This segmentation method allowed the removal of the jet from the ambient flowfield with high fidelity[12], thus facilitating a true case-by-case spatial mask. The rms component has been used previously in the determination of a control surface, albeit at a singular axial location (Cossali et al., 2001). The use of the dynamic ROI and appropriate jet-to-ambient segmentation is believed to be a faithful representation of the nearfield region within the intent of the investigation.

An example of jet segmentation is shown in Figure 147, where the white contour level distinguishes the jet area. The red vectors indicate the flow condition identified as the jet region. It can be seen, as highlighted with the inset figure, that the flow begins to turn substantially, indicating the presence of strong momentum and thus the actual fuel being delivered. The segmented boundary is estimated with an accuracy of ± 1 interrogation area ($\pm 0.238\,mm$). Any misrepresentation is believed to be of minor consequence, as the magnitude of the removed (red) vectors are of similar magnitude[13] to the defined boundary vector. It was decidedly better to be conservative when defining the boundary as any inclusion of a fuel jet vector would substantially skew the measurement. To the author's knowledge, the method employed is the most realistic in defining a jet boundary.

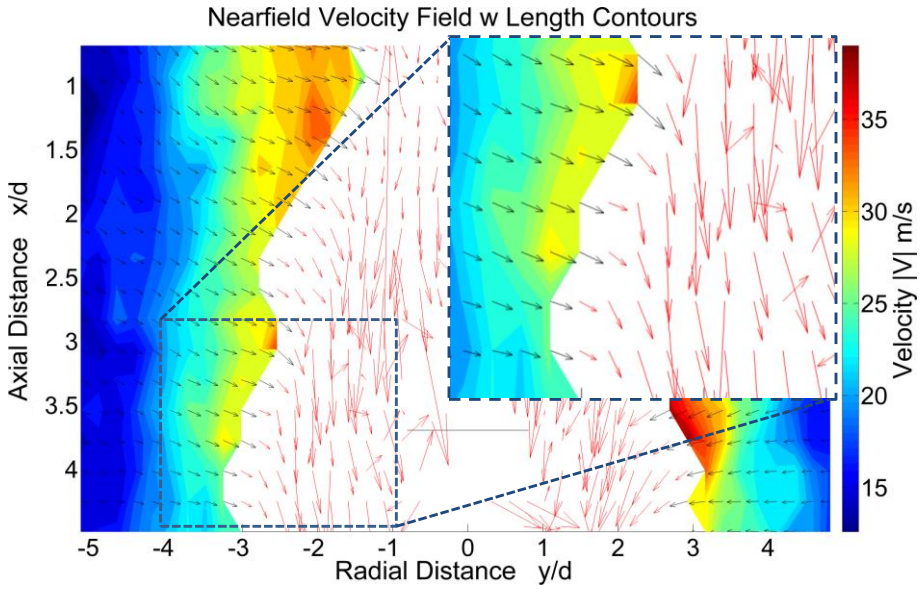

Figure 147, Nearfield velocity profile using ROI and jet segmentation masks. PR60 790 µs aSOI (30% fill level).

[12] All conditions were inspected visually, allowing the alignment of the boundary to the flowfield to be assessed subjectively. Note: As this method was intended for the nearfield region only horizontal assessment (*x*) was conducted. This method does not faithfully represent the jet boundary in the impingement region.

[13] Scales used on red and black vectors were slightly different. On interrogation the actual values ($\bar{u}$ and $\bar{v}$) of the black vectors, which may be the ambient were near-identical.

6.3.1 Nearfield Ambient Flowfield

The influence of the jet on the nearfield ambient flowfield is discussed in this section. With the fuel jet removed from the PIV image, the magnitude and orientation of the flow is discussed to highlight the implications of high PR fuel delivery on the in-cylinder region. This ambient region may encroach on the actual spark plug electrode location and thus it is also important for practical reasons.

The nearfield ambient mean axial velocity component, $V\,(m/s)$, increases, in a largely logarithmic nature, with the pressure ratio. This situation is depicted below for all cases except the earliest; $(215\ \mu s\ aSOI)$. As the impulsively started jet penetrates through the quiescent ambient environment, the jet must exert a large portion of energy into displacing and mixing with the environment. This consequently induces a greater flow interaction where the strong shear presence turns the flow back onto itself. This is perhaps seen with the best clarity in the very early region of delivery where the jet appears as a mushroom, as observed in Figure 81. For unobstructed freestream jets this phenomenon persists, emanating from the counter-rotating vortices at the jet tip; with the flow turning about the approximate centre of the jet head – as observed in Figure 148. This recirculating behaviour has also been shown to exist for gasoline-spray vortices (Arbeau et al., 2004). Figure 149 shows that in all instances the mean velocity is significantly more positive (vertically up) than its later-timed counterparts.

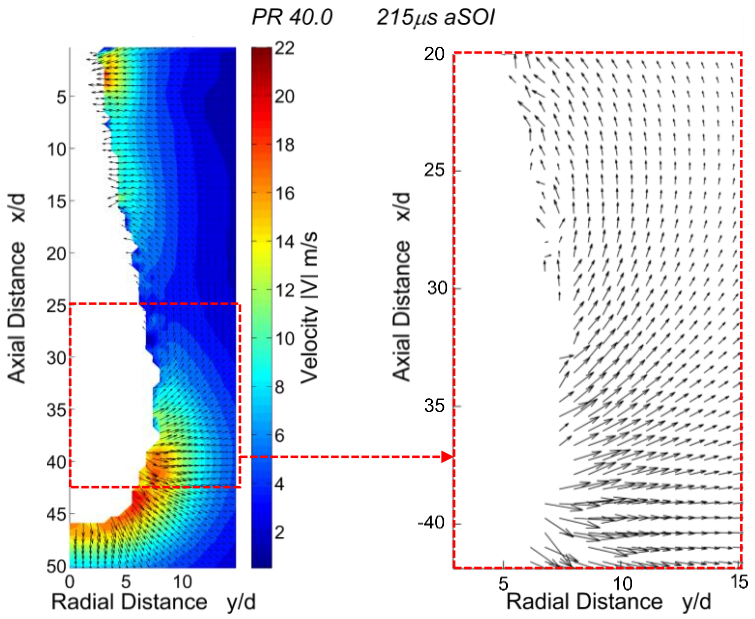

Figure 148, Axial ambient flow emanating from the freestream vortex head. Full jet vectors on flow magnitude contour (left) and vectors for a highlighted region (right). Shown for a CNG PR40 jet acquired at 215 µs aSOI and 20 µs dT, where the fuel jet is approximately removed from the ambient flowfield.

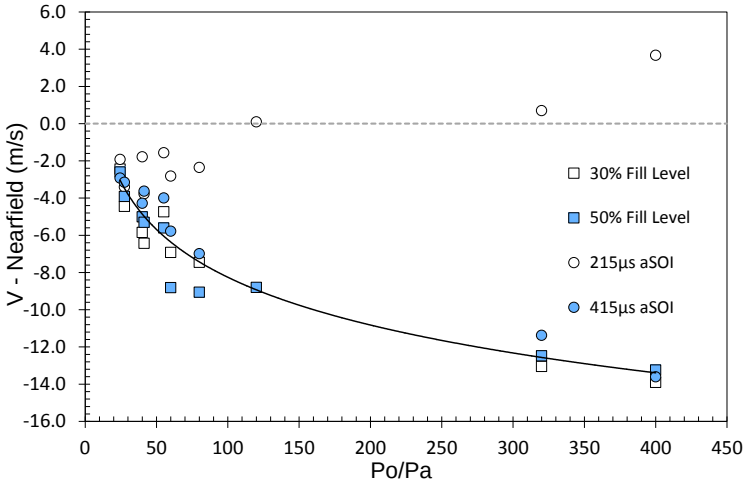

Figure 149, Nearfield mean axial flow velocity, V for high PR CNG jets.

Moreover, at $215\,\mu s\,aSOI$ all jets have just initiated their impingement from first contact in the lowest PR cases to the start of axial development for the highest PR cases. Provided the jet head centre doesn't transition onto the flat impingement surface, the turn up effects will be amplified. Whether or not this small amplification translates upstream to the nearfield region is unknown at present. Examples of the jet head striking the flat surface at $215\,\mu s\,aSOI$ are presented in Figure 160, with discussion on the imping jet effects forthcoming.

With the exclusion of $215\,\mu s\,aSOI$, the resultant velocity $|V|$ profile fits the previously introduced quasi-logarithmic profile, represented in Figure 150. The spread across each of the PR cases indicates that there are other dominant factors influencing the nearfield mean velocities.

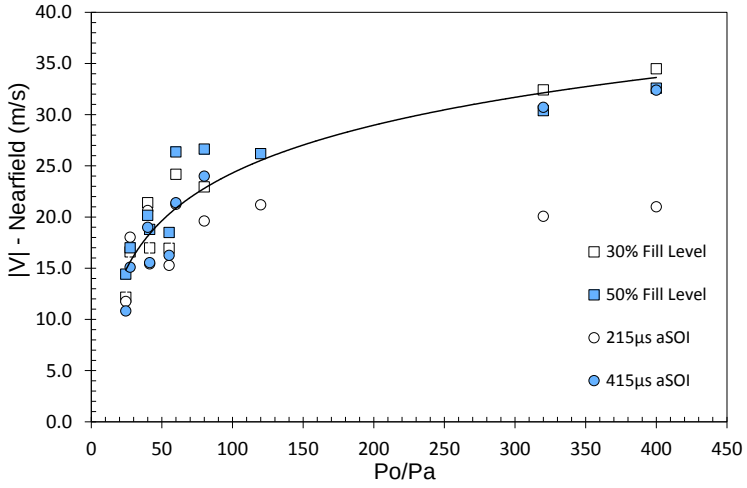

Figure 150, Nearfield mean resultant |V| velocity profile for high PR CNG jets.

The radial velocity component, $U\,(m/s)$, follows a similar trend to $|V|$ albeit with a more scattered profile. As seen in Figure 151, the magnitude of U shows weak correlation to the PR indicating that the orientation of the flow is susceptible to factors other than just PR. In addition,

Figure 151 clearly demonstrates that substantial differences exist in mean flow velocity for similar PRs. Examining PR41.38 and PR40, with respective U magnitudes of; 12.64 and 20.61 m/s, suggests that the PR is not a universal metric. This topic is discussed at length in Section 6.3.2. Figure 151 represents the horizontal flow headed toward the jet as mean values of both sides of the jet boundary.

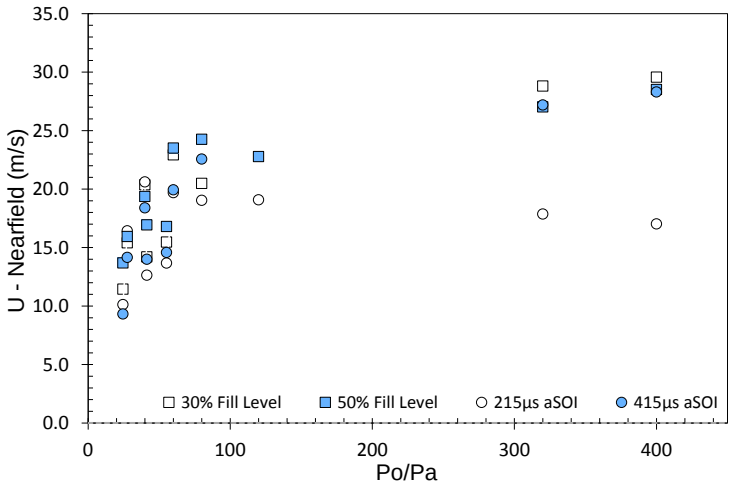

Figure 151, Nearfield mean radial flow velocity, U for high PR CNG jets.

It is clear that the fuel jet has substantial influence on the broader ambient region, with strong flowfield effects present within the nearfield. The flow velocities ($\bar{u}$, $\bar{v}$) were substantial, with mean resultant magnitudes, |V|, ranging approximately between 10 to 35 m/s. The flow velocity was observed to vector toward the jet core suggesting a strong ambient air entrainment where the horizontal flow component is the dominant scalar velocity.

6.3.2 Nearfield Entrainment

The nearfield entrainment was analysed for up to $10x/d$ for all experimental conditions. Through the use of Equation 39, in which the control surface is defined through the previously introduced segmentation method (Equation 81 and Figure 147), information on ambient air boundary could be extracted. At this boundary the velocity data were extracted for calculation of the air entraining into the fuel jet.

Discrete interrogation at a spatial resolution of $5\ x\ 5\ pixels$ ($0.056\ mm^2$) provided a highly resolved investigation but also gave rise to small perturbations. These perturbations in velocity measurement also arise from the high energy shear-layer surrounding the jet core and the proximity of the control surface boundary to such an area. For each interrogation cell, the boundary velocity was normalised relative to the jet-control surface angle (θ) $\bar{u}_n$. The radial distance, r, is measured from the jet boundary location to the jet nozzle centreline, and was taken for the individual jet

halves at each interrogation cell. The asymmetry of measured 2D jet halves was relatively minor and thus the entire jet surface (3D) was assumed to be axisymmetric. The ambient density (ρ_a) employed was idealised from the global ambient pressure and temperature of the quiescent nitrogen medium. This generalisation is commonly assumed (e.g. (Andriani et al., 1996)). The ambient massflow entrained ($\dot{m}_e$) was calculated for $0 < x/d < 10$ for all impinging CNG pressure ratios and PIV acquisition instances (constant time: $215\ and\ 415\ \mu s\ aSOI$ and fixed jet position: $30\%\ and\ 50\%\ fill\ level$).

Figure 152 provides a snapshot of the ambient mass entrained for a range of experiments; the four acquisition instances are shown against their mean (red line) and smoothed mean (black line) values. It can be seen that whilst the smoothed trends are indicative of expectation, the highly-discrete individual measurements provide an insight into the measurement fluctuations. These fluctuations are expected to result primarily from the measurement/analysis method, with flow conditions, whilst turbulent, playing a minor role. This type of discrete investigation would perhaps benefit from a more targeted imaging region (higher magnification within the nearfield) and a greater sample size. Regardless, the smoothed trends are indicative and as discussed later the absolute values normalise to expectation, thus giving good confidence in the values below.

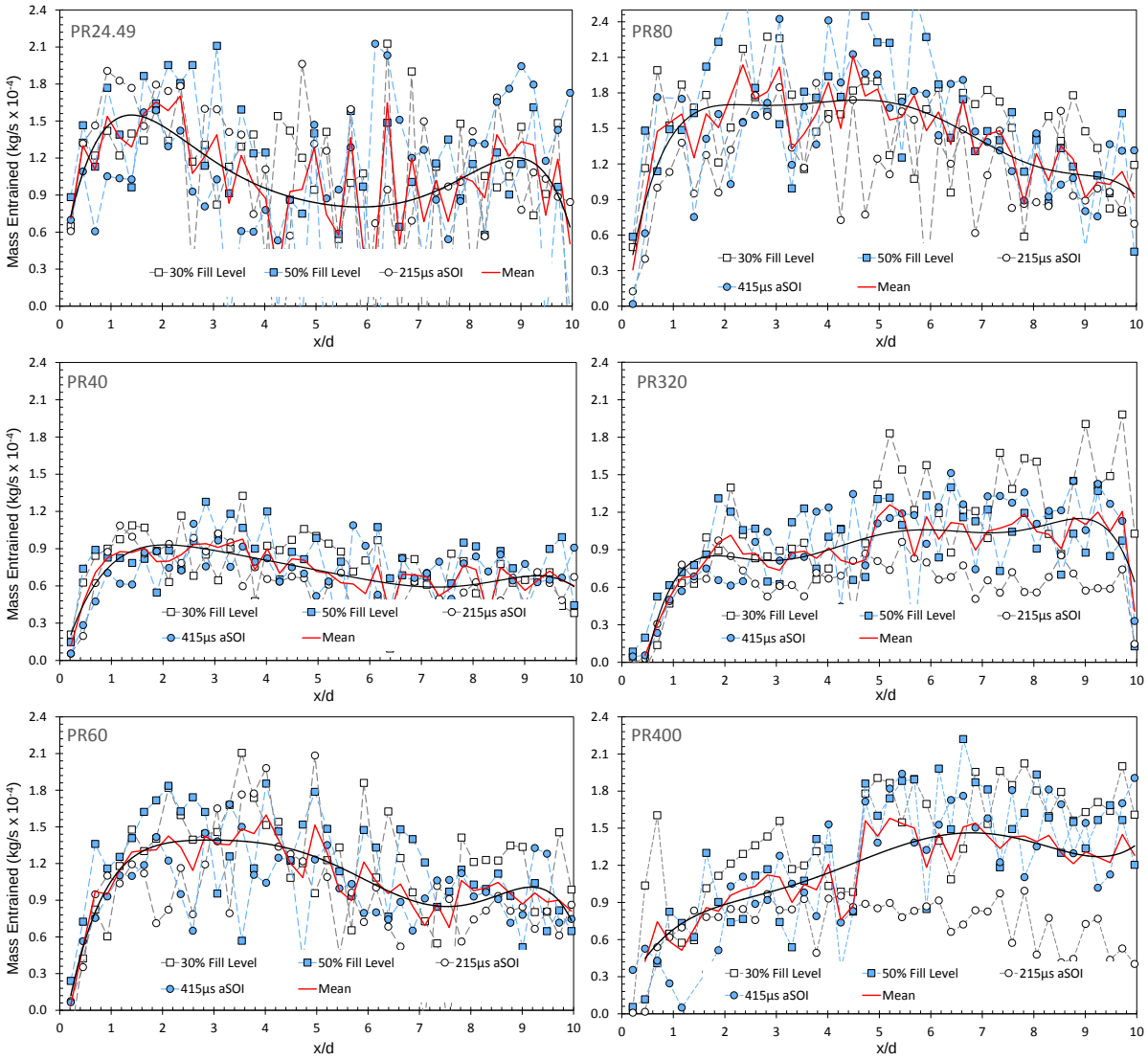

Figure 152, Instantaneous mass entrainment for six different PRs: 24.49, 40, 60, 80, 320 and 400. Red lines indicate mean values at all PIV timing with black lines indicating trend at means values.

Interestingly, there appears to be a high correlation in entrainment mass between experimental series where the ambient pressure is ≥ 1 bar (abs); this is in contrast to the acquisition mean for sub-ambient pressures, where a significantly reduced mass entrained is observed up to $5x/d$. This is best observed in the highest PR case of 400. In substantiation of the ambient pressure (density) effects, each category (equal to, greater than and less than ambient) and each PR and acquisition instance is reduced to a mean value. Figure 153 depicts this collapse, where it is seen that the sub-ambient conditions do not conform to a common line, particularly for $< 5x/d$ where up to 50% reduction in $\dot{m}_e$ is observed.

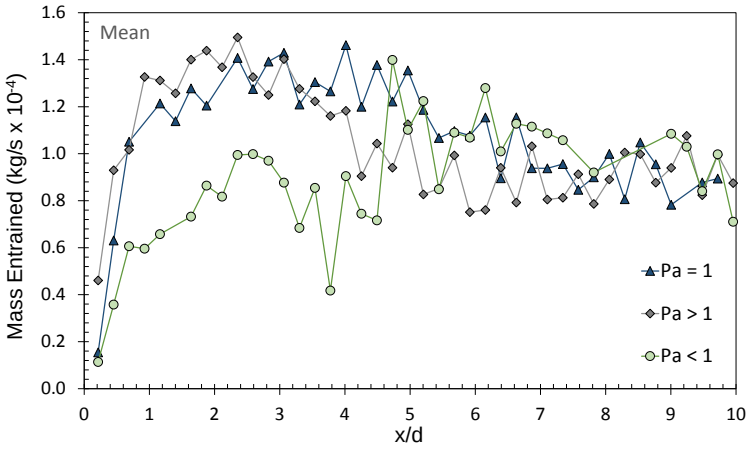

Figure 153, Mean mass air entrainment rate for Pa combined series of high PR CNG jets.

The effects of ambient pressure are further highlighted when PR24.49 and PR27.59 are compared. With a 13% difference in PR but a 69% variance in ambient pressure (P_a), an almost two-fold increase in $\dot{m}_e$ exists for the higher P_a scenario (PR24.49). The boundary geometry (spread angle and radial penetration) were expected to be very similar due to the geometrical PR dependencies, but the flow and the mean boundary-flow velocities were 21% higher for PR27.59. It is evident that the ambient pressure/density has a bearing on mass entrained. The other factor to consider in this particular situation is the upstream pressure/density and hence fuel mass flow ($\dot{m}_f$) delivered; as discussed later. The nearfield entrainment rate for the PR24.49 and PR27.59 acquisition mean, are shown in Figure 154.

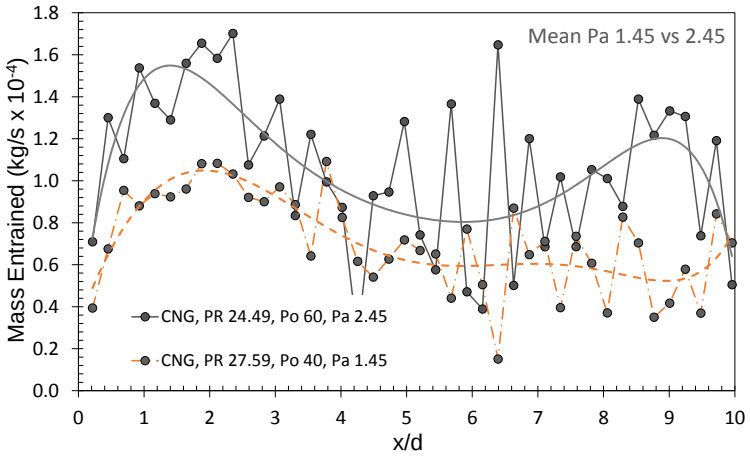

Figure 154, Mean mass entrained for varying high ambient pressures for PR24.49 & PR27.59 CNG jets.

The individual acquisition scenarios can be compared for $P_a > 1$. The cumulative entrained massflow rate across the $\leq 10x/d$ section for different acquisition instances are compared in Figure 155. It is again evident that PR is not a useful metric for mass entrainment, as increasing the ambient density or $\dot{m}_f$ increases the mass entrained.

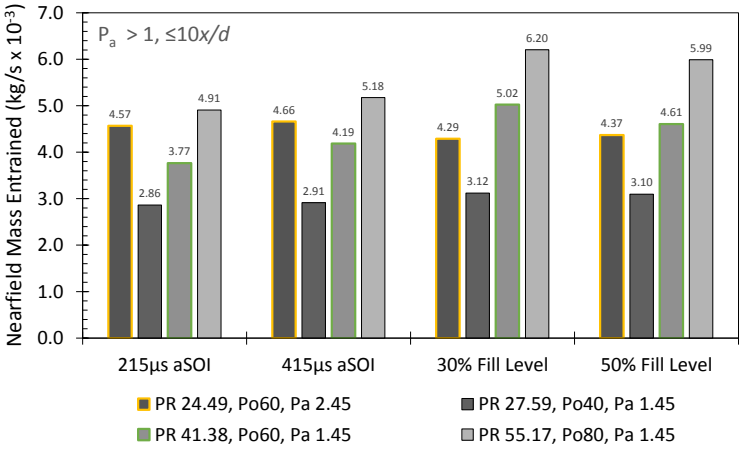

Figure 155, Total mass flow entrained across nearfield for Pa >1 for CNG jets of PR: 24.49, 27.59, 41.38 & 55.17.

Concentrating on the $P_a = 1$ series, one can generally observe a rise in the mass entrained between PR40, 60 and 80. The proportioning is not consistent across the axial location; the greatest discrepancies are seen at the early acquisition and hence jet development times of 215 and $415\ \mu s\ aSOI$. At later $aSOI$ times, at constant jet propagation, a more consistent proportioning occurs. These trends are observed in Figure 156. Since the ambient entrainment rate was captured for axial distances greater than the Mach disc location, the x_{MD}/d locations are overlaid on their respective conditions (red circle markers). Figure 156 shows no consistent change in mass entrainment surrounding the Mach disc or reflection angle boundary-contact point ($\sim 1 x/d\ downstream\ of\ x_{MD}/d$).

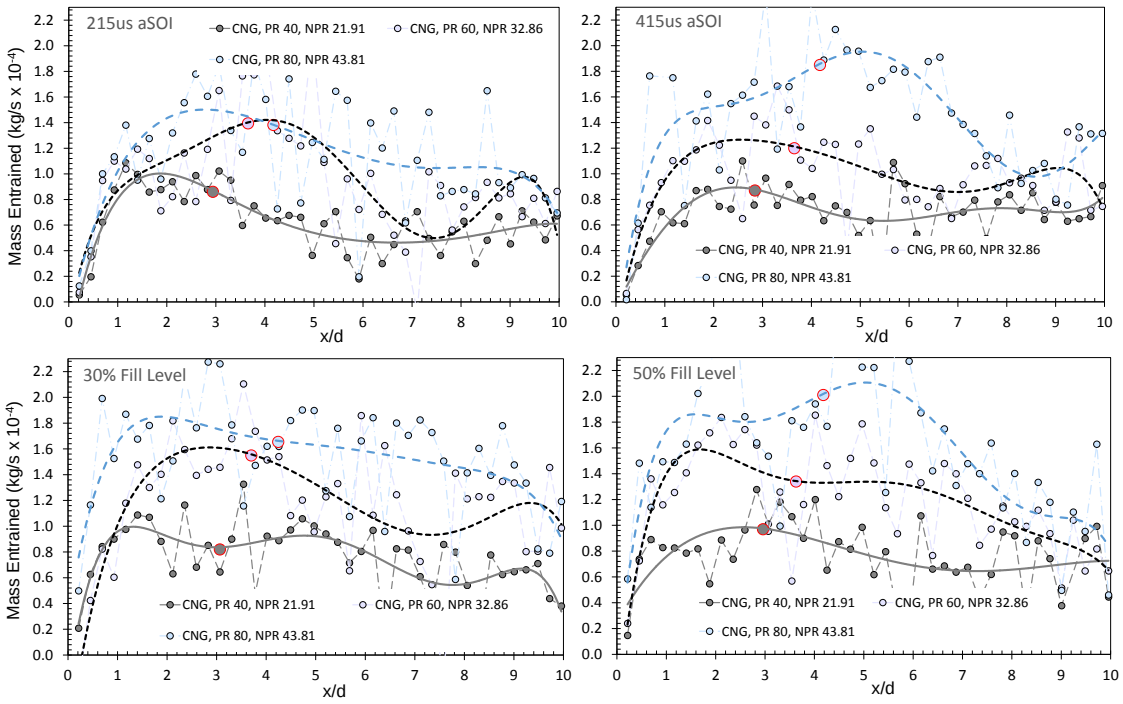

Figure 156, Massflow entrained for PR40, 60 and 80 at various acquisition times. Red marker circles indicate location of the Mach disc.

Collapsing the acquisition instances to a single mean representation yields a highly generalised view of the entrainment behaviour. This is perhaps too great a generalisation, but it does afford a practically convenient view of the $\dot{m}_e$ to PR delivery expectations. These trends are evidenced below in Figure 157. Again the PR40, 60 and 80 conditions are represented, at $P_a = 1$. For individual conditions above and below atmospheric pressure, less distinct correlations between mass entrained and PR were observed for discrete x/d location values.

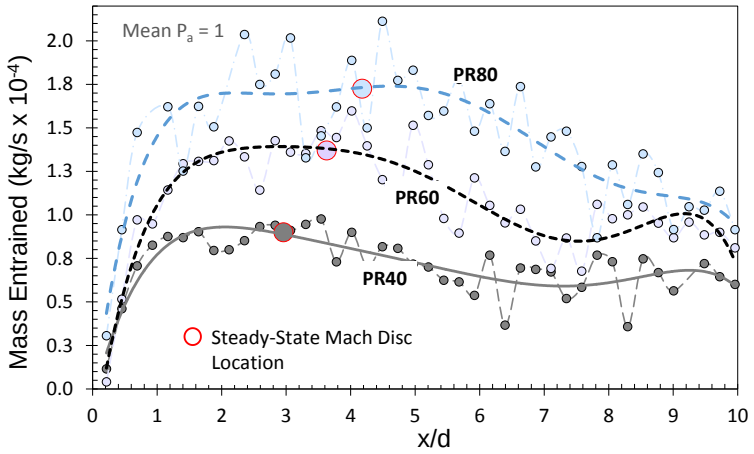

Figure 157, Mean mass entrained for PR40, 60 &80 CNG jets at an ambient pressure of Pa=1. Red circle markers indicate location of the Mach disc.

Investigating the role of fuel delivery on entrainment, two normalisation methods are presented. To this end, the cumulative $\dot{m}_e$ for the nearfield spatial range ($\leq 10x/d$) was totalled and integrated for the acquisition time and divided by the integrated fuel massflow rate, $\dot{m}_f$. The second method employs the nearfield cumulative $\dot{m}_e$ and is divided by the instantaneous massflow rate. The resulting trends are shown in Figure 158, left and right-hand sides, respectively. Again, since velocity is choked at the nozzle exit, any increase in massflow rate is a consequence of a higher upstream pressure and/or needle lift. Whilst both constant time locations ($215\ and\ 415\ \mu s$) are within the steady needle lift region, neither are within the steady flow region (as seen previously with compressible feature development, as shown in Figure 126 and Figure 127). The constant jet location data is also presented to give an indication of later event development for experiments at PR40, 60 and 80. It is apparent from Figure 158 that the entrainment rate increases for an increasing time aSOI. All conditions other than PR24.49 show similar trends for an increase in total nearfield entrainment. PR24.49 exhibited relatively no change in $\dot{m}_e$. Good agreement between the PR cases exists, in that the mass ratio is largely the same for each acquisition instance. The mean variance between PRs for a given acquisition instance, is 5.8 and 6.6% for the integrated and non-integrated methods respectively.

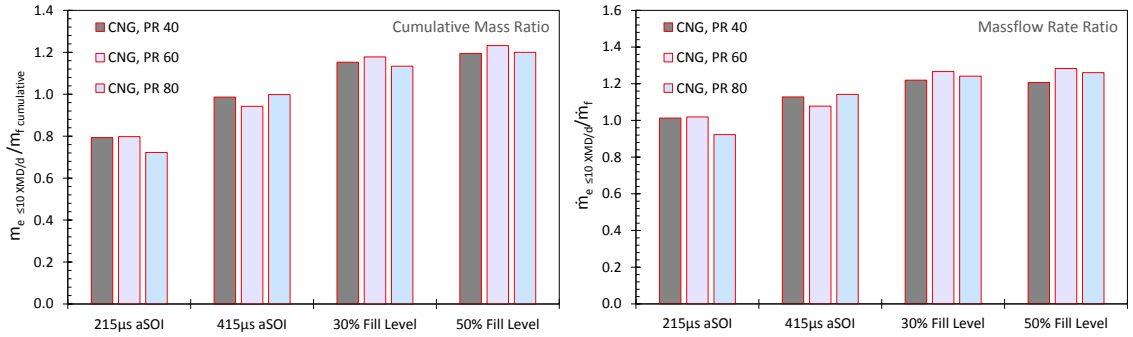

Figure 158, Mass normalised entrainment for up to ≤10x/d for PR40, 60 and 80 jets

Utilising the entrainment coefficient, K_2' (Equation 37), the nearfield entrainment behaviour can be assessed universally, with values depicted in Figure 159. As per previous discussion, it is shown that the ambient density component does indeed affect the entrainment. For all cases other than $P_a < 1$ (PR320 and 400) a relatively flat air entrainment coefficient profile is present. For comparison the mean values across the nearfield are displayed within each plot. The largely consistent and linear K_2' values in this region ($0.091 < K_2' < 0.189$) are close to the 0.183 reported by Boguslawski and Popiel (1979), who deviated from the non-linear representation of Hill (1972). It is clear from the literature that within the nearfield, typically $x/d < 10$, no (current) universal relationship applies to turbulent round jets. Post et al., (2000) perhaps captures this sentiment best. This work, however, makes the following contributions to knowledge of the topic:

I. The jet, whilst predicted to be at steady mass flow, is quasi-steady.
II. A large PR range is presented for a gaseous fuel.
III. The jet exists under impinging conditions with data obtained at four developmental instances.
IV. A high spatial resolution is provided.

The data in Figure 159 are presented such that any influence in ambient effects are highlighted; the in-jet PR effects are presumed to be taken care of through the inclusion of $\dot{m}_f$ and $(\rho_e/\rho_a)^{1/2}$. A key consideration, however, is the inclusion of the jet-induced recirculation effects. The impinging-induced rolling vortices displace the ambient air and set up momentum feeding into the jet. The strength of the vortices and thus ambient gas momentum is proportional to the in-jet velocity and dispersion rate at a given instance. Considering the $P_a < 1$ (PR320 and 400) scenarios, for $t > 215\ \mu s$ the entrainment coefficient is typically 65% higher than at $t = 215\ \mu s\ aSOI$. This deviation is presented in the top loft plot of Figure 159.

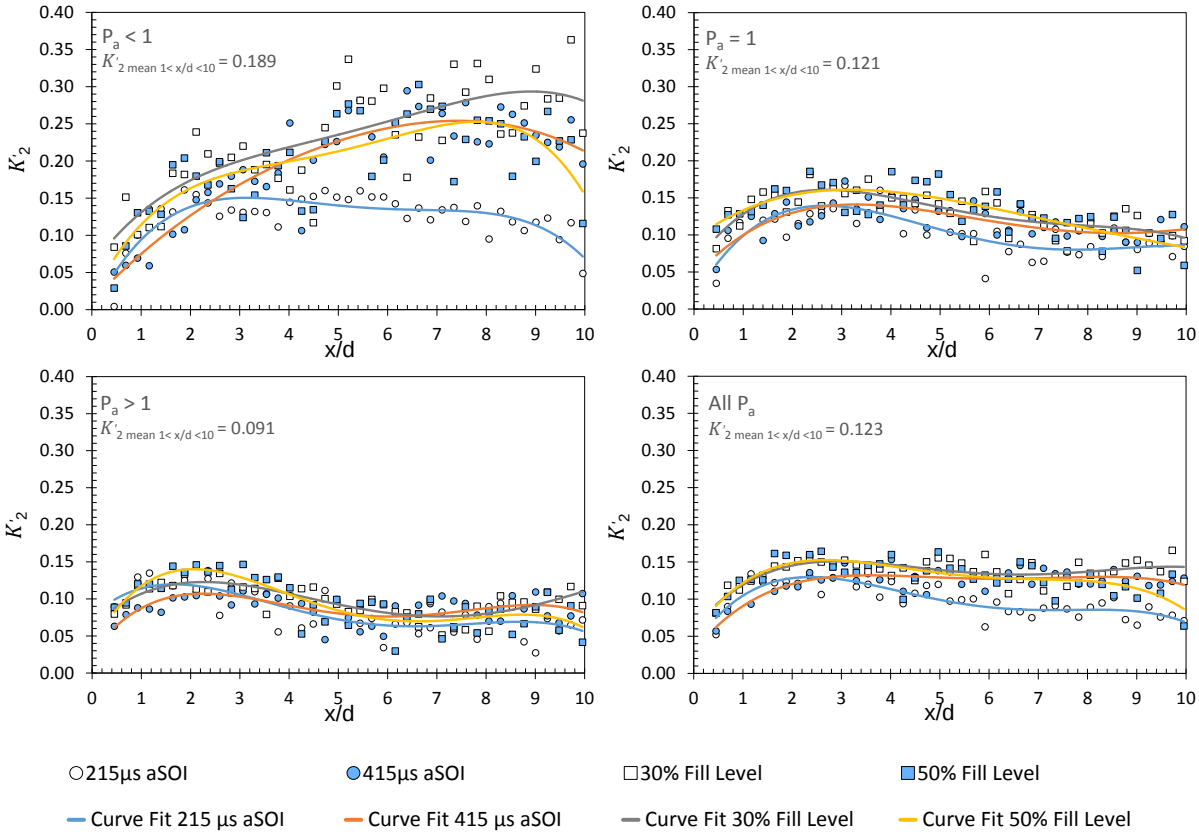

Figure 159, Entrainment coefficient, K'_2, in the jet nearfield for CNG Jet PRs (24.49, 27.59, 40, 41.38, 55.17, 60, 80, 120.00, 320 & 400) at four acquisition instances.

The impinging-induced vortices are shown to displace air into the nearfield entrainment region. Whilst the fuel jet does not feed fuel back into the nearfield, it is evident from Figure 160 that the rolling vortex increases the air velocity surrounding the nearfield. Evidently, the displacement effect is increased with both PR and time aSOI. This increase supports the ~65% higher K_2' value for the PR400 case (as presented) where the development of the rolling vortex is substantial for $t > 215\,\mu s$. It was expected, however, that the greatest momentum addition to the nearfield entrainment would occur where the tangential vortex velocities are aligned toward the nearfield, where the vortex is closest to the jet axis. This is perhaps why the PR400, 349 µs aSOI (30% fill level) shows an intense "connection" between the rolling vortex and nearfield region. It is evident also that the rolling vortex in the PR80 case is too weak to substantially affect the nearfield entrainment.

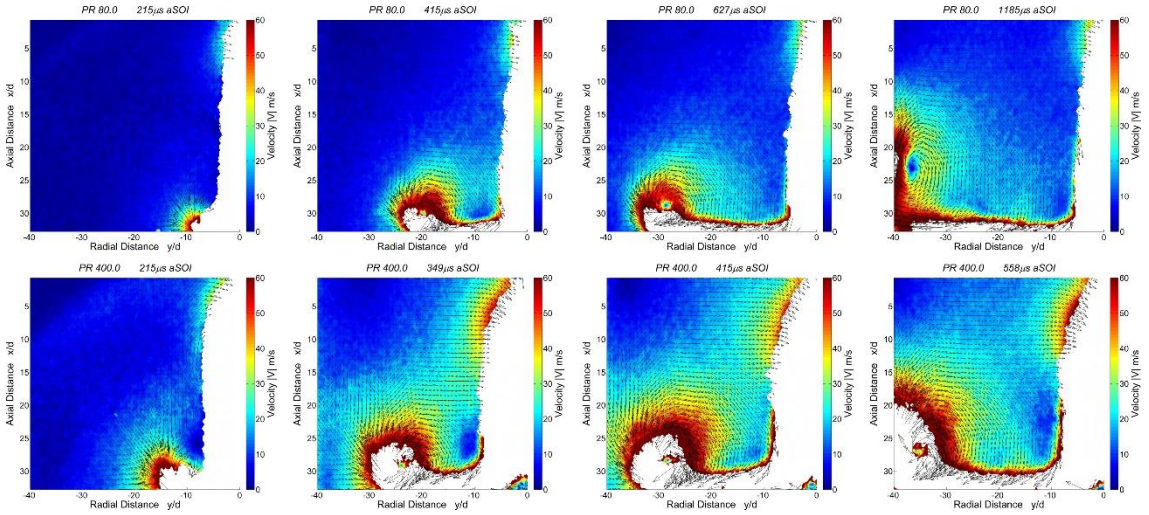

Figure 160, Impinging jet vortex development for PR80 and PR400 CNG Jets. First and last column represent 215 µs and 50% acquisition instances respectively.

In the first column of Figure 160, in both PR80 and PR400 scenarios, the reflected bow wave is present in the top left corner (a higher resolution version of Figure 160 is provided in Appendix X). Whilst largely unnoticeable and inconsequential (for this study), this unique feature - observable in most $t = 215\ \mu s$ impinging experiments - is worth mentioning. The higher PR scenario shows a stronger; larger and wider velocity gradient, and a further frontal location of the bow shock. The bow shock, qualitatively presented in schlieren images (i.e. Figure 125), was also shown to cause a relatively large disturbance in the ambient region in freestream PIV experiments at early aSOI acquisitions ($t < 215\ \mu s$) (not included in this work).

6.4 Implications for Engine Operation

Ultimately, a major concern for ignition quality is the velocity across the spark-discharge gap, with direction and turbulent fluctuation a consideration for flame propagation. If the velocity is too high than misfires may ensue, resulting in unburned hydrocarbon generation (among other consequences). This is of great concern for natural gas engine operation where the greenhouse gas potential of unburnt CH_4 significantly outweighs that of CO_2.

The injection of natural gas into a quiescent environment has shown that the resultant velocities, $|V|$, on the jet boundary (actual and one radial vector preceding) are on average 1.21 times greater than the mean nearfield velocities. For a more discrete analysis of the flow behaviour surrounding the spark plug, an ignition ROI was selected. This $10 \times 10\,mm$ ROI is situated 5 mm axially downstream with the left boundary located 20 mm to the left of the nozzle origin, and is the realistic location for the engine under consideration. Figure 161 depicts the ignition ROI alongside the bulk flow motion of the impinging CNG jet.

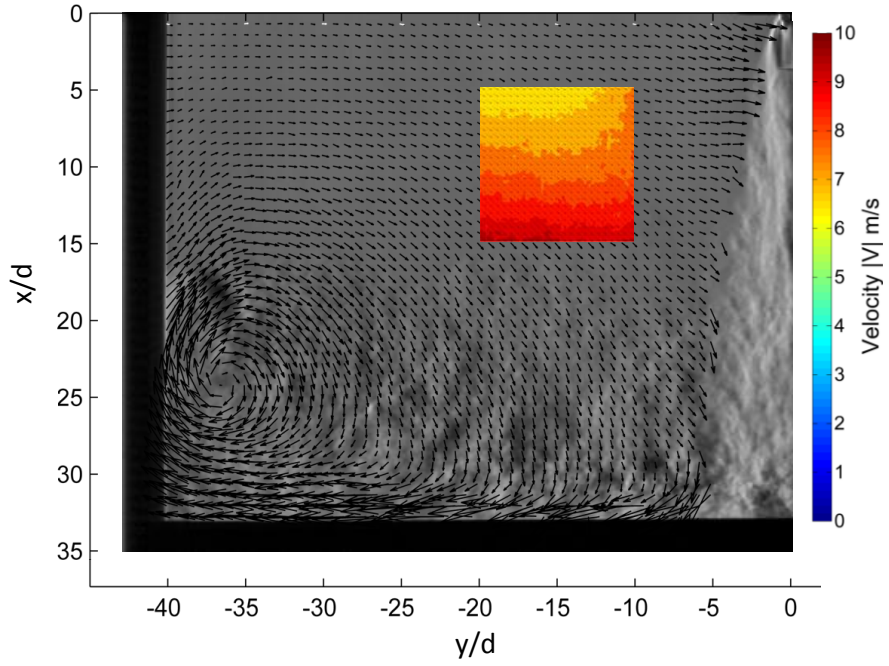

Figure 161, PR60, 50% fill level (1441 µs aSOI) impinging jet. Flow vectors and ignition region velocity contour inset overlaid on schlieren HSV image. Note: Jet core vectors removed for clarity.

Analysis of this constant ignition ROI reveals the expected flow behaviour induced by the high-pressure natural gas injection. These values are representative of quiescent conditions and, as such, are at the exclusion of in-cylinder flow effects. The values presented are, however, indicative

of the trends introduced by varying the injection PR and can be used in conjunction with in-cylinder studies.

The spatial mean of the resultant velocity, $|V|$, is presented in Figure 162 where it steadily increases in magnitude for an increasing PR. One discrepancy to note is the high velocity at PR320 and 400 for the early acquisition time of $415\ \mu s\ aSOI$. High relative velocities for the $415\ \mu s\ aSOI$ case were also seen in experiments involving constant dT times, thus indicating a high measurement consistency. The nearfield mean velocity profiles (U, V and |V|), which capture the effects of the jet expansion region, show similar velocity magnitudes for the three acquisition conditions (see: Figure 149 through Figure 151). The likely reason for the high velocity at PR320 and 400 is the fact that the acquisition time of 415 µs aSOI is indeed greater than the 30% fill level and thus depicts the intermediate flow velocity. As such, and as previously discussed (Section 6.3.1), the impinging jet has a dominant role in the nearfield ambient flow. The recirculation strength is therefore a key influence on the ignition flowfield.

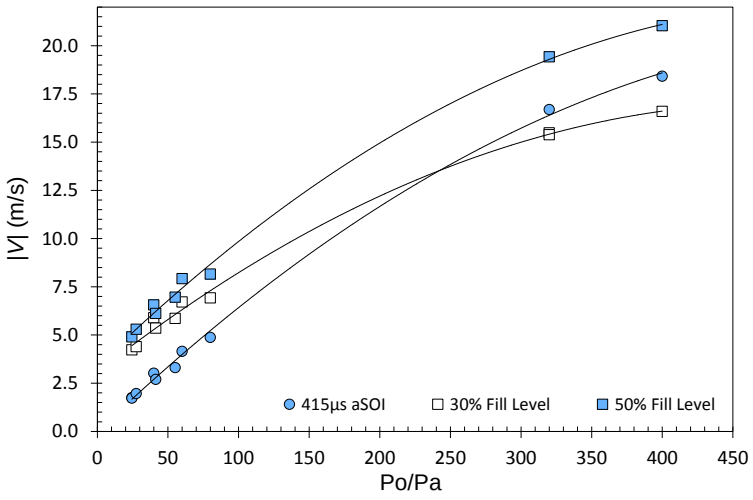

Figure 162, |V| within the ignition region.

Further representation of |V| is presented in Figure 163, which shows a clear trend of increasing magnitude with increasing PR and again, a general increase with $aSOI$ acquisition times. It is clear that the magnitudes present are within an acceptable ignition gas velocity range, but as indicated earlier the high velocity flows will alter the shape (and connection propensity) of the spark-plasma.

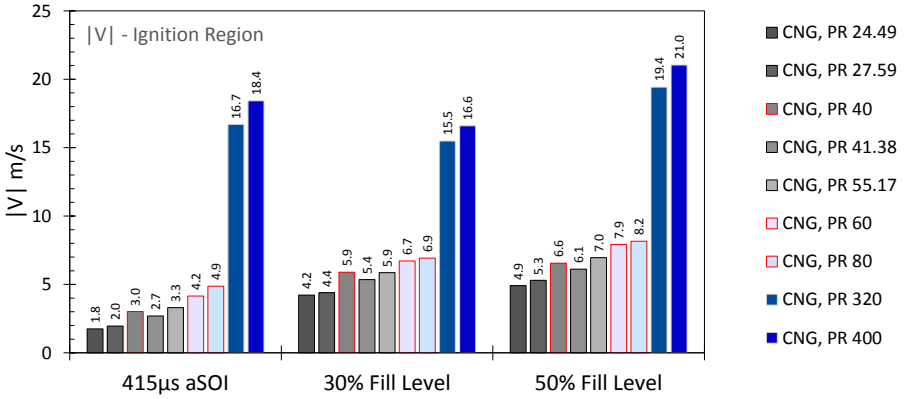

Figure 163, Ignition region mean velocity profile for three acquisition locations for high PR CNG jets.

Individual component analysis reveals that V changes direction based on the jet development. Note that the negative values indicate a flow direction toward the impingement surface. As discussed for the nearfield conditions, the flow initially opposes the fuel jet streamwise direction, a result of the counter-rotating vortex head and initial impinging effects. Moreover, at constant location (30 and 50% fill level) one would assume the direction component to be somewhat similar across the entire PR range, whereas in reality no clear correlation can be seen in vertical (axial) orientation. This suggests that the structure is influenced by secondary factors that cannot be resolved without considering the in-jet velocity distributions. The change in vertical direction occurs in spite of the identical piston boundary and acquisition at near-identical[14] jet-dispersion positions. Conversely, the coherence in the horizontal direction is significant, as the U velocity component grows in direct proportion to the PR and to a significantly large magnitude of $\sim 20\ m/s\ max$.

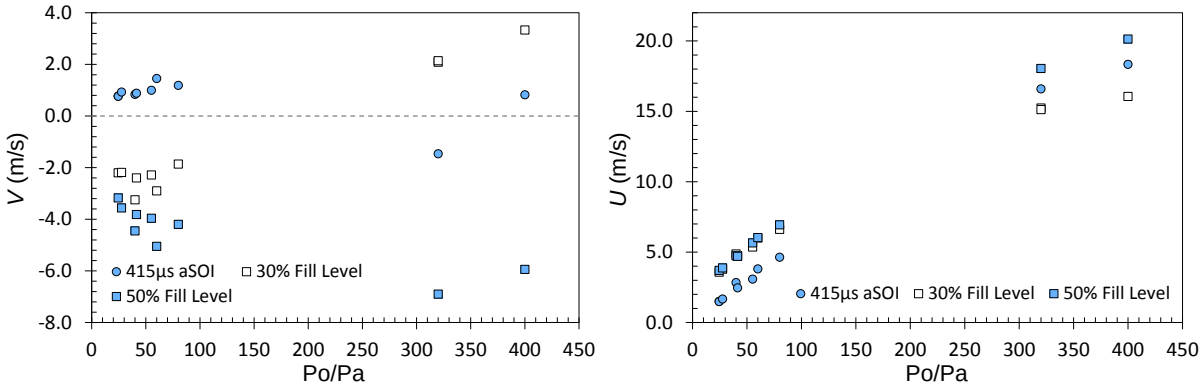

Figure 164, *V (left)* and *U (right)* velocity component for the ignition region for high PR CNG jets.

[14] A small deviation in position is expected for a given $\%\ fill\ level$ and PR. This deviation arises from any schlieren processing errors and uncontrollable timing shifts with injector SOI. These deviations are expected to be minor due to the processing accuracy and temporal resolution of the Schlieren imaging and the relatively low absolute timing difference of $\Delta t\ SOI$ to $t\ aSOI$ ($< 3\%$).

Spatial averaging across the ignition region is convenient for analytical purposes, but fails to reveal the discrete flow behaviour and the magnitude gradients. The velocity profiles for the range of PR and acquisition times are provided in Figure 165 through Figure 167, where more subtle features can be resolved.

At the fixed jet location of 30% fill level, the velocity distribution is governed by the strength of the in-jet velocities (PR dependent), with the highest PR cases forming a more coherent flow profile. The flow magnitude is distributed in a more radial fashion for an increasing PR. The six cases, $24.5 \leq PR \leq 400$, depicted in Figure 165 through Figure 167, show that the scale changes for the highest two PR cases. It can be seen that for $PR > 60$ the propensity for the flow velocity magnitude to exceed 10 m/s is quite high, whereas the cases in which PR is less than or equal 60 to display a scattered distribution of velocities below 10 m/s.

The mean resultant velocities in the ignition region (1.8-21.0 $\mathrm{m/s}$) are within the ignition stability threshold of conventional spark plugs. At the highest PRs considered, 320 and 400, substantial stretching of the plasma-discharge is expected if the flow velocity is unperturbed by the electrode arm. Spatially, the resultant velocity concentrates toward the jet axis with an increasing PR. As expected for greater aSOI acquisition times, the magnitude intensifies toward the lower portion ($\mathrm{x/d} = 15$) where the impinging flow dissipates toward the ignition region.

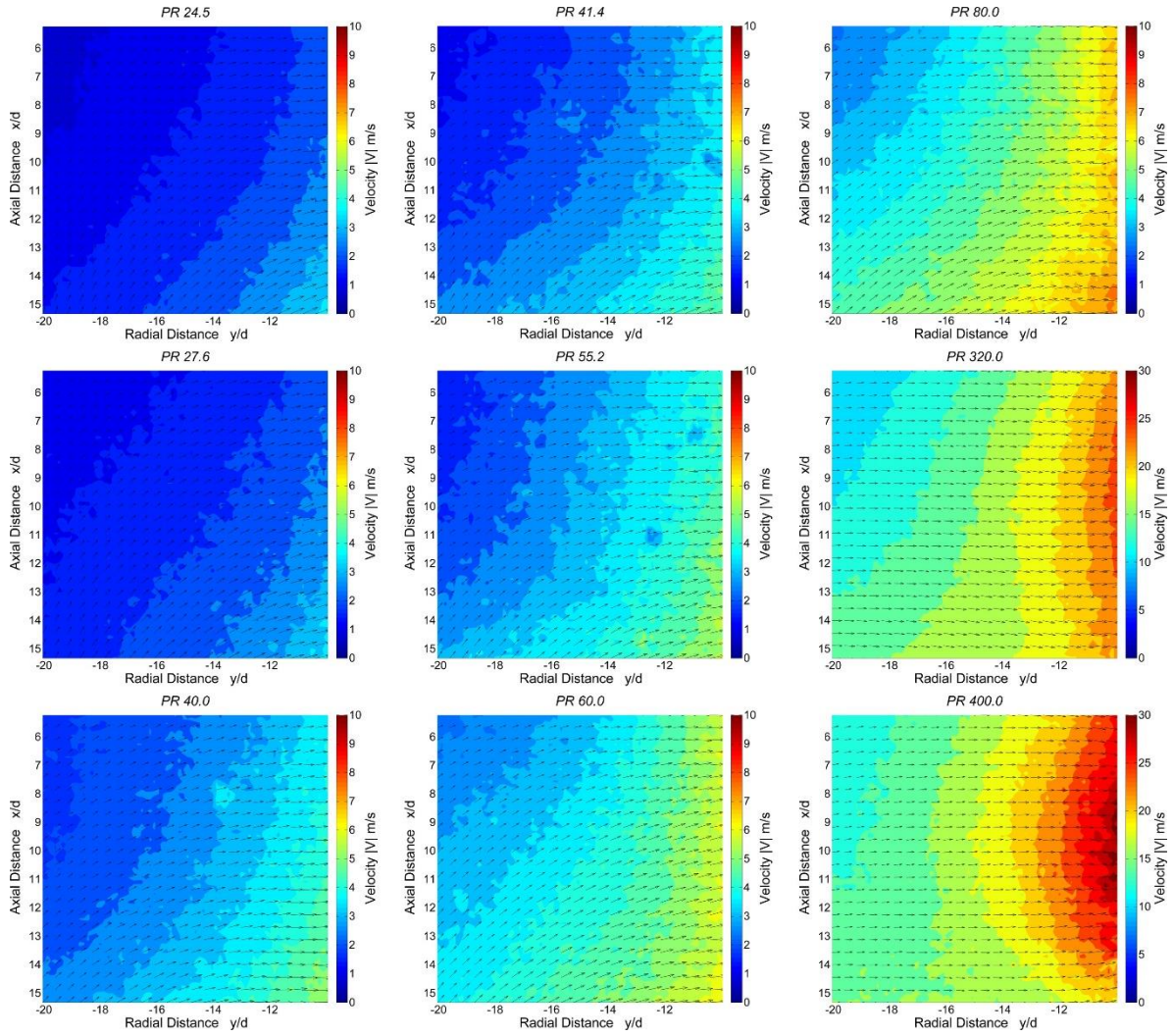

Figure 165, Velocity map for the Ignition ROI at constant time of 415 µs aSOI. Every third vector displayed. Note: scale for 24.5≤*PR*≤80 is 0-10 m/s whereas PR>80 is 0-30 m/s.

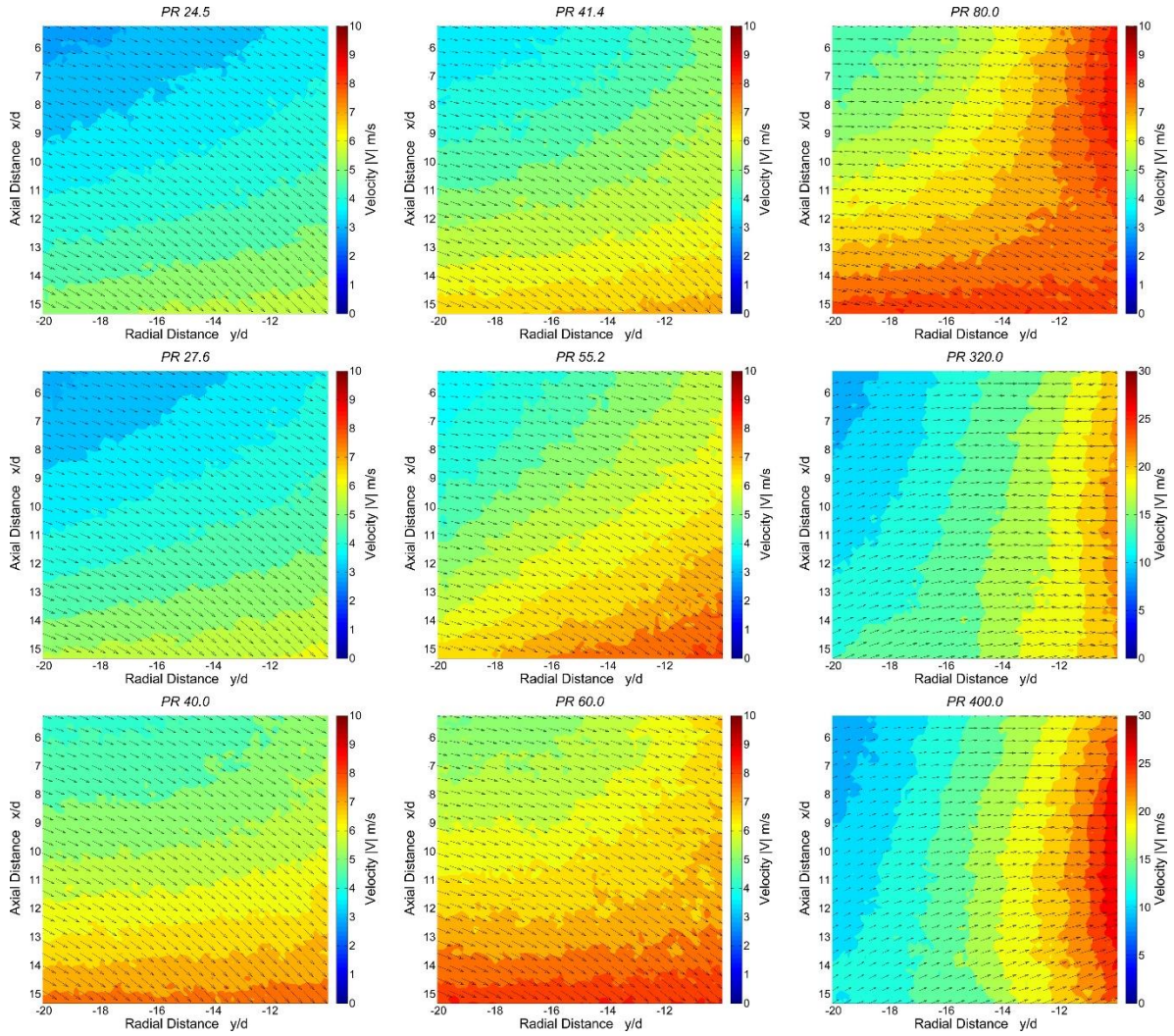

Figure 166, Velocity map for the Ignition ROI at constant location of 30% fill level. Every third vector displayed. Note: scale for 24.5≤PR≤80 is 0-10 m/s whereas PR>80 is 0-30 m/s.

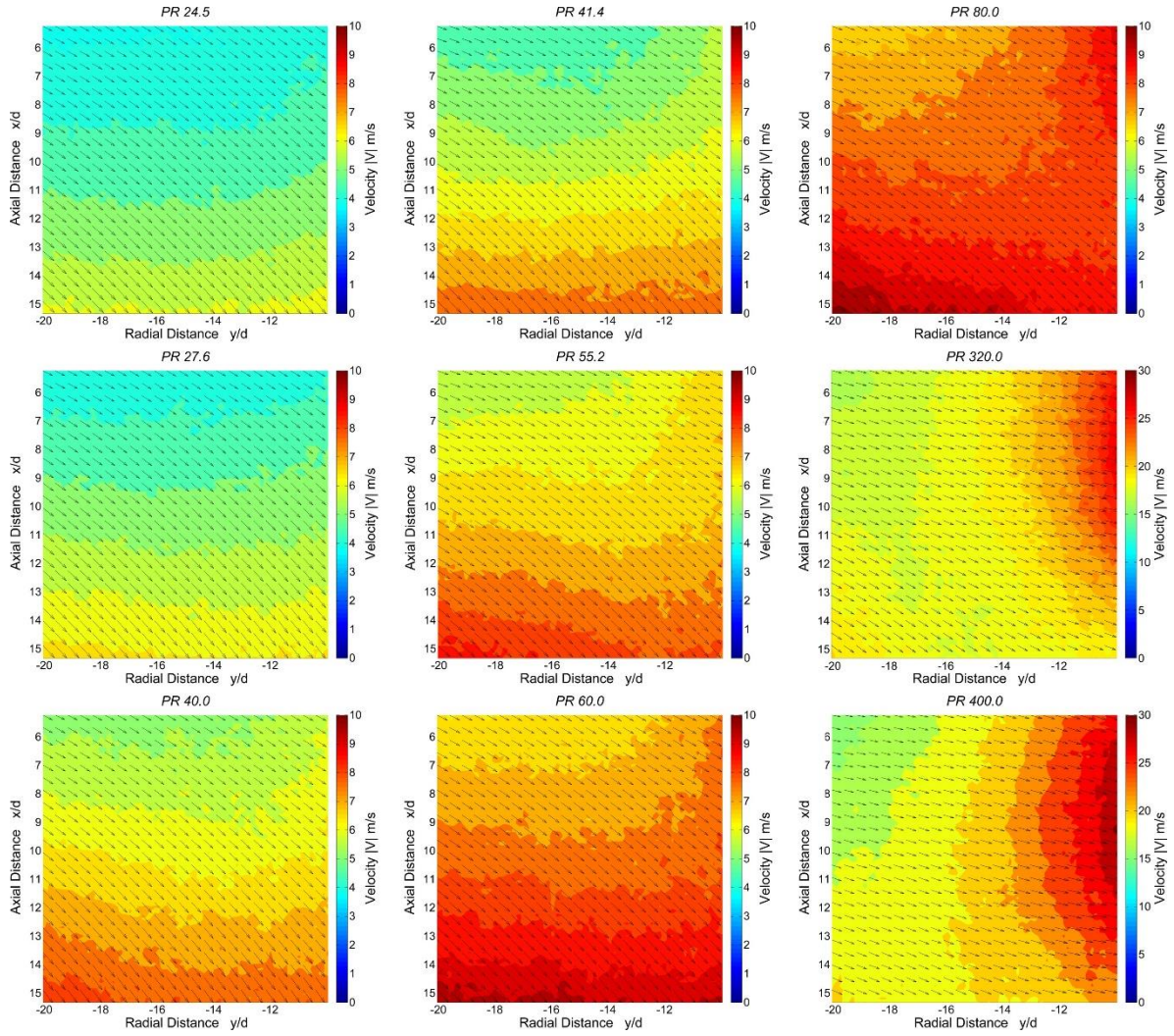

Figure 167, Velocity map for the Ignition ROI at constant location of 50% fill level. Every third vector displayed. Note: scale for 24.5≤PR≤80 is 0-10 m/s whereas PR>80 is 0-30 m/s.

On average the nearfield mean velocity ($|V|$) surrounding the jet was around three times higher than the mean flow in the ignition region. This is a direct result of the spatial separation between the jet and the interrogation area. This trend is repeated in the velocities measured at the jet boundary[15] - the region at which the ambient entrainment is calculated. It can be observed from Figure 168 that nearfield and boundary velocities are in fact quite similar at the lower PRs. Once more the PR relationship is largely logarithmic/power-law in nature.

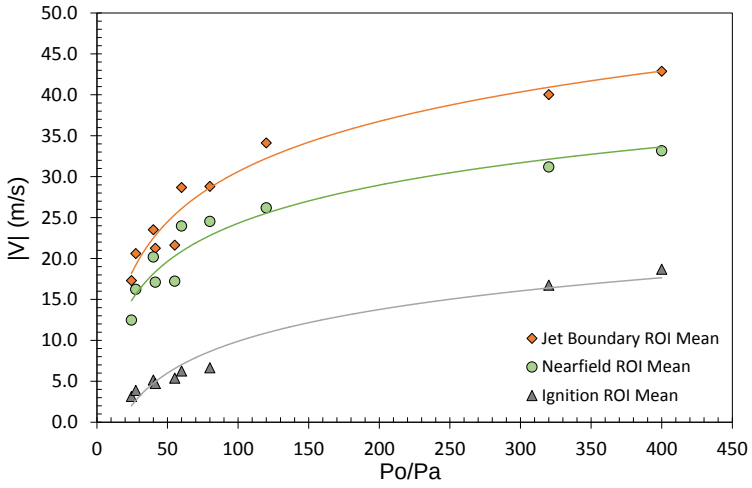

Figure 168, Acquisition mean |V| comparison for the jet boundary, nearfield and ignition regions for high PR CNG jets. Excludes acquisitions at 215 µs aSOI.

Having successfully characterised the ignition region flow velocity profile, attention now turns to the energy levels associated with the flow. The turbulence is profiled using the turbulent kinetic energy method, where the instantaneous velocity fluctuations, u' *and* v', are accounted for in sample rms values u_{rms} *and* v_{rms}.

The turbulent kinetic energy for the flow is considered according to Equation 82, where the two-component flow is assumed to account for two-thirds of the total flow energy. This assumption is based on isotropic mass-based energy. Isotropic flow is assumed on the basis that the fuel flow delivery is asymmetric about the axial centreline and the wall ("cylinder") contact surface is normal to the contact flow direction. In reality, a degree of anisotropic turbulence would be expected; to this end the unmeasured third velocity component, w, is unaccounted for but is assumed to be equal to 1/3rd of the total energy budget.

[15] The boundary and the preceding velocity are taken to smooth any discrete perturbation at the boundary. The velocities preceding the boundary were highly representative of the boundary velocities and thus not expected to alter the absolute magnitude.

Equation 82, Turbulent Kinetic Energy for two velocity components. Source: (Lappas, 2003).

$$TKE = \frac{3}{2}\left(\frac{{u_{rms}}^2 + {v_{rms}}^2}{2}\right)$$

The mean TKE values generally increase with the PR and the time $aSOI$. The mean TKE is essential in determination of the flame propagation effects of kernel development. Increases in the bulk mean TKE should give rise to the turbulent-flame speed and to the flame surface area. This rise in turbulence intensity has been shown to increase both power output and fuel consumption efficiency (Karhoff et al., 2013). The distribution of the TKE in the ignition region is largely homogenous for $PR \leq 80$ within individual acquisition times. Amid a largely uniform profile, the ignition region is scattered, with local high-energy regions. There is, however, a tendency for stronger energy fluctuations nearer the jet axis (approaching $y/d = 0$). Examples of the spatial TKE distributions are given in Figure 169.

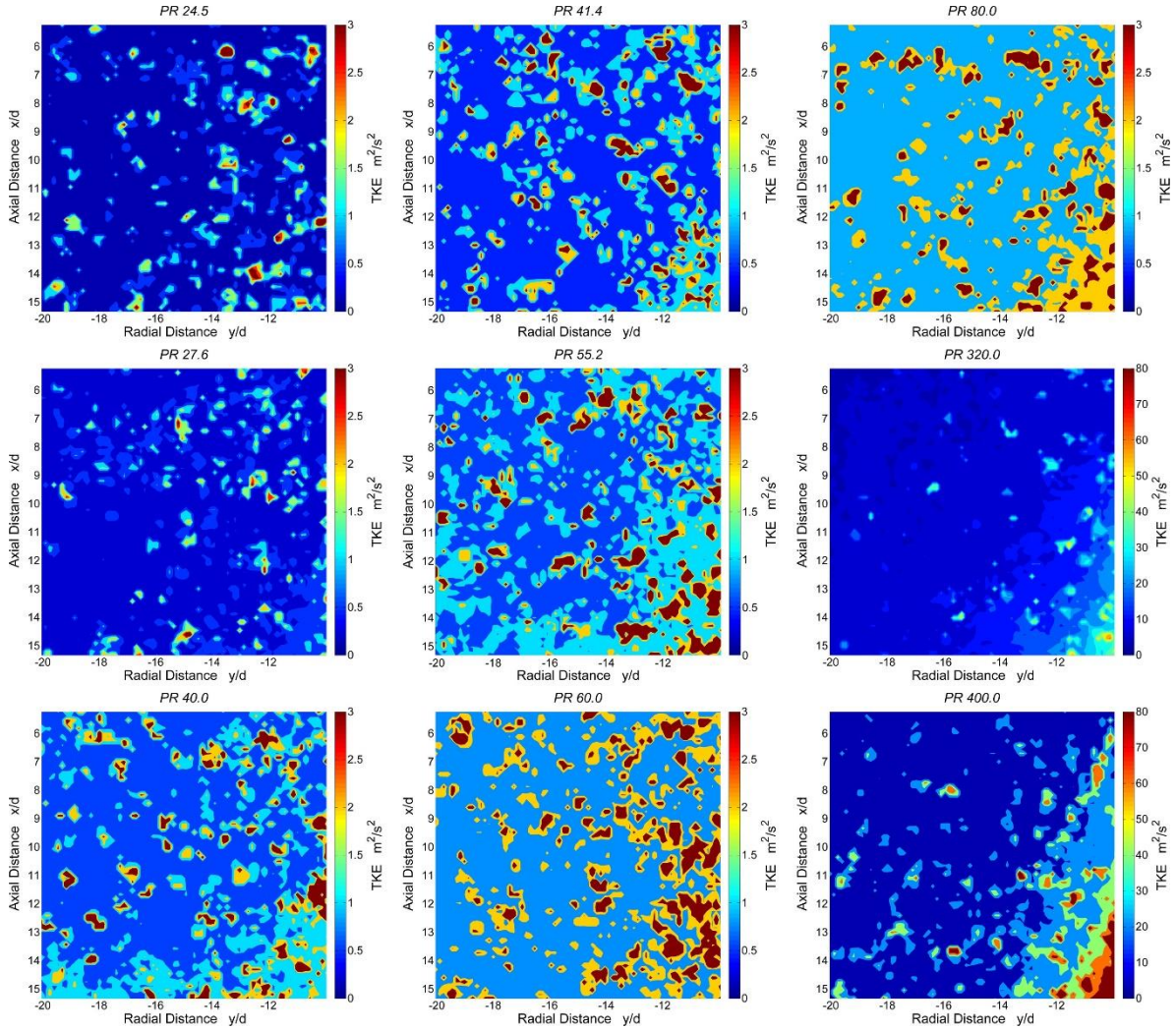

Figure 169, Turbulent kinetic energy for 30% fill level, ignition region for high PR CNG jets. NOTE: PR320 and PR400 are scaled to 80 m²/s² where others are scaled to 3 m²/s².

The mean TKE values for $\mathrm{PR} \leq 80$ are largely similar for all acquisition times. Generally, good linearity exists in this region too, allowing predictability up to moderately high PRs within foreseeable engine conditions. The largely consistent TKE values indicate that as the jet continues to impinge, rolling up nearer the ignition region, the overall jet flow is steady. This is supported by little to no change in TKE magnitude between 30% and 50% fill level, even though a substantial time aSOI has passed (200 to 1069 µs for PR400 and PR27.5 respectively). Moreover, this is in spite of the 50% fill level jets bordering the ignition region (see Figure 167) and still receiving momentum from the steady-state fuel delivery. Two-component TKE values, $0.4\ to\ 2.6\ m^2/s^2$, are supportive of good combustion development; similar magnitudes are achieved when decomposing the large bulk-flow fluid motions (Karhoff et al., 2013, Rimmer et al., 2009).

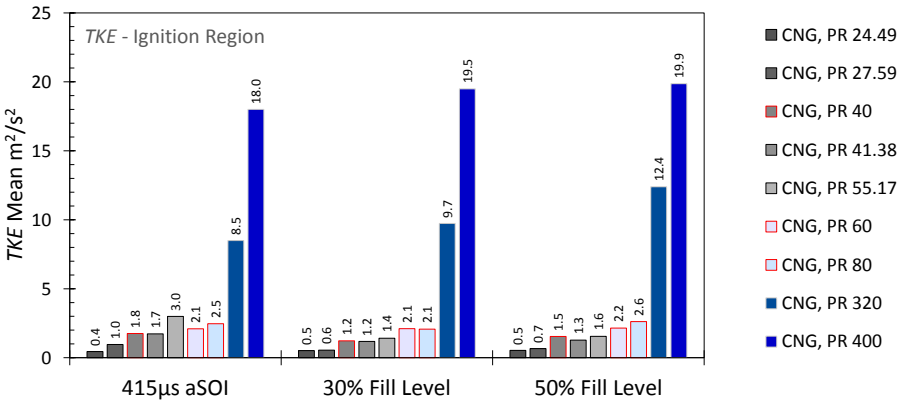

Figure 170, Turbulent Kinetic Energy mean for the ignition region of high PR CNG jets.

Beyond PR80, high TKE levels are present. These high-turbulence fluctuations are present for all three acquisition times, and as such it is expected that the fluctuations are induced from the high in-jet velocity forcing a strong ambient air momentum. More specifically, the ignition region turbulence level is expected to be heavily influenced by the large shear-layer thickness (Figure 136) encroaching on the ignition region (e.g. Figure 134). The concentration profile is best viewed via Figure 171 where PR60, 80, 320 and 400 are compared at the three acquisition locations. Two conclusions about TKE influences can be drawn: the jet development time (as captured for the acquisitions) is relatively inconsequential, and the PR effects are significant.

The shear-layer thickness, as measured at the triple point location, doubles in size across the PR tested range (from 0.83 to 1.63 mm). In fact, for a given time aSOI the jet width at the triple point, $\mathrm{y_{TP}/d}$, is approximated through a positive power-law relationship for a given PR. In contrast, between the earliest and latest aSOI instances there is relatively little change in the shear-layer thickness/jet width as most of the development occurs prior to $415\ \mu s\ aSOI$. For the TKE comparison in Figure 171, it can therefore be inferred that concentration/intensity levels nearest the jet centreline (-10 $\mathrm{y/d}$) are due to the encroaching shear-layer as a consequence of PR. The jet is

nearest the ignition region for PR320 and PR400, where the boundary encroaches within 3.5 and 1.97 mm of the ignition region respectively.

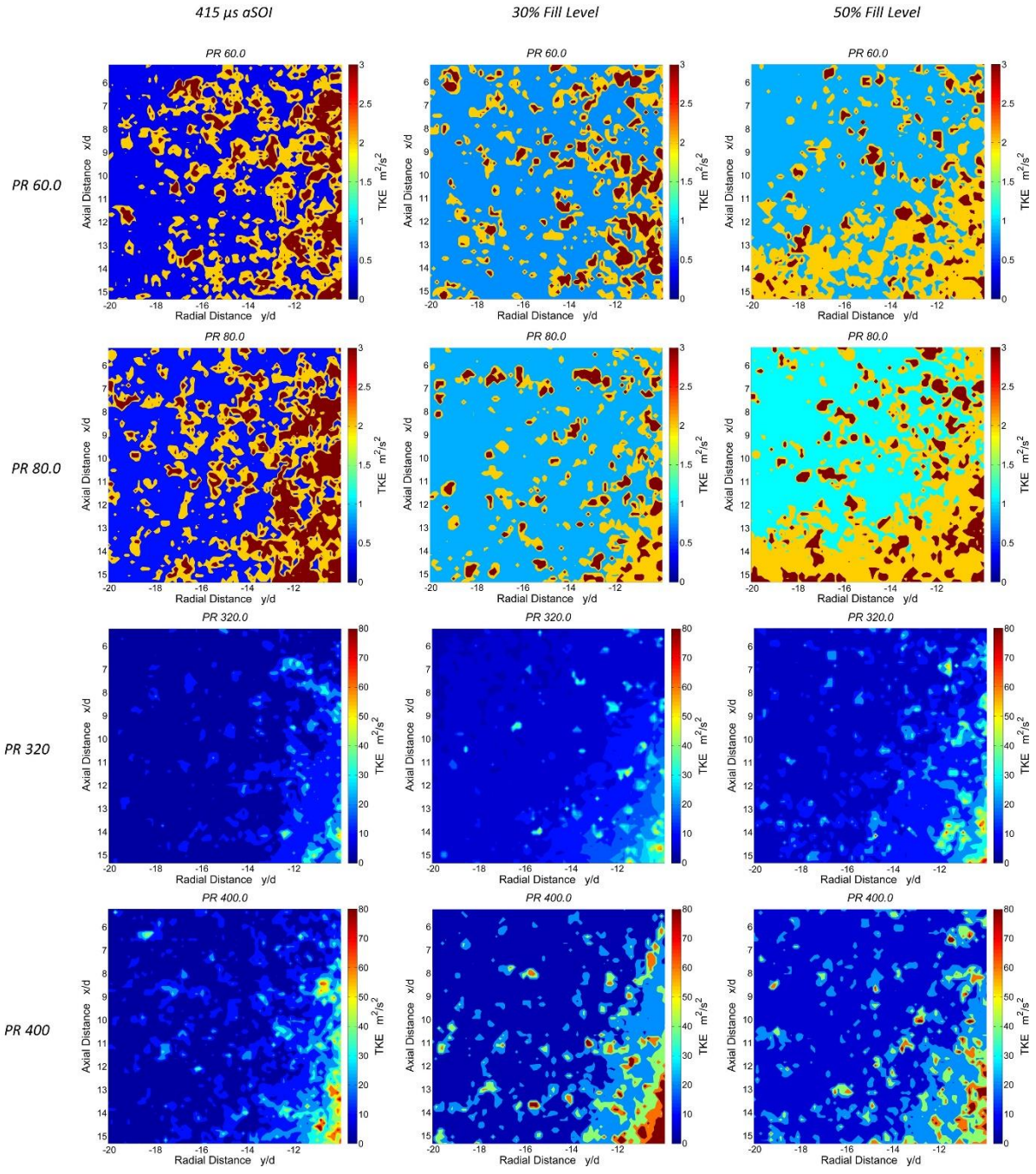

Figure 171, TKE distribution for PR60, 80, 320 and 400 CNG jets. Note: Scale changes for PR>80.

The mean rms values, U_{rms}, are normalised with respect to U and are shown below in Figure 172. Three observations can be made from this comparison. Firstly, the levels of normalised velocity fluctuation for both constant location experiments (30% and 50% fill level) are consistent with PR. Secondly, the magnitude of U_{rms} is greatest for the 415 µs series, where on average it is 1.7 times greater than in the constant location series. Finally, inconsistent U_{rms}/U levels are also seen for

the PR range in 415 µs. This is further evidence for the previous claim that the flow becomes more coherent and steady after surface and wall impingement. Since all measurements were conducted under pulse separation times which allowed a consistent particle displacement (~2-3 pixels), this TKE and rms comparison is believed to be unbiased.

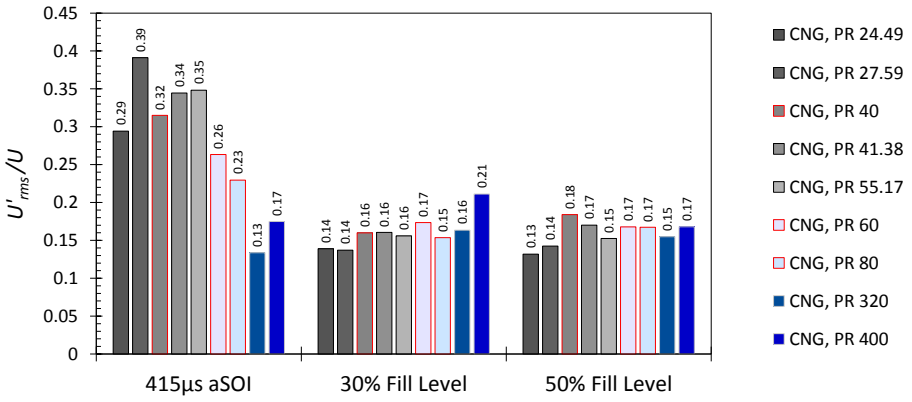

Figure 172, U'_{rms}/U in the ignition region of high PR CNG jets.

6.5 Chapter Summary & Conclusions

The following conclusions were drawn from the analysis of impinging CNG jets (conducted using both schlieren high-speed imaging and PIV) presented in this chapter. These conclusions differ from those of the previous DI-CNG chapter, where the focus is on mixture formation.

i. The newly developed empirical model of the dispersion rate of high pressure CNG jets issued in late injection conditions defines the jet behaviour across the three interaction regimes: freestream, surface (piston crown) and wall (cylinder walls) impingement. The model is representative of a broad PR range (8.3<PR<400) with a mean uncertainty of $\sim 6\%$, and is expressed in Equation 78 and Equation 79.
   Such a representation is useful in comparing jet growth and dispersion rates against PR, demonstrating the benefits of increasing or decreasing the PR against a benchmark. PRs above 120 or below 30 show diminishing returns in mixing/dispersion time for increasing or decreasing the PR.

ii. Condensation of a fuel component is a useful qualitative measure when analysing nearfield compressible structures. This phenomenon reveals the engulfment of the shear-layer immediately after the Mach disc for selected experiment image samples.
   Particles entrain into the jet core through this mechanism and are first sighted $\sim 1\mathrm{x/d}$ downstream of the Mach disc.

iii. The novel segmentation method presented herein successfully removes the jet utilising typical PIV data. It defines the jet boundary at a high fidelity and permits execution of the nearfield flow analysis.

iv. The direction of the flow in the ambient region is dominated by the influence of the jet vortex head in early- and non-impinging conditions. For the freestream cases, strong recirculation (outward and upward) emanates from the vortex head mid-position. This determines the structures of the near-jet ambient flow, as evidenced through the strong axial velocity component (V) and the weak radial component (U) at both the nearfield and ignition (far-field) regions for the early $215\ \mu s$ aSOI experiments.

v. The impinging rolling vortex at $t > 215\ \mu s$ produces a substantial momentum on the ambient air, aiding in nearfield entrainment by $\sim 65\%$ for the two highest PR cases: (PR320 and PR400). The air displacement imparted is dependent on PR and the vortex radial location.

vi. The nearfield entrainment coefficient is constant; on average $K_2' = 0.123$. This is the highest known K_2' spatial resolution for impulsively started fuel jets.

vii. The mean resultant velocity in the three spatial regions investigated (nearfield jet boundary, nearfield region and ignition zone) show a (largely) logarithmic trend for an increasing PR. The nearfield and ignition ambient regions shows a clear separation in absolute velocities. Comparatively, the boundary profile within the nearfield is similar to the entire nearfield region for $PR \lesssim 60$. These trends were indicative of jet delivery times where $t > 215\ \mu s$.

viii. The mean resultant velocities in the ignition region (1.8-$21.0\ \mathrm{m/s}$) are within the ignition stability threshold of conventional spark plugs. At the highest PRs considered (320 and 400), substantial stretching of the plasma discharge is expected if the flow velocity is unperturbed by an electrode arm.
Spatially, the resultant velocity concentrates toward the jet axis with an increasing PR. As expected for greater aSOI acquisition times, the magnitude intensifies toward the lower portion ($\mathrm{x/d} = 15$) where the impinging flow dissipates toward the ignition region.

ix. The two-component turbulent kinetic energy within the ignition region is relatively minor for $PR \leq 80$ across the three acquisition instances ($0.4 < 3.0\ \mathrm{m^2/s^2}$). However, at the highest PRs considered, PR320 and 400, substantially large TKE levels are achieved (c.a. 8.5 and $19.9\ \mathrm{m^2/s^2}$, respectively). These high mean turbulence fluctuations are hypothesised to occur as a direct consequence of the encroaching jet shear-layer. Secondary contributions are hypothesised to arise from the intensity of the impinging vortex recirculation. This is evidenced through the measurement consistency at all three acquisition times and the large TKE levels concentrating discretely toward the jet centreline ($\text{-}10\ \mathrm{y/d}$) and lower portion of the ignition zone.
The turbulence induced by the late injection event is similar to the levels expected from the decomposed in-cylinder bulk flow. These expected additions to the in-cylinder turbulence levels are generally conducive to flame-propagation.

THIS PAGE IS INTENTIONALLY BLANK

7. Conclusions & Recommendations

7.1 Conclusions

This thesis provides a detailed characterisation of the behaviour of gaseous fuel jets issued impulsively from automotive fuel injectors. Such a characterisation was needed to develop a more complete understanding of targeting and dispersion of the fuel, transient fuel jet behaviour at the nearfield region, and the effects of fuel jets on the in-cylinder flow. The behaviour of a fuel jet or flow feature is defined as the physical changes (spatial and temporal) the feature undergoes whilst interacting with its environment. The main focus of this work is on high pressure ratio (PR) CNG fuel jets issued at conditions relevant to spark-ignition engines. The necessity for such a study is concisely outlined in Section 1.1. The study uses schlieren high-speed photography and particle image velocimetry (PIV) to quantify the dynamic and instantaneous flow properties of the fuel jets and their surrounding environment. The fuel jets were delivered into a quiescent nitrogen medium contained within a constant volume chamber (CVC). This practice allowed the in-cylinder pressure and flow caused by gas-exchange and piston motion to be decoupled from the fuel delivery process. The CVC also permitted the inclusion of a stationary boundary to replicate the cylinder boundary locations at 50° bTDC.

Fuel jet targeting is a measure of the geometric boundaries of the jet at any given time. This can be measured, for example, through the maximum axial and radial penetration. In this study, two scenarios were considered; a low pressure ($2.80 < PR < 12.00$) fuel jet issued from a typical port-fuel injector and a high pressure ($40 < PR < 400$) jet issued from a custom-made direct injector. For the low PR jets three fuels were tested: CNG and hydrogen (and 25%CH_4/CH_4 to a lesser extent). For the high PR tests CNG was studied almost exclusively. Targeting was measured in high resolution (temporally and spatially) for early after start of injection times (<1 ms), which were unresolved in existing studies.

Dispersion of the CNG fuel jet ($8.30 < PR < 400$) within the cylinder was measured for late-injection engine-like conditions (50° bTDC) where the fuel jet interacted with the piston crown and cylinder wall surfaces. The jet dispersion is a measure of the how fast the fuel jet, which is entraining and mixing with the quiescent ambient air, propagates through the cylinder.

The transient fuel jet behaviour at the nearfield region was measured through the Mach disc location and diameter, and the radial penetration and shear-layer thickness at the Mach disc location. The nearfield region of transient fuel jets issued at high pressure ratios is an area which has been insufficiently detailed previously. The nearfield is the region within ten nozzle diameters downstream of the jet exit plane. The evolution of the nearfield compressible structures (Mach disc location and diameter and reflection angle) for a highly underexpanded jet ($NPR > 2$) were measured with high fidelity. This is the first study to comprehensively show the histories of the compressible structures of high PR fuel jets. Instantaneous PIV measurements were used to corroborate the dynamic schlieren measurements. The incompressible jet structures such as the shear-layer thickness and jet radial width were also measured and correlated with the compressible features.

Outside of the fuel jet, the effects of fuel jet on the in-cylinder flow behaviour were measured. This is the first experimental study which addresses the late injection of high PR ($40 < PR < 400$) CNG gas, and provides detail of the flow processes and consequences of high PR fuel delivery. To this end, the nearfield entrainment of ambient air is quantified and the flow (velocity and turbulent kinetic energy) within the ignition zone was measured. These entrainment and flow measurements are unprecedented for transient fuel delivery.

This work has shown that transient fuel jets are complex in nature and are greatly affected by the operational constraints of fuel delivery in a spark-ignition engine. The complexity is shown for example between the influences of the normal shock within the jet core on the turbulent air-fuel shear-layer, both of which are functions of the delivery conditions and constraints: pressure and density ratio and injector needle mechanisms. Conclusions for the specific research questions can be found at the end of Chapters 5, 6 and 7. The conclusions for three main research objectives are as follows:

Objective I – To characterise the targeting and dispersion behaviour of the gaseous fuel jet

Characterisation of the freestream jet development in axial and radial directions provides clear expectations of targeting behaviour prior to in-cylinder surface contact. Both low- and high-PR jets were shown to behave as an uninhibited free-jet until very near surface contact. This was shown for very late injection conditions, 50° bTDC (stratified engine operation), with the “piston crown” located ~33.4 mm below the injector tip.

At low pressure and density ratios ($2.80 < Po/Pa < 12.00$ & $0.31 < \rho o/\rho a < 6.85$) the penetration histories of the CNG jets were shown to fall into distinct groupings according to NPR. Three distinct penetration groups were catergorised by; $NPR < 2$, $2 < NPR < 4$ and $NPR > 4$. It was also observed that scaling with the diameter-equivalent normalisation technique (Equation 22); a method that utilises the isentropic nozzle exit density and velocity, does not collapse the CNG

and hydrogen fuel jets to single profile. A shift in penetration rate ($\Gamma{\sim}6\%$) and 'time-base' (66%) is observed between the fuels. For the individual fuels, however, a single collapsed profile was observed.

For direct-injection conditions at high PRs ($40 < PR < 400$) the CNG jet axial penetration were observed to scale to a single time-dependent profile with good agreement. A variation of <3% was observed between the PR jets tested and the linear penetration profile. This is the largest range of fuel jets to be tested within a single study. Additionally, the normalised penetration rate ($\Gamma = 3.19$) was in close agreement (~3%) with the literature (i.e. (Hill and Ouellette, 1999)).

Comparing the ensemble CNG data to a PR60 hydrogen example, a shift in the penetration rate (albeit insignificant at 1.5%) and 'time-base' offset (29%) is observed. This misalignment is substantially lower than what was observed for the low PR PFI cases. For the transient jets tested, it is evident the diameter equivalent model does not adequately reduce multiple fuel jets to a singular penetration profile, although it is extremely successful for a single fuel.

The time for a CNG jet to disperse inside a particular cylinder volume was observed to collapse to a single relationship between PR and fill time. The dispersion rate was measured across the three stages of jet development - freestream, flat-surface and wall impinging, where the cylinder geometry represents an engine time of 50° bTDC. For the wide range of CNG PR tested ($8.3 < PR < 400$), a mean measurement-to-prediction uncertainty of $\sim 6\%$ was recorded. The dispersion model can be used to evaluate the time it takes a particular PR jet to propagate in an engine cylinder - which includes the jet's entrainment and mixing with the ambient air. A relative assessment can shown the gains or losses in cylinder filling time when the PR is increased or decreased, respectively. For the example given of a PR60 CNG jet; PRs above 120 or below 30 show diminishing returns in mixing/dispersion time.

Objective II – To characterise the transient jet behaviour near the nozzle exit region (nearfield)

The internal injector geometry was shown to influence the geometry of the compressible flow structures. For example, the presence of the needle reduced the Mach disc location by ~45%, at steady-state conditions for a PR60 CNG jet. This reduction in the barrel length will inevitably reduce the overall jet-core size. A reduction in jet core size is expected to leave more volume for air-fuel mixing to take place. This is evidenced most clearly through the depiction of entrained ambient flow. The nearfield ($x/d < 10$) compressible structures are impenetrable to ambient flow where it is seen that $2{\sim}3x/d$ downstream of the Mach disc ambient particles begin to be entrained into the jet core region. Turbulent swirls emanating from the shear-layer are also occasionally observed to enter the jet core region at a similar downstream location.

In transient conditions the Mach disc location and diameter were shown to correlate strongly with the needle lift profile. At the nearfield the incompressible flow features, such as the spread angle and shear-layer thickness, were shown to develop in proportion to compressible flow features. This result highlights the importance of including the dynamic internal geometry of the injector when modelling fuel jet behaviour, a typical omission in the numerical modelling field.

The influence of the needle on compressible and nearfield incompressible flow presents an opportunity for control mechanisms to alter the state of the jet, and the mixing level, through adjusting the needle-lift. Thus rate-shaping techniques, commonly applied to liquid fuel delivery, may provide enhanced gaseous fuel delivery. This work is the first to elucidate the effects the internal injector geometry has on the nearfield flow structures for high PR fuel jets (i.e. Section 5.3.1).

Objective III – To characterise the effects of the jets on the in-cylinder flow and turbulence

The effects of the high PR CNG jet on the ambient in-cylinder flow and turbulence were studied for two regions of interest; the nearfield and the spark-plug ignition region. It was shown that the ambient nearfield flow velocities are substantially influenced by the jet. The nearfield ambient flow was analysed through employment of a novel processing method where the jet region was segmented from the ambient flowfield through local filtering of the PIV scalar quantities. This method provides a highly resolved and accurate determination of the jet boundary, and thus allowed quantification of the ambient flow including air entrained into the jet.

For the range tested, $40 < PR < 400$, the nearfield region is characterised by relatively large mean flow velocities, $\sim$10-30 $\mathrm{m/s}$, driven by even higher mean jet-boundary velocities of $\sim$17-42 $\mathrm{m/s}$. The radial velocity component, $\bar{u}$, heavily augments flow within these regions while the axial component, $\bar{v}$ makes a minor contribution. The dominant radial in-flow defines the entrainment of the jet. Moreover, for the impinging jets considered, the time after start of injection was shown to determine the orientation of the flow. For the earliest acquisition, 215 µs aSOI, where the jets were either free or only slightly impinging, the ambient flow was oriented in an axial direction – opposing the jet flow. This flow structure is attributed to the role of the jet-tip vortices, recirculating air back into the nearfield. Increasing the aSOI time allows the role of the jet-tip to be removed (the jet is now always impinging), meaning the near-pure radial component is driven from the bulk convection from free (pressure-differential led entrainment) or forced (impinging roll-up vortices) methods. The forced convection effects are clearest when the entrainment rate is analysed.

Ambient air entrainment rate is shown to be a function of upstream and downstream pressure and mass delivered when considering the turbulent jets studied in this work. The entrainment coefficient, K_2', which is determined by normalising the entrainment rate and the injected mass flowrate to the fuel density ratio (Equation 37). The coefficient was observed to be constant across

the nearfield region ($x/d < 10$) with a mean value of 0.123 for $24.49 < PR < 400$ jets at four aSOI instances. This is in line with some of the lower values reported in the literature for steady-state jets (Boguslawski and Popiel, 1979, Crow and Champagne, 1971). This work is the first to show the consistent nature of K_2' for transient fuel jets, tested over a wide range of high pressure ratios obtained at several acquisition times aSOI.

For the highest-PR jets (PR320 and PR400) where the high-velocity impinging jet imparts a large momentum on the ambient flowfield, a large entrainment rate is observed which was shown through the increase in the normalised metric K_2' by $\sim 65\%$. The convection of ambient air is driven by the large and strong vortices traveling along the impingement surface. The connectivity between the vortex displaced air and the nearfield entrainment is strongest when the vortex is largest and nearest the jet centreline. Specifically, when the largest magnitude vectors at the vortex upper boundary aim toward (tangentially) the nearfield, the air displacement into the nearfield will be greatest. When the jet has developed to these conditions, the entrainment coefficient (K_2') is shown to increase $\sim 65\%$. This highlights the pivotal role that the impinging, high-PR jet has on the ambient nearfield region and in turn the jet's ability to mix, and thus form a combustible mixture. Moreover, this study is the first to highlight and quantify the link between the rolling jet vortex and the nearfield entrainment rate.

In addition to the ambient nearfield region, a detailed study of flow development within the spark plug ignition zone was conducted, including the individual radial and axial flow velocities, $\bar{u}, \bar{v}$, and resultant velocity, $|V|$, alongside the two-component turbulent kinetic energy, TKE. The resultant flow velocities within this region correlate to the same PR dependencies as seen at the nearfield and jet boundary – a largely logarithmic/power-low relationship. The magnitude of the mean velocity (1.8-21.0 $\mathrm{m/s}$) is within the ignition stability threshold of conventional spark plugs. Some consequences noted for higher velocities, assuming the flow remains unperturbed by the spark plug electrode arm, include the propensity for the plasma discharge to stretch significantly. This may have ramifications for early flame propagation, such as extinction. This potential drawback may be offset by the high turbulence levels generated, which increase the flame-surface area after the flame kernel has developed.

The fuel injection induced TKE data show high magnitudes in the ignition region, as compared to measurements conducted in the literature for engines operating without high PR fuel delivery. The quiescent environment allows gas exchange and piston motion in-cylinder flow to be removed, thus the TKE levels result solely from the gas delivery effects. Below PR80 the mean TKE magnitudes, whilst relatively minor compared to those for the highest PR cases ($0.4 < 3.0$ $\mathrm{m^2/s^2}$ and $8.5 < 19.9$ $\mathrm{m^2/s^2}$, resp.), are equal to values generated by gas exchange and piston motion in-cylinder flow. Therefore, at late injection conditions, CNG jets delivered between $24.5 < \mathrm{PR} < 400$ will return turbulence levels conducive to good flame propagation.

7.2 Summary of Original Contributions

The key original components of this thesis are summarised below:

1. A fully representative fuel was tested where the primary investigation utilised CNG. Comparisons were made to other fuels: Hydrogen and a blend of 25%Hydrogen/75%Methane. No previous investigation of this topic has been published.
2. Testing of fuel delivery pressure ratios of between 2.8 and 400. This is the largest known range tested and extends well beyond the previous largest values reported.
3. A largely novel direct injector was created with internal geometry that replicates the physical boundaries anticipated for commercial units. The needle lift and proximity of the needle sealing line to the exit orifice are such representative features.
4. A novel method of analysing ambient-flow PIV data. The jet segmentation method accurately defines the jet-to-ambient boundary with high fidelity, and proved advantageous when deriving critical flow and mixing metrics (e.g. the entrainment coefficient).
5. Previously unpublished details about the transient period of fuel delivery, including high-resolution characterisation of dynamic flow behaviour was provided. The location of the Mach disc, a critical flow component was determined using two optical diagnostic methods: schlieren and PIV.
6. The interplay between compressible and incompressible phenomena within the nearfield was shown for the first time, and a method of controlling such features discussed.

7.3 Recommendations for Future Work

The following are recommendations on how this work could be improved and what future investigations should be conducted in this field:

I. Analysis of the supply line pressure effects and acoustic feedback.
II. Detailed computational fluid dynamics (CFD) investigation of the in-nozzle geometry including transient gas-density profiling and shock-wave interaction.
III. Jet core temperature analysis of the nearfield region.
IV. Effect of fuel constituent; CO2, Ethane, Propane and perhaps Butane.
V. Introduction of more complex piston surface geometries including bowl-shaped profiles.
VI. Laser Induced Fluorescence analysis of concentration profiles. This could be achieved through quantitative acetone-fluorescence.
VII. Experimental characterisation of the transient flow behaviour for a smaller nozzle exit diameter (i.e. $\sim 500\ \mu m$) coupled to a larger needle-lift (i.e. $\sim 60\ \mu m$).

THIS PAGE IS INTENTIONALLY BLANK

Bibliography

ABANI, N. & REITZ, R. D. 2007. Unsteady turbulent round jets and vortex motion. *Physics of Fluids (1994-present),* 19**,** -.

ABRAHAM, J. 1996. Entrainment Characteristics of Transient Gas Jets. *Numerical Heat Transfer, Part A: Applications: An International Journal of Computation and Methodology,* 30**,** 347 - 364.

ADDY, A. L. 1981. Effects of Axisymmetric Sonic Nozzle Geometry on Mach Disk Characteristics. *AIAA,* 19**,** 121-122.

ADRIAN, R. J. & WESTERWEEL, J. 2011. *Particle Image Velocimetry*, Cambridge University Press.

AHMADI, M. & IZANLOO, H. Challenges and Solutions in Natural Gas Engine Development and Production. 17. Aachener Kolloquiuim Fahrzeug- und Motorentechnik, 2008. 363-383.

AKANSU, S. O., DULGER, Z., KAHRAMAN, N. & VEZIROĞLU, T. N. 2004. Internal combustion engines fueled by natural gas—hydrogen mixtures. *International Journal of Hydrogen Energy,* 29**,** 1527-1539.

ALHARBI, A. 2010. *High-Speed High-Resolution Vector Field Measurements and Analysis Of Boundary Layer Flows In An Internal Combustion Engine.* Doctor of Philosophy PhD Dissertation, The University of Michigan.

ANDRIANI, R., COGHE, A. & COSSALI, G. E. 1996. Near-field entrainment in unsteady gas jets and diesel sprays: A comparative study. *Symposium (International) on Combustion,* 26**,** 2549-2556.

ARBEAU, A., BAZILE, R., CHARNAY, G. & GASTALDI, P. 2004. A New Application of the Particle Image Velocimetry (PIV) to the Air Entrainment in Gasoline Direct Injection Sprays. SAE International.

ASHKENAS, H. & SHERMAN, F. S. 1966. The Structure and Utilization of Supersonic Free Jets in Low Density Wind Tunnels. *Rarefied Gas Dynamics, Proceedings of the Fourth International Symposium held at the Institute for Aerospace Studies,* Volume 2.

BAERT, R., KLAASSEN, A. & DOOSJE, E. 2010. Direct Injection of High Pressure Gas: Scaling Properties of Pulsed Turbulent Jets. *SAE Int. J. Engines,* 3**,** 383-395.

BARATTA, M., CATANIA, A. E. & PESCE, F. C. 2011. Multidimensional Modeling of Natural Gas Jet and Mixture Formation in Direct Injection Spark Ignition Engines—Development and Validation of a Virtual Injector Model. *Journal of Fluids Engineering,* 133**,** 041304-041304.

BARATTA, M., CATANIA, A. E., SPESSA, E., HERRMANN, L. & ROESSLER, K. 2008. Multi-Dimensional Modeling of Direct Natural-Gas Injection and Mixture Formation in a Stratified-Charge SI Engine with Centrally Mounted Injector. *SAE Int. J. Engines,* 1**,** 607-626.

BATES, S. C. 1991. Flame Imaging Studies of Flame Development in a SI Four-Stroke Engine. *Dynamics of Deflagrations and Reactive Systems: Flames.* American Institute of Aeronautics and Astronautics.

BAUM, E., PETERSON, B., BÖHM, B. & DREIZLER, A. 2014. On The Validation of LES Applied to Internal Combustion Engine Flows: Part 1: Comprehensive Experimental Database. *Flow, Turbulence and Combustion,* 92**,** 269-297.

BAUM, E., PETERSON, B., SURMANN, C., MICHAELIS, D., BÖHM, B. & DREIZLER, A. 2013. Investigation of the 3D flow field in an IC engine using tomographic PIV. *Proceedings of the Combustion Institute,* 34**,** 2903-2910.

BENITO, E. D. 2010. *The influence on spray behaviour by pressure fluctuations in the injection system.* Master, Chalmers University of Technology.

BERCKMÜLLER, M., ROTTENGRUBER, H., EDER, A., BREHM, N., ELSÄSSER, G., MÜLLER-ALANDER, G. & SCHWARZ, C. 2003. Potentials of a Charged SI-Hydrogen Engine. SAE International.

BEVAN, K. E. & GHANDHI, J. B. 2004. PIV Measurements of In-Cylinder Flow in a Four-Stroke Utility Engine and Correlation with Steady Flow Results. SAE International.

BIRCH, A. D., BROWN, D. R., DODSON, M. G. & SWAFFIELD, F. 1984. The Structure and Concentration Decay of High Pressure Jets of Natural Gas. *Combustion Science and Technology,* 36**,** 249-261.

BOGUSLAWSKI, L. & POPIEL, C. O. 1979. Flow structure of the free round turbulent jet in the initial region. *Journal of Fluid Mechanics,* 90**,** 531-539.

BONELLI, F., VIGGIANO, A. & MAGI, V. 2013. A Numerical Analysis of Hydrogen Underexpanded Jets Under Real Gas Assumption. *Journal of Fluids Engineering,* 135**,** 121101-121101.

BOVO, M. & ROJO, B. 2013. Single Pulse Jet Impingement on Inclined Surface, Heat Transfer and Flow Field. *SAE Technical Paper.* SAE International.

BRUNEAUX, G., CAUSSE, M. & OMRANE, A. 2011. Air Entrainment in Diesel-Like Gas Jet by Simultaneous Flow Velocity and Fuel Concentration Measurements, Comparison of Free and Wall Impinging Jet Configurations. *SAE Int. J. Engines,* 5**,** 76-93.

BUCHMANN, N. A., MITCHELL, D., INGVORSEN, K. M., HONNERY, D. & SORIA, J. 2011. High Spatial Resolution Imaging of a Supersonic Underexpanded Jet Impinging on a Flat Plate. *Sixth Australian Conference on Laser Diagnostics in Fluid Mechanics and Combustion.* Canberra, Australia.

CALEY, D. & CATHCART, G. 2006. Development of a Natural Gas Spark Ignited Direct Injection Combustion System. *Technical Paper,* Technical Paper.

CAPONE, A., SOLDATI, A. & ROMANO, G. 2012. Mixing and entrainment in the near field of turbulent round jets. *Experiments in Fluids,* 54**,** 1-14.

CHAUVEAU, C., DAVIDENKO, D. M., SARH, B., GÖKALP, I., AVRASHKOV, V. & FABRE, C. 2006. PIV Measurements in an Underexpanded Hot Free Jet. *13th Int Symp on Applications of Laser Techniques to Fluid Mechanics.* Lisbon, Portugal.

CHITSAZ, I., SAIDI, M. H., MOZAFARI, A. A. & HAJIALIMOHAMMADI, A. 2013. Experimental and numerical investigation on the jet characteristics of spark ignition direct injection gaseous injector. *Applied Energy,* 105**,** 8-16.

COSADIA, I., BORÉE, J., CHARNAY, G. & DUMONT, P. 2006. Cyclic variations of the swirling flow in a Diesel transparent engine. *Experiments in Fluids,* 41**,** 115-134.

COSSALI, G. E., COGHE, A. & ARANEO, L. 2001. Near-Field Entrainment in an Impulsively Started Turbulent Gas Jet. *AIAA Journal,* 39**,** 1113-1122.

CRIST, S., SHERMAN, P. M. & GLASS, D. R. 1966. Study of the Highly Underexpanded Sonic Jet. *AIAA,* 4.

CROW, S. C. & CHAMPAGNE, F. H. 1971. Orderly structure in jet turbulence. *Journal of Fluid Mechanics,* 48**,** 547-591.

CUSHMAN-ROISIN, B. 2014. *Environmental Fluid Mechanics,* Hanover, New Hampshire, John Wiley & Sons, Inc.

DANTEC DYNAMICS 2013. Dynamic Stutio Users Guide. Denmark: Dantec Dynamics.

DELACOURT, E., DESMET, B. & BESSON, B. 2005. Characterisation of very high pressure diesel sprays using digital imaging techniques. *Fuel,* 84**,** 859-867.

DONALDSON, C. D. & SNEDEKER, R. S. 1971. A study of free jet impingement. Part 1. Mean properties of free and impinging jets. *Journal of Fluid Mechanics,* 45**,** 281-319.

DUBS, P., KHALIJ, M., BENELMIR, R. & TAZIBT, A. 2011. Study on the dynamical characteristics of a supersonic high pressure ratio underexpanded impinging ideal gas jet through numerical simulations. *Mechanics Research Communications,* 38**,** 267-273.

ELVERS, B. (ed.) 2008. *Handbook of Fuels, Energy sources for Transportation*: Wiley-VCH Verlag GmbH& Co. KGaA.

EWAN, B. C. R. & MOODIE, K. 1986. Structure and Velocity Measurements in Underexpanded Jets. *Combustion Science and Technology,* 45**,** 275 - 288.

FAJARDO, C. & SICK, V. 2007. Flow field assessment in a fired spray-guided spark-ignition direct-injection engine based on UV particle image velocimetry with sub crank angle resolution. *Proceedings of the Combustion Institute,* 31**,** 3023-3031.

GERKE, U. 2007. *Numerical Analysis of Mixture Formation and Combustion in a Hydrogen Direct-Injection Internal Combustion Engine.* Doctor of Science, Swiss Federal Institute of Technology.

GONZALEZ, R. C., WOODS, R. E. & EDDINS, S. L. 2004. *Digital Image processing using MATLAB,* Upper Saddle River, N. J., Pearson Prentice Hall.

GORLÉ, C., GAMBA, M. & HAM, F. E. 2010. Investigation of an underexpanded hydrogen jet in quiescent air using numerical simulations and experiments. Center for Turbulence Research, Stanford University.

HATANAKA, K., HIROTA, M., SAITO, T., NAKAMURA, Y., SUZUKI, Y. & KOYAGUCHI, T. 2012. Flow Visualization of Supersonic Free Jet Utilizing Acetone LIF. *In:* KONTIS, K. (ed.) *28th International Symposium on Shock Waves.* Springer Berlin Heidelberg.

HATANAKA, K. & SAITO, T. 2012. Influence of nozzle geometry on underexpanded axisymmetric free jet characteristics. *Shock Waves,* 22**,** 427-434.

HEMDAL, S., ANDERSSON, M., DAHLANDER, P., OCHOTERENA, R. & DENBRATT, I. 2011. In-cylinder soot imaging and emissions of stratified combustion in a spark-ignited spray-guided direct-injection gasoline engine. Gothenburg: Chalmers University of Technology.

HILL, B. J. 1972. Measurement of local entrainment rate in the initial region of axisymmetric turbulent air jets. *Journal of Fluid Mechanics,* 51**,** 773-779.

HILL, P. G. & DANSEHYAR, H. 1987. The Structure of Small-Scale Turbulence and Its Effect on Combustion In Spark Ignition Engines. *Progress in Energy and Combustion Science,* 13**,** 47-73.

HILL, P. G. & OUELLETTE, P. 1999. Transient Turbulent Gaseous Fuel Jets for Diesel Engines. *Journal of Fluids Engineering,* 121**,** 93-101.

HORN, G. & THRING, M. W. 1956. Angle of Spread of Free Jets. *Nature,* 178**,** 205-206.

HYUN, G.-S., NOGAMI, M., HOSOYAMA, K., SENDA, J. & FUJIMOTO, H. 1995. Flow Characteristics in Transient Gas Jet. *SAE Technical Paper,* 950847.

JOHANNESEN, N. H. 1957. The Mixing of Free Axially-Symmetrical Jets of Mach Number 1.40. *Reports and Memoranda.* Manchester: Ministry of Aviation.

JOHANSEN, L. C. R., DE BENITO SIENES, E. & DAHLANDER, P. 2013. Analysis of Transient Compressible Gas Jets Using High Speed Schlieren Imaging. *SAE Technical Paper.* SAE International.

JONES, J. B. & HAWKINS, G. A. 1960. *Engineering Thermodynamics An Introductory Textbook,* New York, John Wiley & Sons.

KAISER, S. A. & WHITE, C. M. 2008. PIV and PLIF to Evaluate Mixture Formation in a Direct-Injection Hydrogen Fuelled Engine. *SAE Technical Paper,* 2008-01-1034.

KARHOFF, D.-C., BÜCKER, I., KLAAS, M. & SCHRÖDER, W. Time-Resolved stereoscopic PIV measurements of cyclic variations in an internal combustion engine. 10th International Symposium On Particle Image Velocimetry, 2013 Delft, The Netherlands.

KLEIN-DOUWEL, R. J. H., FRIJTERS, P. J. M., SOMERS, L. M. T., DE BOER, W. A. & BAERT, R. S. G. 2007. Macroscopic diesel fuel spray shadowgraphy using high speed digital imaging in a high pressure cell. *Fuel,* 86**,** 1994-2007.

KLEINE, H. 2010. Filming the invisible - time resolved visualization of compressible flows. *The European Physical Journal Special Topics,* 182**,** 3-34.

KLEINE, H., GRÖNIG, H. & TAKAYAMA, K. 2005. Simultaneous Shadow, Schlieren and Interferometric Visualization of Compressible Flows. *Optics and Lasers in Engineering,* 44**,** 170-189.

KLEINSTEIN, G. 1964. Mixing in Turbulent Axially Symmetric Free Jets. *Journal of Spacecraft,* 1**,** 403-408.

LACERDA, N. L. 1987. *On the start up of supersonic underexpanded jets.* Doctor of Philosophy, California Institute of Technology.

LAPPAS, P. 2003. *An Experimental and Computational Study of Flow in the Squish Jet Combustion Chamber.* Doctoral Dissertation, The University of British Columbia.

LEE, K. H., LEE, C. H. & LEE, C. S. 2004. An experimental study on the spray behavior and fuel distribution of GDI injectors using the entropy analysis and PIV method. *Fuel,* 83**,** 971-980.

LOVE, E. S., GRIGSBY, C. E., LEE, L. P. & WOODLING, M. J. 1959. Experimental and Theoretical Studies of Axisymmetric Free Jets. Langley, Va: National Aeronautics and Space Administration.

LYOGUN, C. O. & BIROUK, M. 2009. Effect of Sudden Expansion on Entrainment and Spreading Rates of a Jet Issuing from Asymmetric Nozzles. *Flow, Turbulence and Combustion,* 82**,** 287-315.

MAHMOOD, Z., CHEN, A., YIANNESKIS, M. & GANTI, G. 1996. On The Structure of Steady Flow Through Dual-Intake Engine Ports. *International Journal For Numerical Methods in Fluids,* 23**,** 1085-1109.

MARTI-ALDARAVI, P., ROGERS, T. J., DE BENITO, E., HEMDAL, S. & DAHLANDER, P. 2012. A comparison of non-reactive fuel sprays under realistic but quiescent engine conditions for SGDI. *International Conference on Liquid Atomization and Spray Systems.* Heidelberg, Germany.

MATÉ, B., GRAUR, I. A., ELIZAROVA, T., CHIROKOV, I., TEJEDA, G., FERNANDEZ, J. M. & MONTERO, S. 2001. Experimental and numerical investigation of an axisymmetric supersonic jet. *Journal of Fluid Mechanics,* 426**,** 177-197.

MCTAGGART-COWAN, G. P., JONES, H. L., ROGAK, S. N., BUSHE, W. K., HILL, P. G. & MUNSHI, S. R. 2006. Direct-Injected Hydrogen-Methane Mixtures in a Heavy-Duty Compression Ignition Engine. *SAE Technical Paper.* SAE International.

MEI, R. 1996. Velocity fidelity of flow tracer particles. *Experiments in Fluids,* 22**,** 1-13.

MELLING, A. 1997. Tracer particles and seeding for particle image velocimetry. *Measurement Science and Technology,* 8**,** 1406.

MITCHELL, D. 2012. *Coherent structure and shock-vortex interaction in the screeching supersonic jet.* Doctorate of Philosophy Dissertation, Monash University.

MITCHELL, D., HONNERY, D. & SORIA, J. Particle Image Velocimetry Measurements of an Underexpanded Supersonic Jet. Fourth Australian Conference on Laser Diagnostics in Fluid Mechanics and Combustion, 2005 The University of Adelaide, South Australia, Australia

MITCHELL, D., HONNERY, D. & SORIA, J. 2007. Study of Underexpanded Supersonic Jets with Optical Techniques. *16th Australasian Fluid Mechanics Conference.* Crown Plaza, Gold Coast, Australia.

MITCHELL, D. M., HONNERY, D. R. & SORIA, J. 2012. The visualization of the acoustic feedback loop in impinging underexpanded supersonic jet flows using ultra-high frame rate schlieren. *Journal of Visualization,* 15**,** 333-341.

MOHAMAD, T., HARRISON, M., JERMY, M. & HOW, H. G. 2010. The structure of the high-pressure gas jet from a spark plug fuel injector for direct fuel injection. *Journal of Visualization,* 13**,** 121-131.

MUSCULUS, M. P. B. 2009. Entrainment waves in decelerating transient turbulent jets. *Journal of Fluid Mechanics,* 638**,** 117-140.

NABER, J. D. & SIEBERS, D. L. 1996. Effects of Gas Density and Vaporization on Penetration and Dispersion of Diesel Sprays. SAE International.

NAMER, I. & ÖTÜGEN, M. V. 1988. Velocity measurements in a plane turbulent air jet at moderate Reynolds numbers. *Experiments in Fluids,* 6**,** 387-399.

NATIONAL PETROLEUM COUNCIL 2012. Hydrogen-Compressed Natural Gas (HCNG) Transport Fuel. Washington, D.C.

OTOBE, Y., KASHIMURA, H., MATSUO, S., SETOGUCHI, T. & KIM, H. D. 2008. Influence of nozzle geometry on the near-field structure of a highly underexpanded sonic jet. *Journal of Fluids and Structures,* 24**,** 281-293.

OUELLETTE, N. T., O'MALLEY, P. J. J. & GOLLUB, J. P. 2008. Transport of Finite-Sized Particles in Chaotic Flow. *Physical Review Letters,* 101**,** 174504.

OUELLETTE, P. 1996. *Direct Injection of Natural Gas For Diesel Engine Fuelling.* Doctor of Philosophy PhD, University of British Columbia.

OUELLETTE, P. & HILL, P. G. 2000. Turbulent Transient Gas Injections. *Journal of Fluids Engineering,* 122**,** 743-752.

OWEN, K. & COLEY, T. (eds.) 1995. *Automotive fuels reference book, second edition,* Warrendale, PA, USA: Society of Automotive Engineers, Inc.

OWSTON, R. 2010. *Modeling of Combustion in Stratified Hydrogen-Air Mixtures.* Doctor of Philosophy, Purdue University.

OWSTON, R., MAGI, V. & ABRAHAM, J. 2008. Fuel-Air Mixing Characteristics of DI Hydrogen Jets. *SAE Int. J. Engines,* 1**,** 693-712.

PANDA, J. 1998. Shock oscillation in underexpanded screeching jets. *Journal of Fluid Mechanics,* 363**,** 173-198.

PANDA, J. & SEASHOLTZ, R. G. 1999. Measurement of shock structure and shock-vortex interaction in underexpanded jets using Rayleigh scattering. *Phys. Fluids,* 11**,** 3761.

PANIGRAHI, P. K. & MURALIDHAR, K. 2012. *Schlieren and Shadowgraph Methods in Heat and Mass Transfer,* New York, Springer.

PASTOR, J. V., JOSE M, G., JOSE M, P. & ZAPATA, L. D. 2007. Evaporating diesel spray visualisation using a double-pass Shadowgraphy/Schlieren imaging. *SAE Technical Paper*.

PETERSEN, B. R. 2006. *Transient High-Pressure Hydrogen Jet Measurements.* Master of Science (Mechanical Engineering) Master, University of Winconsin-Madison.

PETERSON, B. R. 2010. *High-Speed Fuel and Flow Imaging To Investigate Misfires In A Spray-Guided Direct-Injection Engine.* Doctor of Philosophy Dissertation, The University of Michigan.

PISCHINGER, S., UMIERSKI, M. & HUCHTEBROCK, B. 2003. New CNG Concepts for Passenger Cars: High Torque Engines with Superior Fuel Consumption. *SAE Technical Paper Series*.

PORPATHAM, E., RAMESH, A. & NAGALINGAM, B. 2007. Effect of hydrogen addition on the performance of a biogas fuelled spark ignition engine. *International Journal of Hydrogen Energy,* 32**,** 2057-2065.

POST, S., IYER, V. & ABRAHAM, J. 2000. A Study of Near-Field Entrainment in Gas Jets and Sprays Under Diesel Conditions. *Journal of Fluids Engineering,* 122**,** 385-395.

RA, Y., KONG, S. C., REITZ, R. D., RUTLAND, C. J. & HAN, Z. 2005. Multidimensional Modeling of Transient Gas Jet Injection Using Coarse Computational Grids.

RADULESCU, M. I. & LAW, C. K. 2007. The transient start of supersonic jets. *Journal of Fluid Mechanics,* 578**,** 331-369.

RAFFEL, M., WILLERT, C. E., WERELEY, S. T. & KOMPENHANS, J. 2007. *Particle Image Velocimetry: A Practical Guide,* Berlin Heidelberg, Springer-Verlag.

RAGNI, D., SCHRIJER, F., VAN OUDHEUSDEN, B. W. & SCARANO, F. 2011. Particle tracer response across shocks measured by PIV. *Experiments in Fluids,* 50**,** 53-64.

RICOU, F. P. & SPALDING, D. B. 1961. Measurements of entrainment by axisymmetrical turbulent jets. *Journal of Fluid Mechanics,* 11**,** 21-32.

RIETZSCHEL, J., STADLER, S. & ZHU, Y. 2012. *Fuel Composition Sensing of Compressed Natural Gas.* Masters of Automotive Engineering, RMIT University.

RIMMER, J. E. T., LONG, E. J., GARNER, C. P., HARGRAVE, G. K., RICHARDSON, D. & WALLACE, S. 2009. The Influence of Single and Multiple Injection Strategies on In-Cylinder Flow and Combustion within a DISI Engine. *SAE Technical Paper.* SAE International.

RIZK, W. 1958. Experimental Studies of the Mixing Processes and Flow Configurations in Two-Cycle Engine Scavenging. *Proceedings of the Institution of Mechanical Engineers,* 172**,** 417-437.

ROGERS, T., PETERSEN, P., KOOPMANS, L., LAPPAS, P. & BORETTI, A. 2015. Structural characteristics of hydrogen and compressed natural gas fuel jets. *International Journal of Hydrogen Energy,* 40**,** 1584-1597.

ROLLEFSON, R. & HAVENS, R. 1940. Index of Refraction of Methane in the Infra-Red and the Dipole Moment of the CH Bond. *Physical Review,* 57**,** 710-717.

ROTTENGRUBER, H., BERCKMÜLLER, M., ELSÄSSER, G., BREHM, N. & SCHWARZ, C. 2004. Direct-Injection Hydrogen SI-Engine - Operation Strategy and Power Density Potentials. SAE International.

SALAZAR, V. & KAISER, S. 2011. Interaction of Intake-Induced Flow and Injection Jet in a Direct-Injection Hydrogen-Fueled Engine Measured by PIV. *SAE Technical Paper*.

SALAZAR, V. M. & KAISER, S. A. 2009. An Optical Study of Mixture Preparation in a Hydrogen-fueled Engine with Direct Injection Using Different Nozzle Designs. *SAE Technical Paper,* 2009-01-2682.

SCARCELLI, R., KASTENGREN, A. L., POWELL, C. F., WALLNER, T. & MATTHIAS, N. S. HIGH-PRESSURE GASEOUS INJECTION: A COMPREHENSIVE ANALYSIS OF GAS DYNAMICS AND MIXING EFFECTS. ASME 2012 Internal Combustion Engine Division Fall Technical Conference, September 23-26, 2012 2012 Vancouver, BC, Canada. ASME.

SCHLICHTING, H. & GERSTEN, K. 2000. *Boundary Layer Theory,* Berlin Heidelberg, Springer-Verlag.

SEITZMAN, J. M. 2001. AE3450 Course Notes. Georgia: Georgia Tech, School of Aerospace Engineering.

SETTLES, G. S. 2001. *Schlieren and shadowgraph techniques: visualizing phenomena in transparent media,* Berlin, Heidelberg, New York, Springer.

SHAPIRO, A. H. 1953. *The Dynamics and Thermodynamics of Compressible Fluid Flow,* New York, The Ronald Press Company.

SHICHIDA, T., YOSHIZAKI, H., TSUGA, S., SUGIMOTO, N. & KAMEDA, H. 2014. Numerical Simulation for Ignitability of Spark Plug using Detailed Chemical Kinetics. *SAE Technical Paper.* SAE International.

SHINDELL, D., FALUVEGI, G., WALSH, M., ANENBERG, S. C., VAN DINGENEN, R., MULLER, N. Z., AUSTIN, J., KOCH, D. & MILLY, G. 2011. Climate, health, agricultural and economic impacts of tighter vehicle-emission standards. *Nature Clim. Change,* 1**,** 59-66.

SOANES, C. & KOOPMANS, L. 2012. On the Application of Compressed Natural Gas for an SI Internal Combustion Engine and Two Different Injector Positions. *In:* SUBIC, A., WELLNITZ, J., LEARY, M. & KOOPMANS, L. (eds.) *Sustainable Automotive Technologies.* Melbourne, Australia: Springer.

SOMMERFELD, M. 1994. The structure of particle-laden, underexpanded free jets. *Shock Waves,* 3**,** 299-311.

SONG, L. & ABRAHAM, J. 2003. Entrainment Characteristics of Transient Turbulent Round, Radial and Wall-Impinging Jets: Theoretical Deductions. *Journal of Fluids Engineering,* 125**,** 605-612.

TABACZYNSKI, R. J. 1990. Turbulent Flows in Reciprocating Internal Combustion Engines. *In:* WEAVING, J. (ed.) *Internal Combustion Engineering: Science & Technology*. Springer Netherlands.

TAM, C. K. W. & TANNA, H. K. 1982. Shock associated noise of supersonic jets from convergent-divergent nozzles. *Journal of Sound and Vibration,* 81**,** 337-358.

TAVOULARIS, S. 2005. *Measurement in fluid mechanics,* Cambridge, New York., Cambridge University Press.

TEDESCHI, G., GOUIN, H. & ELENA, M. 1999. Motion of tracer particles in supersonic flows. *Experiments in Fluids,* 26**,** 288-296.

TURNER, J. S. 1986. Turbulent entrainment: the development of the entrainment assumption, and its application to geophysical flows. *Journal of Fluid Mechanics,* 173**,** 431-471.

UNGATE, C. D., HARLEMAN, D. R. F. & JIRKA, G. H. 1975. Stability and Mixing Of Submerged Turbulent Jets At Low Reynolds Numbers. Massachusetts , USA: Massachusetts Institute of Technology.

URBAN, W. D. & MUNGAL, M. G. 2001. Planar velocity measurements in compressible mixing layers. *Journal of Fluid Mechanics,* 431**,** 189-222.

VELIKORODNY, A. & KUDRIAKOV, S. 2012. Numerical study of the near-field of highly underexpanded turbulent gas jets. *International Journal of Hydrogen Energy,* 37**,** 17390-17399.

VERHELST, S. & WALLNER, T. 2009. Hydrogen-fueled internal combustion engines. *Progress in Energy and Combustion Science,* 35**,** 490-527.

VILLANTE, C. & GENOVESE, A. 2012. Hydromethane: A bridge towards the hydrogen economy or an unsustainable promise? *International Journal of Hydrogen Energy,* 37**,** 11541-11548.

VUORINEN, V., YU, J., TIRUNAGARI, S., KAARIO, O., LARMI, M., DUWIG, C. & BOERSMA, B. J. 2013. Large-eddy simulation of highly underexpanded transient gas jets. *Physics of Fluids,* 25**,** 016101-22.

WARREN, W. R. 1953. *The Mixing of an Axially Symmetric Compressible Jet with Quiescent Air.* Doctorate of Philosophy, Princeton University.

WHITE, T. R. & MILTON, B. E. 2008. Shock wave calibration of under-expanded natural gas fuel jets. *Shock Waves,* 18**,** 353-364.

WITZE, P. O. 1974. Centerline Velocity Decay of Compressible Free Jets. *AIAA,* 12.

WITZE, P. O. & DWYER, H. A. 1976. The turbulent radial jet. *Journal of Fluid Mechanics,* 75**,** 401-417.

YOUNG, W. S. 1975. Derivation of the free-jet Mach-disk location using the entropy-balance principle. *Physics of Fluids (1958-1988),* 18**,** 1421-1425.

YU, J., VUORINEN, V., HILLAMO, H., SARJOVAARA, T., KAARIO, O. & LARMI, M. 2012. An experimental investigation on the flow structure and mixture formation of low pressure ratio wall-impinging jets by a natural gas injector. *Journal of Natural Gas Science and Engineering,* 9**,** 1-10.

YU, J., VUORINEN, V., KAARIO, O., SARJOVAARA, T. & LARMI, M. 2013a. Characteristics of High Pressure Jets for Direct Injection Gas Engine. *SAE Int. J. Fuels Lubr.,* 6**,** 149-156.

YU, J., VUORINEN, V., KAARIO, O., SARJOVAARA, T. & LARMI, M. 2013b. Visualization and analysis of the characteristics of transitional underexpanded jets. *International Journal of Heat and Fluid Flow*.

ZENTGRAF, F., BAUM, E., BÖHM, B., DREIZLER, A. & PETERSON, B. Analysis of the turbulent in-cylinder flow in an IC engine using tomographic and planar PIV measurements. 17th International Symposium on Applications of Laser Techniques to Fluid Mechanics, 2014 Lisbon, Portugal.

ZUCKERMAN, N. & LIOR, N. 2006. Jet Impingement Heat Transfer: Physics, Correlations, and Numerical Modeling. *Advances in Heat Transfer,* 39**,** 565-631.

THIS PAGE IS INTENTIONALLY BLANK

Appendices

Appendix I - Engine Model Representation

A simple, single cylinder 1-dimensional model provided the basis for quasi-realistic engine conditions. These conditions are not validated against real engine data but are believed to be a representative enough insight into conditions experienced.

The engine was represented used Lotus Engine Simulation (v5.05) where the engine parameters were set according to (Hemdal et al., 2011). Combustion, heat transfer and friction were modelled using single-Weibe, Annand and H.B Moss correlations, respectively. Camshaft phasing was fixed across the entire speed range (1000 – 6000 rpm) as was ignition to a peak cylinder pressure value (~14 CAD aTDC). The engine model was fuelled using typical gasoline properties at stoichiometry. The engine was throttled to achieve the respective BMEP values whilst the fuelling rate was held constant.

The pseudo-turbocharged model was simply constructed by altering the ambient and intake charge pressure to 50% above atmospheric. This is not an accurate method for representing forced induction, due to pressure profile losses, non-realistic temperature profile, mechanical and thermodynamic effects.

Unless specified, the profiles represent averaged data from the entire speed profile. This is a fairly non-conventional approach for representing otherwise widely variable date but yields a cross-sectional view of typical conditions.

Table 18, 2000-4000 rpm averaged in-cylinder conditions between 120 and 20 CAD bTDC.

	Temperature (K)			*Pressure (Bar)*		
	Min	Max	Mean	Min	Max	Mean
2.0 Bar BMEP, Inlet 1.0 bar	351.44	769.34	466.78	0.40	5.70	1.22
4.0 Bar BMEP, Inlet 1.0 bar	348.88	772.02	466.81	0.50	8.34	1.76
4.0 Bar BMEP, Inlet 1.5 bar	339.16	754.66	454.29	0.50	7.86	1.65

Table 19, 2000-4000 rpm averaged, local in cylinder conditions.

	50 CAD bTDC			
	Temperature (K)	*Pressure (Bar)*	*Density (kg/m3)*	*Distance (mm)*
2.0 Bar BMEP, Inlet 1.0 bar	580	1.920	1.153	
4.0 Bar BMEP, Inlet 1.0 bar	581	2.780	1.667	33.40
4.0 Bar BMEP, Inlet 1.5 bar	566	2.600	1.599	

Table 20, 2000-4000 rpm averaged in-cylinder conditions at constant temperature using nitrogen.

	50 CAD bTDC - Constant Temperature, Nitrogen Filled			
	Temperature (K)	*Pressure (Bar)*	*Density (kg/m3)*	*Distance (mm)*
2.0 Bar BMEP, Inlet 1.0 bar	293.00	1.003	1.153	
4.0 Bar BMEP, Inlet 1.0 bar	293.00	1.450	1.667	33.40
4.0 Bar BMEP, Inlet 1.5 bar	293.00	1.391	1.599	

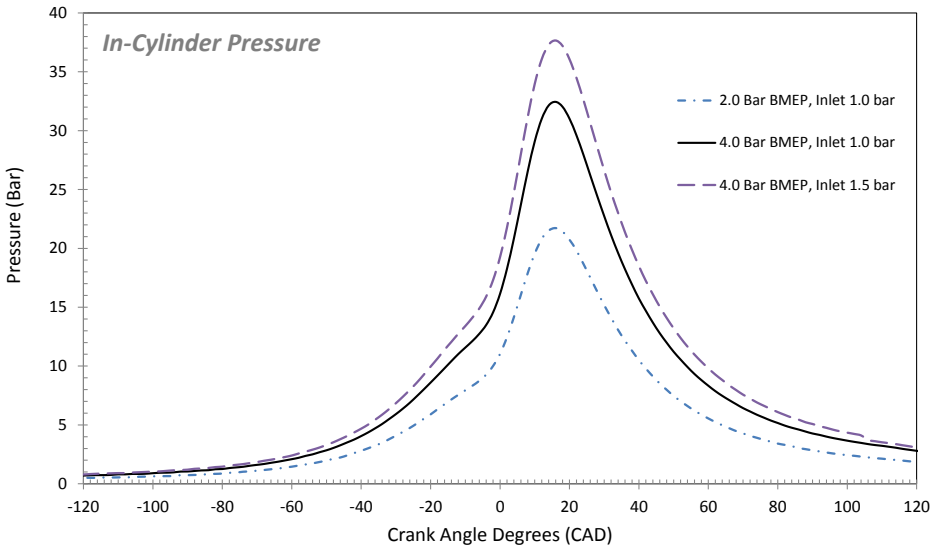

Figure 173, Comparison of speed averaged cylinder pressure for 2 and 4 bar BMEP and pseudo-turbocharged 4 bar BMEP.

Appendix II – Experimental Schedule Low Pressure Ratio (PFI)

Table 21, Low pressure ratio (PFI) schlieren HSV – Freestream Jets.

Po/Pa	*Po*	*Pa*	*ρo*	*ρa*	*ρo/ρa*	*Pe/Pa*	*Fuel*	*Cond*
PR	Bar (abs)	Bar (abs)	kg/m^3	kg/m^3		NPR		
2.80	2.80	1.00	1.845	1.153	1.60	1.53	*CNG*	*FS*
3.00	3.00	1.00	1.977	1.153	1.71	1.64	*CNG*	*FS*
3.20	3.20	1.00	2.108	1.153	1.83	1.75	*CNG*	*FS*
3.40	3.40	1.00	2.240	1.153	1.94	1.86	*CNG*	*FS*
3.80	3.80	1.00	2.504	1.153	2.17	2.07	*CNG*	*FS*
4.30	4.30	1.00	2.833	1.153	2.46	2.35	*CNG*	*FS*
5.00	5.00	1.00	3.294	1.153	2.86	2.73	*CNG*	*FS*
6.00	6.00	1.00	3.953	1.153	3.43	3.28	*CNG*	*FS*
6.00	3.00	0.50	1.977	0.577	3.43	3.28	*CNG*	*FS*
8.60	4.30	0.50	2.833	0.577	4.91	4.70	*CNG*	*FS*
10.00	5.00	0.50	3.294	0.577	5.71	5.46	*CNG*	*FS*
12.00	6.00	0.50	3.953	0.577	6.85	6.55	*CNG*	*FS*
4.30	4.30	1.00	0.356	1.153	0.31	2.28	H_2	*FS*
6.00	3.00	0.50	0.248	0.577	0.43	3.19	H_2	*FS*
8.60	4.30	0.50	0.356	0.577	0.62	4.57	H_2	*FS*
10.00	5.00	0.50	0.414	0.577	0.72	5.31	H_2	*FS*
12.00	6.00	0.50	0.497	0.577	0.86	6.37	H_2	*FS*

Table 22, Low pressure ratio (PFI) schlieren HSV –Impinging Jets.

Po/Pa	*Po*	*Pa*	*ρo*	*ρa*	*ρo/ρa*	*Pe/Pa*	*Fuel*	*Cond*
PR	Bar (abs)	Bar (abs)	kg/m^3	kg/m^3		NPR		
2.80	2.80	1.00	1.845	1.153	0.87	1.53	*CNG*	*Imp*
3.00	3.00	1.00	1.977	1.153	0.94	1.64	*CNG*	*Imp*
3.20	3.20	1.00	2.108	1.153	1.00	1.75	*CNG*	*Imp*
3.40	3.40	1.00	2.240	1.153	1.06	1.86	*CNG*	*Imp*
3.80	3.80	1.00	2.504	1.153	1.19	2.07	*CNG*	*Imp*
4.30	4.30	1.00	2.833	1.153	1.34	2.35	*CNG*	*Imp*
5.00	5.00	1.00	3.294	1.153	1.56	2.73	*CNG*	*Imp*
6.00	6.00	1.00	3.953	1.153	1.87	3.28	*CNG*	*Imp*
6.00	3.00	0.50	1.977	0.577	1.87	3.28	*CNG*	*Imp*
8.60	4.30	0.50	2.833	0.577	2.68	4.70	*CNG*	*Imp*
10.00	5.00	0.50	3.294	0.577	3.12	5.46	*CNG*	*Imp*
12.00	6.00	0.50	3.953	0.577	3.74	6.55	*CNG*	*Imp*
4.30	4.30	1.00	0.356	1.153	0.16	2.28	*H_2*	*Imp*
6.00	3.00	0.50	0.248	0.577	0.23	3.19	*H_2*	*Imp*
8.60	4.30	0.50	0.356	0.577	0.33	4.57	*H_2*	*Imp*
10.00	5.00	0.50	0.414	0.577	0.38	5.31	*H_2*	*Imp*
12.00	6.00	0.50	0.497	0.577	0.46	6.37	*H_2*	*Imp*
2.80	2.80	1.00	0.673	1.153	0.32	1.52	*25%H_2/CH_4*	*Imp*
3.00	3.00	1.00	0.721	1.153	0.34	1.62	*25%H_2/CH_4*	*Imp*
3.20	3.20	1.00	0.769	1.153	0.36	1.73	*25%H_2/CH_4*	*Imp*
3.40	3.40	1.00	0.817	1.153	0.38	1.84	*25%H_2/CH_4*	*Imp*
3.80	3.80	1.00	0.914	1.153	0.43	2.06	*25%H_2/CH_4*	*Imp*
4.30	4.30	1.00	1.034	1.153	0.49	2.33	*25%H_2/CH_4*	*Imp*
4.30	4.30	1.00	1.034	1.153	0.49	2.33	*25%H_2/CH_4*	*Imp*
5.00	5.00	1.00	1.202	1.153	0.56	2.71	*25%H_2/CH_4*	*Imp*
6.00	3.00	0.50	0.720	0.577	0.68	3.25	*25%H_2/CH_4*	*Imp*
6.00	6.00	1.00	1.442	1.153	0.68	3.25	*25%H_2/CH_4*	*Imp*
8.60	4.30	0.50	1.034	0.577	0.97	4.65	*25%H_2/CH_4*	*Imp*
8.60	4.30	0.50	1.034	0.577	0.97	4.65	*25%H_2/CH_4*	*Imp*
10.00	5.00	0.50	1.202	0.577	1.13	5.41	*25%H_2/CH_4*	*Imp*
12.00	6.00	0.50	1.442	0.577	1.35	6.49	*25%H_2/CH_4*	*Imp*

Appendix III – Experimental Schedule High Pressure Ratio (DI)

Table 23, High pressure ratio schlieren HSV - Freestream Jets.

Po/Pa	*Po*	*Pa*	*ρo*	*ρa*	*ρo/ρa*	*Pe/Pa*	*Fuel*	*Cond*
PR	Bar (abs)	Bar (abs)	kg/m^3	kg/m^3		NPR		
8.33	20.00	2.40	13.18	2.77	4.76	4.56	*CNG*	*FS*
9.35	20.00	2.14	13.18	2.47	5.34	5.12	*CNG*	*FS*
10.00	10.00	1.00	6.59	1.15	5.71	5.48	*CNG*	*FS*
20.00	10.00	0.50	6.59	0.58	11.42	10.95	*CNG*	*FS*
40.00	20.00	0.50	13.18	0.58	22.84	21.91	*CNG*	*FS*
40.00	40.00	1.00	26.36	1.15	22.86	21.91	*CNG*	*FS*
60.00	60.00	1.00	39.53	1.15	34.29	32.86	*CNG*	*FS*
80.00	20.00	0.25	13.18	0.29	45.75	43.81	*CNG*	*FS*
80.00	40.00	0.50	26.36	0.58	45.68	43.81	*CNG*	*FS*
120.00	60.00	0.50	39.53	0.58	68.51	65.72	*CNG*	*FS*
160.00	40.00	0.25	26.36	0.29	91.51	87.63	*CNG*	*FS*
240.00	60.00	0.25	39.53	0.29	137.26	131.44	*CNG*	*FS*
320.00	80.00	0.25	52.71	0.29	183.02	175.26	*CNG*	*FS*
400.00	100.00	0.25	65.89	0.29	228.77	219.07	*CNG*	*FS*

Table 24, High pressure ratio schlieren HSV – Freestream Jets captured in the nearfield

Po/Pa	*Po*	*Pa*	*ρo*	*ρa*	*ρo/ρa*	*Pe/Pa*	*Fuel*	*Cond*
PR	Bar (abs)	Bar (abs)	kg/m^3	kg/m^3		NPR		
10.00	10.00	1.00	6.59	1.15	5.71	5.48	*CNG*	*NF*
20.00	10.00	0.50	6.59	0.58	11.42	10.95	*CNG*	*NF*
40.00	40.00	1.00	26.36	1.15	22.86	21.91	*CNG*	*NF*
40.00	20.00	0.50	13.18	0.58	22.84	21.91	*CNG*	*NF*
60.00	60.00	1.00	39.53	1.15	34.29	32.86	*CNG*	*NF*
80.00	40.00	0.50	26.36	0.58	45.68	43.81	*CNG*	*NF*
80.00	20.00	0.25	13.18	0.29	45.75	43.81	*CNG*	*NF*
120.00	60.00	0.50	39.53	0.58	68.51	65.72	*CNG*	*NF*
160.00	40.00	0.25	26.36	0.29	91.51	87.63	*CNG*	*NF*
240.00	60.00	0.25	39.53	0.29	137.26	131.44	*CNG*	*NF*
320.00	80.00	0.25	52.71	0.29	183.02	175.26	*CNG*	*NF*
400.00	100.00	0.25	65.89	0.29	228.77	219.07	*CNG*	*NF*

Table 25, High pressure ratio schlieren HSV – Impinging Jets

Po/Pa	*Po*	*Pa*	*ρo*	*ρa*	*ρo/ρa*	*Pe/Pa*	*Fuel*	*Cond*
PR	Bar (abs)	Bar (abs)	kg/m^3	kg/m^3		NPR		
8.33	20.00	2.40	13.18	2.77	4.76	4.56	*CNG*	*Imp*
9.35	20.00	2.14	13.18	2.47	5.34	5.12	*CNG*	*Imp*
16.33	40.00	2.45	26.36	2.83	9.33	8.94	*CNG*	*Imp*
24.49	60.00	2.45	39.53	2.83	13.99	13.41	*CNG*	*Imp*
27.59	40.00	1.45	26.36	1.67	15.76	15.11	*CNG*	*Imp*
28.78	40.00	1.39	26.36	1.60	16.44	15.76	*CNG*	*Imp*
40.00	20.00	0.50	13.18	0.58	22.84	21.91	*CNG*	*Imp*
40.00	40.00	1.00	26.36	1.15	22.86	21.91	*CNG*	*Imp*
41.38	60.00	1.45	39.53	1.67	23.64	22.66	*CNG*	*Imp*
43.17	60.00	1.39	39.53	1.60	24.66	23.64	*CNG*	*Imp*
55.17	80.00	1.45	52.71	1.67	31.53	30.22	*CNG*	*Imp*
57.55	80.00	1.39	52.71	1.60	32.88	31.52	*CNG*	*Imp*
60.00	60.00	1.00	39.53	1.15	34.29	32.86	*CNG*	*Imp*
80.00	20.00	0.25	13.18	0.29	45.75	43.81	*CNG*	*Imp*
80.00	40.00	0.50	26.36	0.58	45.68	43.81	*CNG*	*Imp*
80.00	80.00	1.00	52.71	1.15	45.72	43.81	*CNG*	*Imp*
120.00	60.00	0.50	39.53	0.58	68.51	65.72	*CNG*	*Imp*
160.00	40.00	0.25	26.36	0.29	91.51	87.63	*CNG*	*Imp*
240.00	60.00	0.25	39.53	0.29	137.26	131.44	*CNG*	*Imp*
320.00	80.00	0.25	52.71	0.29	183.02	175.26	*CNG*	*Imp*
400.00	100.00	0.25	65.89	0.29	228.77	219.07	*CNG*	*Imp*

Appendix IV – Direct Injector Nozzle Tip

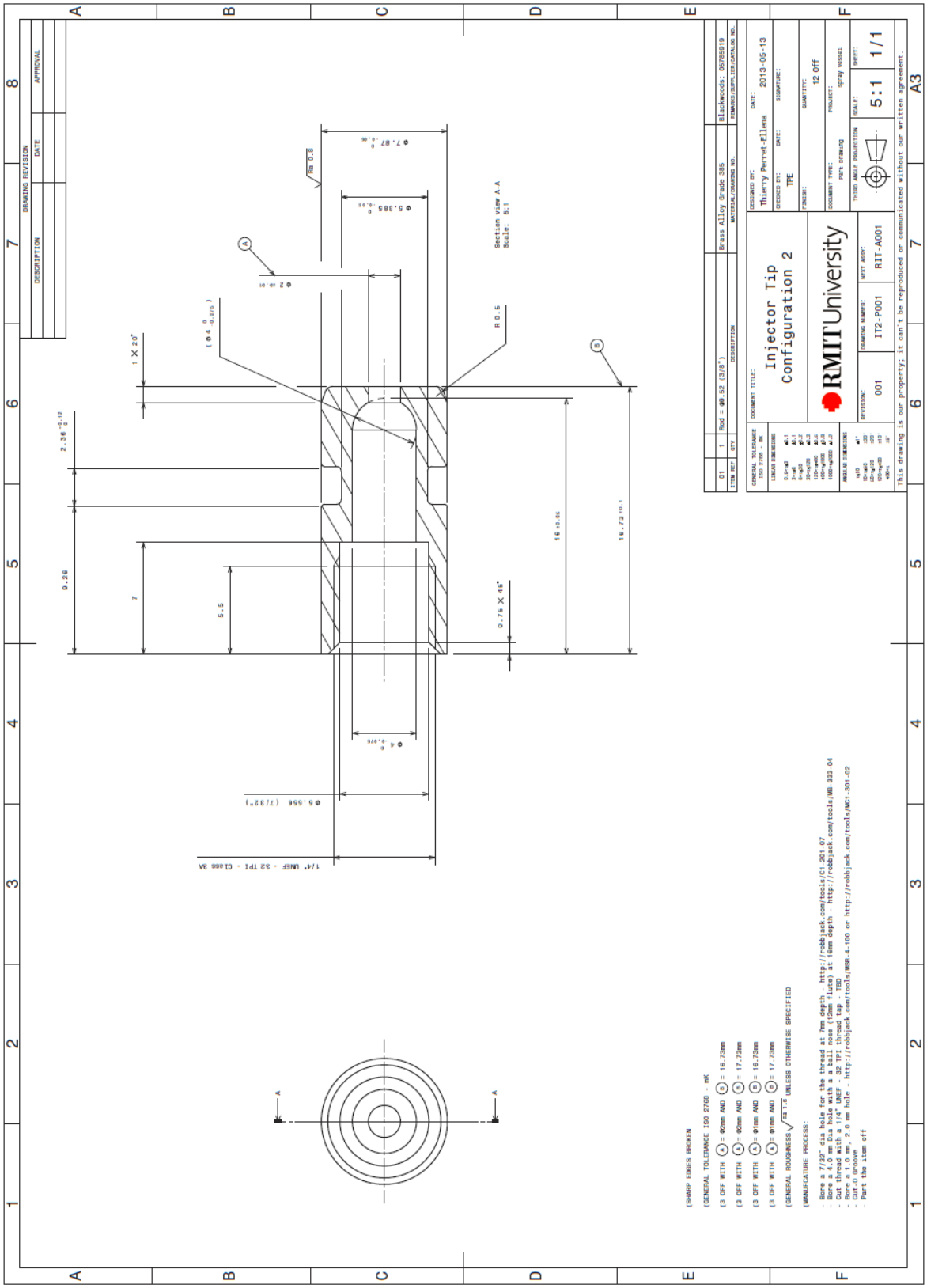

Appendix V – Schlieren High Speed Video Set-Up

Table 26, Schlieren HSV component list.

	Brand/Model	*Specification*
Light Source	CREE/XR-E	Continuously operating LED, 3.78v
Light Source Shaping	Newport/M-SV-0.5	Slit; Width = 0 to 5mm , Height = 12.7 mm
Parabolic Mirror	Edmund Optics	Diameter = 152mm, Focal Length = 1524mm
Flat Mirror	Edmund Optics	4-6 λ, 254 x 254mm
Flat Mirror	Newport/20J00ER.3	≤5λ, 50.8 mm Dia
Cut-Off	OWL/Razor	Blackened razor on position-able mount
Camera	Vision Research Phantom/ Miro or v1610	Refer manufacturer
Camera Lens	Nikon/Nikkor	60 mm f/2.8G ED Macro

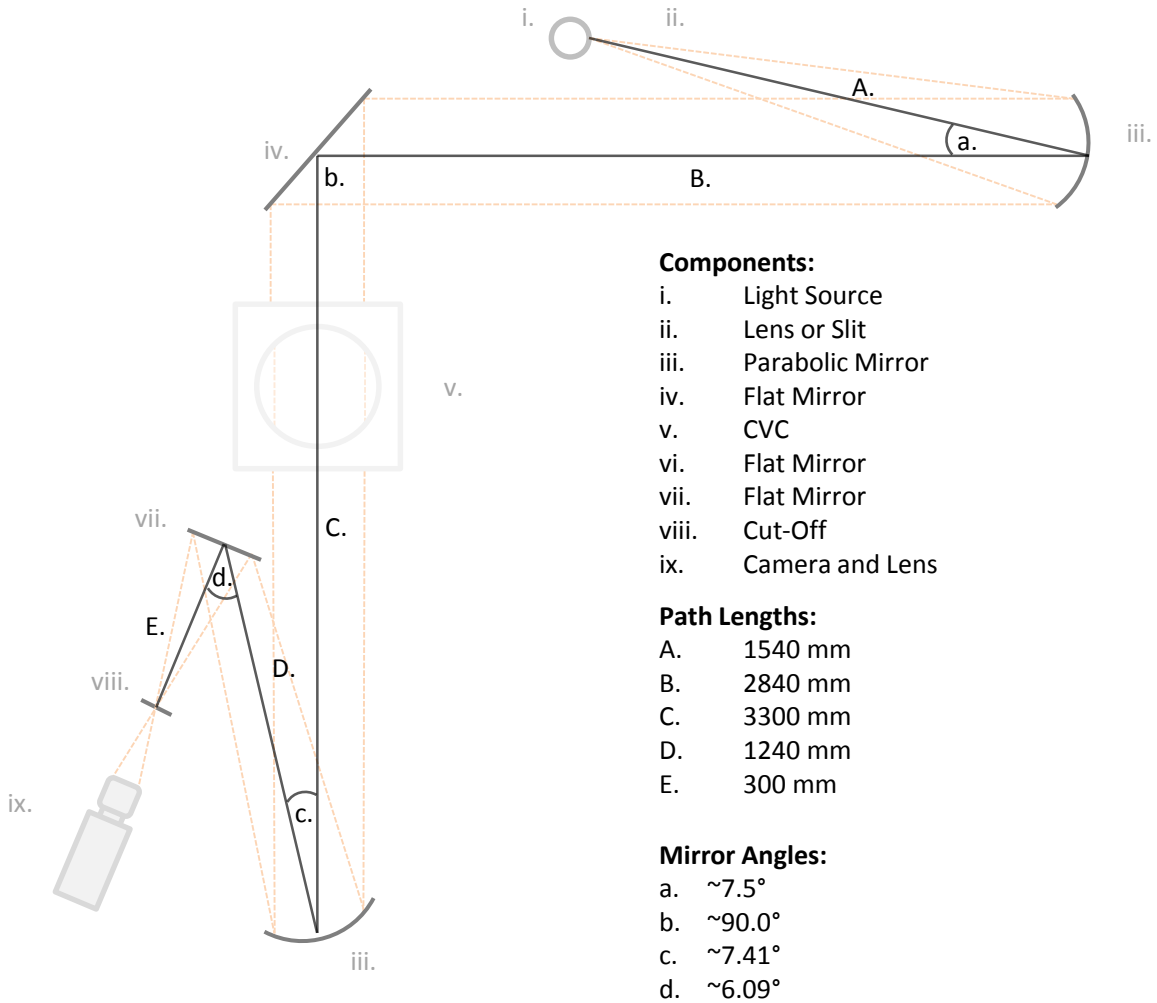

Components:

i.	Light Source
ii.	Lens or Slit
iii.	Parabolic Mirror
iv.	Flat Mirror
v.	CVC
vi.	Flat Mirror
vii.	Flat Mirror
viii.	Cut-Off
ix.	Camera and Lens

Path Lengths:

A.	1540 mm
B.	2840 mm
C.	3300 mm
D.	1240 mm
E.	300 mm

Mirror Angles:

a.	~7.5°
b.	~90.0°
c.	~7.41°
d.	~6.09°

Figure 174, Schlieren layout plan-view.

Appendix VI – Jet Spread Angle

Table 27, Spread Angle Calculations

Authors	*Single or Multi-Point*	*Locations*		*Equation*	*Notes*
		Min	*Max*		
(Naber and Siebers, 1996)	Single	Nozzle Exit	0.5 Z	$\theta = \tan^{-1}\left(\frac{A_{P,Z/2}}{(Z/2)^2}\right)$	
(Naber and Siebers, 1996)	Multi (penetration dependent)	12 mm increments.		$\theta_{I,X} = \tan^{-1}\left(\frac{A_{\Delta P,\Delta X}}{(\Delta X)^2}\right)$	Local dispersion angle for partitions.
(Petersen, 2006)	Single	Nozzle Exit	0.5 Z	$\frac{\theta}{2} = \tan^{-1}\left(\frac{1}{1+4y_z}\frac{A_{P,Z/2}}{(Z/2)^2}\right)$	Modified (Petersen, 2006) approach.
(Delacourt et al., 2005)	Multi (2-Point)	Nozzle Exit	1.5 N_r & 0.7 Z	$\theta = 2\sin^{-1}\left(\sin\left(\frac{\theta'}{2}\right)\sin\left(\frac{\alpha}{2}\right)\right)$ $\theta' = \frac{1}{(Nr_{max} - Nr_{min})}\sum_{r_{min}}^{r_{max}}\theta'_r$	α was the pre-established cone angle.
(Johansen et al., 2013)	Multi (n points)	Nozzle Exit	0.7 Z	$\theta = \tan^{-1}\alpha_{1,t} + \tan^{-1}\alpha_{1,b}$	
(Benito, 2010)	Multi	Nozzle Exit	x/d 18 to 118	$\frac{\theta}{2} = \tan^{-1}\left(\frac{y/2}{(x/d)}\right)$	Liquid Diesel

Appendix VII – Particle Image Velocimetry

	Brand/Model	*Specification*
Laser	Spectra Physics /Quanta Ray PIV-400	Nd:YAG, 10 Hz, 400 mJ @ 532 nm
Sheet Optics PIV	Newport/CSX300 Newport/KBC046 Newport/CSX200	Aspherical Plano-Convex; f = 300 mm Spherical Bi-Concave; f = -25 mm Aspherical Plano-Convex; f = 200 mm
Sheet Optics Standard	Dantec	Height = 35 mm, Width = 0.500 mm, Focal distance = 100 mm, f = 500 mm
Sheet Profile	In-house	Height = 56<100 mm, Width = 0.50-1.00 mm
Dichroic Mirror 1	Newport	1064 nm
Steering Prism	Newport/10SR20	UV Fused Silica, 25.4 mm, λ/10
Camera	Hisense/620	
Camera Lens 1	Nikon/Nikkor	60 mm f/2.8G ED Macro
Camera Lens 2	Sodern Cerco UV	28 mm f/3.5 1990
Energy Meter 1	Dantec	Pulse Energy Meter
Energy Meter 2	Newport/1918-R	Optical Power Meter
Energy Sensor 2	Newport/818P-015-19	Thermopile sensor , 0.19-10.6 µm

Appendix VIII – PIV Timing Location

The following two figures depict the particle image velocimetry constant time ($215\ and\ 415\ \mu s\ aSOI$) and constant location ($30\ and\ 50\%\ fill\ level$) imaging locations against compressible transient phenomena. It can be seen that the constant time locations correspond wholly to the transient region. The $30\ and\ 50\%\ fill\ level$ locations relate to a mix of transient (high PR) and steady state ($PR < 120$), respectively.

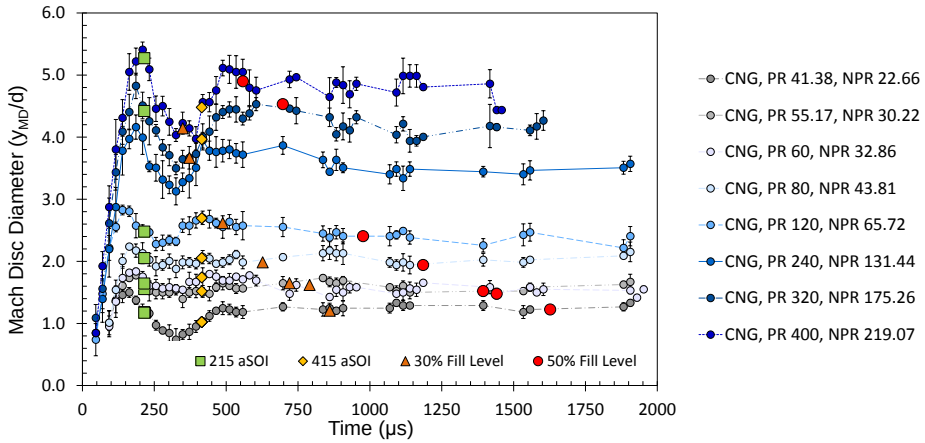

Figure 175, Direct injection high PR Mach disc diameter with PIV timing indicators.

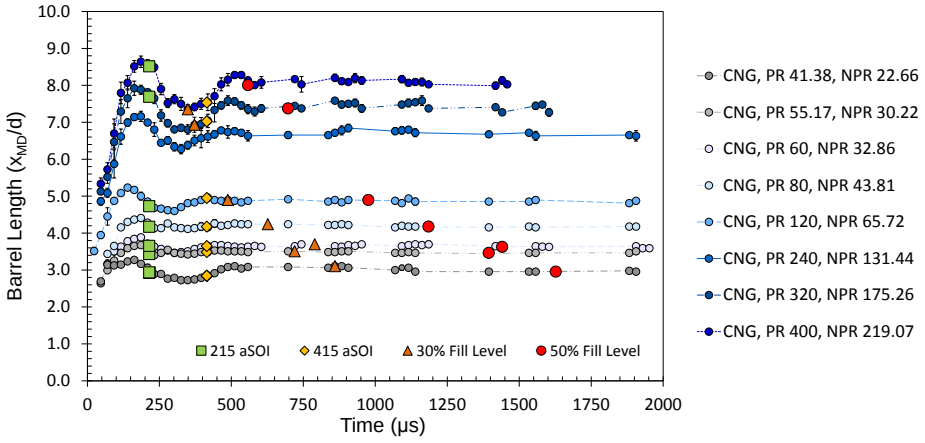

Figure 176, Direct injection high PR barrel length with PIV timing indicators

Appendix IX – Cylinder Filling

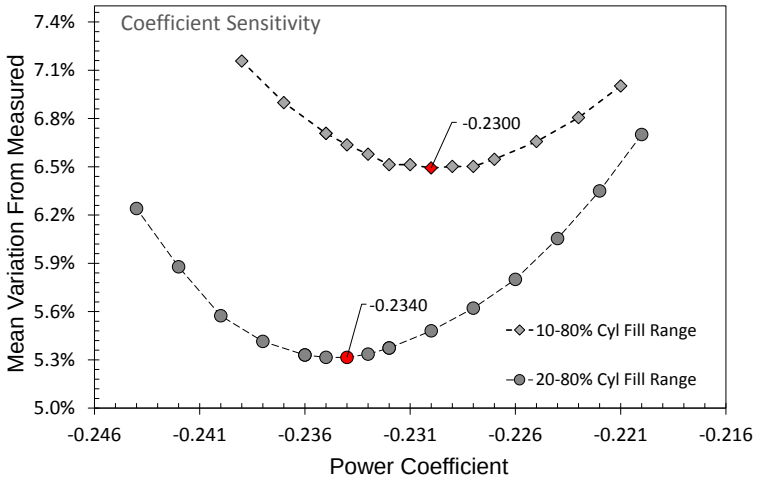

Figure 177, Cylinder fill rate power-law coefficient sensitivity analysis.

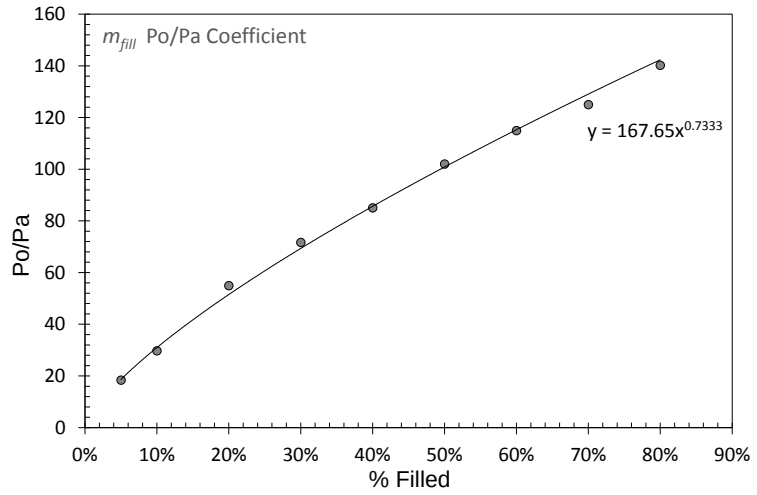

Figure 178, Cylinder fill rate equation coefficient, m_{fill}.

Appendix X – Impinging Jet Vortex

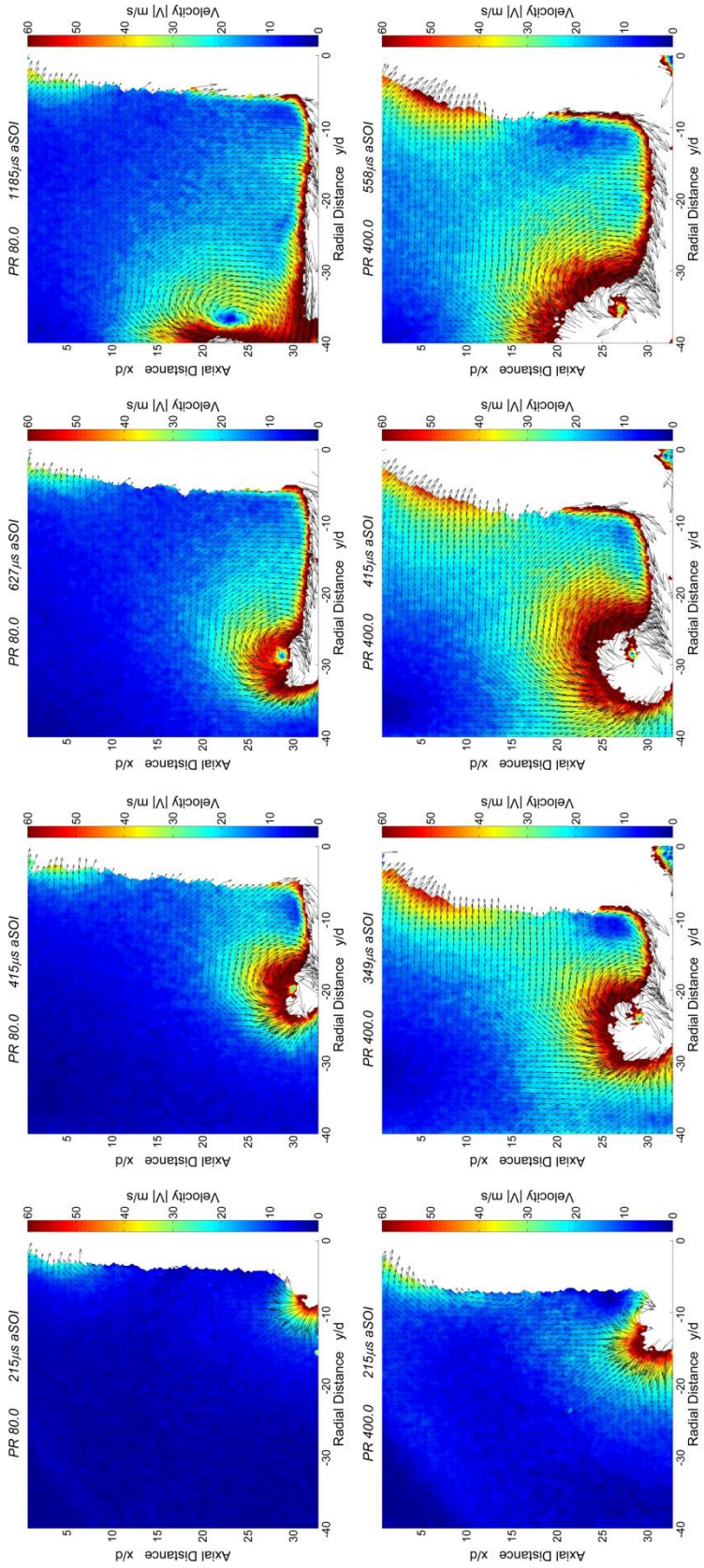

Figure 160, Impinging jet vortex development for PR80 and PR400 CNG Jets. First and last column represent 215 μs and 50% acquisition instances respectively.